ANALYSES OF COMPOSITIONALLY-GRADED CO-CR-ΔMO PROCESSED BY DIRECTED ENERGY DEPOSITION

A Dissertation

by

MICHAEL ALEXANDER LIU

Submitted to the Graduate and Professional School of
Texas A&M University
in partial fulfillment of the requirements for the degree of

DOCTOR OF PHILOSOPHY

Chair of Committee,	Mathew Kuttolamadom
Committee Members,	Satish Bukkapatnam
	Homero Castaneda-Lopez
	Hong Liang
Head of Department,	Ibrahim Karaman

December 2021

Major Subject: Materials Science and Engineering

ABSTRACT

The overarching goal of this work is to investigate the processing, structure and properties of compositionally-graded Co-Cr-ΔMo bulk structures fabricated via Directed Energy Deposition (DED) additive manufacturing. Co-Cr-Mo is a bio-compatible alloy commonly used in hip/knee implants. A bio-inspired strategy to improve surface wear resistance while maintaining the toughness of the bulk structure (*e.g.*, like in mammalian teeth) is to 'tune' the depth-dependent hardness and modulus of the structure via compositional alterations at specific resolutions – elucidating the processing-structure-property framework for realizing this is the motivation for this undertaking. Specifically, this study strives to understand the fundamental influences of laser-based manufacturing process conditions on the resulting macro- and micro-structures, the ensuing material property distributions, and local/global mechanical performance as a function of changing %Mo within the layer-wise structure. For this, experimental designs were deployed to elucidate the effects of process parameters along with compositional differences on the resulting microstructures and mechanical properties of Co-Cr-ΔMo. These helped lay the foundation to understand composition-based laser energy requirements for obtaining structurally-integral parts, the property resolutions achievable, and the resulting mechanical performance implications. With a changing %Mo content, specific types/amounts elemental migrations toward/away from cell boundaries were observed, along with certain intermetallics and carbides being formed at different locations; such spatial composition differences along with the extent of

carbide networks, manifested as sharp hardness transitions. Altogether, this inquiry helped to understand the DED of compositionally-altered structures, the resulting micro/macro structures, and their consequent impact on mechanical properties, thus laying the foundation for the design and manufacture of compositional-graded components.

DEDICATION

This dedication is to my family who has supported me throughout all of my journeys. Further, my friends who I would be nothing without and all those who helped me along my journey. I dedicate this to my startup teammates, the greatest team I could ever ask for.

ACKNOWLEDGEMENTS

I would like to thank my committee chair Dr. Mathew Kuttolamadom for all of his feedback and support these past few years. I would like to thank my committee members, Dr. Satish Bukkapatnam, Dr. Homero Castaneda-Lopez, and Dr. Hong Liang, for all of their support and time.

I would like to thank Nick Barta and Michael Elverud for their support and knowledge. They were instrumental in developing the builds for Co-Cr-Mo via LENS and the subsequent builds henceforth. Specifically their knowledge on compositional gradients allowed the work to be successful.

I would like to thank the staff at the Materials Characterization Facility (MCF) specifically Drs. Andrew Mott, Wilson Seren, and Winson Kuo for all of their help and support.

Thanks also go to my friends especially Jon Marino and colleagues and the department faculty and staff for making my time at Texas A&M University a great experience.

Finally, thanks to my mother and father for their encouragement and support throughout my life. Also, I would like to thank all of my friends who have continued to support and help me throughout my graduate studies.

CONTRIBUTORS AND FUNDING SOURCES

This work was supervised by a dissertation committee consisting of Professor Mathew Kuttolamadom and Professor Homero Castaneda-Lopez of the Department of Materials Science and Engineering, Professor Satish Bukkapatnam of the Department of Industrial and Systems Engineering, and Professor Hong Liang of the Department of Mechanical Engineering.

XRD measurements were performed by Dr. Bandyopadhyay of the Department of Materials Science and Engineering and Dr. Reibenspies of the Department of Chemistry. Michael Elverud and Dr. Nick Barta of the Department of Materials Science and Engineering assisted with all LENS printing including G-code, machine operation, and development of the printing strategy. Dr. Andrew Mott assisted with electro-etching and electron microprobe measurements at the Materials Characterization Facility. Dr. Wilson Seren provided assistance with Nanoindentation and Nanoscratch testing at the Materials Characterization Facility. Dr. Winson Kuo provided the knowledge regarding SEM and EDS measurements. Daniel Lewis and Tejas Umale provided assistance with the optical microscopy section. Yash Parikh provided input towards microindentation and ImageJ assistance.

All other work for the dissertation was completed independently by the student.

NOMENCLATURE

B/CS	Bryan/College Station
CCM	Co-Cr-Mo
DED	Directed Energy Deposition
CG	Compositional Gradient
FCC	Face Centered Cubic
FGM	Functionally Graded Materials
h	Hatch Spacing
HCP	Hexagonal Close Packed
LENS	Laser Engineered Net Shaping
P	Power
SLM	Selected Laser Melting
t	Layer thickness
VED	Volumetric Energy Density
W	Watts

TABLE OF CONTENTS

Page

LIST OF FIGURES

Page

LIST OF TABLES

Page

CHAPTER I

INTRODUCTION

1.1 Aim and Objectives

Additive manufacturing (AM) offers an opportunity to develop hard to manufacture structures with precision and control not possible with traditional methods. In the past forty years, academic and industrial organizations have filed over 3500 patents in relation to AM from 1975 to 2011 [1]. Current AM technology builds structures through layer-by-layer addition thereby reducing the amount of material used and offering more precise control of structure. AM methods provide an opportunity to create near net shaped parts using feed material from the three main material types: polymers, ceramics, and metals.

For all the different types of metal AM fabrication methods that use a laser, there are two major categories: powder bed fusion (PBF) and directed energy deposition (DED) techniques. The former refers to depositing a layer of powder across a bed as a laser or electron beam heats specific areas in a sequence to polymerize the deposited layer with either the substrate or the previous layer in the build. Layers are built upon each other until the specific height of the structure is reached. Examples of this type of metal AM method include selective laser melting (SLM), selective laser sintering (SLS), electron beam melting (EBM), direct metal laser sintering, and selective heat sintering (SHS). These materials are known to possess comparable or improved mechanical properties with respect to wrought or common commercial samples. In contrast, DED techniques feature powder being shot from a nozzle and coinciding with a beam where a

layer of metal deposits on the surface. The nozzle moves in different directions and is not confined to a certain axis. This method proves especially useful to simultaneously deposit and form a part within a similar region [2]. DED has variety of different types as well including directed light fabrication, direct metal deposition, and 3D laser cladding. For the purposes of our discussion, we will be focusing on DED based techniques, specifically Laser Engineered Net Shaping (LENS).

To impart the intended structure and properties, operators must optimize process parameters based on the design and material used. The purpose of this work is to evaluate both resulting structure and properties of Co-Cr-Mo based on varying process parameters and composition. These results can be extrapolated to further Co-Cr-Mo research and establish principles for use on other hard to manufacture materials [2]. In this study, DED-made Co-Cr-Mo bulk structures are evaluated for their aesthetic and material properties. The influence of specific process parameters on the material properties of the structures is analyzed. DED of Co-Cr-Mo is evaluated through manufacturing quality, microscopy and spectroscopy studies, and mechanical testing.

The initial inception of orthopedic implants began as all-metal hip joint replacements. Hampered by poor design, machinability issues, and poor surface finish, these metal joint implants were supplanted by polyethylene bearings. Polyethylene based materials possess their own shortcomings as a considerable portion of individuals were found to be allergic to the implants thus rendering them somewhat useless. Moreover, between 1990 and 2002, the need for total hip arthroplasty revision in the U.S. was on average 17.5% while total knee arthroplasty average 8.2% [3]. Since joint implants are

typically customized to a specific user, these devices have traditionally been created as a straightforward and feasible method to produce an array of implants in the medical devices market. While patient-related factors, like inferior bone quality and high body mass index, are important contributors, the main source of implant failure is wear phenomena and stiffness incompatibility [3]. Implants discharge particles and soluble wear debris that are dissolved into the bloodstream when surfaces contact. In particular, the presence of metal ions in the peripheral blood stream and hip synovial fluid can generate serious side effects on patients that require long-term implant use [4]. The reaction to the wear particles of a variety of biomaterials is considered a pertinent reason for asceptic loosing. Thus, selecting the proper material is a crucial component to reduce wear phenomena.

Literature points to solutions that focus on limiting aseptic [free from contamination] loosing such as wear-resistant ceramics like zirconia-toughened alumina and wear-resistant metals such as Co-Cr-Mo [3]. Co-Cr-Mo offers high hardness and excellent tribological properties such as high resistance to wear and corrosion [4]. The biocompatibility of Co-Cr-Mo alloys promotes their use in biomedical implants like total hip and knee replacements [5-7]. Co-based alloys are also used in aerospace, automotive, power generation, and oil and gas industries to provide wear resistant components and as coatings, particularly in lubrication-starved, high pressure and high temperature, and corrosive environments. With the advent of AM, the design and development of Co-Cr-Mo for biomedical implants is more attractive and feasible due to the ability to make near net shape parts. The rapid melting and solidification cycles within the AM process

have been shown in some cases to affect detrimental intermetallics (typically brittle) that are typically formed during slower cooling cycles. These AM alloys exhibit varied biocompatibility, corrosion resistance, and material properties [8, 9]. Applications such as knee implants, metal-on-metal (MOM) hip joints and dental prosthetics require alloys that possess specific stiffness and high wear-resistance.

Revision surgeries for implants occur most frequently due to structural incompatibility between the implant and original bone. Orthopedic implants are typically made of stiffer materials than natural bone tissue (other than scaffolds which are not made to support load-bearing operations) which changes the stress response differently than normal physiological conditions. Bones are dynamic structures that adapt to variations in mechanical simulation and can self-repair [3]. Stress and strain distributions are controlled by external forces and the contour and properties of the bone. If bones are replaced with a material of different mechanical properties, the stress and strain alignment is fundamentally different regardless of similar load. Due to its higher stiffness, a biomedical device experiences a stress level lower than it should be leading to the bone resorbing, a development called “stress shielding”. Implant supports are weakened during bone resorption around the graft which causes bone fracture and implant loosening [3, 10]. Thus, the utilization of compositional gradients through LENS offers an ability to augment material properties at specific sites that can help reduce the instance of revision surgeries.

Additive manufacturing for medical applications has gained wide implementation due to the beneficial nature of rapid prototyped models for treatments,

diagnosis, implants, and surgical equipment. In 2013, medical and dental industries were responsible for 13.7% of the entire AM industrial revenue [11]. Due to the inefficient standardization and infeasible sterilization of prosthetics, patients' needs cannot be as easily met. Medical products fabricated through AM are moving toward high suitability, low cost, and rapid manufacturing response [12]. Furthermore, metal-on-metal (MOM) bearing surfaces are accruing greater interest in implants specifically for situations where large areas of contact are involved. MOM hip implants have been reported to survive more than 25 years with low wear rates and minimal osteolysis [13].

The overarching goal of this study is to analyze the processing, structure and properties of compositionally-graded Co-Cr-ΔMo bulk structures additive manufactured via Directed Energy Deposition (DED). In particular, the study seeks to understand how compositionally altering Co-Cr-Mo can lead to specific macro- and microstructures that influence the depth-based hardness and modulus. To achieve this goal, the following objectives were coined:

- Conduct a systematic design of experiments to understand how the increase in ΔMo affects the manufacturing process parameters required,
- Analyze the influence of ΔMo on the macro- and microstructures of Co-Cr-Mo fabricated via DED, and
- Correlate the effects of processing parameters and microstructures with the resulting mechanical property changes caused by varying Mo content within the fabricated alloy.

1.2 Motivations

This study is an effort to tune the depth-dependent hardness and modulus to improve surface wear resistance while maintaining the toughness of the bulk structure. Compositionally grading an alloy is a bio-inspired approach to achieve this. Investigations on the DED Co-Cr-Mo alloys are rather limited and even more so regarding compositional gradients.

Structural engineering can benefit from blending 'incompatible' properties like high hardness and ductility. Biomedical implant surfaces can also obtain improvement through compositional gradients. Location or layer-based change of %Mo can tune spatial property distribution. Increasing %Mo on the alloy surface can lead to higher surface hardness, corrosion resistance, and/or wear resistance. Further, increasing Co-Cr-Mo concentration (vs. Ti-6Al-4V) on a surface increases biological cell growth (osteointegration), and increases wear resistance. This is evident in Figure 1 where the increase in Co-Cr-Mo influences not only the wear coefficient, but also, the growth of bone cells. In this case, an optimal percentage of Co-Cr-Mo (86%) yields the lowest wear coefficient and highest probability for growth of bone cells.

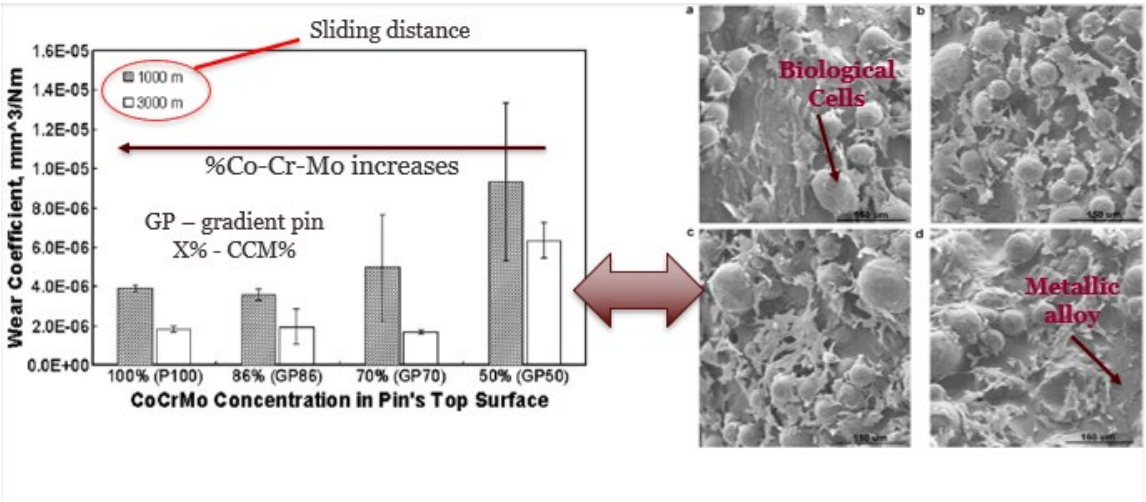

Figure 1: (Left) Effect of Co-Cr-Mo concentration on wear coefficient with corresponding bone cell growth (right) for (a) 50%, (b) 70%, (c) 86%, (d) 100%. Reprinted from [13, 14].

Biomedical implants often require transitions between material interfaces to improve cohesion. Gradients within a coating surface can reduce issues with property mismatches between materials such as Co-Cr-Mo on Ti-6Al-4V as shown in Figure 2. If these mismatches are not addressed, defects such as cracking may occur.

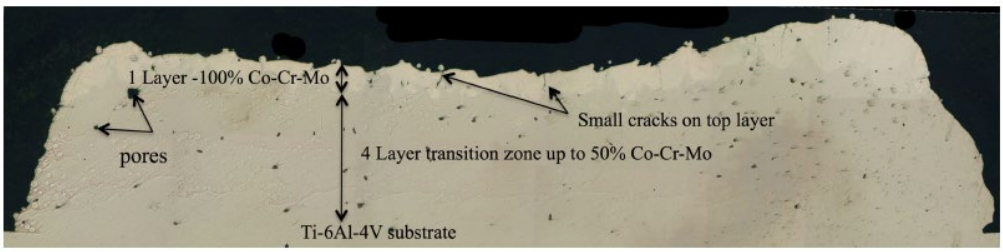

Figure 2: Transition region between Ti-6Al-4V substrate and Co-Cr-Mo coating. [14, 15]. Reprinted from [15].

In metal-metal interfaces like Ti-6Al-4V and Co-Cr-Mo, interfaces between build and substrate can be compositionally graded with the addition of an element (Mo) which can reduce property mismatches and stress concentrations, beyond the typical improvement in cohesion between material. Compositionally graded coatings/interfaces can help prevent delamination at the interface between a substrate and coating.

Finally, this strategy provides insight into the spatial material property distributions of Co-Cr-Mo compositionally graded with increasing Mo via DED [14]. Co-Cr-Mo is a notoriously difficult material to machine thus additively manufacturing builds that are provides great value to industry and academia. Gradients can also tailor depth dependent properties (i.e. hardness) of a coating. Studies such as the one reported here can form the backbone of future work to develop tailorable materials.

CHAPTER II

BACKGROUND & LITERATURE REVIEW

2.1 Laser-based Metal AM

The history of Additive Manufacturing (AM) can be traced back to earlier laser based AM type of work that has been utilized in powder metallurgy, laser welding, arc welding and similar applications for over eight decades [2]. In the 1930s, metal-based AM was first developed through manual layer-by-layer builds made by arc-welding and high pressure [16]. Five years later, Harter expounded on a process where molten beads of weld material could be layered in succession to create a bottom up structure [17]. The 60's and 70's observed the evolution of 'welding-based AM' coinciding with patents on rotary-based, continual arc-welding for AM of solid structures and more [18-20].

By the 1980s, a paradigm shift in AM metal working started with patents from Housholder and Brown et al. which would initiate laser based additive manufacturing [21, 22]. Housholder offered a technical description that was a precursor to powder based feed technology. Brown et al created the basis for DED which further evolved with patent additions by Lewis et al and Jeantette et al [23, 24]. Their contributions lead to the contemporary processes that are employed in laser-based metal AM processes today.

AM constructs parts layer-by-layer through a CNC (computer numerical control) displacement that follows a three-dimensional (3D) model. These models are made by computer aided drawing (CAD) software that create the models in a format such as Standard Tessellation Language (.STL). A designer can develop a part and 'slice' the

part into layers thus informing the CNC which direction to go. Fast fabrication of complex (i.e. composition, geometry) parts such as overhang structures are possible using AM which improves design and application flexibility. Current effects traverse a wide variety of industries including aerospace, corrosion, and medical.

To successfully deposit metal through AM, enough energy must be provided to overcome the enthalpy of fusion and the high melting temperature characteristic of metals [2]. DED creates a part without supports due to its coaxial laser head and nozzle-based powder delivery system. Housed within the same frame as the powder nozzles, the laser provides the required thermal energy to melt powder along the line of deposition. The concentrated laser energy produces a molten pool of liquid metal with a subsurface heat affected zone (HAZ) of varying penetrative depth. Once a layer is deposited, the head raises to accommodate the next build layer [2, 25].

The DED process can be a difficult process to model and control because of its large process space. To generate melting adequate for the layer-by-layer addition process utilized by laser-based techniques, DED and PBF processes may involve a laser or any thermal energy source large enough to achieve the conditions of successful deposition. For laser-based processes, DED processes are classified under the direct laser deposition (DLD) umbrella. A Nd:YAG (neodymium-doped yttrium aluminum garnet) laser is standard for DED systems with a power range of 1-5 kW [26-28]. Other laser types, such as CO_2 and pulsed-wave lasers, can be used if there is enough power to melt the material [24, 29-31]. DED parts may require a post-AM machining process due to the roughness exhibited.

In the latter portion of the 90's, Sandia National Laboratory developed a process called laser engineered net shaping (LENS), another powder-based direct energy deposition technology that incorporates multiple nozzles for more effective powder delivery [24, 32-35]. A depiction of the inner chamber and delivery system is provided in Figure 1. LENS is currently the standard means to developing laser powder feed-based materials thereby making it proprietary eponym for DED.

2.1.1 Directed Energy Deposition

Directed Energy Deposition (DED) is an additive manufacturing (AM) technique that shows great promise in precision manufacture of near-net shape parts. Figure 3 depicts physical events that occur during the DED process over time. Currently, typical parts produced include complex prototypes, tooling pieces, and small-lot production items. DED offers a unique solution to fabricating near net-shape metal parts in that structures are made directly from powder/wire stock thereby circumventing forming operations, such as casting and forging, and post-build machining [36]. DED can create near theoretically dense parts, control a process for accurate part fabrication, tailor deposition parameters for speed, accuracy, and property control, deposit composite and multi materials, fabricate complex geometries through a 3-4 axis system, and can result in mechanical properties similar or better than traditional fabrication routes. This process reduces the post processing operations required in traditional forming operations such as casting, forging, and rough machining [36]. Figure 4 presents a schematic of the DED inner chamber.

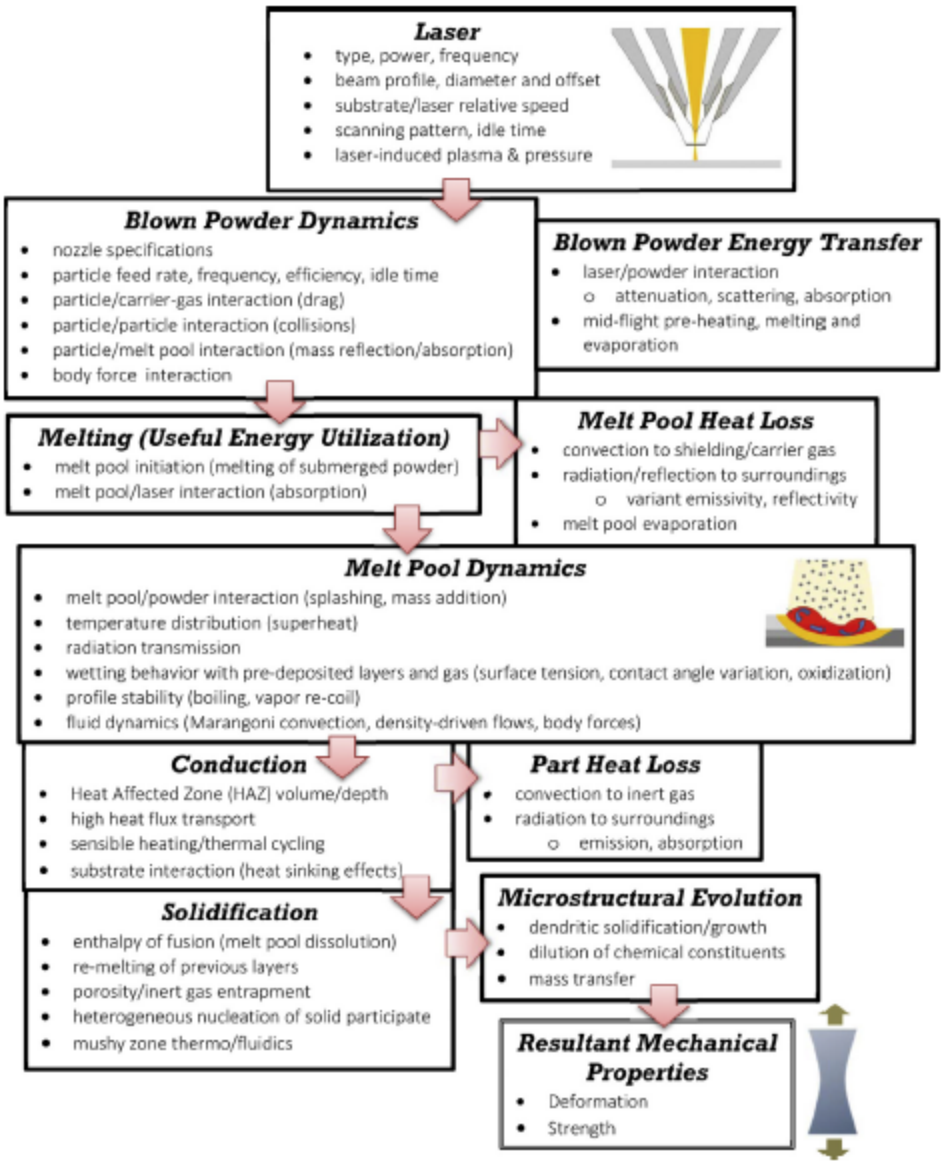

Figure 3: Physical events that occur during DED over time. Reprinted from [2].

The effectiveness of DED process is measured on their powder usage efficiency; the ratio between the powder deposited and the actual amount of powder delivered by the system over a given period. DED processes typically employ powders that fall within the range of 10 to 150 μm and are mostly spherical in shape. Spherical-shaped particles

pack more efficiently which leads to higher bulk densities and hence can also decrease the incidence of trapped inert gas within the melt pool.

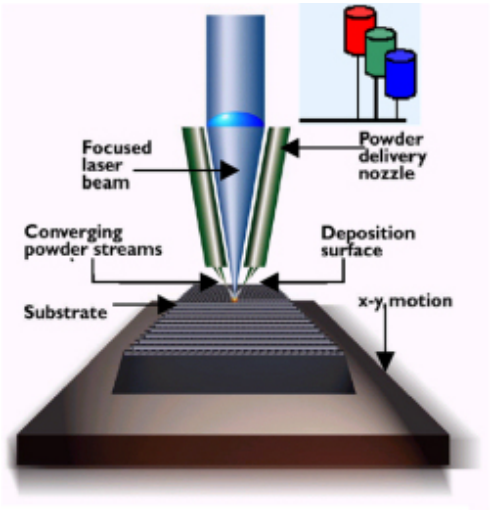

Figure 4: Schematic of laser engineered net shaping (LENS) inner chamber and delivery system. Reprinted from [36].

Deposition efficiency depends on nozzle geometry, angle, powder size distribution, and energy density among others. When deposition efficiency is low, there is a large proportion of unused powder that collects at the bottom of the build chamber. This powder also gathers in hard-to-reach areas within the build chamber thereby rendering recovery difficult. DED's unique powder delivery offers unique functions like repair and coating of parts [37, 38]. Further, the integrated laser-powder feed system helps create functionally graded parts with variable composition and location dependent properties [3, 39, 40]. Due to the nature of the deposition method, different parameters related to the scan speed, laser power, powder feed rate, scan orientation, layer height, and working distance among others must be considered with respect to the overall design

philosophy. Thermal distributions and fluid flow are important considerations as deposition of the powder occurs. The most commonly studied parameters are the melt pool initiation (powder melting), 'intra-part' heat transfer which includes conduction (melt pool to substrate), and heat generation and loss (solid state transformations) [2]. Mechanical tests on DED-made materials have demonstrated in some cases better mechanical properties that rival one made via traditional methods. Mudge and Wald corroborated this in their review of laser engineered net shaping (LENS). Some LENS deposits show improvement in material properties over comparable castings and wrought products [39].

2.2 Functionally-Graded Materials

2.2.1 History of Functional Gradients

Introduced in Japan to describe thermal barrier coatings by Koizumi and Niino, functionally graded materials (FGMs) are structures that possess properties that vary gradually in one or more dimensions to serve unique service requirements. Functional gradients can reduce material property mismatches that occur when joining two dissimilar materials. A variety of industries can benefit from the use of functional gradients including aerospace, biomedical, defense, energy, opto- and thermo-electronics [41-43].

Functionally graded materials (FGM) were borne to mitigate the detrimental effects of thermal stress mismatches and to improve the lifespan of metal-ceramic composites in severe environments [44]. Early attempts at controlling the properties of a

material included carburizing and nitriding for optimized surface characteristics. These operations concern the diffusion of C or N, from the surface towards the bulk of the material thereby augmenting the material properties through a gradual gradation. Technologies that can perform this procedure include chemical vapor deposition (CVD), physical vapor deposition (PVD), powder metallurgy (P/M), thermal spray, sol-gel methods, liquid metal infiltration or alloy infiltration of sintered ceramic material with graded porosity and self-propagating high-T combustion synthesis [45-49]. FGMs are designed through a few primary construction profiles such as parabolic, hyperbolic, or linear, with variably thick layers that depend on the method of development. Typical roles of these constructs can either be an independent system that performs a given role or a top layer that is deposited on a substrate [50].

FGMs are created with the purpose varying specific properties which afford changes in chemical, mechanical, magnetic, thermal, and electrical properties [40]. Studies done on crafting new functionally graded materials focuses on inspiration from nature such as mollusk shells which have hierarchical organization, spider fangs with needle-like injection, and the narwhal tooth which features a graded cementum-dentin junction. Tissues and organs in the human body also follow the structure of naturally developed functionally graded materials. The individual layers offer different properties and functions such as those exhibited in human joints, tendon-to-bone, and cartilage-to-bone that possesses ligaments that joins the tissues together. To emulate the structures that naturally occur, gradients can be constructed through different principles of manufacturing. FGMs are prepared in a process that is constituted of 2 steps: gradation

and consolidation. Gradation processes are completely independent and include the formation of layers of differing composition percentages. Consolidation is performed to diminish or eliminate cracks and discontinuous interfaces by connecting two dissimilar materials [51-53]. Figure 5 depicts different potential material composition property transitions.

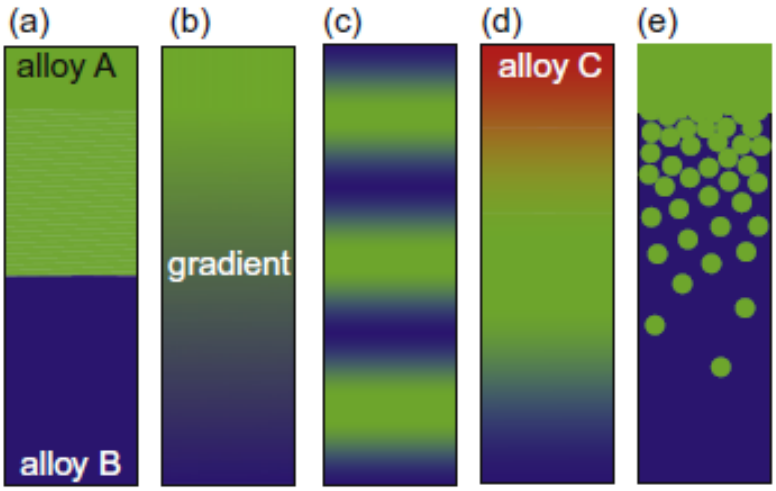

Figure 5: Schematic of different material composition/property transitions. Reprinted from [2].

2.2.2 Types of Functional Gradient Designs

FGMs comprise designs where properties change at a specific region to meet an intended use such that material properties, particularly mechanical, are improved. Currently feasible applications include functionally graded coatings, 3D parts, and scaffolding (devices with porosity gradients). Considering design at different scales could improve overall material properties. Resistance to sliding and impact can be increased by developing a gradient from the point of contact [54, 55]. Transition regions

are typically a cause for concern when joining two dissimilar materials. Two types of functionally graded materials exist: those that are constructed through layer-wise addition to build the part up and those that are developed through diffusion to create a gradient [56]. FGMs can come in three forms: porosity gradients, microstructure gradients, and compositional gradients. In porosity gradients, the amount of porosity varies depending on position in the bulk material. These types of gradients are typically utilized in implant technologies where implant weight can be changed, and the elastic modulus can be improved to emulate human tissue. Porosity gradients can be created either by porosity density gradation or pore size gradation. These two types can be accomplished through variation of powder particle sizes and location dependent synthesis in the bulk material through the gradation process. Microstructural gradients can develop from the solidification process when the material surface is quenched thereby developing improved surface hardness of the material. These gradations can also be created during a controlled heat treatment process. Microstructural gradient FGMs are applied in parts that require increased surface resistance to wear and a tough core to reduce the high impact energies that are experienced during use. Compositional gradients, the focus of this work, are a type of functional gradient that exhibit an increase in the percentage of one type of material at the expense of one or more of the other types of material that exist within that region.

2.2.3 General Methods for Creating Functional Gradients

Functional gradients are possible between different types of materials. Metals and ceramics can be joined together into more seamless structures. In a study performed in 1994 by Giannakopoulous et al, different combinations of geometry, physical properties and compositional gradients were studied for the evolution of curvature and thermal strains along with the initiation of plastic yielding for both thermoelastic and thermoplastic deformation [44]. For their work, elastoplastic analyses were performed on multi-layered materials that featured fixed compositions of metal and ceramic layered upon each other with a compositionally graded interface. The selection of compositional gradient can provide the optimal geometry or maximize mechanical performance.

Conventional fusion welding can affix similar metals and, less commonly, join dissimilar metals [56]. From this practice came the initial use of intermediate layers to separate two dissimilar metals such that the welding operation could become easier [57]. Another common methodology to connect dissimilar metals is to use high-energy density techniques like lasers to preclude cracking and embrittlement issues [58]. Cracking and embrittlement have been linked with insolubility between joining surfaces, mismatch of atomic structure, difference in thermal expansion coefficient, and development of stable brittle intermetallic phases along the compositional gradient [58]. Welding also presents further chemical based challenges regarding nonuniform compositional inhomogeneities which cause susceptibility to corrosion and hydrogen cracking [59].

2.2.3.1 Methods to create Metal/Ceramic Functional Gradients

Combining metals and ceramics has proven to be a somewhat challenging process due to the difference in various material properties. The introduction of an interlayer offers a smooth transition between the two dissimilar materials. In their work, Chmielewski mentions the use of Cr-Al_2O_3 functionally graded interlayers to join ceramics to steel. Another metal-ceramic functionally graded material mentioned by Chmielewski is NiAl-Al_2O_3 for use in automotive valve applications where the final densification method is performed through hot-pressing in an argon atmosphere [50]. Cu-AlN functionally graded materials are also discussed as heat dissipation parts for use in the electronics industry. These materials are fabricated through powder metallurgy methods and possess compositional variation ranging from 10-40% for the ceramic portion.

High velocity oxygen fuel (HVOF) spraying is another method by which a functional gradient between metals and ceramics can be achieved. Valarezo et al. utilizes this technique to impart a damage tolerant coating to a material substrate [60]. The thick functionally graded composite is comprised of 6 layers under a stepwise change in composition from a bottom layer of 100 vol% AISI 316 SS toward a top layer of 100 vol.% hard WC-12Co that was then deposited upon an AISI 316 SS substrate. Disparities between material properties between two constituents sometimes yield thermal and mechanical residual stresses in a structural component. Creating graded structures without a narrow boundary zone offers a reduction in the occurrence of these stresses [42, 54]. Valarezo et al. show compressive stresses exist in the lower metallic

layers due to the peening effect of successive shooting of powder which then moves to high tensile stress in the top layers. This can impart positive residual stresses in a built-up part that remain in the material post fabrication thereby reducing the amount of stress the overall structure can experience before failure. The functional gradient concept has also been applied to thermal stresses through thermal barrier coatings to suppress crack formation along the bond coat and topcoat interface [61-63].

2.2.3.2 Methods to create Metal/Metal Functional Gradients

Metal matrix composites (MMCs) are multi material structures that utilize two different metal materials for the purpose of selective reinforcement such that particular regions exhibit increases in modulus, strength, and/or wear resistance. As such, these structures can extend the industrial application of MMCs over its standalone components. Development of these types of materials can be achieved through a few avenues.

Centrifugal casting requires initial preparation and layout of composite constituents after creating the final product by utilizing certain melt processes. Such operations include but are not limited to: melt infiltration in a graded preform, sintering of gradually stacked powders, and mold filling with melts of varying composition [42]. Electromagnetic field utilization applies one or more external force fields exerting different forces on separate constituents in a liquid composite slurry. Fields that fall in this category include gravitational, thermal, magnetic, electrical, electro-magnetic, ultrasonic and others.

Porous structures are also achievable in MMCs thorough gas reinforcement specialized equipment known as gasars that control external gas pressure and solidification velocity [64]. For surface level structural gradation, techniques to satisfy these specific applications have been developed: chemical treatment, mechanical attrition treatment, severe plastic deformation [65-67].

An early precursor of current laser-based technology, direct laser fabrication, allows for the development of a compositional gradient between two different materials with the same major constituent. Mei et al. was able to reinforce Ti-6Al-4V with TiC as a compositional gradient material through direct laser fabrication by feeding TiC powder and Ti-6Al-4V wire simultaneously to a laser focal point [68]. Composition was shown to change along the length as anticipated due to the variation in feed rate from the different capture efficiencies for the powder and wire. Regions where TiC fraction was high, some unmelted TiC was observed but along large portions of the length of the samples, TiC was completely melted. The completely melted TiC formed primary, eutectic, and secondary TiC phases. The compositional gradient system provided improvement in tribological properties as the TiC reinforcement particles offered optimal friction resistance when 24 vol.% of TiC was included. As is necessary to create successful compositional gradients, the transition region between TiC and the 100% Ti-6Al-4V is basically smooth. The gradual increase in the TiC powder feed rate showed a corresponding increase in hardness of the dual material system. However, upon adding TiC to an amount greater than 74%, brittle features were observed indicated by the observation of surface deep wear tracks that featured some fractures [68].

2.2.3.3 Addressing Challenges in Metal/Metal Functional Gradients

In response to the cracking and embrittlement characterized by melting processes, solid state-based welding processes such as ultrasonic welding (UW) and friction stir welding (FSW)) can avoid the detrimental consequences of joining two dissimilar materials. Ultrasonic welding is typically utilized in thermoplastic parts to join complex features and can be easily customized to fit exact specifications of the welded parts. In the case of friction stir welding, a deformation mechanism joins two materials through a much harder tool thereby creating a weld in solid state [69]. Unlike the joining process of thermally based welding, this mechanism yields a purely mechanical bond which consequently avoids fusion welding problems but develops a miniscule boundary zone between the workpiece metals versus a compositionally graded region [70]. To develop a gradient of properties in a bulk structure, methods of similar principle to those described above such as friction stir processing (FSP) and submerged friction stir processing (SFSP) can be utilized. These methods change bulk material properties through the application of severe plastic deformation over a much larger zone [71].

2.2.3.3.1 Manipulating traditional techniques

In more recent work, new techniques manipulate traditional methods to create compositional gradients. Sam et al offered a centrifugal casting method and post processing heat treatment to study the mechanical and tribological properties of a functionally graded Cu/Al_2O_3 composite [72]. A metal matrix composite (MMC) of Cu-10Sn-5Ni with 10 wt.% Al_2O_3 reinforcement was created through the centrifugal casting

method. An optimizing parametric heat treatment at 450 °C for 3 hours to yield a maximum hardness (269 HV) was further considered. Originally synthesized through sintering techniques copper and Al_2O_3 (alumina) offer higher strength and good corrosion resistance when combined versus the base alloy. For Cu specific MMC's, a functional gradient offers enhanced bond strength at the interface connecting two dissimilar materials that are part of the alloy composition. Centrifugal casting method for creating functionally graded materials were focused on diminishing interfacial stresses, maintaining structural strength and ductility, and developing for certain functions and utilities [73]. Mechanical properties of these composites are typically influenced by their bond strength between constituent materials, homogeneity, and grain size which each need to be optimized in order to reduce risk or failure [74].

2.2.3.3.2 Heat Treatment

Heat treatment provided unreinforced material relief of internal stresses within the composite [72]. These heat treatments allowed for a certain degree of microstructural homogeneity of Ni-Al bronze and the phase coarsening become prevalent as the system was further exposed to the treatment and temperature of solutionizing. Parametric optimization was performed to create the best combination for maximum hardness [72]. An elevated temperature quench in the range 70-1500 °C for the Cu-Ni alloys developed extremely hard and brittle martensitic beta phases followed by an aging that brought on the preferred ductility and strength [72]. When these alloys are formed through powder metallurgy, an enhancement of 20-40% to wear resistance is imparted along with

stronger resistance to bending [75]. Tribology of these Cu MMCs have been analyzed regarding the applied load, volume fraction of the reinforcement particles, sliding velocity, sliding distance, and the nature of the reinforcement. In these studies, load had the largest effect on wear rate. In the Sam study, samples were prepared from an inner region that featured reinforcement phase rich in alumina that formed due to the centrifugal force. Solutionizing occurred at 620 °C for 60 min before the samples were quenched by water at room temperature. These specimens were then aged after the quench at different temperatures of 400, 450, and 550 and times of 1-3 hours. A combination of microstructure analysis, X-ray diffraction (XRD), Vickers hardness test, tensile test, adhesive wear test, and worn surface analysis were performed [72]. Their results indicated that the wear rate would initially decrease but increase with velocity while load and distance caused a wear rate increase. Furthermore, the 20 wt.% increase of the Al_2O_3 particulate reinforced Cu MMCs provided an improvement to the dry sliding wear when produced by centrifugal casting. In these tests, sliding distance is shown as the most dominant factor. Aged specimens at 400 °C showed a lack of precipitation. The specimen aged at 450 °C showed a continuous stream of white phase that created a strengthening effect. Tensile tests performed after the heat treatment showed a suppression of the onset of plasticity but increased the brittleness. Wear rate testing performed through a pin-on-disk tribometer showed that the belt of interlocked particles provided an even distribution of stress across the surface thereby reducing the initial wear rate. Certain strategies can be used to facilitate proper cohesion and desired properties of an FGM. Distinct strategy is important as small alterations can yield large

differences in the resultant component. The most prominent of these include powder mixture strategy, interfacial layers, process parameter regulation, and gradation strategy.

2.2.3.3.3 Powder Mixture Method

The mixture of powders can promote the creation of functionally graded materials that would be difficult to fuse together when in bulk. Kinoshita et al offer a technique to develop a compositional gradient through slurry-pouring [76, 77]. This provides a way for particles to sediment downward under gravity thereby creating a large and continuous compositional gradient. The only issue that arose from this method comes from the challenge of controlling particle settlement initiation. Despite this challenge, Kinoshita et al created a simulated gradient pattern from 100% Ti from one surface to 100% ZrO_2 at the other from a buffer zone of 250 mm. Further numerical simulation predicted the particle movement in the suspension medium from the formation of the gradient to predict its development. The model utilized the Stokes' law to describe the spherical solid particle velocity during movement in liquid with high viscosity [76, 77].

Jayachandran et al proposed that a mixed-powder pouring method would allow easier development of a desired compositional gradient [78]. This work utilized spark plasma sintering (SPS) method along with crushed ice to provide precise manipulation of particle settling. SPS provides an opportunity to condense a material and reduce grain growth from the quick heating rate and low firing temperature. The method proposed included the mixing of powders with more than two types of particles of varying size

and/or density thus exhibiting different velocities in a suspension and subsequent sedimentation under gravity. In a subsequent Vickers hardness test, the measurement of gradient confirmed the presence of the desired functional properties. Powder pre-mixing strategies can provide a solution when two materials cannot be combined due to material incompatibility.

2.2.3.4 Functional Gradients via AM

Additive manufacturing presents an opportunity to manufacture successful functional gradients by creating interfaces that mitigate issues with solidification cracking. Layer deposition can improve disparities in thermal expansion coefficients between two materials. Without consideration of the deposition strategy, functional gradients made through AM can suffer from lack of fusion defects and detrimental material phases. Further study can offer a procedure to forming functional layers.

AM is being utilized to create materials with site-specific properties (MSP) [79]. Like structures that appear naturally, a material with smooth variations in material properties allow proper utilization of the raw materials available. Traditional manufacturing methods typically impart discrete changes between material properties when joining two dissimilar materials, however through gradual change of material properties from location to location, a variety of advantages can be afforded. For example, improved bonding between dissimilar materials can be achieved [80]. Mechanical stress concentrations are decreased thereby improving component lifetime [44, 55, 81]. Thermal stress characteristic of combining materials with different

expansion coefficients is decreased. Finally, crack growth rate between materials is decreased by eliminating disparities between material properties. With such features, MSPs are employed in biomaterials, defense, energy conversion, and many other practices [79]. The common characteristic here is regarding the gradient of property change that determines the response of the MSP. In fact, empty spaces in a material can produced as such to be defined as its own unique phase with specific properties that serve a purpose to the overall integrity of the system. Changing the flow rate of powder hoppers during powder feed methods can help produce smooth gradients between two dissimilar materials. A priori consideration toward the final product includes pre-mixing of powders and the transport of material during layer remelting to ensure that the process path proceeds as intended otherwise unintended regions with brittle phases may develop.

Single-phase functionally graded materials are developed when a composite is created from one phase due to the combination of chemical elements of one phase into another phase. Before additive manufacturing, this typically occurred through a sintering process where the material would become single-phase but would possess a changing chemical composition as a result of the solubility [40]. These types of FGM are less common as the most reoccurring designs of FGMs are those with a multiphase chemical composition [82]. For multiphase chemical composition FGMs, the different phases depend on compositional quantity of material reinforcement and the conditions upon which the material was manufactured. Upon introducing more material of one or more type to a system, a sequence of phase transformations and precipitations may occur. Zhang et al. mention a series of phase evolutions that forms along the compositional

gradient as the ratio between Cr and Ni is increased. Furthermore, increased percentage contents of different phases also increased as the Cr/Ni ratio grew [83]. Upon introducing more material of one or more type to a system, a sequence of phase transformations and precipitations may occur. Reichardt further proposes that the addition of Cr to a system featuring Ti-6Al-4V joined to 304L SS with a V interlayer would prove beneficial in a simple linear gradient system by avoiding the unfavorable formation of the sigma phase along the build direction [84].

As shown in Figure 6, DED can be used to tailor the chemical and structural properties of a component by varying the powder feed rate of each material during deposition. These builds are known as functional gradients, advanced composite materials that possess compositional and microstructural variations that change over the volume of the bulk. Functional characteristics come from compositional gradients that impart tunable properties along one or more dimensions [50]. This requires a smooth transition in chemical composition, morphology, or structure. In these builds, smooth transitions reduce detrimental properties or occurrences such as stress singularities.

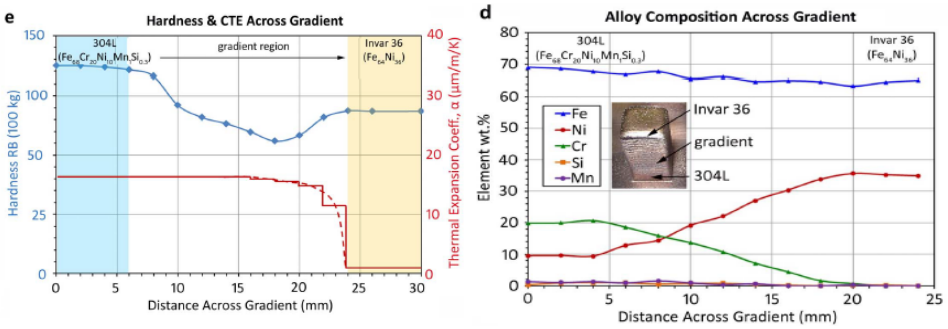

Figure 6: (Left) Hardness and CTE Across Gradient and (Right) Alloy composition across gradient. Reprinted from [25].

The challenge for AM functionally graded materials is deciding on the exact process parameters for proper adhesion. Khalen and Kar showed DED processes possess 19 significant dimensionless parameters including material density, thermal conductivity, laser beam diameter, power, scan speed, powder feed rate, powder size, among others [85]. One measurement tool used in various works is the volumetric energy density (VED) which is a unifying parameter that contains laser power (P), scan speed (V), layer thickness (t), and hatch spacing (h). P/V is the linear heat input. The energy density (E) known as the total energy input per volume is specified by the following equation [1]:

$$E = \frac{P}{V*h*t} \quad [1]$$

The above energy equation has found use in analogous traditional manufacturing routes like welding but is valuable in AM calculations to predict layer height/width and the probability that melting occurs [86]. Thermodynamic studies indicate that exothermic mixing between two metallic elements can provide additional heat to a molten pool thereby reducing the incidence of unmelted powder.

To mitigate problems posed by thermal and fluid forces, proper selection and preparation of powder is crucial. Proper powder preparation begins with a process such as gas atomization, water atomization, or plasma rotating electrode processing (PREP) [87]. The angle of the powder feed nozzle(s) and the feed rate influence the powder stream shape, speed, laser intensity distribution, and temperature distribution. Next, the mass of the powder must be factored into the momentum of the powder as it is shot from the nozzle. To account for the movement of powder that occurs in DED, an equation for

the linear mass density is provided in [2]. The ratio $\frac{dm^*}{dt}$ of flow rate divided by the laser traverse velocity (dl/dt) is the maximum powder amount that can be deposited over a unit length of laser movement.

$$\frac{dm^*}{dt} = (\frac{dm^*}{dl})\frac{dl}{dt} \quad [2]$$

Through these measures, a design of experiments can be made to measure the efficacy of the DED process regarding the printing of Co-Cr-Mo single composition and compositional gradient bulk structures.

Selecting process parameters is crucial to the creating functionally graded materials via DED. Powder feed rate is influential to providing the right amount of powder in relation to laser power to ensure successful deposition. Particle stream and laser beam diameter should match to increase powder efficiency. Interlayer dwell time, the period between successive layer deposits, can determine the success of deposits and shape of the build [88, 89]. Xiong et al. report that fine powder particles can cause abnormal growth during the sintering process thereby influencing mechanical properties [90]. In comparison, Krishna reports that the finer powder size of an alloy powder can aid in the quicker and facile melting of an alloy [13]. The inverse phenomena are also observed when larger, higher melting temperature powders are introduced to a liquid metal pool where some large alloy powders may not melt completely. Powders with a large size distribution can be sieved together to fill the density of empty spaces between particles which increases the density of the feedstock powder. Thus, resulting structures from this methodology are typically much more structurally sound than one made with powder that was not previously sieved. Typical DED procedure employs spherical

powder with size range from 45-150 μm to diminish trapping of inert gas in the melt pool and final part porosity. From the powder delivery system, gas is pumped from a feeding line to move powder from containers on the machine. Gas can be replaced with propellant but this has structural/chemical consequences for the final component structure [24].

Working distance can be an overlooked parameter that proves to be oversimplified in some cases. This is due to the tendency to immediately dismiss working distance as simply being equal to the z-height increment. Working distance allows for a constant distance from the platform to be maintained throughout the build thus affecting laser effectiveness and ability to build. When a laser is placed too far from the platform with too little laser power, ineffective melting may occur. When a laser is placed too close with a high laser power, excessive melting may cause the part to warp. As such, it is imperative to discover a proper scanning strategy that leverages the optimal collection of variables at the disposal of the user to create the intended part.

For powder bed and powder fed AM technologies, scan strategy has been heavily studied to influence the rapid solidification of the molten metal. Carroll et al studied the build of bimetallic IN625 and 304L SS bimetallic structure by rotating the building component by 60 degrees between each layer [56]. Since dendrites grow in a continuous columnar fashion parallel to the build direction, a 60-degree hatch angle creates a continuous yet disorganized microstructure that lacks extensive dendritic growth across layers. The gradient region exhibits connected structural features [56, 91]. In some constructions, columnar dendrites formed at the build regions closest to the substrate

while closest to the most recently built regions, equiaxed grains are observed as reported by multiple studies. Figure 7 provides a depiction of the different types of grains specific to an EBM melt [92].

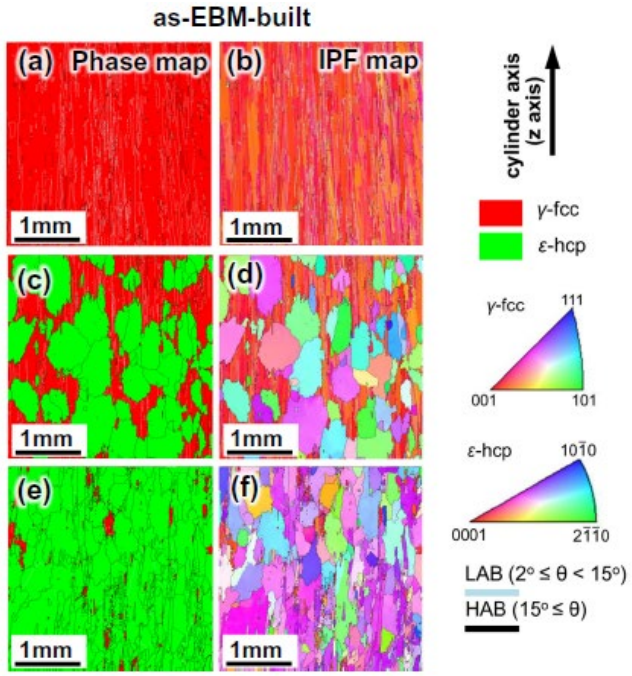

Figure 7: Left equiaxed grains at the top of EBM melt. Right: Columnar grains. Both shown through EBSD analysis. Reprinted from [92].

To achieve the properties attributable to LENS technology, careful attention must be paid to the heat transfer from the laser to the substrate and build layers. Heat transfer acts as a driving force that directly or indirectly affects part quality and structural integrity as influenced by the material coupling, thermally driven solidification, and microstructural evolution. Thermal and fluid forces act together as deposition of the metal powder occurs. The most common parameters focused on are the melt pool

initiation (powder melting), ‘intra-part’ heat transfer which includes conduction (melt pool to substrate), and heat generation and destruction (related to solid state transformations) [2]. Knowledge and optimization of the laser-based process demands a mastery of thermal and fluid interactions that occur during the build. The thermal and fluidic behavior of the melt pool and intra-part heat transfer offer significant insight into the final component quality [2]. Interlayer dwell time, the period between successive layer deposits, can determine the success of deposits and shape of the build [88, 89]. Without proper knowledge of the interaction between laser energy input and powder, alloy powder can remain unmelted which leads to a structure that possesses various defects and structurally unacceptable cracking.

2.3 AM Compositional Gradients

Compositional gradients are a type of functional gradient that exhibit an increase in the percentage of one type of material at the expense of one or more of the other types of material that exist within that region. Compositional gradients have been a designable utility since the development of functionally graded materials in the 1980’s [3]. Manipulating composition can lead to the formation of microstructural features that change the overall material structure from traditional joining of materials.

Before additive manufacturing, this typically occurred through a sintering process where the material would become single-phase but would possess a changing chemical composition as a result of the solubility [40]. These types of FGM are less common as the most reoccurring designs of FGMs are those with a multiphase chemical

composition [82]. For multiphase chemical composition FGMs, the different phases depend on compositional quantity of material reinforcement and the conditions upon which the material was manufactured. Upon introducing more material of one or more type to a system, a sequence of phase transformations and precipitations may occur. For example, Zhang et al. mentions a series of phase evolutions that forms along the compositional gradient as the ratio between Cr and Ni is increased. Furthermore, increased percentage contents of different phases also increased as the Cr/Ni ratio grew [83]. The application of these compositional gradients can be tailored to improving material characteristics. Addition of certain elemental compounds in a gradient can lead to beneficial suppression of deleterious phase forms that may arise from the interaction between dissimilar materials. Microhardness is shown to increase across a sample build path such as when Cr/Ni is introduced to a steel substrate [83]. A study performed in 1991 by Matlock and Olson determined the effects of compositional gradients through Cahn-Hillard analysis which examines the degree upon which local surface energy varies in the presence of a compositional gradient. In their work, solidified alloy components are analyzed for crack propagation with respect to orientation of solidification and profile of compositional deviation. These alloys were metal matrix composite weld deposits on austenitic stainless steels using wires filled with refractory metal cores and welded through gas tungsten or gas metal arc methods. Despite the lack of direct control of composition, the methods of this era are still able to produce particulate metal matrix weld deposits with uniform spatial particle distributions [93]. Furthermore, Matlock and Olson were able to determine that critical radii of an alloy

system decrease significantly as the presence of a compositional gradient is increased. As such, the blunting of the radius of fracture leads to a reduction in the susceptibility to fracture. A decrease in critical radii also results in an enhanced rate of nucleation of the second phase. This implies that as-cast or as-welded metals that possess large compositional gradients should be subject to facile formation of second phases. Gradients disrupt the phase stability prediction methodology since both localized variations and potentially large local composition gradients need to be considered when figuring out the susceptibility of forming a certain secondary phase [93]. The Cahn-Hillard model predicts that stacking fault energy changes across the cored metal and locations of steepest compositional gradients produce the largest disparities in stacking fault energy [94].

From their work, the location of cracks was found to correspond with regions of the highest compositional gradient. Fatigue crack growth measurements also indicated that the resistance to fatigue cracking is directly related to the local compositional gradient and by proxy the local stacking fault energy. A variety of other studies have further corroborated that high temperature mechanical properties are strongly influenced by compositional and microstructural gradients and their relative magnitudes [93].

2.3.1 Compositional Gradients via DED

While other methods have proved somewhat effective, Additive Manufacturing (AM) yields the most effective solution for the development of compositional gradients in metallic materials without the large transition regions. Of the techniques that can

successfully create compositional gradients, direct energy deposition (DED) methods can deliver smooth transition between layers. DED can create compositional gradients in metal components through adjustment of the volume fraction of metallic powders that are transported to the melt pool with respect to position [56]. This process is the most suitable due to the multiple nozzle delivery that adjusts the rate at which powder is added such that a final structure can be made based on powder percentages. Gross porosity and other lack of fusion defects were absent of graded structures between layers in Co-Cr-Mo deposited on the surface of Ti-6Al-4V [13]. Espana et al. used LENS to develop porous and compositionally graded structures using Co-Cr-Mo deposited upon a Ti-6Al-4V substrate (Figure 8) in order to lower stiffness and retain the excellent wear resistance [14]. The laser must be operated at a high enough power to properly melt the powder while not causing damage to the underlying microstructure due to rapid heat cycling. Through this process, detrimental phases may arise in the gradient zone while solidifying [56].

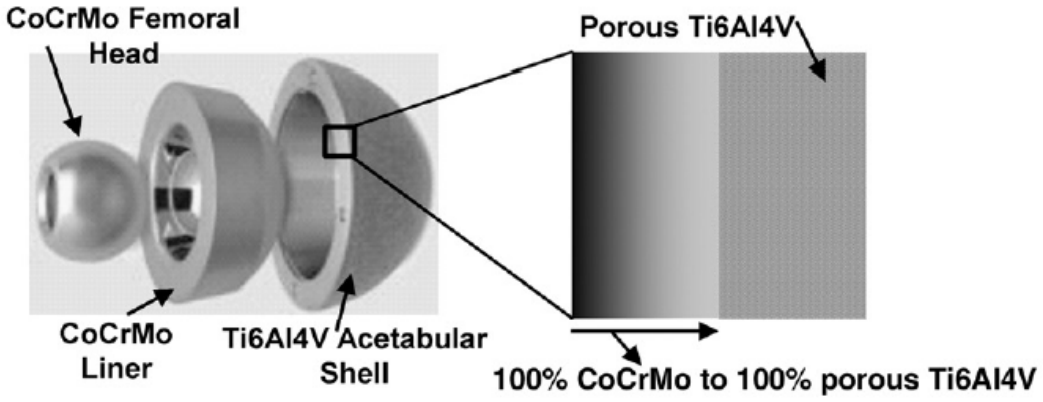

Figure 8: Compositionally graded Co-Cr-Mo upon porous Ti-6Al-4V. Reprinted from [14].

Powder blends can be used to develop complex alloys which possess identical properties to pre-alloyed powders in DED. These elemental blends must take into account the change in laser absorption coefficient, melting point, concentration and enthalpy of mixing which each have a large influence on the necessary laser power for chemical consistency [95]. Furthermore, powder feed rates can significantly affect the outcome of the part development. Krishna et al. discovered that the different feed rates that were optimized for Co-Cr-Mo deposition upon Ti-6Al-4V substrate yielded fully melted powder, less pores, and good transition between fully pure regions of each element [13]. A compositional gradient between SS316 and IN625 was also developed through LENS by careful control of individual powder feed rates [96].

Some of the issues that arise from processing two different materials through DED come from differences in thermal and optical properties. As DED is a laser-based technology, two different materials may be difficult to join should they possess entirely opposite material properties within these spectrums. Laser absorbance has proven to be a difficult property to circumvent should the optical properties of two materials largely differ. A material that would reflect much of the laser beam is difficult to transmit energy to, making successful DED development questionable. Unless enough power is generated, these types of materials typically experience lack of fusion effects such as porosity, poor layer adhesion, and generally detrimental properties arising from lack of structural integrity. These materials can prove useful when the effect of laser dampening is desired such as in creating porous structures from metals [14, 42, 97].

Compared to these materials are those with excellent laser absorption properties which also provide their own drawbacks and benefits. When these types of materials encounter laser-based power sources, they are inclined to absorb much of the energy which can serve to cause low viscosity melts that may spread too thin depending on the nature of the application. Another drawback of absorbing much of the energy from the laser is an increased dilution of the final structure [98]. Material properties and microstructure are strongly influenced by the thermal history of the build which includes the scan strategy, size, and geometry of components. Due to the proclivity to absorb laser power, these powder-based materials typically do not experience the lack of adhesion effects mentioned about their counterparts. Specifically, these powders will typically be utilized to a larger degree than powders that have lower absorptivity. Low absorptivity powders are more inclined to liquify and join the melt pool rather than remaining as loose granules embedded into the final structure.

Thus, it remains a challenge between any material combination to find the correct combination of process design that will allow for uniform melting and proper adhesion of the final LENS product. Second, the final structure composition and properties can decidedly influence the strategy behind LENS printing. To mitigate the issues pertaining to joining two dissimilar materials, special attention has been allocated to the interface between the two materials. Interfaces can be a challenge in metal powder deposition of dissimilar materials. A couple studies performed by Onuike et al on the compositional gradations of Inconel 718-Copper alloy bimetallic structure and Inconel 718-Ti-6Al-4V touched on a few of these challenges [43]. Their work (Figure 9) sought to create a

unified structure between the two materials using two approaches: direct deposition with a steep immediate jump from one material to the other at the interface and a gradual compositional gradient that slowly changed the chemical makeup from one pure end to the other [43]. Steep interfaces can reduce the structural integrity of the final piece due to the lack of adhesion that can occur from connecting dissimilar materials. A graded structure can mitigate these issues by providing a slow transition from one material to the other so the layers can be fused more easily.

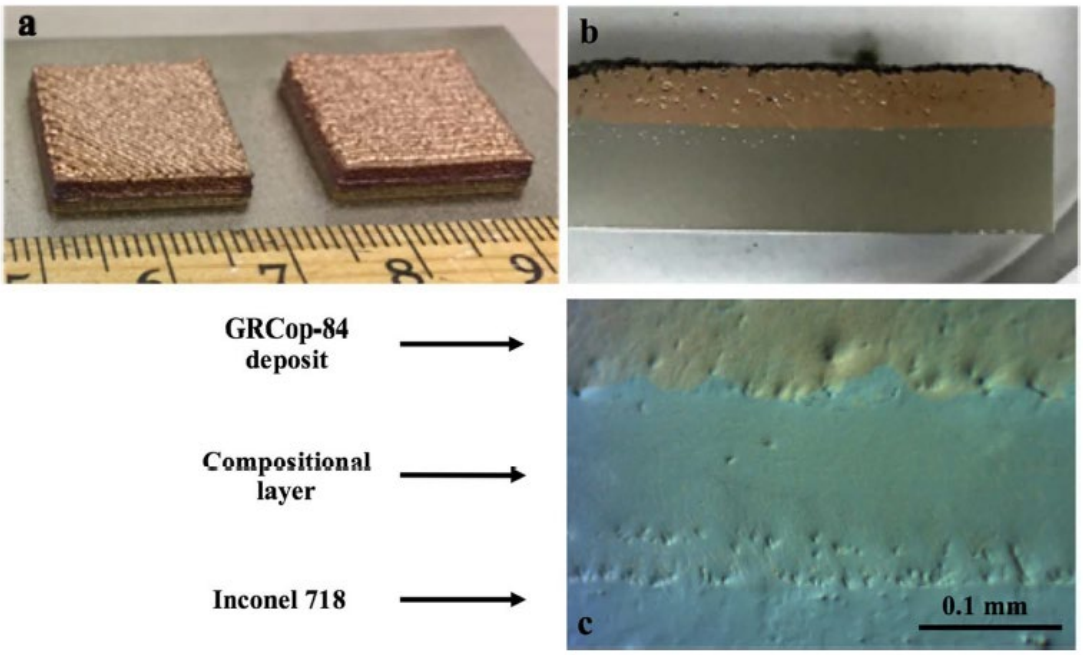

Figure 9: Printed bimetallic structure of IN718 and GRCop-84: (a) Uncut samples (b) sample cross-section, and (c) optical image of compositional grading layer. Reprinted from [43].

Kim et al deposited IN718 powders onto AISI 4140 steel substrates to determine the compatibility between dissimilar metals with an emphasis on bonds at the interface

and fracture behavior of the dual material bulk structure [99]. Cylindrical pillar specimens were made from AISI 4140 alloy steel substrate for one side while the other side of the specimen was made of as-deposited IN718. Their results prove that two dissimilar metals can exhibit good metallurgical bonding at the interface as no fracture failures were found at the substrate or the interface. Each specimen found failure in the as-deposited IN718 region which indicates that the as-deposited layer adhesion is insufficient when the sample experiences typical stress conditions. This represents a common problem for LENS structures as the powder fed method can lead to lack of fusion effects from partial melting of powders or large melt pools that may depress the layer height. As such, the structural integrity will be most stable when a parameter range can be established that will not cause the onset of such unfavorable effects.

Ram et al. successfully produced a Ti-TiC coating upon a Ti-64 substrate through LENS despite the previous reports that very high TiC content results in cracking at the substrate/coating interface. Their solution was to grade the coating percentage from 0-60 vol. % similar to a study performed by Liu and Dupont where TiC content was increased from 0-95% [100, 101]. Specifically, due to the 3-level powder pre-mix variation from 20 to 60 vol% rapid cooling rates in the LENS process, Ram was able to successfully deposit the Ti-TiC graded coating upon the Ti-64 substrate.

As mentioned previously, the strategic addition of an interfacial layer that promotes bonding of dissimilar materials can vastly improve the properties of a final component. Krishna reported that an interface layer of Cu or Co deposited between the substrate and the LENS deposits would improve bonding strength [13]. Adams

corroborates a similar beneficial effect in depositing a Ni interface layer between Fe and Cu weld deposits. The Ni layer Inconel 625 requires a large amount of Ni for the Cu deposits to be placed upon [102]. This interlayer prevents solidification cracking upon the deposition of Cu and improve minimization of thermal stresses that occur at regions that join dissimilar materials that possess a large disparity in thermal expansion properties. One layer of IN625 is enough to prevent solidification cracking between steel as martensite was shown to form within the heat affected zone of the tool steel substrate during LENS deposition. Copper was then deposited upon IN625 as shown in Figure 10 with limited solidification cracking. The amount of material necessary for a proper interface varies by material components but is a necessary consideration to make a cohesive final component. This same concept is utilized in bond coats between a substrate and a topcoat in order to facilitate the adhesion and stability of the topcoat [3]. As an extension to this, a multi-layered and continuously graded coating can be developed to further improve the adhesion between the substrate and topcoat. This is important for coated metallic implants as bond coats are anticipated to improve the coating endurance which reduces the onset of metal ion release and curtails the fatigue from load-unload cycles of the implant during use.

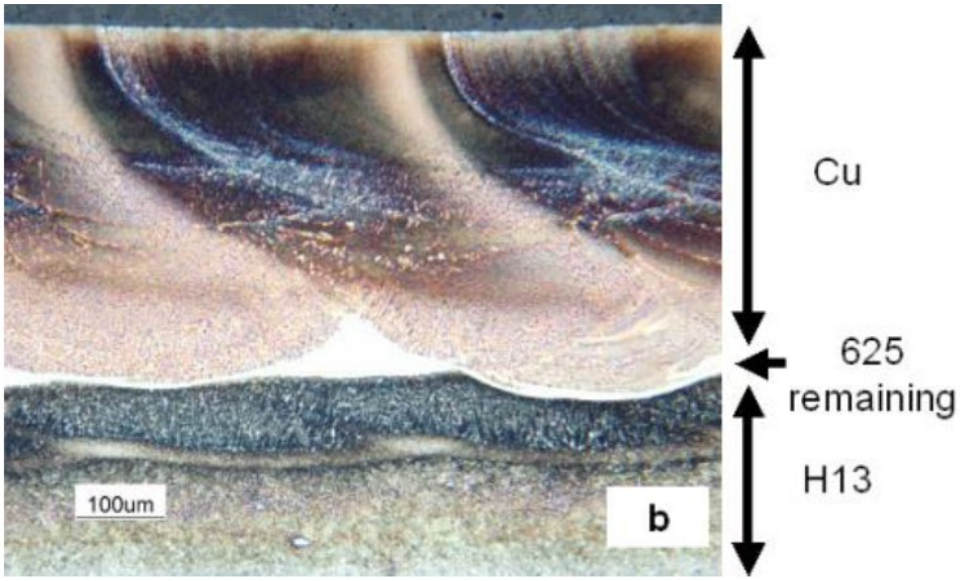

Figure 10: Low Magnification views of a layer of pure copper laser deposited onto H13 tool steel with IN625 interfacial layer. Reprinted from [102].

As expected of AM structures, optimization of process parameters improves the joining of two different materials. Zhang et al report that regulating process parameters refines the grain morphology and component mechanical properties [103]. Xiong et al. have found that working distance adjustments can lead to microstructural improvement. Their work suggests that the z-height increment of the machine should be set to the actual layer thickness to keep a constant working distance [90]. A study of enhancing Ti through Ti boride whisker (TiBw) performed by Hua et al. also corroborates that shorter working distance leads to improved specimen density and microstructure. Shorter working distances can lead to lower laser intensity which shortens the melt pool and reduces the layer thickness when deposition happens at the focal plane of the laser beam. Hua further explains that when the working plane is higher than the focal plane

microstructures with alternating layers disappear [104]. Furthermore, an increase in laser power is also shown to improve the density of the final part with less internal defects.

2.3.2 Choice of AM method for compositional gradients

Strategic implementation of gradients can prove crucial toward the final structural integrity of part and its material properties. The widespread adoption of additive manufacturing-based research has prompted its use in variety of functional gradient processes. Of the two techniques, powder bed and laser-based technologies are the most prominent in terms of research area. Laser metal deposition provides the freedom of producing functionally graded materials in a single process. Like other AM processing techniques, optimization of process parameters for specific material combinations creates a better part such that the final composition is specifically tailored to an application. Furthermore, premixing of powder before the deposition process provides a higher resulting density powder that limits the detrimental effects that are posed by less dense powders [82]. Having powders in separate hoppers has also shown to be effective in building the composite with the proper composition control. Segregation does not then occur due to the different densities of powders [105]. LENS machines can synthesize compositional gradients when operators utilize different feed rates for each of the respective powders' nozzles in order to deposit the material with the correct proportions onto the substrate or already built material. With microstructure control of this magnitude, it should come as no surprise that undesirable secondary phases exhibited in prior contemporary manufacturing methods can be

avoided through the layer by layer build up approach of LENS or other similar AM methods. While ideally this would result in a continuous structure each time, process parameters must be chosen properly to ensure the integrity of the resulting build. As such, there remains a necessity to choose an adequate material that fits in to compositional gradient deposition on another material substrate.

Choice of AM method requires a great deal of evaluation as each development process possesses its own set of drawbacks and benefits. Various works have noted that different AM methods yield comparable mechanical properties but may differentiate in surface texture depending on the deposition method employed. Zhai and Galarraga performed studies on the microstructure and static properties of powder bed fusion method electron beam melting (EBM) and powder fed method (LENS) [106]. From their work, it was observed that tensile properties of both LENS and EBM Ti-6Al-4V were higher than mill-annealed samples. A comparison between the AM methods shows that LENS Ti-6Al-4V has slightly lower strength and higher ductility because of a lower fraction of martensitic α’ phase. The martensitic phases are not seen in EBM Ti-64 because of the powder bed heating leading to improved ductility than LENS Ti-6Al-4V. As shown in Figure 11, LENS furthermore displays the highest surface roughness values while EBM builds show finer surface finishes depending on a fine powder precursor.

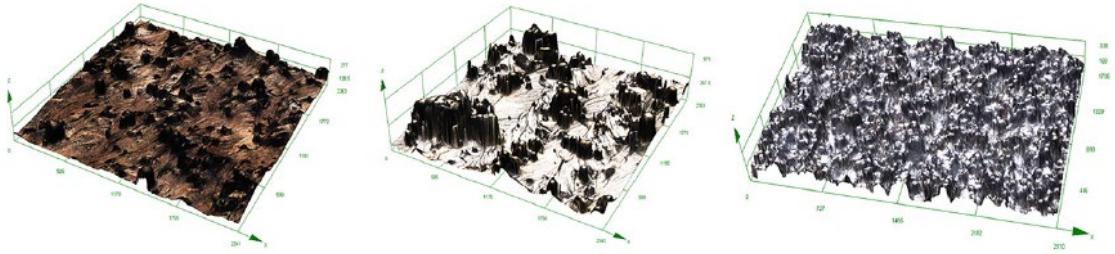

Figure 11: Surface roughness projections for (a) LENS low power, (b) LENS high power, and (c) EBM builds. Reprinted from [106].

Zhai further posits that in most cases while LENS shows comparable mechanical properties to conventionally manufacture components, optimization of process parameters could improve the final part fabrication and properties. Attar et al. offer a comparative study comparing LENS, SLM, and casting processes on fabricating commercially pure Ti by investigating critical aspects of densification and balling effects [107]. Their study found that the differences in the microstructure, specifically between SLM and LENS, are primarily due to varying cooling rates and energy densities during each respective process. Furthermore, SLM possesses higher mechanical properties in compression and hardness due to the influence of microstructure formed during its cooling process. LENS also employs a higher amount of linear energy density and specific point energy to obtain the same degree of densification as displayed in Figure 12 [107].

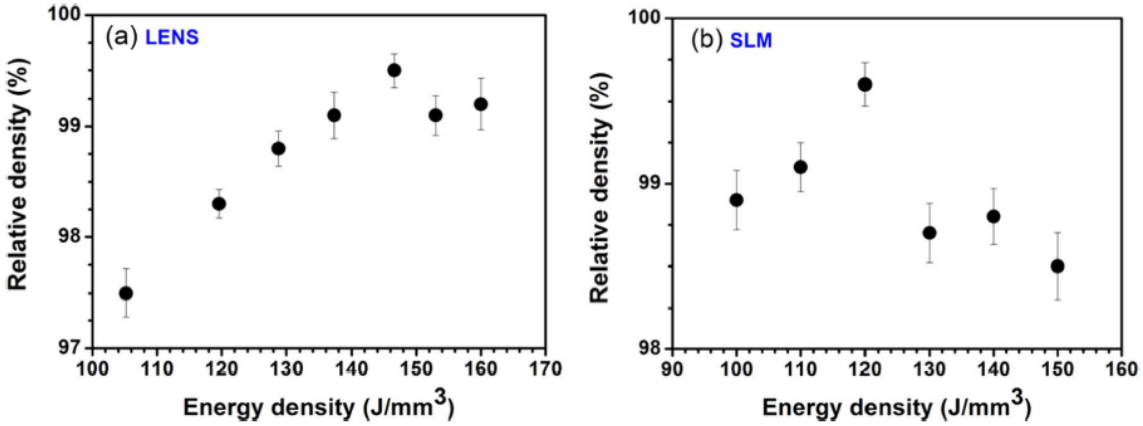

Figure 12: Relative density and energy density relationship for CP-Ti produced by (a) LENS and (b) SLM. Reprinted from [107].

Though it may appear that LENS is the inferior process when compared to EBM and SLM, LENS provides a geometrical freedom that is not characteristic of either process. For example, in studies we performed for a part manufacture with a helix like design, it was observed that while EBM and SLM could produce the part, support structures would be required to help facilitate the build and then would need to be removed as necessary. LENS, on the other hand, was able to fabricate the part without the need for supports due to the design freedom of the machine itself lending to designing complicated geometrical parts. As the machine used in this study was the MT-X, machining on the part could be done to remove any textures that may have formed reducing the incidence of those features on the final component. For the purposes of this work, LENS was pursued due to the understanding posed in performing previous studies which would further illuminate better practices with respect to the amount of degrees of freedom possible for LENS.

In a study performed by Zhai et al, the tensile strength of Ti developed by LENS was shown to be like that of a wrought structure but possessed lower ductility. Heat treatments were found to increase the ductility post fabrication [106]. Their observations confirm the development of columnar grains due to the draining of heat from the substrate. Furthermore, they report that heat affected zones can be seen at the build-substrate interfaces from partial melting of the substrate. Layer bands due to microstructural coarsening are also a feature of partial remelting of previously built layers. Sterling also observed that LENS Ti-6Al-4V has a shorter fatigue lifetime than wrought materials as a result of lower ductility and associated porosity [106]. As compared to EBM, both LENS and EBM have a higher tensile strength than annealing. For LENS, specifically, the presence of phase transformations and intermetallic phases can cause a lower ductility or unfavorable properties unsuitable for specific applications. Amsterdam and Kool also confirmed fatigue performance of LENS-deposited Ti-6Al-4V and Inconel 718 were found to comparable to wrought counterparts [108]. In contrast, Kobryn and Semiatin investigated fatigue and fatigue crack growth performance of laser deposited Ti-6Al-4V and discovered that the lack-of-fusion porosity occurring in deposited layers contributed to much of the anisotropy in mechanical properties. When compared to wrought materials, the laser deposited samples displayed lower fatigue strength and fracture toughness. A secondary hot isostatic pressing procedure eliminated the lack of fusion porosity and improved the fatigue strength of the laser deposited Ti-6Al-4V to that of the wrought materials. LENS fabricated Ti-6Al-4V possesses lamellar microstructures that have a lower threshold but higher fracture toughness than

conventional mill-annealed Ti-6Al-4V which contains equiaxed alpha phase in a beta matrix [109].

2.3.3 Graded Interfaces

In some AM based studies, this manifests as simply depositing a part upon a substrate. Kim et al deposited IN718 powders upon 4140 steel substrates to study the interfacial bond and fracture failure mechanisms. Their work shows that some materials can simply be deposited without issues with metallurgical bonding as their hybrid specimen showed no fracture failure at the substrate or the interface [99]. This phenomenon can be explained through the work of Savitha et al who joined IN625 and SS316 as shown in Figure 13. Their study reports that a small transition zone is formed between two materials that are dissimilar but compatible for metallurgical bonds [96]. Krishna found that gradient coatings with a gradual transition from composition from 100% Ti-6Al-4V at the bottom to 86% Co-Cr-Mo alloy at the top reduces failure and attains a better interfacial bonding [13]. Furthermore, the wear properties of this 86% Co-Cr-Mo alloy top layer structure are better than a straight line 100% Ti-6Al-4V to 100% Co-Cr-Mo. This change occurs due to the presence of severe cracking at the 100% layer despite the nonexistence of intermetallic compounds as reported in their study. Wilson remarks that the interface between a coating a substrate should be a blend of Co-Cr-Mo alloy and Ti-6Al-4V material that remains devoid of cracks [15].

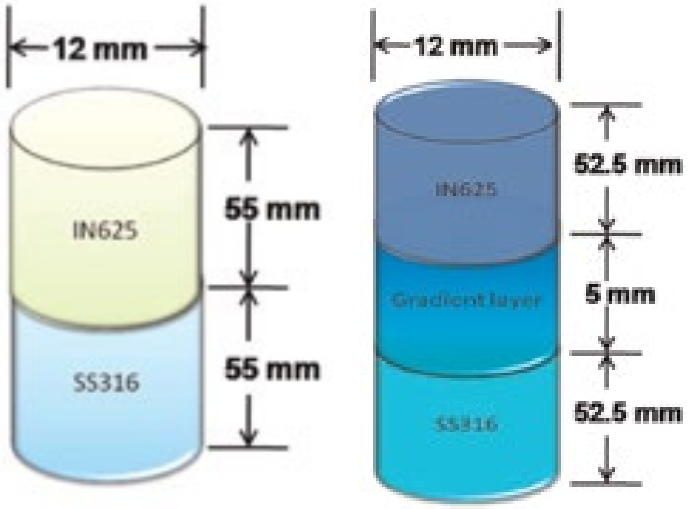

Figure 13: (Left) A structure with a discrete interface versus (right) a structure with a continuous gradient. Reprinted from [96].

In another DuPont study, Ni-based alloys Inconel 625 and Monel 400 were deposited by LENS to act as an interface between H13 tool steel and pure copper [102]. Employing graded interfaces can blunt the occurrence of solidification cracking when a material is deposited upon the surface of a substrate as evidenced by Adams and DuPont. Thermal stresses that develop at joints between dissimilar metals from very different thermal expansion properties can also be minimized with the presence of an interlayer. Dissimilar materials further present the challenge of phase formation that proves detrimental to the final material structure such as the development of martensite in tool steel when Inconel 625 is deposited upon H13 tool steel [102]. Adams and DuPont also show that the choice of material is also a crucial consideration when determining the integrity of the final structure. For instance, Monel 400 proved to possess a copper content too high for the prevention of solidification cracking whereas Inconel 625. In

fact, the choice of material can reduce the necessity to include extra material necessary for other materials.

The methodology of proper material choice can be gleaned from analogous material studies. For example, Adams and DuPont noted that the binary Fe-Ni and Ni-Cu weld deposits did not display solidification cracking thereby promoting Ni-based materials as an interlayer. Balla demonstrates the beneficial aspect of compositionally graded interlayers in a study that aims to use a Zr coating on stainless steel through LENS. The compositional gradation between the ceramic coating and the substrate offers a reduction in discontinuity of thermal expansion coefficient between the top and bond coats thereby minimizing the residual stress in the coatings. The effects of disparities in thermal expansion coefficient between two dissimilar materials can further be mitigated if a functionally graded coating is applied [95]. Obielodan provides another anecdote of graded transition between Ti-6Al-4V/10%TiC dual materials. While the graded structure did little for the flexural strength in comparison to dual-materials made of compatible materials, this joint design offers significant benefits to tensile strength.

In the work of Savitha et al. on the influence of interfaces on discrete and compositionally graded structures, it is shown that when the powder feed rate of AM machines is changed gradually or discretely, the yield strength of the resulting material of two materials varied in strength is always comparable to material with the lower strength [96]. Their studies investigate the interfacial and material properties of compositionally graded LENS structures of Inconel 625 and SS316. An optical micrograph of the IN625 and SS316 transition zone in the CG sample is shown in Figure

14. Similar to how other dual materials were fabricated, this structure was built through layer wise deposition while paying close attention to the control of individual alloy powder feed rates [96]. Though sharp interfaces are typical of direct deposition structures without the presence of a compositional gradient, Savitha et al reported that for discrete and graded deposits, the change in composition near the interface is gradual. To gage the gradation effect, hardness measurements were taken of successive layers in the transition zone from the SS316 until the pure IN625 layer was reached. The hardness measured followed a gradient like the increase in IN625 proportion as successive layers were deposited. Layer strategies can prove to be a cause for great concern as compositions of layers can determine the success of deposition. Reichardt reports that certain composition percentages in her study proved unable to be deposited without cracking [84]. While ideally one could synthesize a structure where 100% of one material could be built upon in a step wise structure from 100% of another material, the result does not necessarily yield exactly linearly correlative results.

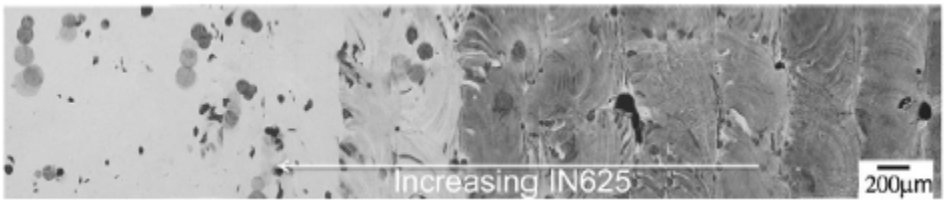

Figure 14: Optical micrograph of IN625-SS316 transition zone of CG sample. Reprinted from [96].

2.3.4 Graded Coatings

Compositionally graded coatings present a much different challenge than typical built-up structures due to their small build height. Bio-coatings can be incredibly beneficial and help osteointegration, limit reaction to foreign bodies, lower the incidence of infection [3]. Graded coating structures are emerging through the development of multi-layered and continuously graded coatings. These coatings consist of a bond coat that operates to improve the adhesion and stability of the functional topcoat. Bond coats increase coating durability by hindering the release of metal ions from the metal substrate and decrease fatigue experienced during cyclic loading-unloading of the implant during operation [3]. Typically, compositional graded materials have a large region of thickness upon which a gradient can be constructed with a more forgiving tolerance value. Furthermore, the laser deposition process may impart a much different structure than anticipated upon introduction of the laser to the blown powder. As the size of the coating height is a fraction of the process window that would be typically encountered in a bulk material, different strategies must be employed for successful deposition and functional properties.

Bandyopadhyay et al deposited Co-Cr-Mo coatings on a Ti-6Al-4V substrate at varying compositions to determine the optimal deposition composition that offers the best material properties [13]. Their study reports that 86% Co-Cr-Mo upon a Ti-6Al-4V substrate provides the best combination of material properties. This proves counterintuitive as one would assume that 100% would offer the optimal properties.

However, this assumption is shown to be false as mechanical property studies by Bandyopadhyay have shown. When mixtures of alloys are combined, tailoring the composition of each alloy presents a challenge specifically in the melting and subsequent deposition operations of LENS. For a material like Co-Cr-Mo, which has a much lower melting point (1260-1265 °C) than an alloy such as Ti-6Al-4V (1604-1660 °C), immediate melting can prove challenging as the absorbed heat from the melt pool decreases the temperature of the melt pool. Increasing Co-Cr-Mo percentage also influences the size and morphology of the Co-Cr-Mo alloy phase due to the thermodynamics that result from the higher volume fraction in the molten alloy pool. The LENS process typically exhibits extremely high cooling rates (10^3-10^5 K/s) which can then lead to very fine graded structures upon solidification [13].

Liu and DuPont utilized LENS to deposit TiC upon a Ti substrate (Figure 15) [100]. The controller in LENS provides imaging of the melt pool area during the deposition of the functionally graded part. Increased dimensional accuracy can be achieved through the melt pool area controller in LENS but does not control other properties of the deposited part. Ram et al performed a similar study but deposited a TiC composite coating on a Ti implant substrate [101]. Their coatings feature a mixture of coarser unmelted/partially melted TiC particles and finer, discreet resolidified TiC particles uniformly distributed in the Ti matrix. As such, not only does such a coating structure provide a compositional component but a geometrically beneficial formulation.

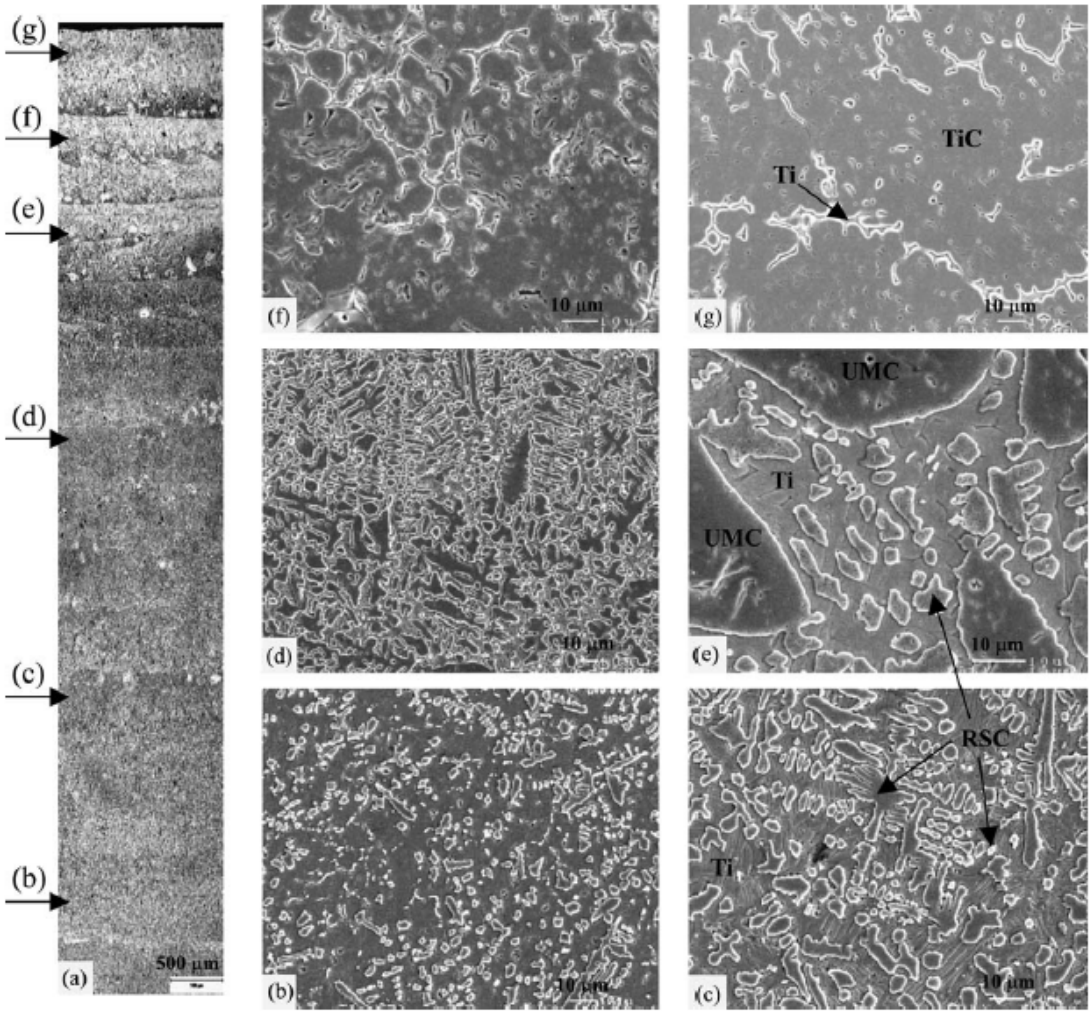

Figure 15: Functionally graded deposit microstructure with increasing TiC content from (b) to (g). Reprinted from [100].

For the purposes of our study, Co-Cr-Mo alloy was chosen due to its wide application in biomedical, manufacturing, aerospace, and corrosion fields. From previous work on Stellite and other Co-Cr-Mo structures, determining the layer resolution possible for various Co-Cr-Mo alloy percentages proves to be a worthwhile pursuit to understanding not only the nature of compositionally graded structures but also the capabilities of LENS on creating overlays and bulk structures.

2.4 Co-Cr-Mo: Processing, Structure, and Properties

2.4.1 Allotropes of Cobalt

Cobalt is a strategic and critical metal in industry specifically in defense-related applications and exports to industrialized nations [87]. These industrial consumers are known to allocate cobalt toward heat resistance superalloys, corrosion and wear resistant alloys, magnetic materials, high speed tool steels, and cemented carbides. Co alloys are biocompatible which allows their use as surgical instruments, dental and orthopedic implants. Co base materials, specifically those with Cr, are lauded for their resistance to corrosive effects in the human body [13, 110-112]. With high Cr content, a thin passive layer forms on the surface of the component as a strong Cr oxide layer prevents the underlying matrix material from corrosive damage. Biocompatible alloys such as Vitallium and Stellite (Co-Cr-Mo), Alacrite (CoCrWNi), and Havar (CoCrNi), are some of the most commonly used for medical implants [87]. These alloys provide a wear and corrosion resistance preferable for implants especially metal-on-metal (MOM) components.

Pure Co exhibits two allotropes: ε-phase (HCP) at low temperatures and γ-phase (FCC) stable at higher temperatures. In pure Co, ε-phase transforms into the γ-phase at 430 °C (A_s) through a diffusionless martensitic means. The reverse transformation occurs at the martensite start temperature 390 °C (M_s) upon cooling [113]. Plastic deformation known as strain-induced transformation (SIT) can also induce the γ to ε transformation (Figure 16) and is further enhanced if the alloy is kept at temperatures around 800 °C before cooling down. SIT is beneficial for Stellite 21 by bestowing

excellent galling resistance and enhanced stress accommodation ability. A transformation within these circumstances is influenced by the cooling rate, temperature, grain size of the parent phase, the length of solution heat treatment before aging. When pure Co is alloyed, the allotrope stability is modified thereby influencing the starting transformation temperatures A_s and M_s. For the specific instance of Co-27Cr-5Mo-0.05C, A_s moves to 970 °C.

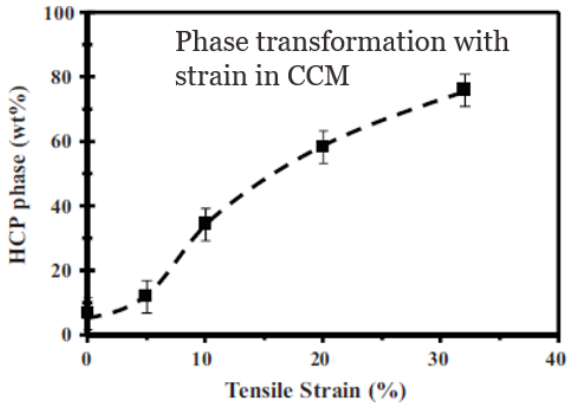

Figure 16: Phase transformation of FCC (γ) to HCP (ε) in CCM. Reprinted from [114].

2.4.2 Elemental additions to Co-Cr-Mo

Much of the usefulness of cobalt comes from its inclusion as a base for alloys. Making the first discovery of cobalt-based alloys at the turn of the 20th century, Elwood Haynes discovered the promising properties of high strength and stainless nature of binary Cobalt-Chromium alloy. Haynes' choice of the name Stellite reflected the star-like luster of CoCr alloys [87]. Figure 17 presents the properties of Co-based hardfacing alloys. Though Co-base alloys are the most popular material type, Co has been included

in commercial maraging steels which possess large amounts of Ni, Co, and Mo and very low C contents, a known impurity in these steels. In contrast to its presence as a base, Co in these steels can range from 8.5-12.5%. Its main function is to lower Mo solubility in the martensitic matrix thereby increasing the Ni_3Mo precipitate that develops during age hardening [87].

2.4.2.1 Chromium

Chromium, a predominant carbide former, creates Cr rich carbides that provide additional solution strengthening and oxidation and corrosion resistance. The most frequent carbide in Stellite alloys is the Cr-rich M_7C_3 type. When considering low-C alloys like Stellite 21, Cr-rich $M_{23}C_6$ carbides are most frequently observed. Figure 17 provides a depiction of material properties of different Co-based hardfacing alloys specifically in the Stellite family. Cr is also known to modify the thermal coefficient of expansion in Co-Cr-Mo alloys [115]. While increasing Cr content can prove beneficial to some properties of Co-Cr-Mo alloys in conjunction with other elemental additions, its presence does not intrinsically improve the alloy strength. The addition of Cr is known to stabilize the epsilon (ε) phase [116]. Cr addition is a known corrosion inhibitor that depending on its relative percentage can impart a variety of properties to the alloy. Above 10 wt.% Cr concentration, the material becomes more noble. However, increasing past 25 wt.% Cr promotes the Cr-rich sigma (σ) phase precipitate which makes the material more active as the sigma (σ) phase boundaries are deficient of Cr

[117]. Despite providing a measure of higher strength, carbides can act as centralized regions for corrosion-based processes due to the depletion of Cr at the phase boundaries.

2.4.2.2 Tungsten and Molybdenum

Tungsten and molybdenum were recognized as powerful strengthening elements within a CoCr system. Haynes further determined the high strength of Stellite alloys at elevated temperatures and henceforth promoted their use as cutting tool materials. Early success of the initial Co-based cutting tool materials afforded their use in weld overlay form as a coating to protect surfaces from wear starting from 1922. Known as "hardfacing", these alloys were placed on plowshares, oil well drilling bits dreading cutters, hot trimming dies, and internal combustion engine valves and valve seats [87].

These materials find regular use in heat resistant superalloys, corrosion resistant and wear resistant alloys, magnets, high speed tool steels, and cemented carbides [87]. Stellite alloys display great tribological properties due to the beneficial low stacking fault energy of Co, hard carbide formation, and a solid solution strengthened matrix [113]. What has prompted an increasing interest in cobalt and its alloys for AM processes is its biocompatibility, which parlays its use in orthopedic implants. These properties stem from the crystallography of cobalt, solid solution strengthening effects from the inclusion of Cr, W, and Mo, the formation of metal carbides, and corrosion and heat resistance imparted by alloying elements. W and Mo similarly offer matrix strengthening properties because of their large atomic size. Al Jabbari reports that CoCr alloys exhibit enhanced mechanical properties through the addition of tungsten (W) and

Molybdenum (Mo) [112]. When employed in the matrix, these solute atoms reduce dislocation flow. Large quantities of either (such as in Stellite 1) lead to their participation in carbide formation during the solidifying process for alloys and promotion of M_6C precipitation. W promotes the formation of the intermetallic σ phase while complex hard phase combinations such as Co_3Mo/W_3C act as detriments to the fatigue properties to a material in operating conditions [118]. Alloying with Mo offers improvement in ductility and promotes the formation of eutectic carbides over the complex variant mentioned before. Mo has been shown to suppress the coarse carbide M_7C_3 which causes larger weight loss during wear examination [119].

When Co acts as an alloy base, it features an unstable, face centered cubic (FCC) crystal structure with a very low stacking fault energy [87]. This instability occurs during extreme cooling of elemental Co when FCC morphs into a hexagonal close packed (HCP) crystal structure at 417 °C. For most Co alloys, the transformation temperature is higher. As this transformation can prove obtrusive, the FCC structure in Co and its alloys is typical at room temperature. Transforming to HCP occurs only under condition of mechanical stress or extended time at elevated temperature. As a result of the unstable FCC structure and accompanying low stacking fault energy, Co-based alloys exhibit high yield strengths, high work-hardening rates (from interactions between stacking faults), limited fatigue damage under cyclic stresses, and the ability to absorb stresses (the transformation from FCC to HCP) [87]. The limited chemical driving force in alloyed Co further causes a sluggish transformation on cooling. Co alloys thereby exhibit a combination of two phases: ε and metastable γ at room T. Mechanical

properties of the alloy are influenced by the volume fractions of the two Co allotropes such as when ductility increases as the amount of γ phase increases [113]. Furthermore, the low stacking fault energy of the residual γ phase helps to increase the alloy work hardening capability and galling wear resistance by obstructing movement of dislocations.

2.4.2.3 Carbon

For alloys that feature carbides, high-C alloys are typical for service in wear applications. Lower C alloys are utilized in high temperature service or corrosion resistance and associated corrosion wear inducing operations. Of known corrosion resistant alloys, Co-Cr-Mo with moderately low C content was created with express need to perform as a suitable investment-cast dental material. The biocompatible alloy material known as Vitallium still exists today for use in surgical implants. Around the time of WWII, these same alloys were placed in investment casting trials for aircraft turbocharger blades and other elevated temperature applications once an improvement to the alloy's structural stability was provided. This early high temperature material, known today as Stellite 21, is a contemporary alloy that resists wear. Early alloys and contemporary variants primarily differ in relation to the control of C and Si, which were both early alloy impurities. Current Stellite alloy grades also feature C and W contents that influence the amount and type of carbide formation in the material during solidification [87]. Stellite alloys further differentiate from each other through C content and, therefore, carbide volume fraction in the material. Moreover, cooling rates and

slight chemistry changes can heavily affect sizes and shapes of carbide particles in Stellite alloys.

C is a beneficial alloying element that imparts various beneficial mechanical properties depending on application. The presence of up to 0.35 wt. % C in Co-Cr-Mo reacts with the major alloy constituents to form carbides. It is generally understood that fine carbide precipitates contribute to increases in strength whereas coarser precipitates lead to embrittlement. Asgar and Peyton report that spherical and discontinuous islands of carbides contribute to the most ductile structure while grain boundary carbides diminish ductility [120]. Similar to the study by Podrez, Bettini et al mentions an island-like structure described as a constellation of carbides that primarily form at grain boundaries or randomly distribute throughout the matrix [117]. These formations depend on heat treatment parameters and the subsequent cooling rate. Bettini used Scanning Kelvin Probe Force Microscopy (SKPFM) to identify the relative nobility of the carbides in these alloys but suggested that the carbide boundaries are preferential corrosion/dissolution zones. The effect of carbides on local dissolution processes was further evaluated by Electrochemical Atomic Force Microscopy (EC-AFM) measurements which helped determine the non-uniform structure and composition of Cr and Mo carbides. This non-uniform composition is proposed to possibly play a role in differences of observed dissolution rates. As mentioned previously, Co-Cr-Mo alloys form a protective thin passive corrosion resistant film comprised of mostly Cr_2O_3 along with minor amounts of Co- and Mo-oxides. Fine carbides also further provide better wear resistance. Yan et al verified that C increases the surface energy of high C Co-Cr-

Mo alloys versus low C Co-Cr-Mo alloys although the mechanism is not completely understood [4]. Chiba et al. described how low-C Co-Cr-Mo alloys display enhanced wear resistance versus high-C cast Co-Cr-Mo alloys due to the prevention of strain induced martensitic transformation (SIMT) from the increase in stacking fault energy. This mechanism results in a lower surface fatigue resistance. Chen et al. showed a similar result in their work on low C and high C-forged Co-Cr-Mo alloys [4, 121]. Regardless of hardness, carbides can be ripped off during wear which can result in third-body wear.

Carbon has shown applications in the prevention of adverse reactions that occur from metal implants, specifically metallosis that may occur in metal-on-metal (MOM) bearings. The accumulation of metal wear from adverse reactions to metal debris and aseptic osteolysis can lead to later life prosthetic loosening [122-124]. Koseki et al investigated the wear properties and friction coefficients of C ion implantation (CII) surfaces with further applications as surfaces for MOM bearings in artificial joints [122]. The resulting surfaces showed featureless, smooth surface topography like untreated Co-Cr-Mo alloys. In comparison to untreated Co-Cr-Mo alloys, CII-treated bearings possessed lower friction coefficients, improved resistance to catastrophic damage, prevention to wear debris adhesion to surfaces. Their work shows that C can stabilize the wear status of a structure through a lower friction coefficient and the low permeation of partner materials. Both features circumvent the adhesion of wear debris and the circumstance of excessive wear [122]. Another report using plasma source ion implantation was also able to implant C atoms into metal substrates [122, 125]. Fisher et

al applied a thin diamond-like C (DLC) film to Co-Cr-Mo alloys which was shown to reduce the creation of wear debris and the emission of metal ions [126]. Carbide formation is greatly influenced by physical and chemical factors primarily concerning the main alloying elements that comprise their composition and structure. Cooling rates upon completion of any thermomechanical process have the ability to affect shape and size [117]. The influence of alloying elements on the material response of Co-Cr-Mo alloys is well documented throughout various literature, but certain elements can strongly affect the performance of the alloy in various conditions.

Property	Stellite 21	Stellite 6	Stellite 12	Stellite 1	Tribaloy T-800
Density, g/cm^3 (lb/in.^{3})	8.3 (0.30)	8.3 (0.30)	8.6 (0.31)	8.6 (0.31)	8.6 (0.31)
Ultimate compressive strength, MPa (ksi)	1295 (188)	1515 (220)	1765 (256)	1930 (280)	1780 (258)
Ultimate tensile strength, MPa (ksi)	710 (103)	834 (121)	827 (120)	620 (90)	690 (100)
Elongation, %	8	1.2	1	1	<1
Coefficient of thermal expansion, °C^{-1} (°F^{-1})	14.8 × 10^{-6} (8.2 × 10^{-6})	15.7 × 10^{-6} (8.7 × 10^{-6})	14 × 10^{-6} (7.8 × 10^{-6})	13.1 × 10^{-6} (7.3 × 10^{-6})	12.3 × 10^{-6} (6.8 × 10^{-6})
Hot hardness, HV, at:					
445 °C (800 °F)	150	300	345	510	659
540 °C (1000 °F)	145	275	325	465	622
650 °C (1200 °F)	135	260	285	390	490
760 °C (1400 °F)	115	185	245	230	308
Unlubricated sliding wear (a), mm^3 (in.^{3} × 10^{-3}) at:					
670 N (150 lbf)	5.2 (0.32)	2.6 (0.16)	2.4 (0.15)	0.6 (0.04)	1.7 (0.11)
1330 N (300 lbf)	14.5 (0.90)	18.8 (1.17)	18.4 (1.14)	0.8 (0.05)	2.1 (0.13)
Abrasive wear(b), mm^3 (in.^{3} × 10^{-3})					
OAW	...	29 (1.80)	12 (0.75)	8 (0.50)	...
GTAW	86 (5.33)	64 (3.97)	57 (3.53)	52 (3.22)	24 (1.49)
Unnotched Charpy impact strength, J (ft · lbf)	37 (27)	23 (17)	5 (4)	5 (4)	1.4 (1)
Corrosion resistance(c):					
65% nitric acid at 65 °C (150 °F)	U	U	U	U	S
5% sulfuric acid at 65 °C (150 °F)	E	E	E	E	...
50% phosphoric acid at 400 °C (750 °F)	E	E	E	E	E

(a) Wear measured from tests conducted on Dow-Corning LFW-1 against 4620 steel ring at 80 rev/min for 2000 rev varying the applied load. (b) Wear measured from dry sand rubber wheel abrasion tests. Tested for 2000 rev at a load of 135 N (30 lbf) using a 230 mm (9 in.) diam rubber wheel and American Foundrymen's Society test sand. OAW, oxyacetylene welding; GTAW, gas-tungsten arc welding. (c) E, less than 0.05 mm/yr (2 mils/year); S, 0.5 to less than 1.25 mm/yr (over 20 to less than 50 mils/year); U, more than 1.25 mm/year (50 mils/year)

Figure 17: Properties of Co-base hardfacing alloys. Reprinted from [87].

2.4.2.4 Effect of other common elemental additions to Co-Cr-Mo

While the effects of alloying elements have been expounded upon in previous sections, there are still many combinations that require discussion. Earlier editions of CoCr alloys were subject to the addition of Ni. Before the inception of Mo as a more biocompatible addition, Ni was added to CoCr due to its ability to reduce the formation of stacking faults while also providing stability to the FCC-based γ phase of the Co-matrix [127]. Ni is known to enhance the ductility of CoCr metallic alloys and provide stability to the FCC structure due to its improved tenacity of the Co-matrix. When Ni exists in large quantities, Co-Cr-Mo alloys can be alloyed with Cu (0-4 mass%) to improve the corrosion behavior of the resulting alloy when exposed to neutral chloride solution. In their study, Yang et al. finds that higher amounts of Cu causes a significant enhancement on corrosion resistance through its capability of strengthening the passivation properties of the alloy and prolonging the oxidization of dominant Cr(III) in the passive film into a more soluble Cr(V) [128]. Another study further shows that the addition of 2 mass% Cu leads to a considerable improvement to corrosion resistance of NiCo-Cr-Mo alloy in aqueous HF acid solution, despite the incurrence of severe plasticity [128].

Studies have shown that Ni is a human allergen that creates hypersensitivity as compared with other metallic or ceramic materials used in similar applications. These inflammatory responses are correlated with Ni-Cr alloy restoration and recede upon the removal of Ni from the system [115]. Novel methods have been employed to reduce the presence of Ni while simultaneously keeping the same beneficial properties of improved

ductility and workability that are the result of the inclusion of Ni. In response to this, Mo has become a more acceptable standard in human implants as a result of these studies. When studied against conventional Co-Cr-Mo alloys, the ultralow-Ni Co-Cr-Mo alloys were shown to have significantly lower Ni ion elution [129]. This would imply that ultralow-Ni Co-Cr-Mo alloys have enhanced safety and suitability for implants. Hiromoto et al had fabricated alloys with fine grain size under ASTM F75 specification using thermo-mechanical techniques [129]. These alloys exhibit higher corrosion resistance versus conventional Co-Cr-Mo alloys in vitro and possess a two-fold higher wear resistance [18-20]. The improvement of safety in Co-Cr-Mo alloy implants was further surveyed by Sonofuchi et al (Figure 18) who observed ultralow-Ni (< 0.01%) Co-Cr-Mo alloys with and without Zirconium (Zr). It was determined that Ni ion emission was much lower in the ultralow-Ni Co-Cr-Mo alloys with or without Zr proving that the ultralow-Ni Co-Cr-Mo are much safer than conventional Co-Cr-Mo alloys. This runs counter to the findings of Kurosu et al who report an addition of 0.05% Zr suppresses the Ni ion release in vitro [21, 22] thereby improving the safety of implants. Sonofuchi deduce that the difference in manufacturing methods and the resulting surface area. As their study utilized forged alloys, metal ion emission could possibly be limited due to the low surface area and thus the beneficial features of Zr addition could be repressed.

For Co-Cr-Mo alloys, Titanium is a common alloying element that is introduced in varying amounts depending on the intended use of the final alloy piece. For the mixture of Co and Ti, high temperature operation can lead to the formation of a number

of intermetallic compounds (similar to those referenced in previous sections), such as Ti_2Co, $TiCo_2$, and $TiCo_3$ [130]. Carbide formation can be augmented when other minor elements are introduced. Due to its high affinity to C, Ti has a facile interaction with the C within the metal matrix and the residual unbound element dissolves into the solid solution [115]. Even a small proportional increase from 4% to 6% may produce similar carbide structures but the propensity to segregate is more apparent with the increase in Ti. Peter and Rosso show grain orientation effects with the increase in higher Ti content [115]. Grain growth begins at the alloy core before growing into a different direction. The microstructure growth confers a large amount of compressive stress which jointly produces residual stress in the alloy and a decrease in alloy workability. Thus, the level of Ti alloying can greatly influence the microstructural development by homogenizing the microstructure of the alloys which causes general effects on the alloy behavior.

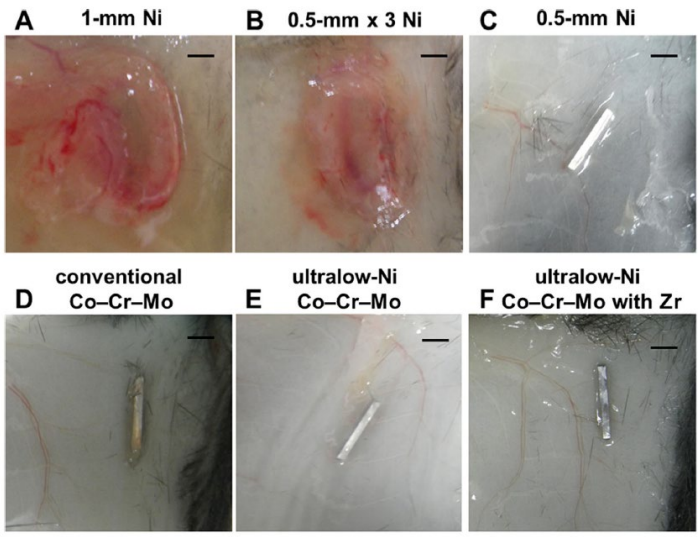

Figure 18: Macroscopic images of skin inflammation of conventional Co-Cr-Mo vs ultralow-Ni Co-Cr-Mo. Reprinted from [129].

In CoCr alloys, N addition has been shown to improve the ductility of these alloys. For a Co-33Cr-9W system, the addition of N aids in stabilizing the γ-phase thereby improving the ductility. The stabilization of the CoCr γ-phase is achieved through a suppression of the athermal γ to ε martensitic transformation that occurs as the material cools down and is reported to be antagonistic to ductility [131, 132]. In their work, Yamanaka et al added Cr_2N powder in excess to Co-Cr-Mo with a slightly reduced Cr content such that adding the Cr_2N powder yielded a Cr concentration of 33 mass%. When N is introduced to Co-Cr-Mo, a nanostructure evolves in relation to Cr_2N phase, a hexagonal crystal structure which is stable in the system is conjectured to be the reason for the improvement in γ-phase stabilization [131, 132]. Thus, it came as no surprise that the alloys exhibited a single γ-phase matrix because of the high concentration of N. Alloy strength and N concentration have a direct correlation. In conjunction with an increase of C, Yamanaka found that yield strength (measured by 0.2% offset) of the alloys improved as well. Elongation to failure was also subject to improvement although the enhancement mirrored more of a bell curve centered around 0.1 mass% C. Improved ductility was associated with values below 0.1 mass% C whereas further C content increases began decreasing the ductility value. From these studies, it is shown that C concentration of ~ 0.1 mass% is optimal for balancing strength and ductility of the as-cast alloys. When compared to wrought Co-Cr-Mo alloys, the increase in C allowed for comparable strength, acceptable ductility, and good corrosion resistance [116].

The precipitation of nitrides also further strengthens Co-Cr-Mo alloys [132-134]. N in Co-Cr-Mo has been surmised to segregate and suppress the formation of ε-martensite at the cell boundary, which suggests an improved solubility of Cr or Mo through inclusion of N in Co-Cr-Mo alloys. Specifically, this tendency has been seen in N-containing Ni-free austenitic steels [133]. A study performed by Yoda et al (Figure 19) analyzed the effects of Cr and N content on microstructures and mechanical properties of as-cast Co-Cr-Mo alloys for dental applications. The increase of Cr content in N-containing alloys saw an increase in lattice parameter of the γ-phase. N-free alloys displays the same lattice parameter due to the small atomic radius difference between Co and Cr.

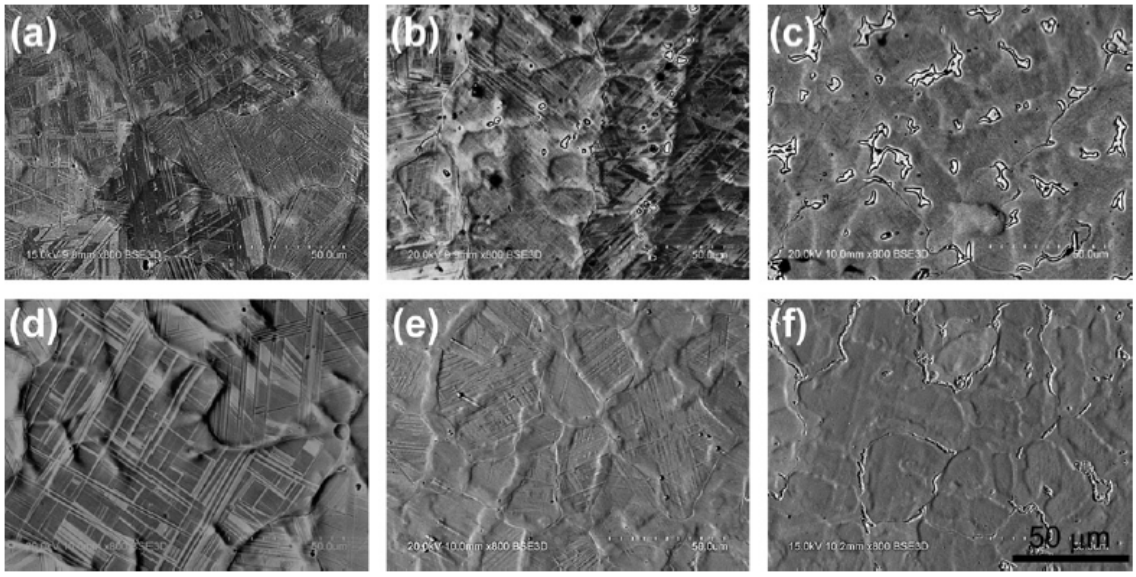

Figure 19: BSE images of Co-Cr-Mo alloys N-free (a-c) and N-containing (d-f) with increasing Cr content. Reprinted from [133].

Compositional analyses by EDS and XRD showed that N-containing alloys possessed Cr and Mo concentrations at the N-enriched cell boundary which stabilizes the γ-phase and increases its lattice parameter. The proof strength, ultimate tensile strength (UTS) and elongation of these N-containing alloys increased with a rise in Cr content. These effects are manifest as a decrease in working hardening behavior. Lee et al corroborated this sentiment with a study that proved high Cr and N contents in Co-Cr-Mo alloys showed higher strength and ductility than cast Co-Cr-Mo alloys (ASTM F75) [133]. This was reasoned to be due to the formation of ε-phase after tensile testing as the deformation mechanism might switch from strain-induced martensite transformation (SIMT) to another mechanism like twinning or dislocation slip with increasing N content. In comparison to this, N-free alloys had no correlation with Cr content and exhibited low strength and limited elongation. These mechanical properties were caused by the formation of strain induced martensite formation following tensile tests. BSE images show the presence of HCP (έ) and BCC (γ) phases; however, these N-free alloys have a constant γ phase lattice parameter regardless of Cr content. Yoda surmised that the lattice parameter stays consistent due to the small atomic radius difference between Co and Cr.

A complementary study to this was performed by Yamanaka et al with the purpose of developing high strength and ductility in biomedical CoCr cast alloys through simultaneous doping with N and C. Electron probe maps for increasing C content are provided in Figure 20. The strategy employed here was two-fold: concurrent doping of the CoCr alloy with N and C was supplemented through increasing the Cr content to

increase N solubility [116]. From the N doping, the development of the hard σ-phase, a Cr-rich intermetallic compound, was remarkably reduced. Furthermore, the increase in C concentration leads to finer grains and carbide precipitation in the microstructure thereby improving the strength of the alloy [116]. Tensile ductility was also shown to improve with an increase in C concentration though only up to a certain amount. A maximum is reached at a C concentration of ~0.1 mass% and decreases henceforth with further C doping. Synergistically, adding C did not have a detrimental effect on the corrosion resistance. However, despite the stability imparted by N to microstructural phases, the γ-phase is not thermodynamically stable; subsequent plastic deformation at room temperature can lead to the shift to epsilon-martensite phase.

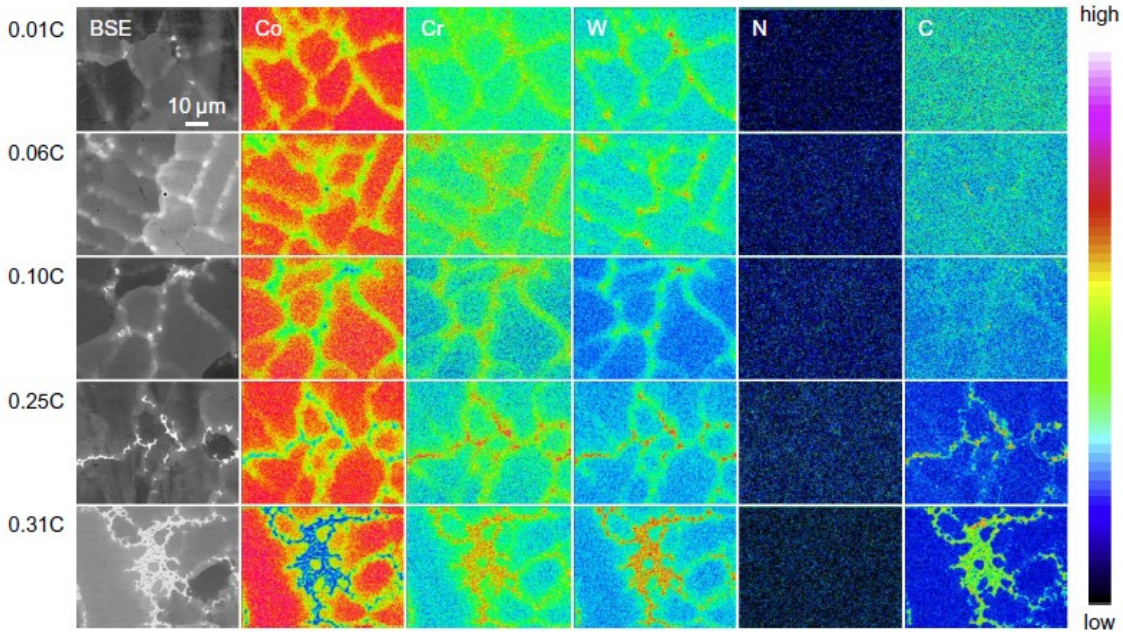

Figure 20: SEM-BSE micrographs with electron microprobe maps with increasing C content. Reprinted from [116].

Si is another common alloying element that typically resides in Co-Cr-Mo alloys in amounts less than 1%, however some studies have utilized the benefits of larger amounts of Si. Adding up to 5 wt.% Si to Co-Cr-Mo, Podrez et al observed a γ solution FCC lattice interlaced with precipitates of intermetallic phases. In their study, the γ phase grains were found to possess numerous stacking faults. A local chemical analysis by an X-ray microanalyzer showed Mo in analyzed phases indicating that Mo solidifies in the same lattice positions as Cr, due to similar lattice parameters and atomic radii (FCC). Regarding carbide formation, Cr is thus easily substituted by Mo. As far as segregation of elements of Cr and Mo, Cr concentration ranges from 33 at.% in solid solution to 42 at.% at precipitates while Mo concentration ranges from 2 at.% in the dendrites to 10 at.% in interdendritic areas. TEM imaging performed by Podrez et al. showed intermetallic precipitates within the FCC lattice γ solution [135]. Micro-analysis results were further corroborated by TEM as the γ phase grains displayed many stacking faults, which could perhaps be influenced by contemporary manufacturing techniques. Addition of Si in Co-Cr-Mo systems provides improvements in material properties such as hardness, tensile strength, good fluidity in liquid phase, dimensional variation with restricted limits in heating time at high temperatures, high resistance to corrosion in simulated physiological environments, realization of a crystalline microstructure, and good biocompatibility, without influences on the human body [136]. As Si content is increased, the percentage of the alloying elements decrease, but major reductions are seen by the principal element, Co. The addition of Si is a relatively recent development in the alloying of Co-Cr-Mo. CoCrWSi and Co-Cr-MoSi alloys have gained recent

traction with various research groups [137]. Its effect has been reported to be similar to Cr, Mo, and W [137]. Elemental Si is known to stabilize the HCP phase of Co-Cr-Mo while also possessing the ability to change the microstructure of as cast and heat-treated alloys. For Ni-containing alloys, Si imparts good casting properties and enhanced ductility. Si also has beneficial modifications to the shear bond strength that occurs between porcelain and CoCr metal substrates that are common in metal-ceramic dental restorations [137]. In work performed by Minciuna et al, XRD patterns were analyzed for Co-Cr-$MoSi_1Mn_1$ and Co-Cr-$MoSi_5Mn_1$. For both alloys, the gamma phase (FCC), $M_{23}C_6$ carbides, and pi (π) (s)/eta (η) phases. The π and η phases, identified by Alfirano et al, have a M_2T_3X-type carbide with β-Mn structure and M_6C-$M_{12}C$-type carbide structure, respectively [137]. The XRD results also showed that more peaks assigned to the $M_{23}C_6$ carbide was concurrent with higher Si content thereby implying that increasing Si content leads to the formation of $M_{23}C_6$ carbide. Regardless of the chemical compositions, the contents of Cr, Mo, Si and C were elevated in the zones between dendrites and reduced in dendrite zones. In comparison, the content of Co and Mn in dendritic regions were higher than within the interdendritic zones. From the tensile testing performed, increasing the amount of Si leads to a higher fraction of carbides which correlates with a decrease in failure strength and elongation values. An increase in Si further leads to a corresponding increase in hardness as reported from the observed microstructure and mechanical properties from the tensile tests [137]. Henriques performed an analysis on Co-Cr-Mo alloyed with 2.2 wt.% Si and found that the regions between dendrites of the as cast alloy possess three phases of different

chemical compositions but all three exhibit elevated amounts of Cr, Mo, and Si when compared to the dendritic regions.

When Co-Cr-Mo is alloyed with 5% Si, combinations of type $Co_{(x)}Mo_{(y)}$ and $Cr_{(y)}Co_{(x)}Si_{(z)}$ precipitate and radically change the mechanical properties of the alloys. When Si is added to a commercially pure Co-Cr-Mo alloy, an improvement in mechanical properties, specifically hardness, could be observed because of the resulting fine grain structure along with the formation of solid solutions with Co and chemical compounds: $Cr_{(y)}Si$ and Mo_2Si. The original variation of Co-Cr-$MoSi_5Mn_1$ alloy, although showing an improvement in properties after Si addition was only viable for medical apps once they were quenched and put into a solution. Vizureanu et al further raised Si content in Co-Cr-Mo to as high as 7 wt.%. The resulting alloy shows similar constituents of $Co_{(x)}Mo_{(y)}$ and $Cr_{(y)}Co_{(x)}Si$ which transforms the mechanical properties in the alloys. Furthermore, the high amount of Si causes an increase in the elastic modulus E which imparts a resistance to plastic deformation to the alloy. The alloys with 7% Si also exhibited alternative values around the average values characteristic of the Co-Cr-Mo system alloy which could correlate with a difference in carbide arrangement. This offers improvements in certain material properties whether directly or indirectly.

2.4.2.5 Addition of Mo to Co-Cr based alloys

For the purposes of this work, the addition of Mo has been evaluated. Increasing Mo in CoCr base alloys provides improvements in density, microhardness, and sliding wear behavior as shown in Aherwar et al. [138]. In their study, biomedical Co-30Cr

alloys were prepared with varying weight percentages of Mo from 0-4 wt.%. Density was improved from 7.2 to 8.7 g/cc as Mo percentages increased. Moreover, when normal load and sliding velocity were applied in steady-state wear tests, the highest percentage of Mo (4 wt.%) provided maximum wear resistance over other alloy compositions. Atomic Force Microscopy (AFM) corroborated this result as the surface profile generated showed that the 4 wt.% Mo alloy experienced less penetration and wear from the prior tests. Increasing Mo content allows Cr to stay in the solid-solution matrix over the formation of Cr-rich carbides. Thus, the corrosion resistance of the parent alloy is improved due to the formation of a dense passive Cr-oxide film on the surface of the material. Mo and Cr also decrease the stacking fault energy and stabilize the ε-phase further improving the mechanical properties of the alloy.

In NiCrMo, Mo addition has also shown to improve localized corrosion resistance through the impedance of dissolved portions of the broken down passive film and precipitation on the film that shields against ion diffusion through the film [128]. This occurs through the oxidation of Mo(IV) on the outermost film into Mo(VI) which forms soluble MoO_4^{2-}. The dissolved MoO_4^{2-} anions are cation-selective thereby preventing the diffusion of Cl^- and other ions, a process which promotes the growth of an inner oxide film.

Stellite 21 differs from the other forms of Stellite due to its inclusion of molybdenum, instead of W, to act as a solid solution strengthener. Furthermore, Stellite 21 possess a considerably lower C content. The combination of these two factors and the presence of Cr in the solid solution (versus in Cr_7C_3 carbides) affords Stellite 21 a

superior corrosion resistance to the other Stellite variants. Like Stellite 21, the 700 series (703, 706, 712, and 720) was later developed around the premise that the W in these alloys is replaced by Mo with contents that range from 5-18%. The 700 series is known to offer excellent corrosion resistance in reducing conditions. The carbides in these alloys also feature molybdenum partitions which thereby enhance wear resistance, a dual tribocorrosion defense [139].

Co-Cr-Mo is identified as the hardest known biocompatible metal alloy possessing good tensile and fatigue properties [13]. From the large amount of Cr content in the alloy, Cr oxide provides a protective layer for the material below the surface. As described previously for other CoCr based alloys, the volume fraction, size, shape, and distribution of C particle precipitates afford Co-Cr-Mo its characteristic wear resistance. Grain size of the material also provides a crucial consideration to impart superior tensile and fatigue properties. Gupta et al created ternary phase diagrams to help quantify the effects of melding CoCr with other alloying elements. From their work, it is reported that at a 31.5 wt.% Cr, Mo and Cr effect an increase in melting temperature of the resulting alloy [140]. While typical gamma phase (FCC, A1 structure) that is formed from the L phase exhibits stability up to 950 °C before a martensitic-like transform to epsilon phase (HCP, A3 structure) should begin [141]. Fortunately, the gamma phase in dental alloys exhibits phase stability up to ambient temperature.

2.4.3 Phase Diagrams of Co-Cr-Mo

In the CoMo binary diagrams from the ASM handbook, Massalski shows that the Co-Mo system possesses four intermediate phases Co_9Mo_2, Co_3Mo, Co_7Mo_6(μ) and σ [140]. μ and σ phases develop from peritectic reactions L + α ↔ σ at 1620 °C and L + σ ↔ μ at ~1510 °C, respectively. Here, α is the BCC terminal solid solution of Mo. A eutectic reaction L ↔ μ + γ occurs at 1355 °C. Three peritectoid reactions μ + γ ↔ Co_9Mo_2, Co_9Mo_2 + μ ↔ Co_3Mo and a possible ↔ occur at 1200, 1025 and ~700 °C, respectively. Co_9Mo_2 and σ phases experience eutectoid decomposition Co_9Mo_2 ↔ γ + Co_3Mo at 1018 °C and σ ↔ α + μ at ~1000 °C. On the other hand, Cr-Mo is an isomorphous system with a minimum of 1820 °C at 12.5 at.% Cr [140]. A miscibility gap below ~800 °C is observed in the BCC α solid solution of Cr-Mo. Between the binary systems of CoCr, CoMo, and CrMo, eight intermediate phases have been reported.

Rideout et al. first studied the ternary Co-Cr-Mo system at 1200 °C with Cr and Mo up to ~65 mass% each [142]. The isothermal section is provided in Figure 21. Parts of the σ phase from the Co-Cr binary and the μ phase from the Co-Mo binary as narrow phase regions moving toward each other approximately along a line of ~41 mass% Co. In the Co-Cr-Mo system, one ternary intermediate R phase develops between the composition ranges of ~39-44 mass% Co and ~38-43 mass% Mo, respectively. The boundary of the FCC γ-phase boundary is shown with maximum Mo solubility of ~21 mass% while BCC α-phase boundary could not be determined.

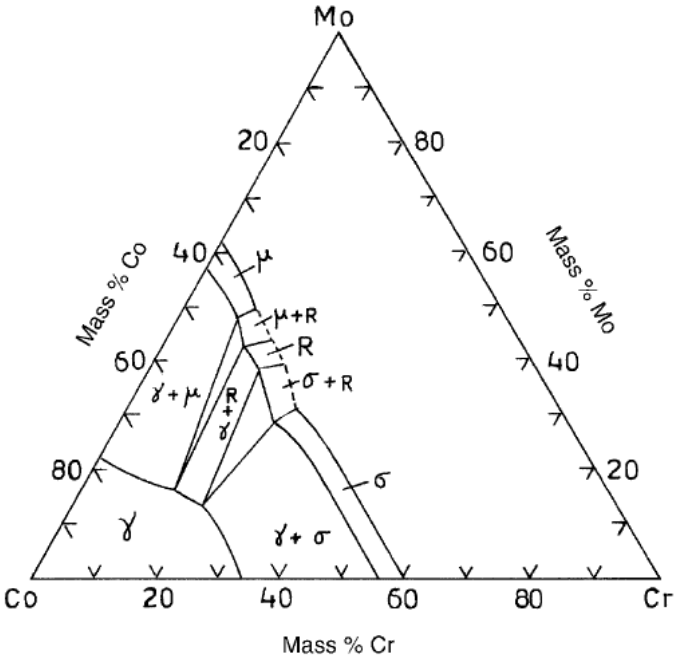

Figure 21: A partial isothermal diagram of Co-Cr-Mo system at 1200 °C. Reprinted from [142].

An isothermal section at 1300 °C was later studied by Darby et al. as shown in Figure 22. The purpose their study was to determine the extent of the σ phase of the CoCr system and whether it spread toward the σ phase of the CoMo system. The isothermal section at 1300 °C exhibits a wide σ region from the CoMo to CoCr binary regions. Between the σ and μ phase regions, Darby et al. show a new intermediate phase D that shows similarities to the R phase found at 1200 °C.

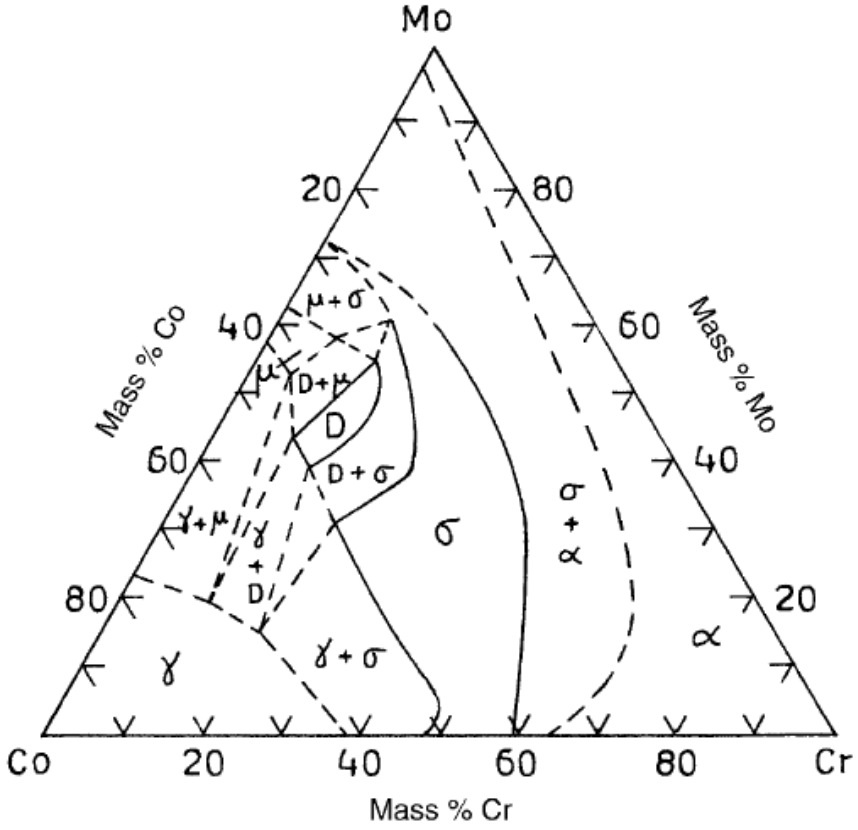

Figure 22: An isothermal section of Co-Cr-Mo system at 1300 °C. Reprinted from [143]

The phase diagrams presented are in agreement with the binary phase diagrams presented in the appendix from 1955 to 1958. Gupta offers an improved Co-Cr-Mo system at 1300 °C as shown in Figure 23. This amended ternary phase diagram considers the σ phase stability for the CoMo and CoCr binary systems at different temperatures. Based on the data, the σ phase is proposed to have three-phase equilibrium with α and γ phases at 1300 °C in the CoCr binary region. Currently, no other ternary phase diagrams are provided for the Co-Cr-Mo system.

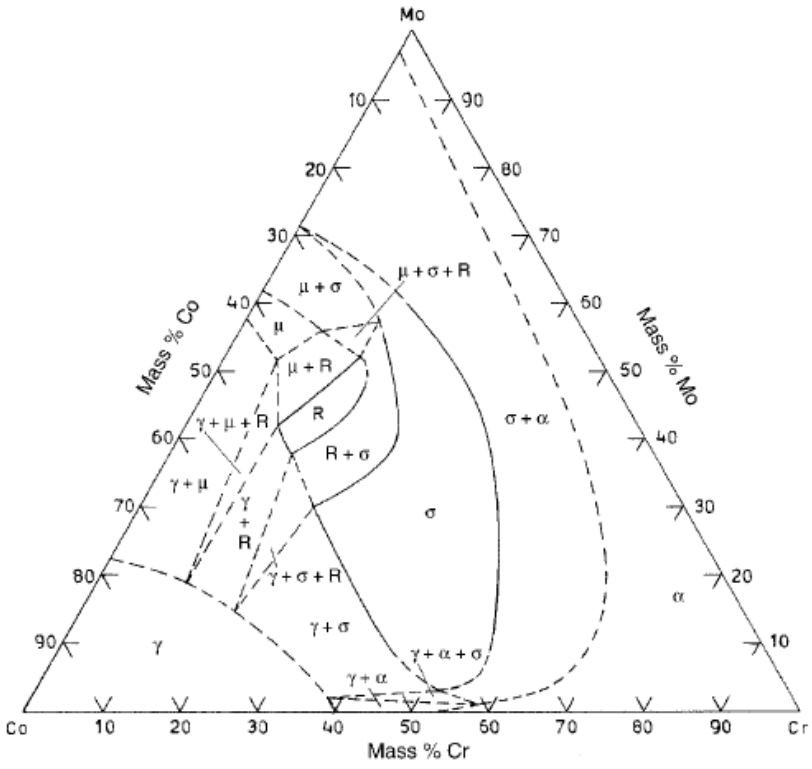

Figure 23: Isothermal section of Co-Cr-Mo system at 1300 °C via Gupta. Reprinted from [140].

The solid solution of Co, Cr, and Mo creates dendritic structure with interspersed carbide precipitates [135]. Each elemental addition creates an array of different carbides. High Cr content leads to a large proportion of $M_{23}C_6$ (M= Co., Cr or Mo) carbides along with smaller portions of M_7C_3 and M_3C_2-types [135]. Other elemental additions in the alloy create M_6C and MC-type carbides [7, 9]. It is known that the $M_{23}C_6$ and M_6C are formed during eutectic solidification or precipitation. The conversion from $M_{23}C_6$ to M_6C occurs upon annealing at 1230 °C before complete dissolution of the carbides occurs between 1250 °C and 1270 °C [4]. A large factor to structure formation in these materials is the high solubility of alloying elements in γ-solid solution. Thus, solution

hardening is not the only possibility, but so is decomposition control that creates stable phases that lead to precipitation hardening that occurs due to interdendritic carbide participates that form with these additional alloying elements [135]. In a Co-Cr-Mo alloy, the Cr content can measure as high as 22 wt.% such that the resulting matrix is comprised of a solid solution of all three elements with an A1 (γ) lattice [135, 140, 144, 145].

In as-cast Co-Cr-Mo alloys, phases have also been reported besides those with conventional carbides based on the variation of C content (0.12-0.35 wt.%) such as σ-phase (Co. (Cr, Mo)) and mixed carbide/nitride phase, π, among others [146]. The intermetallic compound σ-phase is a close-packed tetragonal that exists with the γ- or ε-phases over a wide temperature and composition range. With the presence of Cr being a significant proportion of the system, at elevated temperatures, the γ-matrix of Co-Cr-Mo can absorb C up to a maximum value of ~0.25 mass% at 1550 K [116, 147]. Additional studies have shown that the addition of C stabilizes the γ-phase [116, 147, 148]. The σ phase provides no strengthening of alloys and is typically avoided as it is an undesirable brittle phase [116, 149]. N addition is known to mitigate the occurrence of σ-phase precipitation though heat treatments are known to precipitate the σ-phase as well [133, 134, 150]. An increase in W content has been shown to stabilize the γ-phase as well, but an overabundance of W increases the volume fraction of the σ-phase [151]. Another intermetallic compound, the rhombohedral R-phase arises upon the enrichment of W in the microstructure and appears only in low temperature regions.

For CoCr alloys with Mo concentrations greater than 4 wt.% and C, M_6C carbides form more frequently than $M_{23}C_6$ [127, 152]. The W precipitate exhibits greater stability than the Mo carbide and possesses a complex chemical composition. A secondary M_6C carbide also forms due to a reaction between elemental configuration MC and the solid solution: MC + gamma (γ) -> M_6C [135]. These carbides are not confined to their current structure though as thermal treatment such as aging of the alloys promotes conversion of the M_6C carbide to $M_{23}C_6$. This secondary carbide is fine-dispersive thereby imparting improved mechanical properties to Co alloys. Both M_6C and $M_{23}C_6$ have FCC crystal structures with a similar cubic lattice parameter a = 1.06-1.1 nm. This is shown by Podrez et al who performed x-ray local chemical micro-analysis that revealed Mo in the analyzed phases [135]. Mo and Cr are thus proven to share the same lattice sites and therefore have similar lattice parameters and atomic radii (FCC crystal structure). For the formation of carbides, Mo acts as a facile substitute for Cr. Through the binary phase diagram of CoCr, for 31.5 wt.% of Cr, Mo and Cr are shown to decrease the melting temperature. γ phase (FCC) solidifies stably from L until 950 °C upon which martensitic-like transformation to ε phase (HCP, A3) starts. Other research points to the γ phase in dental alloys remaining stable down to ambient temperatures [135]. In their work on the effects of Mo on the properties of CoCr dental alloys, Matkovic et al. established that samples of Co-Cr-Mo that have compositions near the optimal composition of $Co_{60}Cr_{30}Mo_{10}$ exhibit a typical dendritic solidification dual-phase microstructure. Slight addition of Cr and a reduction in Mo results in dual phases that differ slightly in composition and subsequent material properties. Mo is

further understood to reduce the grain size of Co alloys thus creating the previously mentioned solid solution strengthening and improvement in mechanical properties [153].

2.4.4 Manufacturing Methods of Co-Cr-Mo

Co-Cr-Mo has been manufactured through a variety of traditional and additive manufacturing methods. Each method imparts different material properties due to the nature of the procedure, how the part is constructed, and the nature of the precursor materials. Depending on the specific application and timeframe upon which a part is required, each approach offers its own strategic benefits.

2.4.4.1 Casting

Casting is a common manufacturing procedure for Co-Cr-Mo alloys. Microstructure of as-cast Co-Cr-Mo alloys display a non-homogeneous nature with a distribution of dendrites within the solid solution. Room temperature as-cast Co-Cr-Mo possesses an FCC metastable matrix from a slow transformation to the stable HCP phase [154]. In the as-cast condition, Ni and N free Co-Cr-Mo alloys demonstrate low ductility from σ phase formation within the interdendritic region leading to brittle fracture [116, 132, 148]. An earlier study by Clemow and Daniell found a transformation of interdendritic $M_{23}C_6$ carbides to M_6C in as-cast alloys that were solution treated followed by a 15 min annealing process [155]. Kilner et al observed that second phases of lamellae in cast Co-Cr-Mo are primarily $M_{23}C_6$ precipitates [111]. Further in their work, annealing at 1225 °C for 1-2 days dissolved the $M_{23}C_6$ carbides into the matrix.

Another type of carbide that appeared like long prismatic needles were hypothesized as being M_7C_3 type. In nanoindentation tests performed by Liao et al, carbides of the $M_{23}C_6$ and M_6C type were formed through eutectic solidification or precipitation as well as a new mixed phase that is comprised of ~100 nm fine grains. This mixed phase was observed to consist of mostly $M_{23}C_6$ type with alternating richness of Co or Cr when processed by nano-beam procession electron diffraction [118]. Mo-rich $M_{23}C_6$ carbides in the mixed hard phases did not occur from segregation from casting. Liao et al explained that a metastable single phase $M_{23}C_5$ carbide occurs only during fast cooling. The chemically different but structurally identical $M_{23}C_6$ carbides are the more thermodynamically stable in the mixed hard phase that aggregated during Liao's tests. The thermodynamic stability is implied through annealing of the samples at 1230 °C for 1 hour which coarsened the carbides but did not change compositions. At lower temperatures, for example below 700 °C, $Mo_{23}C_6$ exhibits lower Gibbs free energy than $Cr_{23}C_6$. Senior et al details the partitioning of Mo in $M_{23}C_6$ type carbides during the aging of CrMoV steels [156]. When annealed, these CrMoV steels demonstrate coexistence between $M_{23}C_6$ and M_3C or M_6C carbides which show sluggish kinetics [156, 157].

Cast alloys are typically compared to wrought alloys as both are subject to heat treatments to impart various material properties. Cast materials have been shown to have higher yield, tensile, and creep strengths to which these materials are applied. Karaman reports that as cast dental samples exhibit a microstructure with a large amount of second phases spread in different directions. The Cr and Mo-rich second phase

precipitates in the cast samples are known as the σ-phase that remains from dendrites forming as part of the CoCr alloy cooling [11]. These alloys are usually stronger than similar wrought compositions due to the higher C content as a part of casting. Furthermore, cast materials are less expensive in initial costs. Wrought materials have their own range of benefits. Due to the thinner sections inherent in wrought materials, thermal fatigue is reduced by promoting more resistance to thermal cycling and shock. In early comparative work on cast versus wrought alloys, wrought alloys were observed to have better corrosion resistance [6]. This is due to the smooth surfaces that wrought alloys exhibit that prevent accelerated corrosion. Nanoindentation has also shown that cast specimens have lower hardness than their wrought counterparts [118]. For the repair of stainless steel or nickel alloys, wrought materials keep the level of ductility necessary for repairability. Cast materials commonly fail due to brittle fracture from corrosion which makes them difficult to repair through welding. Wrought alloy manufacturing Wrought alloys typically feature a finer grain size and a more finely distributed collection of carbides. This leads to the chemical homogeneity and improved corrosion behavior of wrought alloys [6]. Liao attributed the homogeneous $M_{23}C_6$ array structure to be due to repeated heating and deformation operations [5]. Lee et al studied the properties of hot forged wrought alloys and noted a strong correlation between C content with microstructure and mechanical properties [158]. Another report from Rodriguez et al stated that lower C content in Co-Cr-Mo alloys may cause greater chemical and microstructural homogeneity and thereby improve corrosion resistance [159]. A Co-based cutting tool alloy with compositional variations in Mo (3-15%), Cr (25-35%), and

C (0.5-2.5%) and a minimal presence of W (< 1%) was studied by Wu et al to provide industrial cutting tools for operation in aggressive media. These alloys were found to possess enhanced resistance to abrasive and corrosive attack [160]. Their observations of the character of the microstructure denote banding and occasional twinning with grains of size larger than 20 μm represent at least 20% of the alloy volume while another 20% were grains of size smaller than 5 μm. Moreover, the formation of finely dispersed Mo carbide particles that occur from the 3-15 wt.% prove to be beneficial in a tough, corrosion resistant Co-based alloy matrix [160].

2.4.4.2 Powder Metallurgy

Subtractive manufacturing comes with the drawback of a great deal of material waste most often due to unused product. Other conventional methods require shaping and forming of a large mass of material which can prove cost prohibitive when compounded over time. When cost effectiveness is a concern for part development, such as in producing large volumes of small rudimentary shapes, powder metallurgy of Stellite alloys can be a viable option. Powder precursor Stellite parts exhibit remarkable wear resistance and mechanical properties which ensure reliability required for environmentally complex applications such as aerospace bearings and industrial saw teeth [87].

Powder metallurgy (P/M), like any other method, demands its own set of optimal process parameters that ensure that the resulting product is to specification. Using medical grade Co-Cr-Mo powder alloy mixture, Rodrigues et al looked to optimize P/M

process parameters for the best combination of properties to combat environmental corrosion associated with dental fixtures. Different sintering temperatures have considerable effects on the physical, mechanical and electrochemical properties of the alloy [6]. Vidal et al further show the influence of heat treatments on material properties [161]. Applied thermal treatments can affect the alloy microstructure which changes wear resistance, mechanical properties, biocompatibility, and corrosion resistance. Sintering between 900 °C to 1100 °C can lead to carbon precipitation at grain boundaries while above this temperature, no carbide precipitation is observed [162]. The absence of carbide precipitation indicates carbide instability at temperatures above 1100 °C and a reduction in strength due to the disappearance of the carbides. Rodrigues found that optimized hot working provides microstructure control which yields grain refinement and mechanical properties enhancement. Rapid cooling also presents an array of different effects such as the formation of athermal ε-martensite in Co-Cr-Mo alloys. These rapidly cooled alloys featured 3-4 times as much ε-martensite than what is observed in conventional alloys. This was speculated to be an effect of the powder structure providing preferable nucleation sites for athermal ε-martensite [163].

Another type of sintering, green compact sintering, followed by rotary cold repressing and heat treatment was found to favor the formation of the ε HCP-phase for the former post processing treatment and homogeneous α-Co structure in the latter heat treatment. This method helped to improve the strength of the material while simultaneously imparting a measure of ductility to provide adequately rounded mechanical properties.

Traditional manufacture of Co-Cr-Mo based prosthetic devices have been fabricated through investment casting. In recent years, implants have been forged and machined using wrought Co-Cr-Mo feedstock. Wrought Co-Cr-Mo implants feature finer grains with an optimum configuration of carbides. Further finishing procedures can provide a better surface finish than cast Co-Cr-Mo which leads to improved service performance [13]. While LENS has been utilized for some manufacture of Co-Cr-Mo, a wealth of information on the LENS based manufacture of Co-Cr-Mo does not exist.

2.4.4.3 Reference Alloy ASTM F-75

The work performed here focuses medical grade Co-Cr-Mo thus there is a natural comparison to medical grade ASTM F-75. The element composition of ASTM F-75 is as follows: Cr 27.0, Mo 6, Ni 0.73, C 0.25, Si 0.94, Mn 0.36, Co balance. The composition of ASTM F-75 was used to print the samples discussed in the next few sections. ASTM F-75 LENS microstructure contains fine equiaxed and coarse columnar cells of varying size. SEM plots of cast ASTM F-75 (Figure 24) indicate intergranular carbides where carbides accumulate at the grain boundaries. From reference XRD plots, FCC-co, metal carbides, and intermetallics exist in the microstructure. In comparison between ASTM F-75 and its wrought counterpart ASTM F1537, F-75 outperforms F1537 in Vickers hardness tests for microhardness (400 vs 350, respectively) and nanohardness (900 vs 700, respectively). Specifically, for HV(0.5), ASTM F-75 has a hardness value range from 266-345 for cast Co-Cr-Mo. Further, friction coefficients are typically below 0.6.

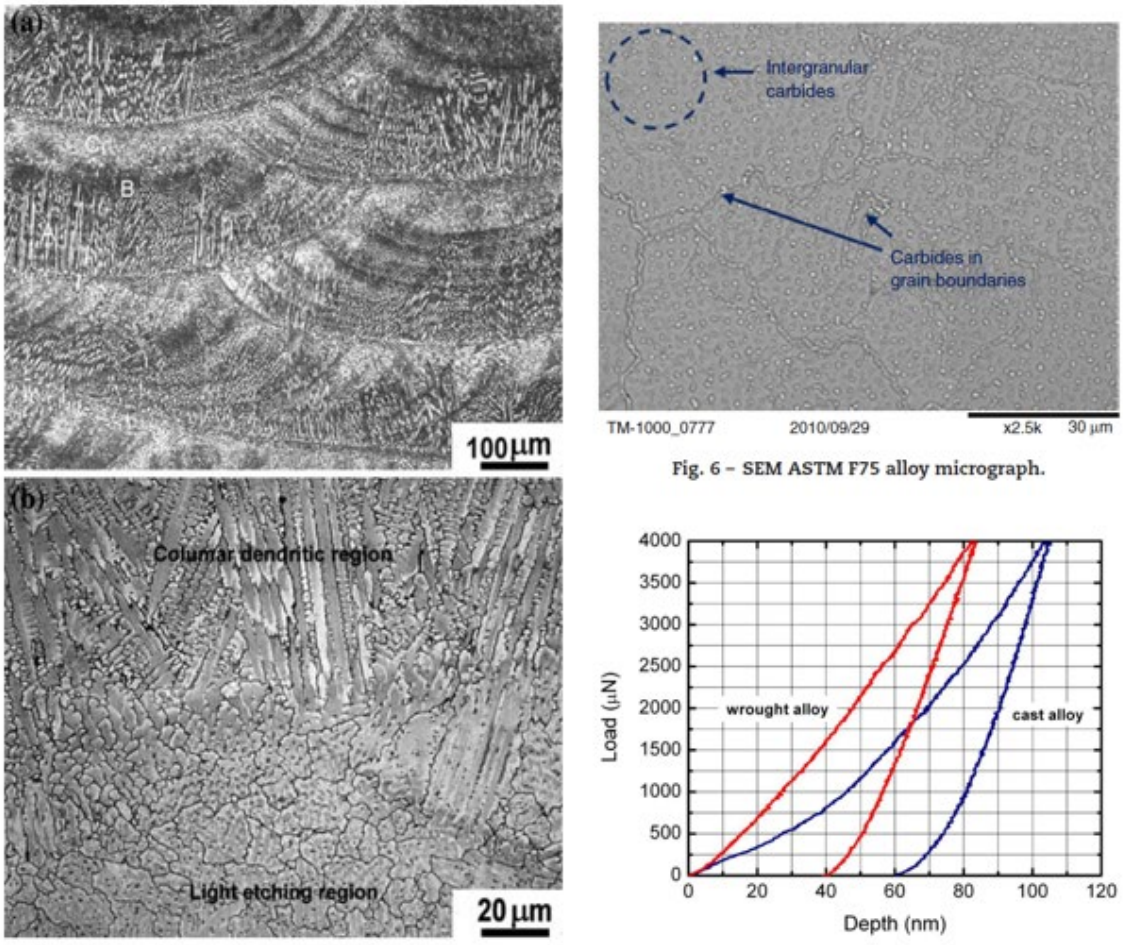

Figure 24: SEM micrographs of LENS (left) and cast (top right) ASTM F-75 with loading curves for cast and wrought alloys (bottom right). Reprinted from [164].

2.4.4.4 Laser-based AM of Co-Cr-Mo Alloys

Due to various beneficial material properties and an ability to be synthesized into a layer-by-layer structure, Co-Cr-Mo alloys have gained attention as a material for use in Additive Manufacturing technologies. The incredible design flexibility afforded by AM methods can circumvent some of the difficulties in machining Co-Cr-Mo such as short life cycle of cutting tools and plastic deformation [153]. Since Co-Cr-Mo alloys keep

their strength and hardness at elevated temperatures, machining proves difficult to accomplish. The low thermal conductivity, high strain hardening, and high hardness at increased temperature and high wear resistance exhibited by Co-Cr-Mo alloys contribute to the inferior machinability rating.

In typical AM design processes, rapid cooling and strong temperature gradients have a strong influence on the resultant microstructure of a printed part. Selective laser melting utilizes a small powder range at 15-45 μm. The small starting powder size leads to SLM samples of smaller grain sizes that have mean diameters within the powder size range. For example, SLM of Co-Cr-Mo alloy was able to produce cellular structures with cell boundaries that were Mo rich and suppress carbide and martensite phase formation at the surface of the material [7]. Karaman reports that SLM produces a homogeneous structure that does not possess unwanted intermetallic phases. Further computational analysis shows that the grains are small but elongated with size varying from between 10 to 80 μm [11].

Takaichi reports long columnar grains divided by second phase thin layers attributed to processing parameters [9]. Figure 25 provides images of SLM and as-cast alloy for comparison. From the heat produced by the laser melting process, the core of each SLM part is comprised of the ε phase of Co-Cr-Mo. With these features acting in synergy, a higher corrosion resistance is able to be obtained while a reduced amount of metals is released into the surrounding environment versus that of cast counterparts. A unique texture exhibited by the part from the melt pools is attributed as the main contributor to the observed differences between SLM and cast parts. In reports provided

by Jevremovich et al and Takaichi et al, SLM Co-Cr-Mo alloys improve on the biocompatibility and corrosion resistance of conventionally cast materials [8, 9, 11]. This was attributed to the fine cellular structure and elongated grains analogous to a bundle of straws, where Cr and Mo were present at the grain boundaries.

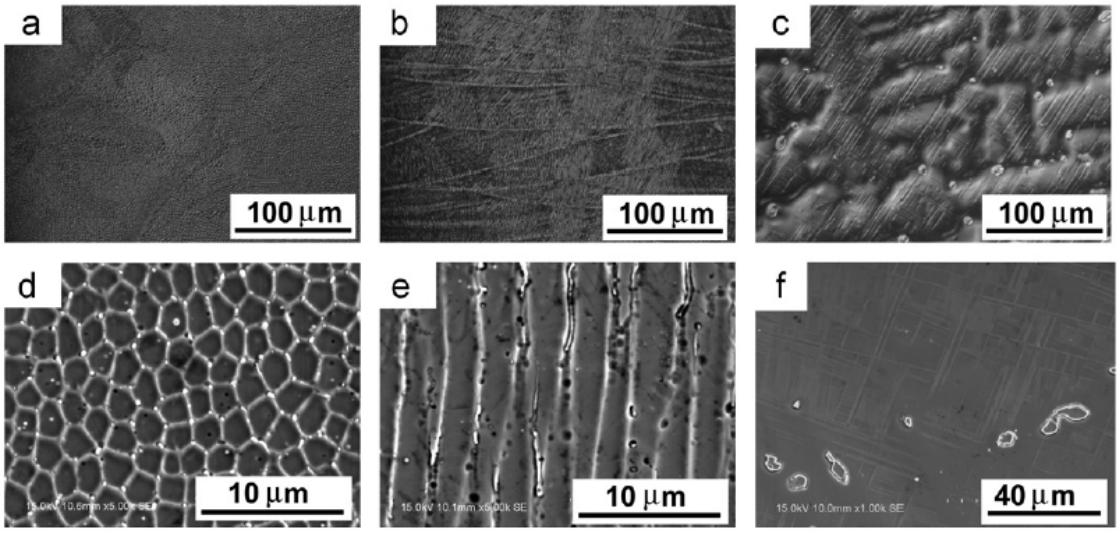

Figure 25: Microstructures of SLM build (a-b) and as cast (c) alloy indicating equiaxed and columnar sections (d,e). Reprinted from [9].

With the advent of additive manufacturing utilizing powder materials, it has almost become a requirement for a material to be able to be converted to powder. An inability to synthesize structures layer by layer can lead to a decline in usefulness for future applications. As such, it is encouraging to see that versions of Stellite alloys can also be employed in powder metallurgy (P/M). With the macro- and microstructural precision that is being offered through AM methods, these processing routes can present precise compositional ratios and spatial arrangements to provide the most beneficial

combination of properties. Such precision offers a large assortment of potential avenues for development and growth. Variation of gradation from the interface between substrate and coating top surface can be tailored to the specification of the material's intended use.

After parts are created, cooling rates can create cause vastly different microstructures. AM parts are typically the beneficiary of higher cooling rates due to the small dimensions of the sample [11]. The work performed by Karaman et al (Figure 26) evaluated the microstructural differences between AM based and cast samples. As cast samples contained large amounts of second phases in several different directional alignments. These second phase precipitates known as the σ phase possess a large amount of Cr and Mo and are hard and brittle. The precipitates are remnants of dendrite formations that occur as a result of cooling. SLM samples show a more homogeneous structure without the presence of the second phase precipitates. Computational analysis further corroborated this observation as SLM samples showed small, somewhat elongated grains with grain sizes on average much less than cast samples. Furthermore, larger grain masses possess multiple sub grain boundaries while grain structures show little to no texturing along each sample direction. This contrasts with Takaichi et al who reports that long columnar grains showing strong orientation preference were each separated by thin layers of second phase [9]. Such a difference was reasoned to be because of different processing parameters. While various reports have tabulated what process parameters were used in their specific study, there appear to be no consensus on which process parameters will reliably produce a certain structure with specific attributes.

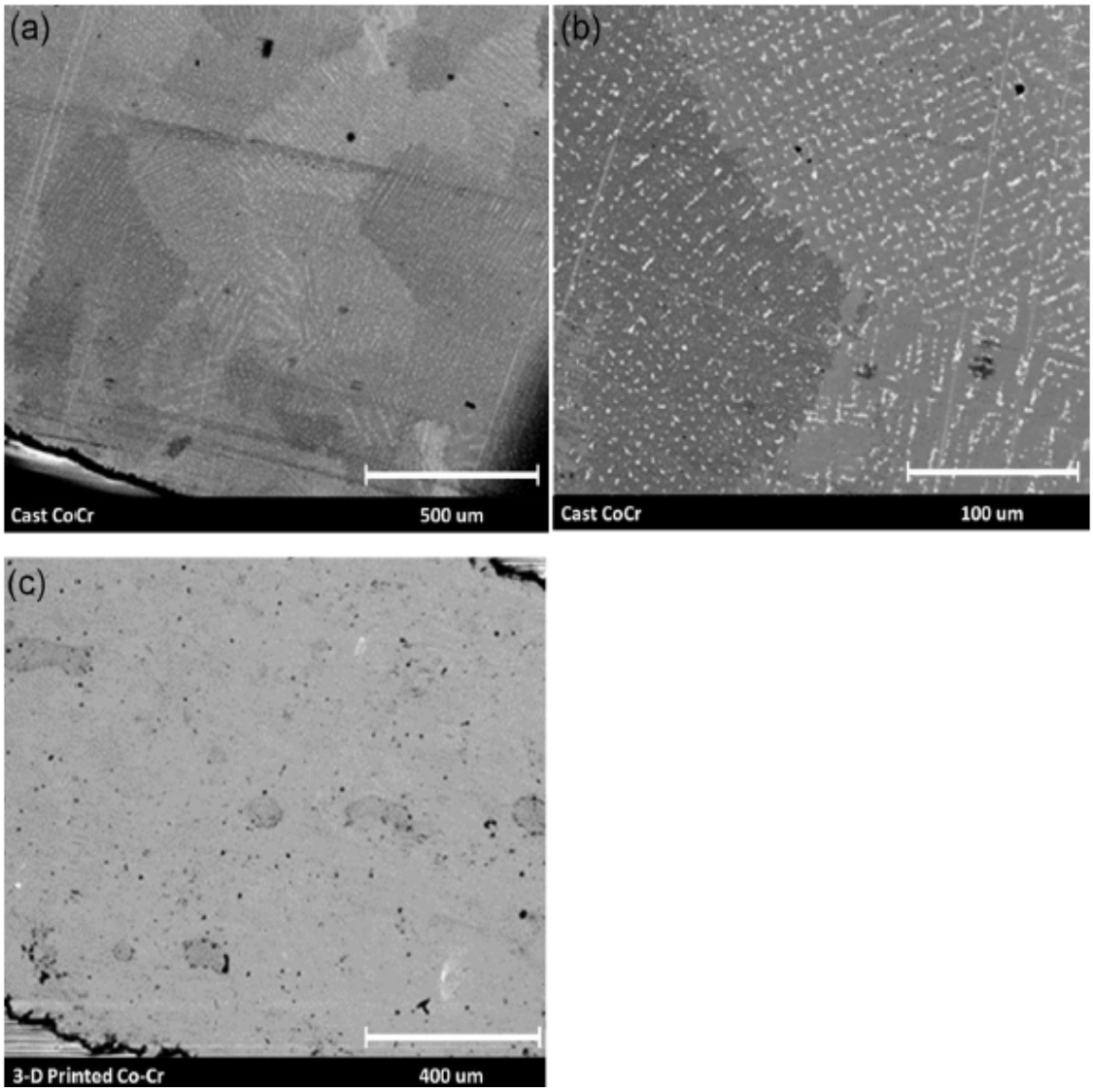

Figure 26: BSE images of as-cast (a,b) and SLM made Co-Cr-Mo from the bottom surface of a clasp sample. Reprinted from [11].

Although delving into process parameter analysis proves beneficial to the study of structural Co-Cr-Mo components, individual investigation of the printing of individual element components in Co-Cr-Mo can provide insight into methodology for improving the material properties and structural integrity of a component. Additive

Manufacturing of Cobalt and Chromium single element structures have not been referenced to the knowledge of the author, however CoCr based materials are a common powder metallurgy precursor. In comparison, Mo has been 3D printed as a single element structure which can help offer various insights into the printing process.

To print pure Mo structures, Faidel et al performed a study using SLM to determine the possibility of manufacturing high density parts. Mo is particularly difficult to work with due to its ability to withstand high temperature and high thermal absorptivity. To circumvent these issues, Faidel looked to analyze energy-based parameters such as laser power, spot velocity, and the powder layer thickness to achieve high density [165]. Laser beam reflectivity was further considered once useable reference values were obtained through preliminary experiments on a TZM-sheet and Mo-powder. In this preliminary work, the SLM parameters used for stainless steel were shown to not produce a continuous layer [165]. The Gaussian laser intensity distribution of the laser beam causes an insufficient power intensity for Mo to be melted. The only part where the intensity is properly reached is in the center part of the geometry (diameter ~50 μm) and not the entire square (~ 200 μm diameter) [165]. In order to solve this issue, an overlap parameter was included to string the laser weld tracks together resulting in a gapless arrangement such that the standard machine parameters could be utilized in these track overlaps for the following experiments. For the succeeding work, powder particle size of 10-25 μm with a tolerance of 0.2% was a controlled factor specifically for use in SLM. The laser power was kept at a maximum of 200 W through all the experiments along with an effective spot diameter of 50 μm that went unchanged.

Faidel et al chose to vary only the spot velocity, layer thickness, and overlap parameter to develop high density parts. Experiments were run by keeping 2 of the 3 parameters constant and changing the other two. This is a strategy that the work herein adopts for a portion of the preliminary testing of process parameters to yield fully dense parts. Faidel discovered that stable parts could be built from Mo powder regardless of high porosity. Perhaps even more revealing were the results of experiments where an overlap of 10 μm and 30 μm was investigated. While the structure at 10 μm possessed a homogeneous smooth surface, the structure at 30 μm exhibited various defects and a significant increase in porosity. This was attributed to the higher heat input which doubled from 200 J/mm^3 to 400 J/mm^3 which resulted in higher thermal strains and massive deformation of the layer. The added heat also disrupted the adhesion between layers. As to be expected, changing the scan speed had corresponding changes to the heat transfer to existing layers. Lower velocities lead to more heat transfer as the laser meanders for a longer period than at a higher velocity where the laser energy does not penetrate the part below. Finally, the evaluation of the layer thickness further played a role in how heat could be transferred to the surface of the material. Lower thicknesses were shown to possess consistent and smoother surfaces and structures. This was correlated with the lower volume of powder that was melted with the laser beam which allowed for insufficient power parameters to still provide enough energy input to melt the particles and weld them to the surface of the part [165].

With the increasing interest in powder materials due to the onset of additive manufacturing, there has been a focus on the feasibility and efficiency of converting

metals to powder form to carry out printing. An inability to synthesize structures layer by layer can lead to a decline in usefulness for future applications as these laser-based processes become ubiquitous. As such, it is encouraging to see that versions of Stellite alloys can also be employed in powder metallurgy (P/M). Cost-effectiveness notwithstanding, these powder precursor materials have outstanding wear resistance and mechanical properties and have proven reliable for needs in any applications from aerospace bearings to industrial saw teeth.

2.4.4.4.1 Functionally Graded Co-Cr-Mo via DED

With the precision that is being offered through AM, the powder-fed methods can provide more accurate compositional ratios and spatial arrangements to provide an optimal combination of properties. Such precision offers an endless assortment of potential avenues for development and growth. Variation of gradation from the interface between substrate and coating top surface can be tailored to the specification of the material's intended use. For example, a LENS deposit may not resist wear as readily should it possess carbide phases that are irregularly shaped, very thin, long, and interconnected particles that exist as a continuous network. Should this type of carbide phase encounter dry/rubber wheel wear test conditions, it offers less resistance to wear for the matrix. In comparison, optimally sized, regularly shaped carbide particles with uniform dispersion in the substrate microstructure provide much greater wear resistance. For the case of abrasive wear, Ram conjectures that the reason behind this disparity is due to the order of magnitude difference between the carbide sizes referenced [166].

While Ram voices concern about the incidence of continuous film-like networked carbide phases or thin, long connected carbide phases in LENS fabricated Co-Cr-Mo deposits affecting tensile ductility and fatigue properties of the material, they report that these morphological features did not affect the hardness of the Co-Cr-Mo deposits.

As the abilities of LENS devices becomes more sophisticated, their utilization in creating surgical implants can become a conventional method. The human body contains a corrosive environment to various metals implemented as surgical implants. One metallic alloy combination exists that both provides structure capability but also necessary wear resistance. Co-Cr-Mo and Ti-6Al-4V in combination offers the proper range of attributes, however, previous studies had reported metallurgical incompatibility [13]. These issues stem from formation of intermetallic compounds and the manufacturing process that yielded residual stresses that cause coating delamination [166]. To mitigate this effect, gradient coatings have become the most effective method to applying these coatings while maximizing their beneficial properties.

A series of consecutive studies was performed by Bandyopadhyay et al on functionally graded Co-Cr-Mo coating on Ti-6Al-4V alloy structures. Through LENS, the addition of compositionally graded Co-Cr-Mo coatings were adhered to the surface of Ti-6Al-4V substrates. In the initial study by Krishna and Bandyopadhyay et al, increasing percentages of Co-Cr-Mo alloy were built layer by layer before undergoing imaging and subsequent microhardness testing [13]. An SEM micrograph of the Co-Cr-Mo gradient printed on Ti-6Al-4V is provided in Figure 27. While previous manufacture methods yielded alloy combinations that form intermetallic compounds, such as Ti_2Co,

$TiCo_2$, and $TiCo_3$, the Co-Cr-Mo coat deposited on the Ti-6Al-4V alloy through LENS creates a metallurgically compatible interface between the alloys and improves surface hardness [13]. Further mismatches in elastic moduli, thermal expansion coefficient and hardness between Co-Cr-Mo and Ti-6Al-4V creates excessive residual stress in the coatings upon which cracks and layer separation occur [13]. In their work, Krishna et al employed LENS to fabricate functionally graded Co-Cr-Mo-coated Ti-6Al-4V alloy cylinders that exhibit an intact interface between the two alloys and surface hardness enhancement. This was achieved by gradual transition from 100% Ti-6Al-4V alloy at the bottom to increasing amounts of Co-Cr-Mo upwards over the thickness of four layers.

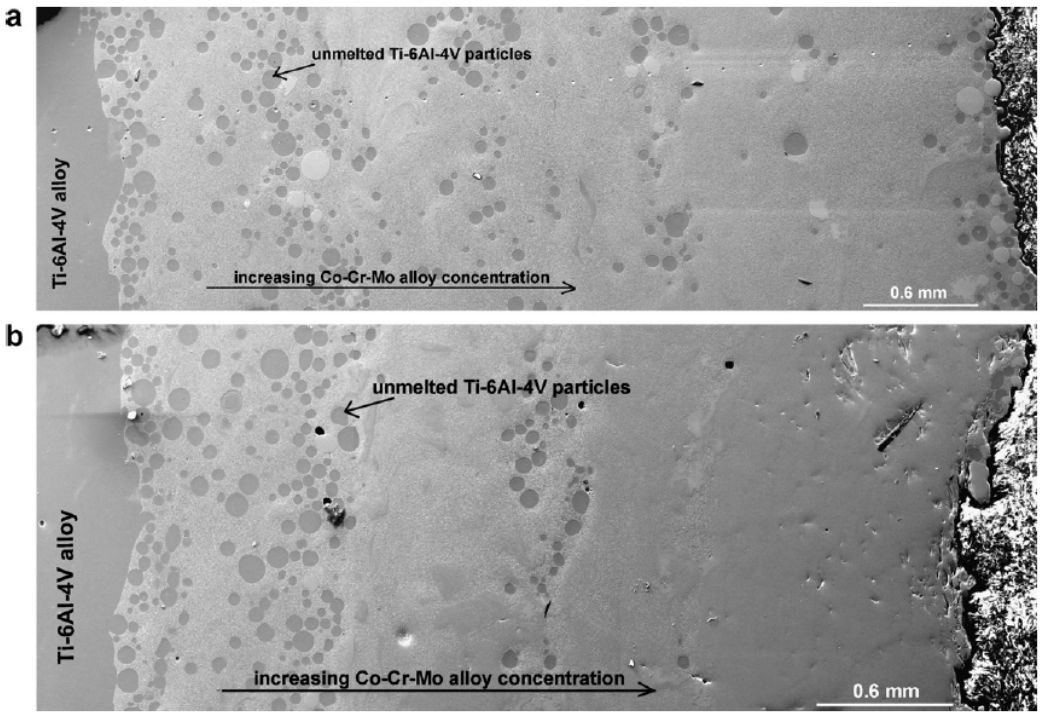

Figure 27: Microstructure of LENS Co-Cr-Mo graded coating on Ti-6Al-4V alloy (a) 50% Co-Cr-Mo alloy at the surface and (b) 86% Co-Cr-Mo alloy at surface. Reprinted from [95].

Compositional grading reduces failure and secures the interface between the alloys. Perhaps most interesting was the occurrence of radial cracks and delamination close to the upper region of the transition interface which shows a metallurgical mismatch when composition reaches 100% Co-Cr-Mo. Tests on compositionally graded structures with varying top surface compositions of 25%, 50%, 70% and 85% were then performed to judge the optimal compositional parameters that yield the structure with a highest structural integrity. While the first six layers deposited were 100% Ti-6Al-4V, the next 5-6 layers were subject to variations in Co-Cr-Mo composition. Next, changing the power from 200W to 450 W changed the porosity at the Ti-6Al-4V portion at the transition region between the two alloys [13]. Further, powder feed rate for Co-Cr-Mo alloy increased from 0-46.5 g/min over the transition layers while Ti-6Al-4V was deposited from 17.5-0 g/min over the same amount of deposits.

Microstructural characterization and microhardness indentation are used by Krishna et al. to quantify the compositional gradient across the layers. Micrographs obtained of a longitudinal cross section showed that these graded structures displayed sufficient connection between each layer minus any evidence of gross porosity, cracks, or lack of fusion effects [13]. Unmelted and partially melted Ti-6Al-4V powder were found in the first layer of the transition and at interfaces between individual layers although less unmelted Ti-6Al-4V powder were seen at individual layers versus the first layer of transition region. The presence of unmelted powder gradually decreased from these areas of concentration towards the top surface of the coating with an accompanying increase in Co-Cr-Mo content. More importantly, the transition region of

these structures was devoid of intermetallics, which are typically detrimental to the structural integrity of graded materials. The composition of the gradient region was determined through energy-dispersive spectroscopy (EDS) in SEM showing a Co concentration gradient in the transition region of the gradient structures [13]. This rise in Co-Cr-Mo concentration coincides with a hardness increase occurring from 25%-86% in the coating. In a work focused on deposit of Co onto Ti-6Al-4V substrate, Majumdar et al transitioned from pure Ti to Co over 10 layers [15]. While this work did offer some illumination on the process of premixing and pre-placing powder on the metal substrate, there was no definitive quantification of the layer resolution that offers the configuration for optimal structure-property-performance. Co-Cr-Mo alloys have also been deposited upon Co-Cr-Mo alloy substrates using LENS. While the particle size variation was large (40-150 μm), studies have shown that the deposition of Co-Cr-Mo alloy onto Co-Cr-Mo substrate was possible. As the deposit and the substrate were of the same material, the interface between first layer and substrate showed no porosity nor cracks and lack of fusion defects [167]. In these studies, process parameter effect prevalence was measured through three major factors: laser power, feed rate, and scan speed. It was determined that the powder feed rate displayed the strongest influence (75.35%) on deposit thickness versus scan velocity (15.94%) and laser power (8.71%) [167]. Carbide precipitates were present in each deposit at grain boundaries or at interdendritic regions. Still, it appears that lower energy input may have been the cause of the noticed improvement in tribological properties. Residual stresses in deposited coatings have been an issue to delamination of layers upon overlay. XRD analysis has shown that LENS deposited

coatings mostly retained feed stock powder phases except in the case of deposits where the peaks were broader than the feed stock powder peaks. This phenomenon was attributed to residual stresses within the material.

For LENS based Co-Cr-Mo, Ram reports that epitaxial growth features that a prominent in weld metal solidification exist at the substrate/deposit junction. The heat affected zone (HAZ) shows no presence of carbide particles which would imply that the temperatures in the HAZ reach up to 1200 C, the typical solution treatment temperature. This HAZ region is diminutive (25-30 um) because of the very low and extremely localized heat generation associated with the LENS process. Individual layers feature a blend of slightly coarser columnar dendrites and very fine equiaxed dendrites [166]. Differences in the deposit microstructure occur due to the local variation in solidification conditions. Microstructural variation can also arise from thermal cycling from LENS associated with stacking of previously deposited material onto newly deposited material. LENS solidification structures are reported to be very fine due to the extremely high cooling rates. Carbide particles are reported to be present as a thin continuous in the columnar dendritic and equiaxed dendritic regions found in the deposit microstructure. However, carbide particles concentrate primarily in between dendritic regions throughout the deposition microstructure demonstrating that their formation occurs during the later stages of solidification. This accumulation initiates due to the expulsion of C at the S/L interface which then gathers in the interdendritic liquid. Ram reports that the carbide average volume fraction in the LENS microstructure is similar to the wrought substrate at about 6.5 vol.%. As for the size, shape, and distribution of carbides

in the LENS microstructure versus that of the wrought, the microstructures differed greatly. Ram characterizes the carbide particles in the LENS microstructure as very thin (< 1 um thick) and long versus the primarily globular, uniformly distributed carbide particles of the wrought microstructure [166]. SEM micrographs of interdendritic carbides is shown in Figure 28. For LENS the carbide phases occur as a continuous network at various locations.

As an extension of the initial Co-Cr-Mo coating work of Krishna et al, Espana and Bandyopadhyay et al focused on applying LENS to develop porous and functionally graded structures for load bearing implants. Osteolysis that causes wear was mitigated by consolidating structures with compositionally graded Co-Cr-Mo coating on porous Ti-6Al-4V through LENS once again. LENS offered the additional benefit of keeping the chemistry of biocompatible alloys the same thereby preserving in vitro and in vivo biocompatibility [14]. Their focused effort to improving cell-material interactions through open porosity structure and increasing wear resistance through a hard coating on the other end led to significant improvements to the implant in vivo in operation duration.

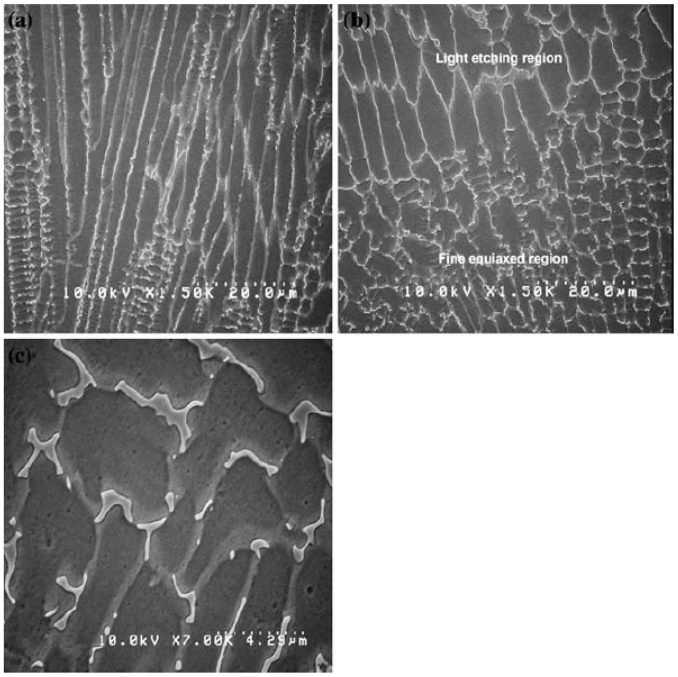

Figure 28: SEM analyzed microstructures of LENS Co-Cr-Mo indicating interdendritic carbide particles (a) columnar (b) fine equiaxed and (c) equiaxed at higher magnification. Reprinted from [166].

After the work by Espana, another work by Bandyopadhyay reported the mechanical properties observed in the different composition distributions using optimized LENS process parameters [168]. Here, the 86% Co-Cr-Mo top surface layer was reproduced to create crack free coatings. More importantly when compared to Ti-6Al-4V alloy surface hardness, the gradient coatings with 86% Co-Cr-Mo exhibited an increase in >80% in surface hardness along with more than twice the living cell density in comparison to the 100% Co-Cr-Mo alloy layer [168]. In a study by Wilson et al., coatings of Co-Cr-Mo were laser deposited onto not only Ti-6Al-4V but also SS316L substrates for biomedical applications [15]. Similar to the previously mentioned work, compositionally graded biocompatible coatings were built with transition of 0-100% Co-

Cr-Mo from the metal substrate to the top layer. This study highlighted the importance of controlling cooling rate to reduce the thermal expansion disparity between the two materials. With the inclusion of Co-Cr-Mo deposits onto SS316L substrates, a comparison between the two types of structure could be made. Both structures showed sufficient bonding strength as per the ASTM standard requirement [15].

Another area of development receiving a significant amount of attention considers the combined effect of wear and corrosion known as tribocorrosion. As Co-Cr-Mo based implants are subjected to the internal environment of the human body, continuous wear and corrosion occurs through bodily fluid in vivo thereby resulting in tribological film, wear debris, and metallic ions [4]. When wear and corrosion act synergistically, materials irreversibly transform in corrosive environment or aqueous fluid through tribocorrosion. Moreover, the mechanical loading situations such as sliding, slip, vibration, and weight bearing cause further analytical issues.

From the studies shown here, it can be concluded that performing studies specifically on tailoring the composition and therefore properties of LENS Co-Cr-Mo can provide a breadth of knowledge not previously offered by other comprehensive studies. As a biologically compatible alloy, the application of Co-Cr-Mo in implant technologies proves the necessity for further study under the scope of additive manufacturing. The work performed in this study should illuminate questions as to whether LENS Co-Cr-Mo is suitable for various components that need to be manufactured in designs only achievable through AM and require superior surface wear properties and corrosion resistance.

2.4.5 Interplay of Co-Cr-Mo microstructure and properties

Once a Co-Cr-Mo alloy has been created, its unique combination of properties such as high strength, toughness, wear resistance, and low thermal conductivity reduces the machinability of this alloy. Lower machinability leads to accelerated tool wear and reduced tool lifespan. Co-Cr-Mo alloys are defined primarily through the starting composition (i.e. low or high C content), manufacturing conditions (i.e. casting, forging, AM), and the subsequent thermal treatments (i.e. solution heat treatment, HIP, or sintering) that are themselves dependent on both time and temperature [169].

Extensive literature has been produced that shows these three factors have the ability to considerably modify the microstructure of the alloy and thus the mechanical, tribological, and chemical properties [169]. In a study on metal-on-metal (MOM) bearings, Cawley studied sample coupons of ASTM F75 Co-Cr-Mo alloy that underwent different combinations of thermal treatments (solution heat treatment, hot isostatic pressing (HIP), or sintering). Between each thermally treated sample, there was a large variability of carbide level and morphology. The as-cast alloys were shown to have greater abrasive wear resistance in comparison to single or multiple heat-treated materials. Cawley found in this work that the microstructure, specifically the volume fraction and size and distribution of carbides, prove to be critical to the growth of a wear resistant system [169]. SEM micrographs of the Co-Cr-Mo blocky carbides are shown in Figure 29.

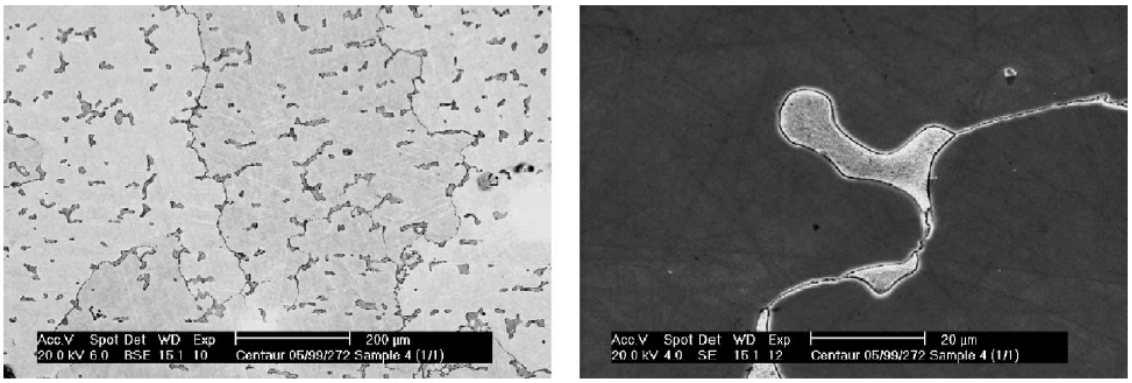

Figure 29: SEM micrographs of as-cast Co-Cr-Mo blocky carbides rich in Cr and Mo. Reprinted from [169].

Solution treatments have been shown to eliminate the presence of certain carbides in Co-Cr-Mo alloys. Taylor and Waterhouse solution treated Co-Cr-Mo at 1250 °C for 2 hours and only found $M_{23}C_6$ block carbides through XRD and TEM [170]. Furthermore, Caudillo et al did not find any carbide structures other than the $M_{23}C_6$ type [171]. While these two studies differ in the shape of the crystal features, chemical compositions of the carbides are also in dispute. Clemow and Daniell noted fractions of Mo and Cr of 6% and 35%, respectively, while Devine and Wulff noted them to be 20% and 35%, respectively [155] [110]. Kilner reported a similar Mo content to the latter study, but a much higher Cr content at 59% [111].

2.4.5.1 Wear Resistance of Co-Cr-Mo

Of all the applications of Co-base materials, their use as coatings is the most referenced in literature. Wear-resistant hardfacing alloys can be deposited by traditional means of welding or thermal spraying such as plasma arc spraying or high-velocity

oxyfuel powder spray. CoCr alloys, such as Stellites that contain fluctuating amounts of W, Mo, and/or Ni and Tribaloy alloys both were used as hardfacing materials in their initial inception. Types of coating that have received a great deal of attention for Co-based alloys are Co-Mo base conversion coatings that can act as replacements for chromate conversion coatings due to their health and safety risks and increasing regulatory scrutiny [87]. The Co-Mo process, where Co and molybdates are used versus chromates, offers the final product corrosion protection and paint adhesion required for the aerospace industry. To assess the structural integrity of coatings, an initial discussion of tribology can help illuminate the facets of the process that must be improved upon.

When considering the interaction of two surfaces meeting one another, it is pragmatic to define this contact within the framework of a tribology. Tribology refers to the science and engineering of contacting surfaces in relative motion. Two surfaces that slide against one another create a load that is carried by asperities of nanometer to micrometer size [5]. Upon contact, the force of friction becomes apparent with influences from the wear medium surface roughness, and other extrinsic factors. A study provided by Hutchings utilizes a simplified model known as the Archard Equation that considers only plastic deformation and surmises that wear rate inversely correlates with hardness [172]. However, real tribological systems show that friction is much more complex due to factors such as surface fracture, fatigue, grain rotation, and corrosion per tribo-chemical reactions leading to material loss. These factors correlate with the structure and chemical composition of the constituent phases and grain/phase boundaries, and their mechanical properties [5, 118]. Wimmer et al observed the

removal of carbides under high local contact stresses which cause surface fatigue through indentations and consequent abrasion [173]. These local contact stresses are further dependent on the elastic modulus and hardness of the material.

There are three main types of wear that are mentioned throughout literature: abrasive, sliding, and erosive. Abrasive wear mechanisms are encountered upon introducing hard particles, or hard projections (on a reverse plane), that are pressed against and subsequently moved in relation to the surface. Of this type, there are two modes of abrasion relative to the condition. A crushed abrasive medium indicates that a high stress condition has prevailed. This occurs when hard particles are ensnared between metallic surface when in motion. An intact abrasive medium indicates a low-stress abrasion meaning that the moving surfaces came into contact with packed abrasives like in the example of soil and sand [87]. For alloys such as Co-base wear resistant alloys, a hard phase allows general resistance to abrasion. Resistance scales with the volume fraction of the hard phase as well as the size and shape of the hard phase precipitates contained in the microstructure, and the size and shape of abrasive species [87].

Sliding wear presents the most complex response between materials of the three sliding conditions. When two surfaces are pressed together and move relative to one another, sliding can occur. Metallic surfaces are particularly vulnerable to damage type especially when little or no lubrication exists. The mechanisms by which this occurs can be through one or up to three different mechanisms. Under an environment of high surface temperatures, oxides can influence the sliding wear process when coupled with

low wear rates either through high ambient temperatures or frictional heating. Oxide growth rates are known to increase dramatically with increase in temperature. A mechanism known as fretting results from the combination between oxide growth rates and sliding-abrasive wear process. Fretting results from high contact stresses and a breakdown of the oxide films thereby leading to actual metal-on-metal contact. These conditions may lead to a cold welding of the surfaces which would require small pieces to fracture away from the original interface in a process known as galling. A considerable transfer of metal between the surfaces and a macroscopic deformation of each surface is a usual effect of this condition. The final mechanism, erosion, deals with fatigue below the surface when two materials periodically press together thus introducing cyclic stress conditions. Material losses are prevalent when fatigue cracks nucleate and grow at a specific depth.

By itself, Co possesses a beneficial crystallography that contributes to good wear resistance. When solid solution strengtheners are added, there is a marked improvement in wear as well as other mechanical and chemical properties. Co-base coatings are typically used to improve wear resistance on hardfacing alloys through welding or thermal spraying deposition. Stellite alloys are the most commonly used for this application. Conversion coatings are another type of metal coating where the surface of the part undergoes a chemical or electrochemical conversion into a protective barrier. Co/Mo base coatings are under development as conversion coatings to replace chromate conversion coatings, due to their well-documented health and safety risks leading to increases in regular scrutiny. The process by which Co/Mo is made uses Co and

molybdates (a compound containing an oxoanion with Mo in its highest oxidation state of 6) versus chromates (a compound containing an oxoanion with Cr in the oxidation state of 6) and imparts corrosion protection and paint adhesion, a requirement of the aerospace industry specifically on Al alloys. The excellent wear resistance exhibited by Co-Cr-Mo alloys allows for their use in biomedical and manufacturing applications. The advantage of Co-Cr-Mo alloys is underlined in a study of wear properties of biomedical Co-Cr-Mo alloys focused on displaying biomedical inertness and wear resistance. Co-Cr-Mo alloys exhibit unique self-polishing abilities during articulation thereby reducing the occurrence of accelerated wear [167]. Traditional cast and wrought Co-Cr-Mo alloys possess $M_{23}C_6$ and M_6C (where M=Cr, Mo, Co) carbides at grain boundaries and interdendritic regions that contribute to the high strength and wear resistance of these alloys [167]. It has also been reported that the wear resistance of Co-Cr-Mo is predominantly controlled by the morphology and extent of hard carbide particles within the microstructure [166]. When subject to wear conditions, Co-Cr-Mo alloys exhibit a mechanical response that is dominated by strain-induced martensitic transformation (SIMT), which causes cracks to form during plastic deformation. Despite the cracking, wear resistance of the alloy after SIMT demonstrates a drastic improvement. To impart specific material properties, heat treatments are performed post fabrication to modify the electrochemical and tribological properties of high C Co-Cr-Mo alloys specifically those that possess fine grains with large grain boundary area [167].

2.5 Knowledge Gaps

Based on the literature review conducted, a number of research gaps have been identified when conducting the DED of compositionally-altered Co-Cr-Mo alloys:

1. Suitable manufacturing process parameters for the DED of Co-Cr-Mo alloys are not known.
    a. And especially the effects of ΔMo on the required process parameters.
2. The influence of DED process parameters on the Co-Cr-Mo microstructure needs to be understood.
    a. Influence of adding ΔMo to the DED Co-Cr-Mo microstructure is not known.
3. Lack of knowledge on influence of process parameters and microstructures on resulting properties (for DED Co-Cr-Mo, ΔMo)
4. Compositional and property resolutions achievable are not known.
5. Lack of studies on the local and global performance of compositionally graded Co-Cr-ΔMo.

As the size scale of technology has reached the nano-level, there has been great interest in pairing nanotechnology with engineering disciplines such as nanorobotics for the diagnosis of illness and site-specific drug-delivery. To accomplish this, nanoscale tribocorrosion proves vital to the understanding of nano-phenomena and the development of electrochemical nanobots which take influence from bacteria models [4]. With its excellent wear characteristics alongside additive manufacturing technology, Co-

Cr-Mo could perhaps find application as a tribocorrosion resistant outer shell for such nanodevices to stave off degeneration from occurring as quickly.

The advent of additive manufacturing matched with the speed at which electronics are consistently improving create an exciting realm of possibilities for technological advance. Further study on melding various disciplines could lead to the development of entirely new research areas and technology with a large impact on a consistently shrinking world.

In this work, the manufacturability of bulk Co-Cr-Mo structures are explored through LENS, and the influence of specific process parameters on the material properties of the structures are analyzed. The reported work is part of a larger effort to fabricate compositionally graded Co-Cr-ΔMo alloys with tailored mechanical performance for biomedical implants and other tooling applications.

CHAPTER III

RESEARCH METHODOLOGY

This work focuses on the processing-structure-property-performance framework pertaining to the DED of compositionally-graded Co-Cr-Mo, as shown in Figure 30. Through this work, relationships between the process parameters and macro- and microstructures can be determined. Physical and chemical properties measured will be compared with performance of the material. Understanding these interwoven phenomena will contribute to the knowledgebase via the following research questions.

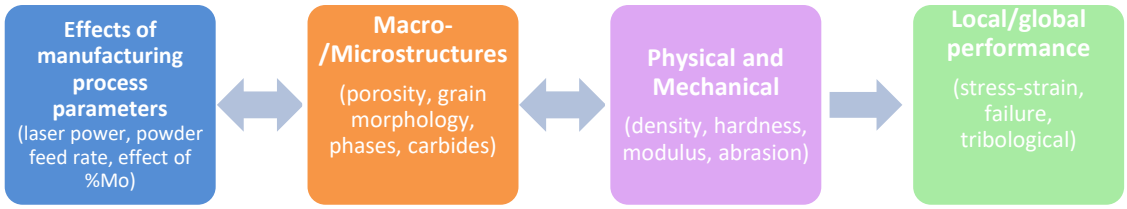

Figure 30: Processing-Structure-Property-Performance framework for this research.

RQ 1: What is the effect of the increase in ΔMo on the process parameters required?

This inquiry seeks to investigate the differences in the process parameter set needed for successful Co-Cr-Mo builds that have a different percent fraction of Mo.

Task 1-A: Make design of experiments and print single composition and compositionally graded samples.

Task 1-B: Characterize the samples produced macro- and microscopically.

Outputs: Correlation between the process parameters and quality metrics

RQ 2: How does an increase in ΔMo do to the macro- and microstructure?

This inquiry seeks to analyze the effects of additional Mo on the microstructure of the alloy.

Task 2-A: Quantify/correlate microstructure via SEM/EDS, XRD, and microprobe.

Task 2-B: Confirm distribution of components via EDS across horizontal and vertical planes.

Outputs: Connection between increasing Mo content and the microstructure

RQ 3: What are the effects on mechanical properties due to varying Mo content?

Measuring mechanical properties provides information regarding whether the addition of Mo is beneficial to the structural integrity of different Co-Cr-ΔMo.

Task 3-A: Measure mechanical properties changes of Co-Cr-Mo with increasing Mo content via nanoindentation, nanoscratch, and microindentation.

Task 3-B: Correlate microstructure with properties and compositions.

Task 3-C: Measure mechanical properties of compositionally graded Co-Cr-Mo

Outputs: Property distributions from utilizing different %Mo in Co-Cr-Mo via LENS and the manufacturing range of structurally acceptable Co-Cr-ΔMo and influence of increasing Mo on the properties of Co-Cr-Mo.

A snapshot view of the major tasks involved are grouped as follows:

Processing	Structure	Property	Performance
- Print compositionally graded samples with different layer resolutions per %Mo increase - Determine recipes that utilize process parameters that yield corresponding performance	- SEM: Obtain micrographs of compositionally graded Co-Cr-Mo samples (Figure 3) - EDS: Obtain spectra to ascertain composition of large area and individual parts of microstructure - XRD: Determine the microstructural elemental constituents and different phases that have formed	- Nanoindentation: Determine nano-properties of individual microstructural features including nanohardness and elastic modulus - Nanoscratch: Assess nano-abrasion and nanoscale resistance to scratch	- Microhardness testing: Determine the aggregate properties of microstructural phases to get a sense of global mechanical performance - Bending Tests: Determine where fracture occurs and pinpoint root cause of the problem (microstructure or manufacturing wise)

CHAPTER IV

MATERIALS AND METHODS

4.1 Materials

Laser Engineered Net Shaping (LENS) was utilized to develop the samples. LENS was performed using the Optomec MRS LENS 3D printer. Co-Cr-Mo alloy powder was obtained from Powder Alloy Corp (Ohio). Co-Cr-Mo powder was purchased within the specification of +45µm/-150µm as per the design specifications of Optomec. An SEM micrograph of the Co-Cr-Mo powder is provided in Figure 31. Co-Cr-Mo and Mo powders were purchased for the following experiments. Purchased Mo powder falls between +15µm/-45µm. Table 1 shows the particle size analysis and Table 2 shows the elemental report for Co-Cr-Mo provided by Powder Alloy Corp.

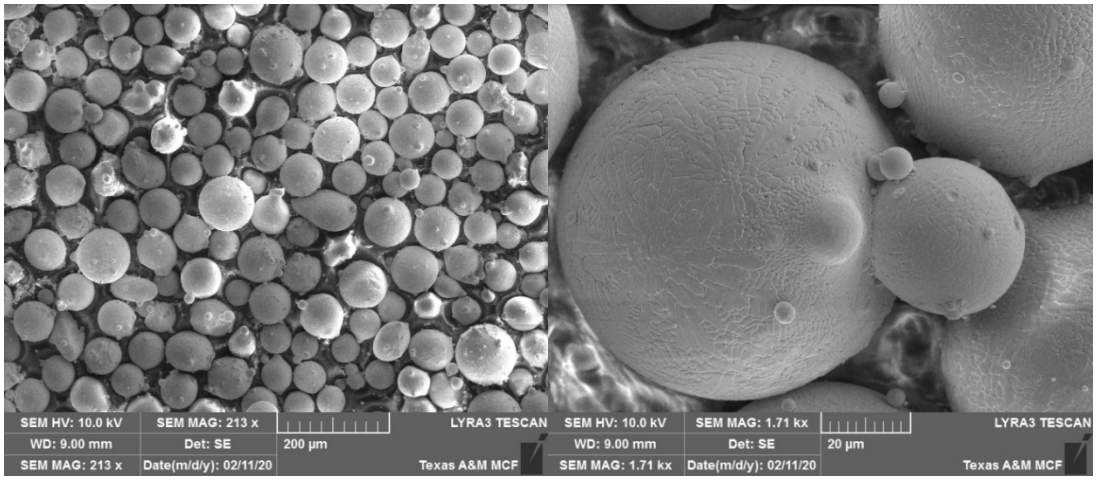

Figure 31: Co-Cr-Mo powder as received from Powder Alloy Corp.

Table 1: Particle Size Analysis (Percent). Microtrac conforms to ASTM B-822 and Sieve Analysis conforms to ASTM B-214.

Sieve	**+140**	**-325**
Results		
Max% of powder	95% of powder under 105 microns	95% of powder over 44 microns

Table 2: Elemental Report for ASTM F-75 Co-Cr-Mo

Element	Cr	Mo	Ni	Fe	C	Si	Mn	Co	N
Results	28.2	5.5	0.06	0.13	0.05	0.35	0.46	Balance	0.12

4.2 Experimental Methodology

4.2.1 Equipment and Procedures Used

Compositional gradients were created using the Optomec MRS LENS 3D printer by augmenting the composition percentage of powders. By premixing the powders, facile mixing was promoted which made the development of compositional gradients a much simpler proposition than before.

To initially test the properties of bulk printed Co-Cr-Mo through the Optomec MRS LENS (Figure 32), 5 mm^3 samples were printed, analyzed with electron microscopy, and underwent mechanical testing. Co-Cr-Mo and Mo powders were obtained from Powder Alloy Corp (Ohio) with 45-150 μm and 45-75 μm, respectively.

Samples were printed via strategies formulated based on LENS based studies by Krishna, Espana, Das, Wilson, Mantrala, and Ram, which printed a Co-Cr-Mo coating layer upon different alloy substrates [13-15, 97, 166, 167, 174]. As these studies all are based on depositing a limited number of layers upon a substrate, the strategies gathered

from each study were then adapted to a bulk structure after comparison to different types of SLM based studies [7, 9, 11, 175, 176]. The combination between the insights gained from LENS and SLM along with an initial round of printing provided bounds for which the initial batch of prints were made. Starting from the work of Krishna et al, a 400W power was chosen to begin initial prints. The next pertinent variable process parameter to study was revolutions per minute (RPM). An Optomec correspondent provided a range of typical rpm values of 3, 5, and 7 rpm.

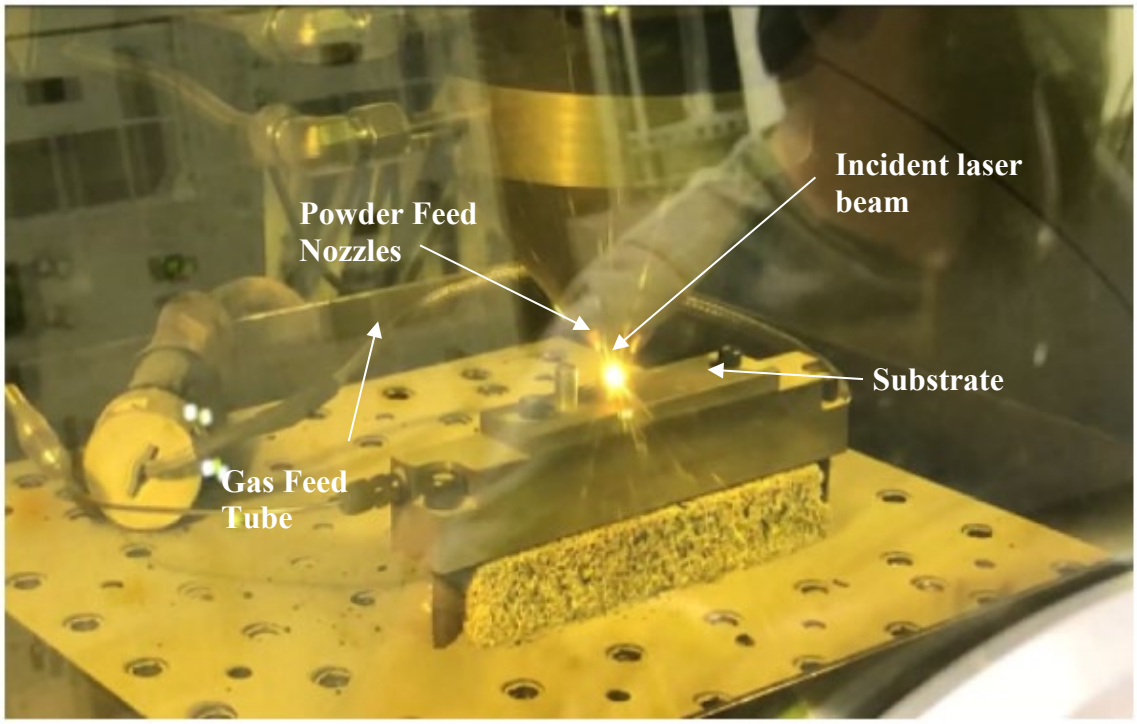

Figure 32: MRS-LENS machine used in the study.

This initial batch of prints yielded discoloration in the in all three printed parts at the power level leading to the belief that the power level was too high for proper

printing. The power was lowered for the next round of three prints to 300W to determine a lower bound for the discovery of an optimal printing power. Prints that were made at this power did not build large enough structures and possessed prints that bowed inward. From this, it could be determined that an intermediate power between the bounds would iteratively improve the quality of prints. Thus, a power of 350W provided taller builds and more structurally sound builds than those at 300W. Table 3 presents the process parameters for the design of experiments in the first study.

Table 3: Process parameters of Design of Experiments 1

300W	3 rpm	5 rpm	7 rpm
350W	3 rpm	5 rpm	7 rpm
400W	3 rpm	5 rpm	7 rpm

4.2.2 Optical and Scanning Electron Microscopy

Samples were removed from the substrate plate through electric discharge machining (EDM). Next, samples were brought to an optical microscope small scale images at 100x and 300x magnification were taken for regions denoted top, medium, and bottom. These regions were equally spaced segments that helped quantify the effects of thermal gradients and build direction throughout the initial first run of samples. Figure 33 provides the optical microscope used for both designs of experiments.

Figure 33: Zeiss Axio Observer 7 optical microscope.

After these initial images were taken, samples were sectioned along the longitudinal build direction using a diamond saw. Half of each sample was then embedded in Bakelite. Embedded samples underwent typical metallography. Samples were prepared in a two-step procedure. First, SiC grinding papers of 600 and 1200 grit were used to reveal the sample from the Bakelite surface. Next, each sample was polished using diamond polish with three different micron slurries in the following order: 9 μm, 6 μm, 1 μm. After achieving a mirror finish, samples were then prepared for analysis.

Initially, SEM images were taken of the outside surface of the non-embedded Co-Cr-Mo LENS samples. This offered a sense of the amount of unmelted powder, shape of melted layers, and the texture on the outside surface after manufacture. Figure 34 presents the SEM used in the study.

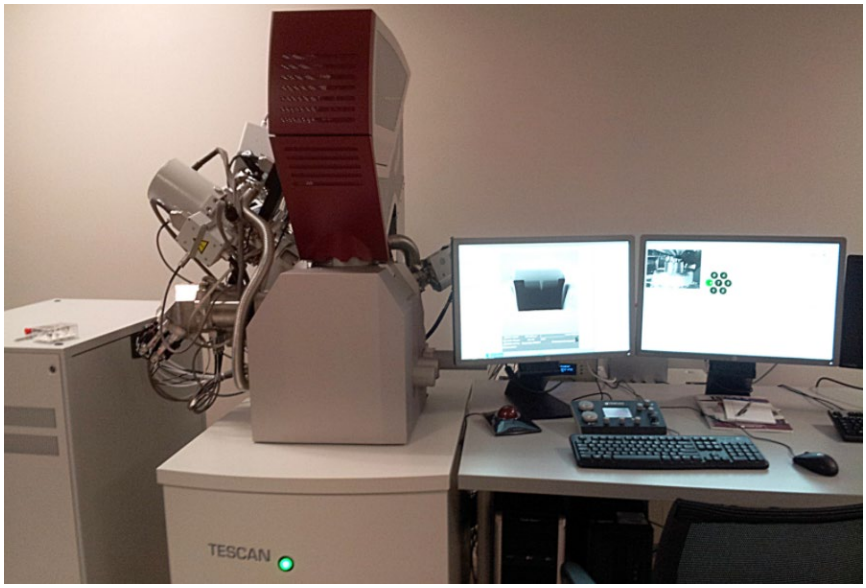

Figure 34: Tescan LYRA-3 Model GMH Focused Ion Beam Microscope.

After EDS analysis, samples were analyzed using an electron microprobe as shown in Figure 35 to create elemental maps corresponding to composition within the microstructure. This provided color coordinated imagery that corresponded to the amounts of Co, Cr, Mo, and Si within the microstructure.

Figure 35: Electron Microprobe.

4.2.3 Mechanical Property Testing

Once these initial images were obtained, the embedded samples underwent microindentation using a Vickers Hardness tester. Vickers tests were performed with a 10 s indentation and 0.5 setting. Microindents were taken three at a time in the top, middle, and bottom regions of the sample to ensure quality of measurements and repeatability of results. Regions were differentiated by visually determined segmentation into thirds to help isolate regions that may show the influence of thermal gradients. Literature has pointed to longitudinal grains existing at the bottom of builds due to heat dissipating into the substrate from the sample during fabrication. As the build continues, deposited layers take longer to cool due to the additional molten layers that are stacked

upon each other. This thermal concentration leads to the equiaxed grains that have been referenced in various pieces of literature. For these samples, Vickers hardness values were recorded. Figure 36 presents an image of the Buehler Wilson VH1102 microhardness tester used in the study and the indent design for both experiments.

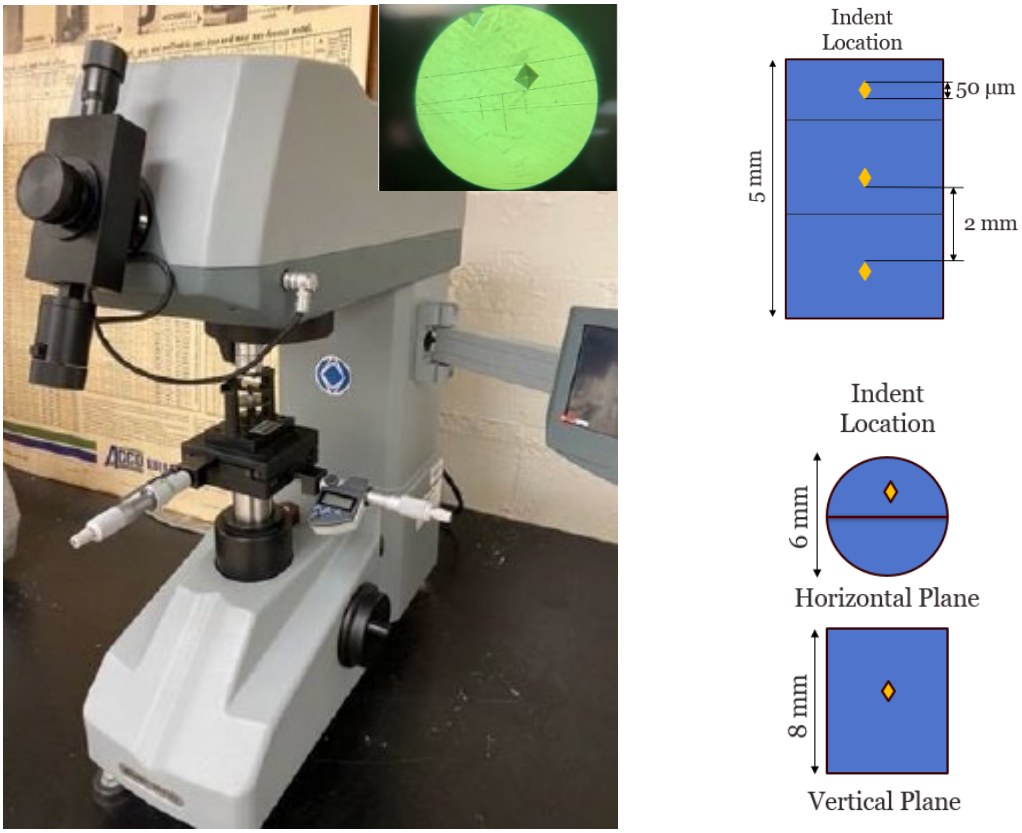

Figure 36: Image of Buehler Wilson VH1102 microhardness indenter with an indent (inset) and location of indents for DOE 1 (top-right) and DOE 2 (bottom-right).

After completing these microindents, nanoindentation was performed on samples in a similar manner as the previously performed indents. Samples were indented using a Berkovich standard probe with 250 μN and the Oliver Pharr method. Indentation was calibrated using a quartz disc. Indents were made in a 5 second quick approach, 2 second indent, and 5 second release pattern. Rather than three indents, a square pattern of four indents per region were taken a considerable distance away from any microindents on the surface of the sample. Indentation depth was measured alongside hardness and reduced modulus to determine the mechanical properties of the sample. Figure 37 presents the Hystiron triboindenter.

Figure 37: Hysitron TI-950 Triboindenter nanomechanical test apparatus.

Next, the samples were exhibited to scratch tests using a conispherical tip. Samples were scratched with 250 μN force for 250 μm. The force of scratches gradually

increased with scratch length. Instead of delivering scratches to the three regions individually, the test was set up to determine differences in scratch behavior between regions. Thus, two scratches were made on each sample with each displacement being placed across the border of different regions (i.e. a scratch occurring across the top-middle boundary). Figure 38 presents a macroscopic image of the scratch on the surface of a sample with an illustration of a scratch location.

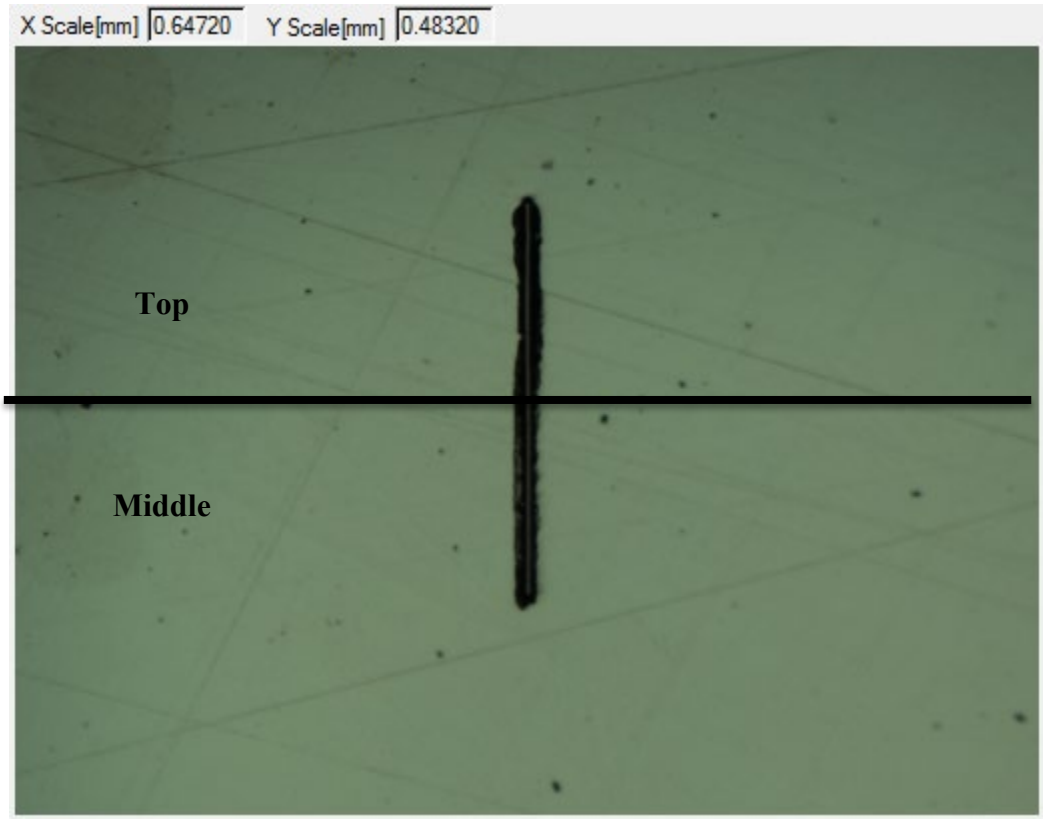

Figure 38: Nanoscratch on the surface of the sample with an indicator of distinct locations.

To understand the influence of placing additional elements into a Co-Cr-Mo structure, similar additive studies were analyzed to gather adequate strategy.

Sahasrabudhe utilized LENS to compositionally grade CaP into Co-Cr-Mo for improvement in hardness and other mechanical properties [177]. In the second design of experiments, Mo was added in increments of +3% up to +21% Mo. For this set of samples, the 350W power was utilized based on the success of the 350W prints from the first design of experiments. Due to the higher melting point of Mo, a second set of samples for the +15% Mo to +21% Mo increments was printed at a power of 450W.

Samples were initially macroscopically observed by measuring each samples individual diameter and height to determine how closely each built to the specified build dimensions. The procedure is shown in Figure 39. Each sample was once again measured using optical microscopy at different scales on the outside and inside of the sample to determine outer structure and the microstructure, respectively. Afterwards, each of sample's layer height and cell size was compared against the addition of Mo. Each of samples then underwent observation under SEM while elemental content was measured using EDS similar to the previous design of experiments. The samples then were further studied using XRD to determine the growth of phases as Mo is added. Once this was complete, selected samples from the first and second design of experiments were measured using a microprobe to develop maps for the +0%, +6% and +18% samples to determine the elemental distribution as Mo content is increased. Mechanical properties of the second design of experiments were then measured using microindentation, nanoindentation, and nanoscratch tests.

Figure 39: Macroscopic measurements of Co-Cr-ΔMo Samples

4.2.4 Development of compositional gradient printing procedure

The next evolution of our study pertains to creating compositional gradients within Co-Cr-Mo. As a standalone structure built by LENS, Co-Cr-Mo possesses excellent material properties on par with traditional manufacturing methods. With the affordances that LENS offers, an exploratory study into augmenting the alloy composition was conducted. As mentioned previously, these types of functionally graded materials have taken inspiration from biological constructs [40]. The work performed here takes similar inspiration by compositionally grading the percentage of Mo to varying degrees of thin and bulk constructs to study the final microstructure and associated material properties. As Mo possesses a higher melting temperature and laser reflectivity as a standalone element, it was conjectured that a proper ratio between the two powders mixed before printing would offer an optimal structure with the highest structural integrity.

To develop samples that were structurally stable, the LENS machine requires calibration to deposit the required material. The first step is to measure the powder flow

of powders from the nozzle head at different RPMs (i.e. 2-6 RPMs with a step size of 0.5) along with a constant carry gas flow rate to develop a “calibration curve” of the mass flow in the LENS system for that particular powder, within the used hopper, and specific position. Through this procedure, the particle size distribution can be normalized by accounting for powder density which yields two tight clusters or curves known as the “volumetric flow curves”. These clusters of curves share nearly identical slopes with the only difference being the hopper where the powder flows from (large or small). The following assumptions were made: volumetric flow curves are inherent to the machine, mass flow of a system can be predicted by finding the slope of the appropriate volumetric flow cluster, the cluster can be translated to mass flow through density. The mass flow calculations are then determined through the resulting curves.

After the necessary parameters are determined, the mass flows are then converted to RPMs for the specific hopper through the mass calibration curve. The RPM values are input to the machine. The LENS process then begins until builds are complete, or an emergency stop has occurred by the machine operator for safety reasons. Mass flow rate can be changed by controlling the hopper containing the specific material.

From the previous two design of experiments, the power, base speed, and carry gas flow rate were already determined. Since Co-Cr-Mo and Mo have powder densities that are higher than average and feed rate of Mo is relatively low due to its density, the large hoppers were used to make sure that enough powder was available to complete the build in one run. From here, the slope and intercept of the volumetric flow calibration curve was calculated through the linear regression tool in Igor Pro. The slopes for both

of the known powders (Co-Cr-Mo and Mo) using the large hoppers were determined. There were no significant differences between the two values as they were identical to the 5th decimal place. Although both curves have near identical slopes, intercepts did slightly vary. The lighter material intercepted at 0.001 while the heavier crossed at 0.024. The 0.024 intercept was chosen in order to be conservative. Since Mo was 25% more dense than Co-Cr-Mo, it was used to calculate RPMs from 0.5 to 10 for determining the most reasonable values for mass flow of varying compositions. With the given range of RPMs, the volumetric flow was calculated through the volumetric slope, intercept, and value of RPM (equation of line: y = mx + b) where y is the volume of powder for a certain RPM, b is the intercept of the linear regression, a is the slope of the linear regression and x is the specific RPM.

The process was repeated for each value in the RPM range. Mass flow slope and intercept were calculated through translating the respective volumetric flow value from the materials' respective densities. This process helped develop the necessary additional Mo for a particular composition into RPMs. Calculating the potential mass flow rates for the desired compositions required considering all possible Co-Cr-Mo RPM values. This helped determine the additional Mo. The required RPM is then determined by solving the reverse linear regression equation ($x = \frac{y-b}{m}$) with the mass slope and intercept for Mo. Target composition is attained through adding powder to the melt pool; thus, the selected parameters must be considered to make sure the right amount of each powder was used for the desired composition. To do this, a classification criterion was created:

- RPM < 0: Unusable – impossible; not feasible to achieve composition

- 0 < RPM < 0.1: Choose if no other valid option; stable mass flow may not be possible within this range
- RPM > 0.1: Preferred, use as a first selection; confidence held for stable mass flow at RPM > 0.1

The classification system provided an algorithm for final decisions for RPMs at the desired compositions by minimizing the amount of powder flow for Co-Cr-Mo while using the largest possible mass flow of Mo for compositional accuracy. Once this objective was complete, the compositional gradient prints were made to the compositional accuracy.

Based on these measurements, each compositional gradient sample was printed with additional Mo from +3% to +8% Mo. The difference between each of the samples was the number of layers per each additional %Mo. For the C1 sample, an increase in Mo occurred every two layers. The C2 sample was increased in %Mo per layer. The C3 sample was increased by 0.5% per layer. These samples were developed in this way to determine the resolution capability of the LENS machine. The sample design is shown in Figure 40.

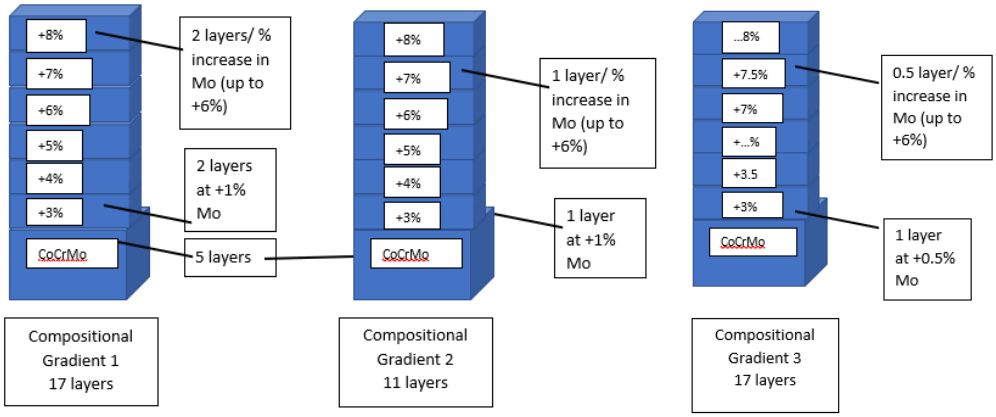

Figure 40: Sample Design for Compositionally Graded Co-Cr-Mo.

Once the samples were printed, each compositional gradient sample was analyzed using SEM and EDS similar to the previous design of experiments. EDS measurement helped determine whether the amount of Mo was up to the specific percentage utilized to print the sample. Last, the graded samples underwent nanoindentation to measure appreciable hardness and elastic modulus differences between percentage increase.

CHAPTER V

EXPERIMENTS AND RESULTS

Figure 41 presents a flow chart of the experimental methodology. This experimental methodology was followed to prepare and characterize each of the builds from all three studies.

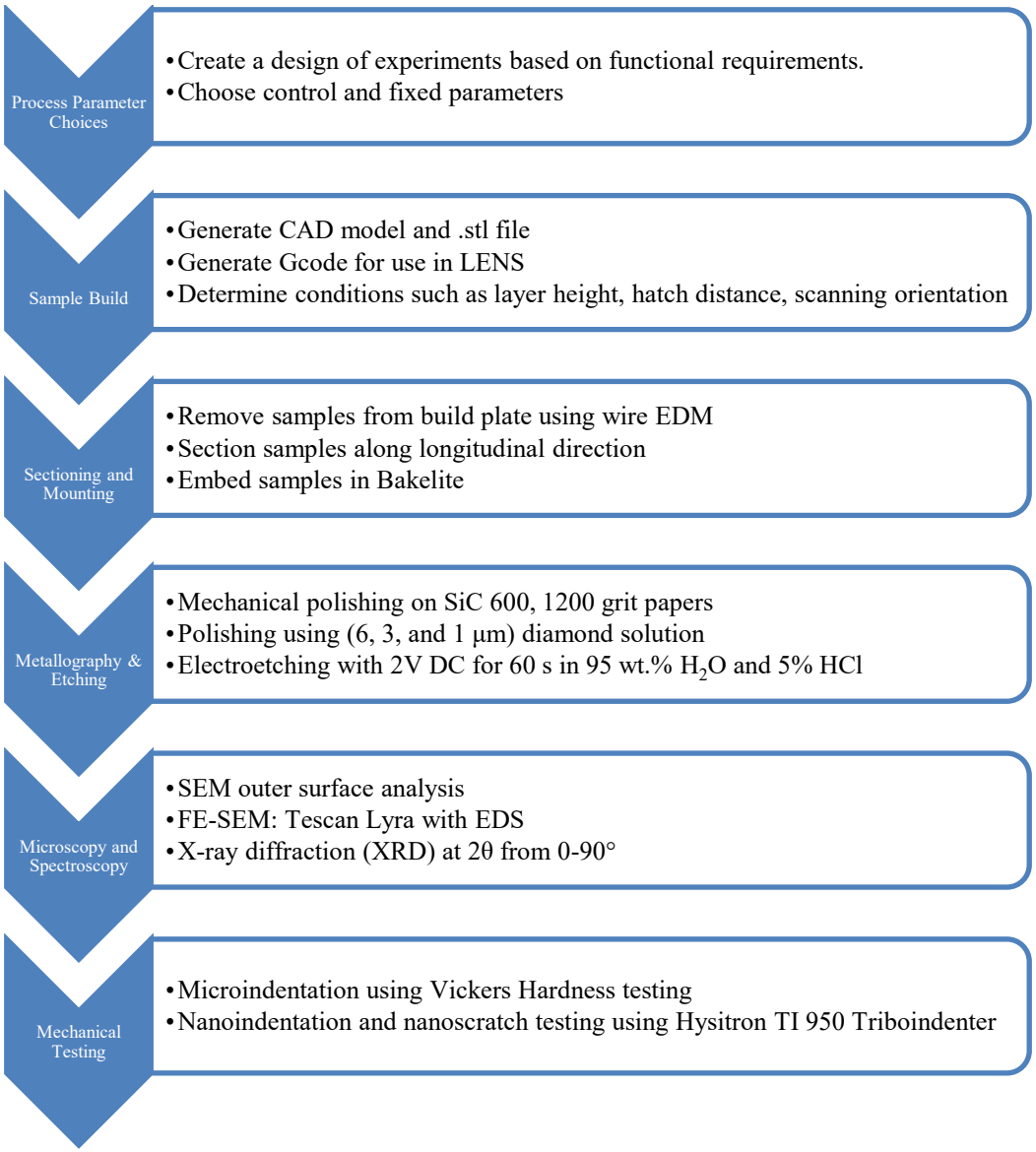

Figure 41: Flow Diagram of experimental procedure.

5.1 Effect of the increase in ΔMo on the required process parameters (RQ 1)

To create dense parts with Co-Cr-Mo alloys, volumetric energy density per unit time must completely melt the powder and avoid material vaporization [12]. Second, weldability of powder material must be good with low oxygen content. Last, the oxygen content in the manufacturing chamber must be low.

In the first design of experiments, ASTM F-75 Co-Cr-Mo builds were made using the Optomec MRS LENS 3D printer. Co-Cr-Mo alloy powder was obtained from Powder Alloy Corp (Ohio). Co-Cr-Mo powder was purchased within the specification of +45μm/-150μm as per the design specifications of Optomec.

Samples were printed using a schema based on LENS studies by Krishna, Espana, Das, Wilson, Mantrala, and Ram, which printed a Co-Cr-Mo coating layer upon different alloy substrates [13-15, 97, 166, 167, 174]. As these studies all are based on depositing a limited number of layers upon a substrate, the strategies gathered from each study were then adapted to a bulk structure after comparison to different types of SLM based studies [7, 9, 11, 175, 176]. The combination between the insights gained from LENS and SLM along with an initial round of printing provided bounds for which the initial batch of prints were made. Starting from the work of Krishna et al, a 400W power was chosen to begin initial prints. The next pertinent variable process parameter to study was revolutions per minute (rpm). An Optomec correspondent provided a range of typical rpm values of 3, 5, and 7 rpm. This initial batch of prints yielded discoloration in the in all three printed parts at the power level leading to the belief that the power level was too high for proper printing. The power was lowered for the next round of three

prints to 300W to determine a lower bound for the discovery of an optimal printing power. Prints that were made at this power did not build large enough structures and possessed prints that bowed inward. From this, it could be determined that an intermediate power between the bounds would iteratively improve the quality of prints. Thus, a power of 350W provided taller builds and more structurally sound builds than those at 300W.

Samples were removed from the substrate plate through electric discharge machining (EDM). Next, samples were brought to an optical microscope small scale images at 100x and 300x magnification were taken for regions denoted top, medium, and bottom. These regions were equally spaced segments that helped quantify the effects of thermal gradients and build direction throughout the initial first run of samples. Optical microscopy was performed on the Kohler T800. Figure 42 provides optical images of a Co-Cr-Mo LENS sample.

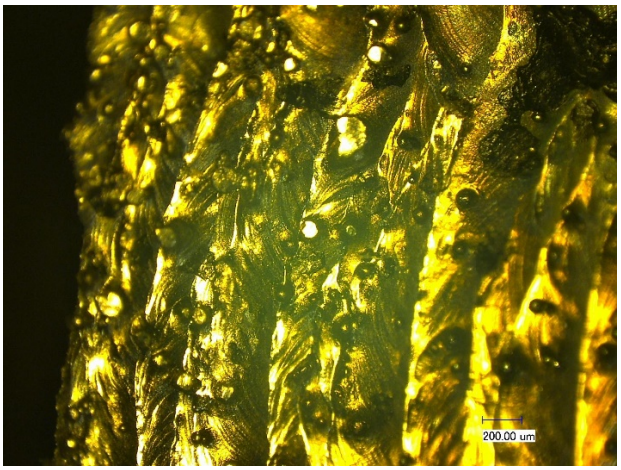

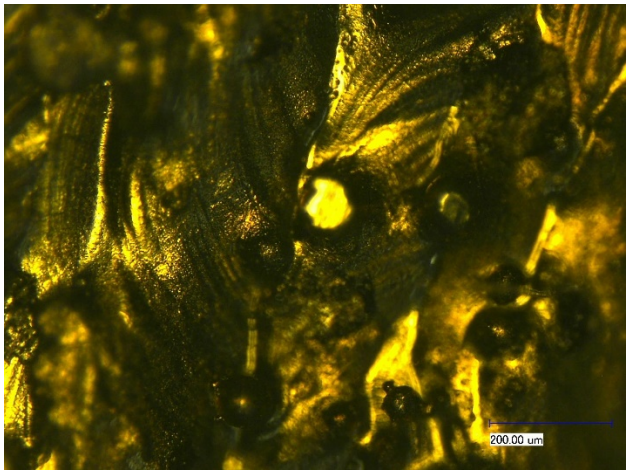

Figure 42: Optical images of Co-Cr-Mo in the bottom region at 100x (top) and 300x (bottom).

5.1.1 Task 1-A: Create design of experiments spanning VED-based design space and create samples.

Seven of the nine prints were successfully built to set dimensions showing the relevance of power and powder feed parameters on the success of bulk CCM LENS prints. Figure 11 shows the process parameters used in the design of experiments for Study 1. Deformation is evident in a few of the samples. Samples display a large amount of unmelted single powder and multi-particle assemblies on the surface when observed under optical and scanning electron microscopy. This may have been due to the scanning speed and powder feed rates creating conditions that promoted partial melting of the powder. Unmelted powder can create surface textures that are detrimental to the mechanical properties of LENS samples and contribute to surface roughness.

The 3 RPM samples at 300 W and 350 W did not build to the 5 mm height set on the system. Both samples exhibit a center that droops below the four corners of the

sample. This implies the powder feed rate and power combination was insufficient to properly deposit layers as the build height increased. The drooping center is due to a large melt pool and material vaporization [12]. Further complications may have developed due to the scan speed. While this value was chosen as an average value between the range of speeds observed in literature, the machine setting showed immediate drawbacks. The speed of the powder nozzle moving in a 25 mm^2 process area causes rapid stop and go movements. This abrupt jarring motion causes the powder to move in various directions and splatter around the inner chamber of the LENS machine.

In the first design of experiments, ASTM F-75 Co-Cr-Mo builds were made using LENS shown in Figure 43. All prints were successfully built, but with differing final heights, showing the relevance of power and powder feed parameters on the success of bulk Co-Cr-Mo LENS prints. Table 4 presents the process parameters used in the design of experiments for Study 1.

Figure 43: Optomec 750 MRS LENS Machine.

Table 4: Process parameters for DOE 1.

Process Parameters	Value
Laser Power [P] (W)	300, 350, 400
Powder Feed Rate (RPM)	3, 5, 7
Scan Speed (m/s)	8.6
Layer Thickness (μm)	250
Scan orientation	90°

Macroscopic defects are evident in a few of the samples. The as-built samples and an SEM micrograph of the 300W 5 RPM sample is shown in Figure 44 for reference. Samples display a large amount of unmelted single- and multi-particle clusters on the surface when observed under optical and scanning electron microscopy. This may have been due to the scanning speed and powder feed rates creating conditions that

promoted partial melting of the powder. Unmelted powder can create surface roughness that is detrimental to sample surface quality.

The 3 RPM samples at 300W and 350W did not build to the 5 mm height set on the system. Both samples exhibit a center that droops below the four corners of the sample. This implies the powder feed rate, scan speed, and power combination was unsuitable to properly melt/deposit layers as the build height increased. The speed of the powder nozzle moving and changing directions in a 25 mm^2 process area causes rapid stop and go movements. This abrupt jarring motion causes the powder to move in various directions and splatter around the inner chamber of the LENS machine.

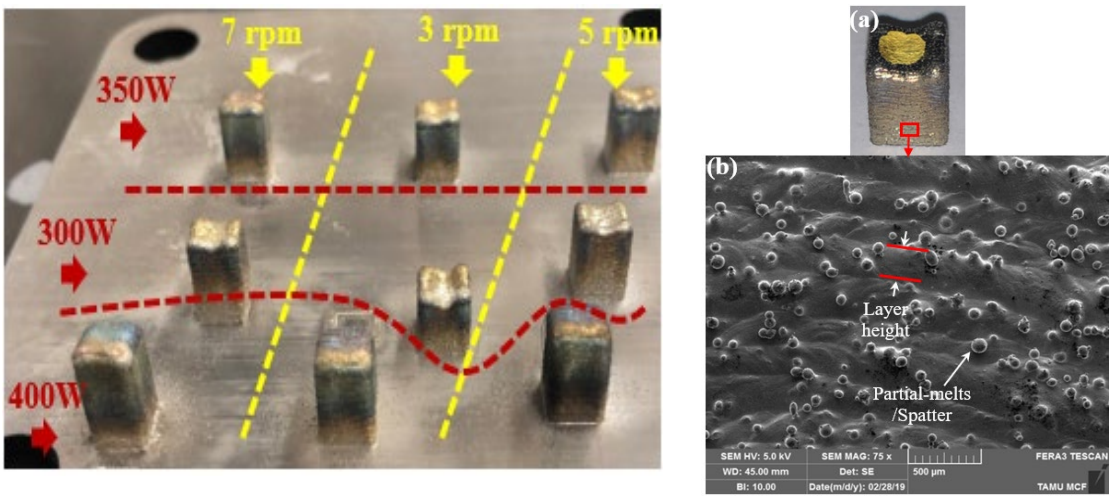

Figure 44: (Left) As-built Co-Cr-Mo samples on build plate. (Right) 300W – 5 RPM Co-Cr-Mo Sample: (a) Perspective macro view (cubic block has about 5 mm side), (b) SEM image of a side-bottom region.

For the second DOE shown in Table 5, cylindrical samples were made with the following dimensions of diameter and height (6 mm x 8 mm) on a stainless-steel plate

using Laser Engineered Net Shaping (LENS). Samples were created by adding a percentage of Mo to the melt pool via the four-nozzle delivery process of LENS. Process parameters were derived from the previous study performed on Co-Cr-Mo samples.

Table 5: Co-Cr-%Mo prints with layer size 0.254 mm, hatch distance 0.15 mm, scan orientation 90°.

Parameter Set (Mo content)	Power (W)	Power Feed Rate (RPM)	Scan Speed (m/s)
Process Parameter 1 (+6%, +9%, +12%, +15%, +18%, +21%)	350	5	8.6
Process Parameter 2 (+15%, +18%, +21%)	450	5	8.6

Processing of Co-Cr-ΔMo structures was analyzed to determine which set of process parameters would result in better art quality and properties. Table 5 presents the process parameters for this round of builds. 350W was carried over from the previous study as samples made at this power had performed best compared to the other two powers utilized. The second power 450W was chosen due to the possible difficulties that adding Mo posed. The high melting point (2623° C) of Mo presented a problem with assimilation into the lower melting point Co-Cr-Mo (1350° C). As these samples were built with two sets of process parameters, the mechanical properties differ between samples and sets as expected.

Process parameter set 1 (PP1) was the only set with Mo additions from +6% to +12%. Macroscopic analysis of +6% Mo showed no discoloration and was the smallest built sample. Figure 15 provides a macroscopic image of the Co-Cr-ΔMo samples. Each

sample contains typical surface defects characteristic of DED powder delivery. Satellites or wavy structures are both prominent features on the top surface of most samples. As the Mo percentage increased, samples went from displaying individual satellite structures to top layers that exhibit waviness, a structural defect. The lower percentage Mo samples appear to have no discoloration. As Mo percentage grows, the discoloration appears to follow the same pattern as the samples from the previous study. The samples with the highest percentage of Mo begin to show a blue tint as the layers form near the top. Furthermore, feed rate for the Mo hopper must increase to deliver higher Mo percentage samples. Since this causes more powder to be delivered to the melt pool, these higher percentage samples are taller than those of lower percentage.

SEM micrographs were taken of the outer surface of each sample as shown in Figure 45. Each sample exhibits a large amount of unmelted powder spatter on the surface. Unmelted powder exists as either single or fused particles. At +6%, only a small amount of unmelted powder is present. The +15% sample showed the most amount of unmelted powder, but the prevalence of these surface features lowers slightly in the highest two additional percentages (+18%, +21%). This unmelted powder is due to blown powder spatter sticking to the surface of the sample. Individual layers appear to bow slightly upwards or downwards as layers are deposited. Multiple layers appear to fuse in some instances to create thicker layers. The uneven distribution of layer thicknesses lowers the aesthetic quality of the part and may require additional machining.

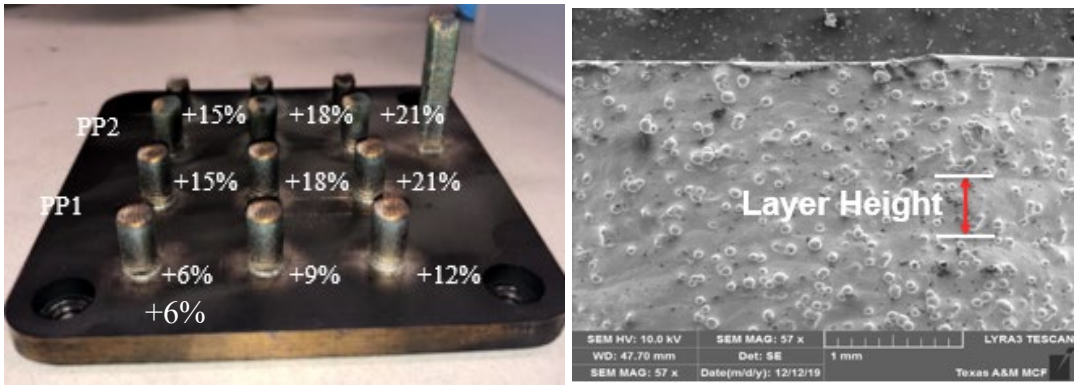

Figure 45: Reference Image for Co-Cr-%Mo after LENS run for process parameter 1 (PP1) and process parameter 2 (PP2) (left) and SEM micrograph of Co-Cr-%Mo outer side surface (right).

For the second process parameter (PP2) set, the higher power caused these samples to be much darker than their counterparts. These samples show a smaller proportion of blue discoloration. Due to the higher power, these samples were taller than the first process parameter set as the larger volumetric energy density melted more powder. These samples feature bands of discoloration with alternating layers showing some blue tint and darker regions. For all samples, those made with higher powder feed rate built slightly larger. This is to be expected as the delivery of more powder with higher power leads to thicker layers. All samples show a bronze tint around the top surface where the end of the build occurs. Table 6 presents the length and diameter of each of the DOE 2 samples for PP1.

Table 6: Length and Diameter of DOE 2 Samples measured via Vernier Calipers

(mm)	+0%	+3%	+6%	+9%	+12%	+15%	+18%	+21%
Length	9.0	8.8	8.0	9.2	9.1	8.0	9.1	9.2
Diameter	4.0	4.0	4.0	4.0	4.0	4.0	4.0	4.0

Compositionally graded samples were built to the programmed dimensions. Like all samples produced through LENS in this series of studies, unmelted powder exists across the entire outside surface. Samples display similar manufacturing defects such as waviness and bowing layers. C1 built with the least amount of structural defects but did show some discoloration in the topmost layers. The smallest sample C2 and highest resolution sample C3 show the largest incidence of bowing. This is most likely the result of the layer size-percent increase combination which creates melt pools that drag layers toward center. This drooping of layers was consistent for all layers in C2 and C3 as shown in Figure 46.

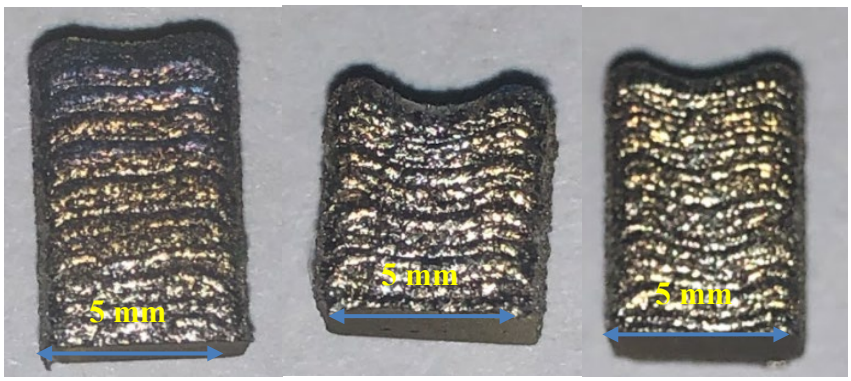

Figure 46: Images of C1 (Left), C2 (Middle), and C3 (Right).

After analyzing the process parameters utilized in each study performed, a plot was developed to compare the DOEs and other relevant work performed by the author as shown in Figure 47. From the work performed, power is shown to be more influential than RPM. There is a larger effect on microstructure that power has on layer size,

nanoindentation and nanoscratch results. RPM affects the microstructure and has a higher effect on microindentation.

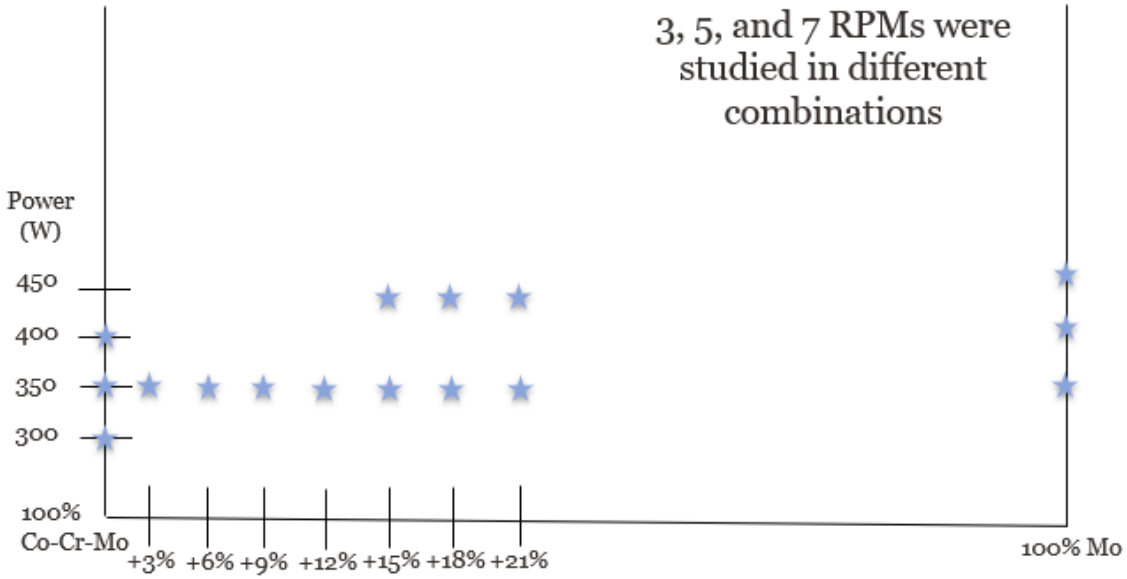

Figure 47: VED Process Parameter Space for DOE 1 and 2 plotted with a study performed on pure Mo (more details in Appendix C.

5.1.2 Task 1-B Characterize samples at macro- and microscales

5.1.2.1 Macrostructure Analysis of Co-Cr-ΔMo

Optical micrographs were obtained at various scales for each of the samples in DOE 1 and DOE2 for both vertical and horizontal orientations. In these micrographs shown in Figure 48, the inset shows the size of individual layers and grains. The inset image shows the delineation of melt pool boundaries along with heights of each layer. Layer heights appear to grow smaller as the number of layers is increased. Grains became apparent at 50 μm. These are indicated by the red lines separating individual grains in the image below. Grain boundaries appear as interconnected lines that run

alongside adjacent grains. These grain structures confirm that cells oriented on direction indicate a grain. There was no significant porosity of defects observed in the optical images. The microstructure appears for the most part uniform.

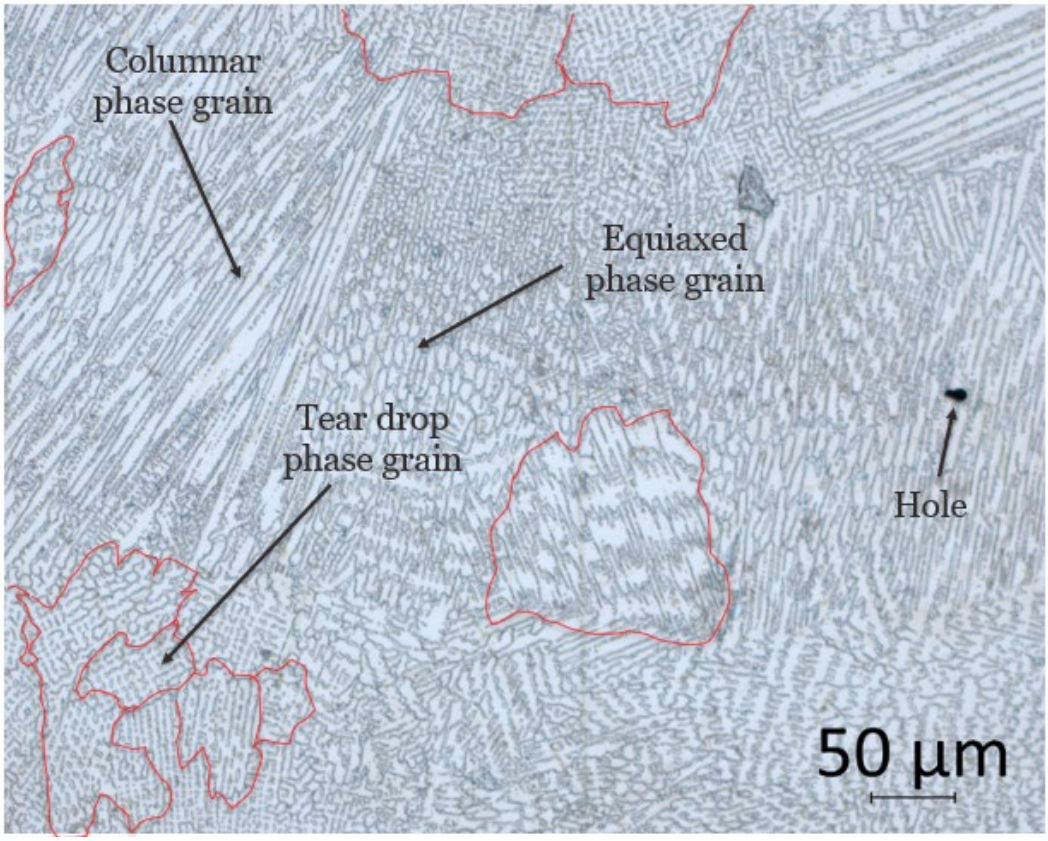

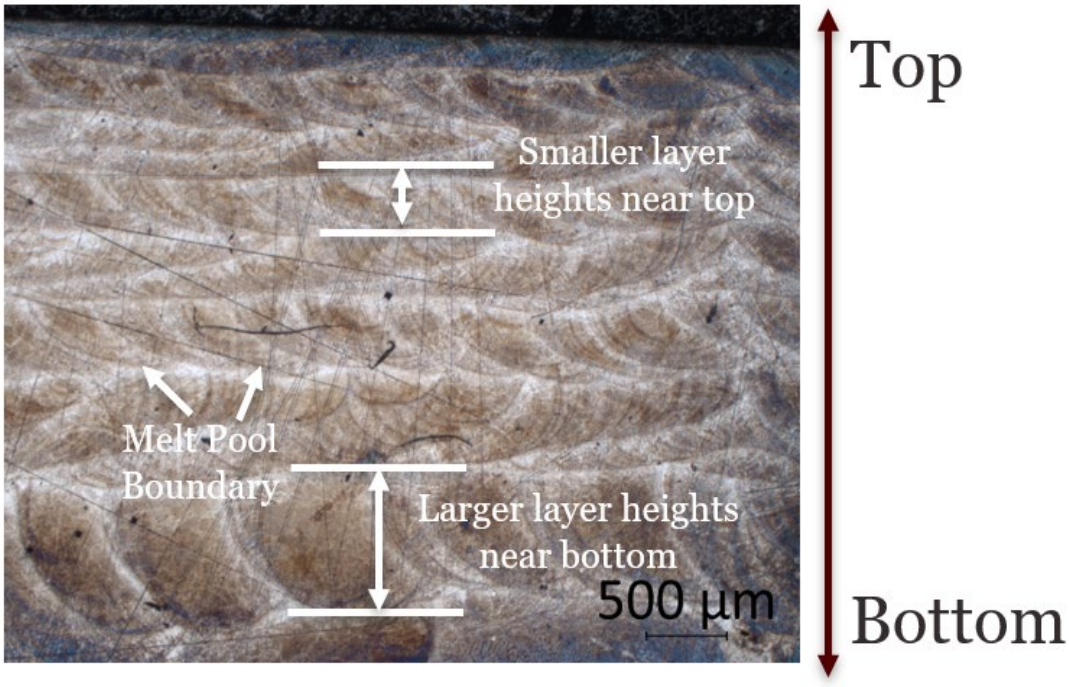

Figure 48: Optical micrographs at 50 µm (top) and 500 µm (bottom) with annotated microstructure phase regions and layer height indicators.

Further analysis of the process parameters against the macrostructure reveals various trends regarding the manufacturing of LENS Co-Cr-Mo. In Figure 49, the layer height and cell size of individual samples is measured against the +%Mo in each sample. There is an upward trend of increasing layer height at Mo content is increased. The cell size for PP1 samples also shows an upward trend while the PP2 samples show a decline in cell size with increasing %Mo.

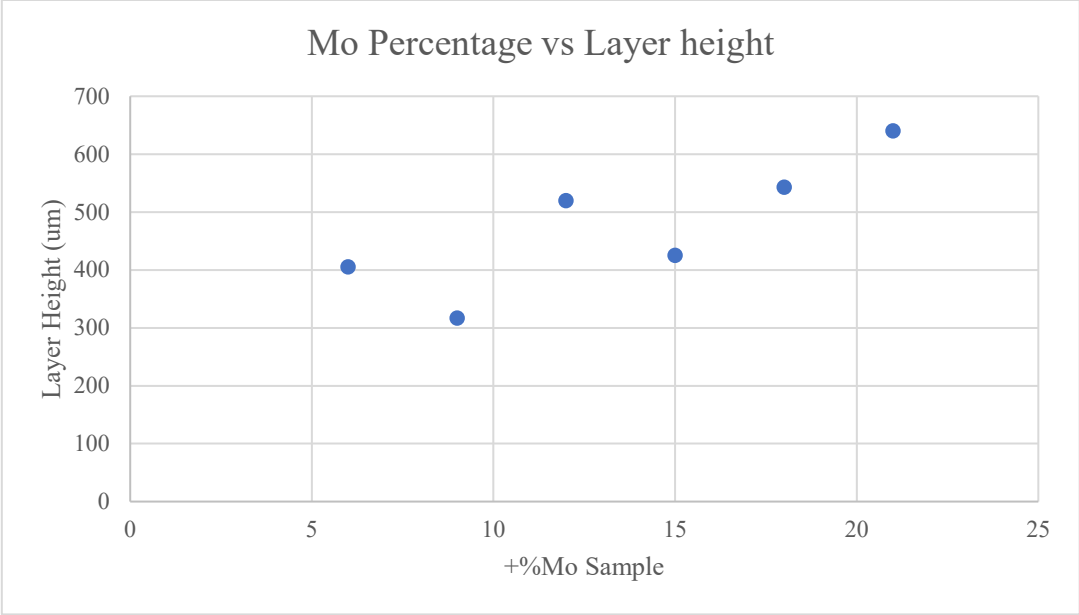

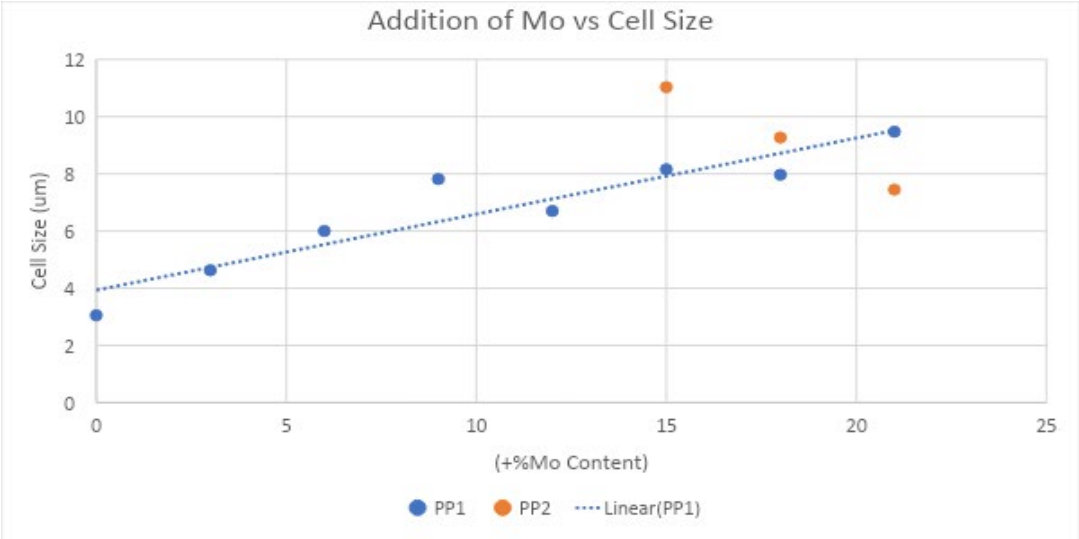

Figure 49: Influence of Mo addition vs macro features in Co-Cr-Mo.

There are variety of factors that contribute to the observations made here. The 400W 3 RPM samples have the largest cell size – most likely due to higher energy density which is known to lead to larger cells. The addition of higher %Mo corresponds

with higher powder feed rate of the Mo which lead to larger average layers. This would explain the increase in layer size despite the same power being used.

5.1.2.2 Microstructures of Co-Cr-Mo as a Function of Process Parameters

Examination of the SEM micrographs show how fast cooling rates characteristic of laser-based AM processes influence the size, shape, and texture of grains. Figure 50 presents the micrographs of the LENS Co-Cr-Mo with annotated microstructure features. These features contribute to an aggregate of material properties such hardness, stiffness, and abrasion resistance. The longitudinal direction of Co-Cr-Mo LENS sample showed a mixture of microstructural phases.

Figure 50 presents the DOE along with corresponding microstructure images. Three different phases appear prominently: a phase with equiaxed cells, a phase with long cells mixed with the underlying matrix, and a mixed phase consisting of the long columnar cells and smaller equiaxed cells. Equiaxed phases possess cells with an average width of 3-6 μm. Long grain phases have lengths between 60-100 μm and width between 2-4 μm. The mixed phase possesses much smaller fine, equiaxed cells with an average width of 1-3 μm. In these mixed phases, equiaxed cells and long, columnar grains appear to generate a lamellar structure wherein one layer appears after the other. Images of top, middle, and bottom regions feature relatively similar proportions of each phase observed.

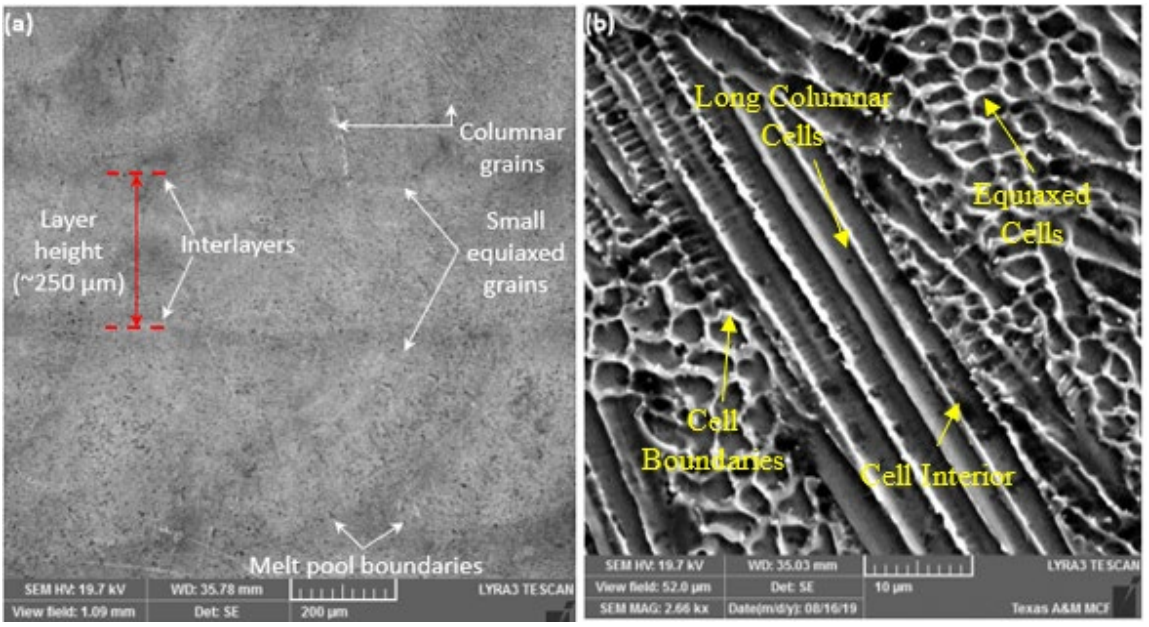

Figure 50: SEM Micrographs of LENS Co-Cr-Mo with annotated microstructure features.

Small carbides were observed in all microstructures indicated by small bright particles. In the 300W series of samples, the size of these carbides was in a range of 1-2 µm. The 400W series of samples display much more pronounced carbides within the size range of 1-5 µm. The carbides are distributed in an array throughout the microstructure of each sample.

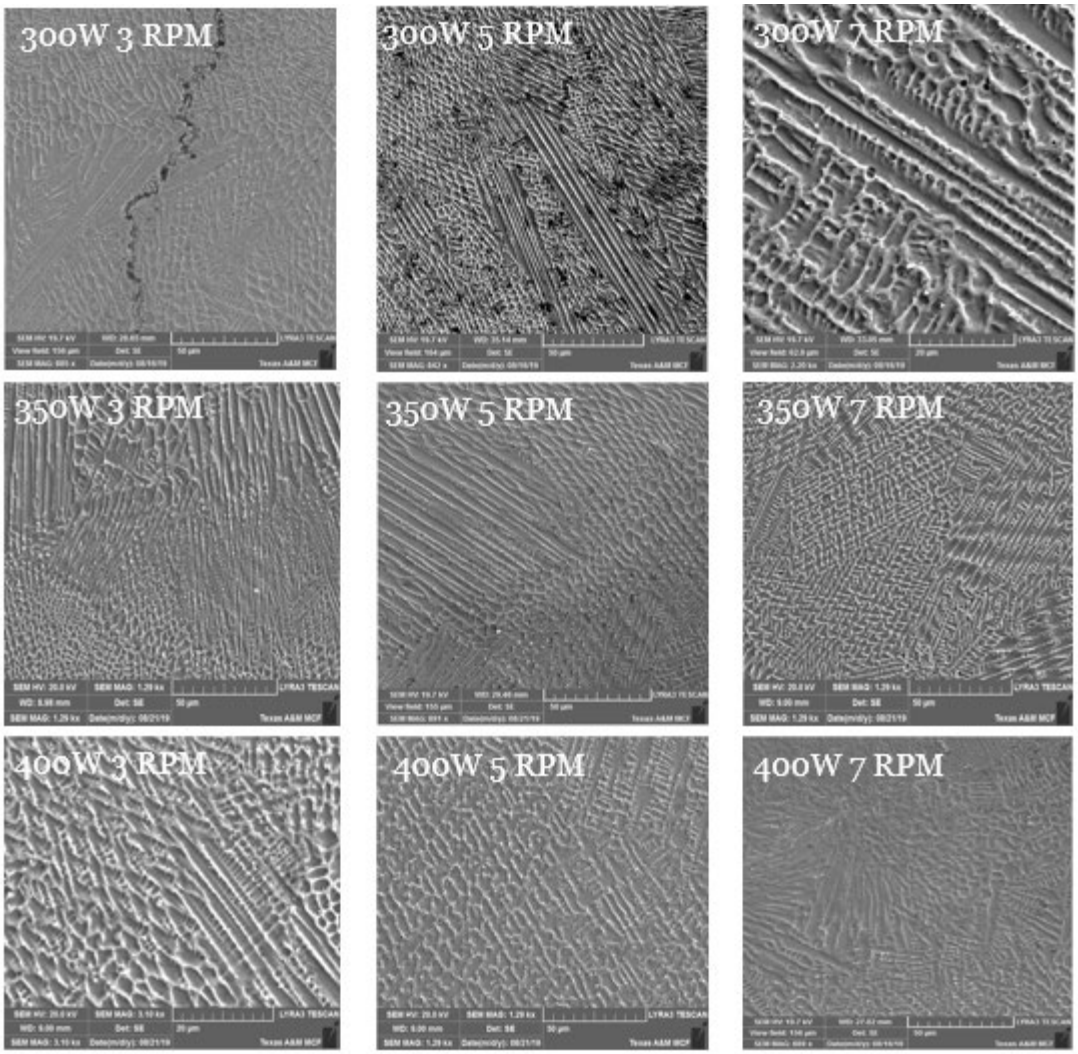

Figure 51: Microstructures of DOE 1 of each set of process parameters.

In the second DOE, the change in the microstructure indicates growth that occurs at the cell boundaries. Figure 52 shows the progression of the microstructure as more Mo is added for PP1 and PP2. The first process parameter set shows a change in phase after +12% Mo. In comparison to the microstructure of PP1, the second process parameter set shows more connected but thinner cell boundaries than the same +%Mo sample counterparts in PP1. At the cell boundaries and especially triple junction points, Mo-rich

features grow. There is a rise of interconnected regions as Mo increases. The formations begin as loose islands. As Mo increases, regions begin to connect as cell sizes decrease.

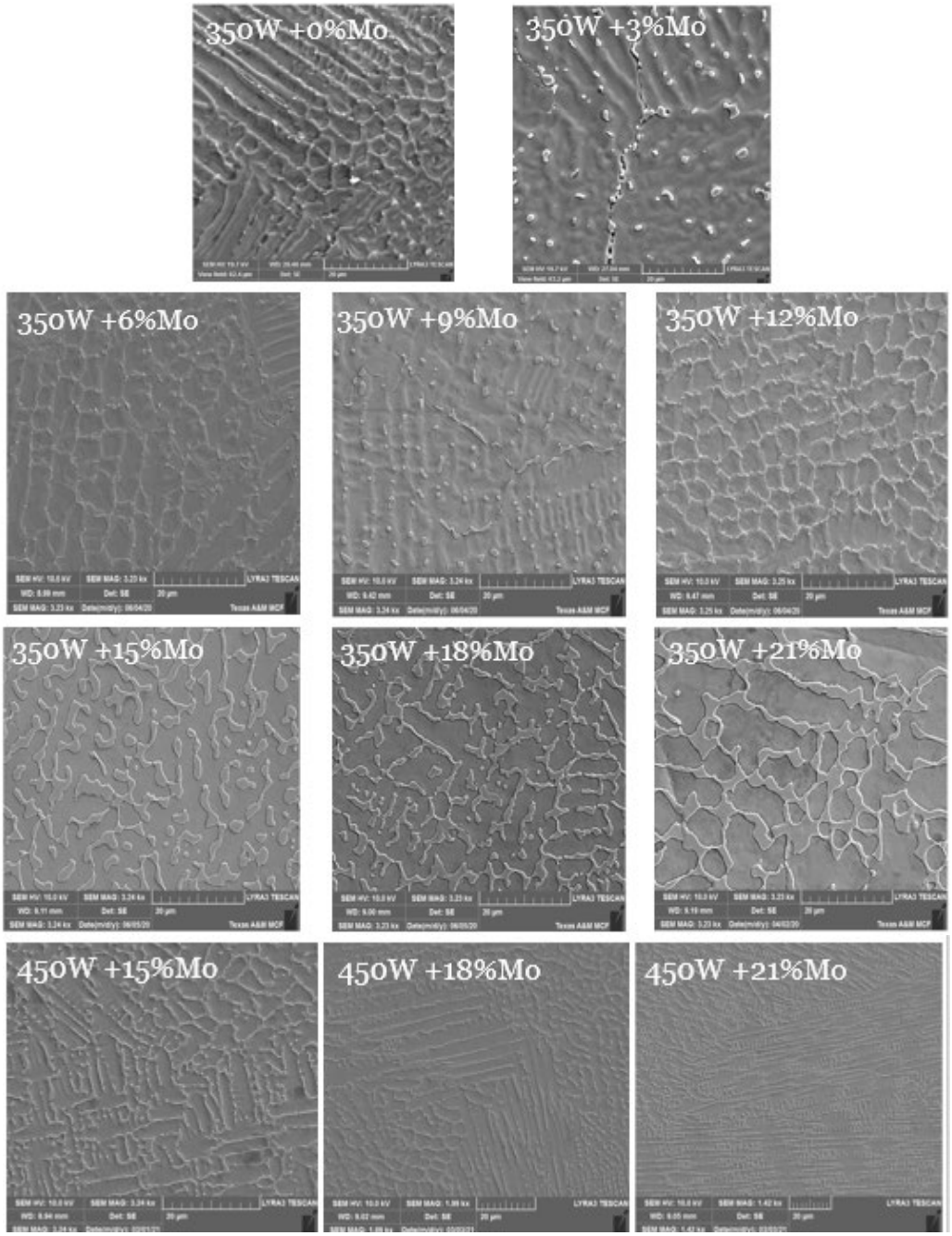

Figure 52: Microstructure of DOE 2 for process parameter set 1 and 2.

5.1.3 Summary of Results and Deductions

The following are the results that were obtained during the course of answering the first research question:

- For DOE 1 [Process Parameter Study]
    - Sample heights generally increase with power and powder flow (RPM)
        - Only contradiction: 300W, 7 RPM built taller than 350W sample of the same size
- For DOE 2 [ΔMo Study]
    - Aesthetic quality was different for the two-process parameter sets
        - PP1 builds are shorter than PP2
        - PP2 samples are much darker than PP1
- Consideration of flowability and effective density of powders through chamber is critical for deposition of single composition and compositionally altered samples
    - The relative powder feed rates of Mo and Co-Cr-Mo need to be adjusted to reach desired final compositions
- Discoloration was prevalent in higher power samples
- Top surfaces of sample exhibit waviness and satellites (besides spatter)
- LENS manufacture leads to defined equiaxed and columnar cells in microstructure not observed in traditional methods like casting

From these results, many deductions can be made regarding LENS Co-Cr-Mo manufacture and the corresponding macro- and microstructures. Optimization of powder feed rate when depositing powder between two nozzles is necessary to create samples.

For HV (0.5) microhardness of all samples was greater than the literature reports of 266-345 for cast ASTM F-75. The microstructure of the printed samples was also similar to LENS and SLM Co-Cr-Mo from literature. Further, the friction coefficient reported is greater than or comparable to literature values for ASTM F-75.

For the first design of experiments, discoloration can be avoided by the combination of lower scan speed and lower power or higher powder feed rate and lower power (i.e. < 400 W). This effectively results in lower volumetric energy density (VED). For Co-Cr-Mo, the 350W 5 RPM sample yielded the best combination of the three metrics (build height, highest hardness, and no discoloration).

For the second design of experiments, the process parameters studied in DOE 1 may be good enough even with the change in %Mo. The processing causes larger cells as power increases. From +0%Mo to +12%, the 350W power has best overall set of mechanical properties and aesthetic quality (layer size, discoloration avoidance, etc.). For +Mo% from +15% to +21% 450W performed better. The higher power yielded a more well-defined microstructure, but darker exteriors on sample surfaces. This is most likely due to higher power melting more Mo powder and introducing to melt pool creating dendritic structures. The lower power yields higher % of secondary phase with island growths rather than well-defined features.

The top layers of the sample are smaller in thickness. This is due to the substrate at the bottom acting as a heat sink leading to larger layers. The top layers have a lower rate of heat dissipation leading to vaporization thus resulting in thinner layers and the

bowing of layers as the structure is built for cubic samples. Last, manufacturing via LENS leads to defined equiaxed and columnar cells not observed in traditional casting.

5.2 Effects of changing ΔMo on the macro- and microstructure (RQ 2)

5.2.1 Task 2-A: Quantify/correlate microstructure related defects and manufacturing quality.

Analyzing the three different powers yields a variety of structural conclusions. Figure 53 provides the parameters of DOE 1 against microstructural features. The most prominent microstructural features exist in 300W. Individual grains and neighboring phases appear to be packed more densely than in the other two power levels. From the micrographs, as power increases, the average grain size increases, and a larger proportion of underlying matrix can be observed. While all three samples show equiaxed grains, the quality of these grains significantly reduces with the increase in power. Furthermore, the quality between RPM is also evident. For 400W 7 RPM samples, the carbides that are prominent for 300W samples appear to just be emerging from the underlying microstructure. While there is evidence of similar structures in lower power levels, speckles of carbides peak out from the underlying microstructure as though their formation appears to be incomplete. These results imply that higher power levels yield larger grain growths and may have an influence on the texture quality of the underlying matrix.

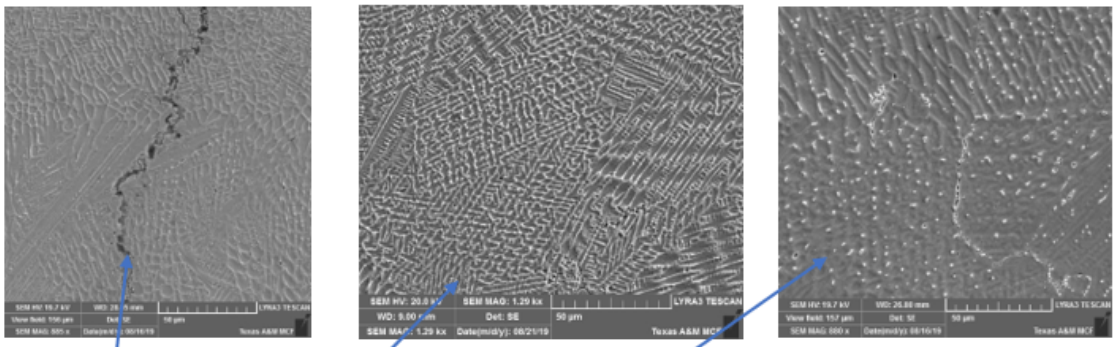

Power (W)	Scan Speed (mm/s)	Powder Feed Rate (RPM)	Layer Height (mm)	Hatch Spacing (mm)	Energy Density (J/mm³)
300	8.6	3	0.254	0.15	915.5832265
300	8.6	5	0.254	0.15	915.5832265
300	8.6	7	0.254	0.15	915.5832265
350	8.6	3	0.254	0.15	1068.180431
350	8.6	5	0.254	0.15	1068.180431
350	8.6	7	0.254	0.15	1068.180431
400	8.6	3	0.254	0.15	1220.777635
400	8.6	5	0.254	0.15	1220.777635
400	8.6	7	0.254	0.15	1220.777635

Figure 53: DOE process parameters for LENS built of Co-Cr-Mo corresponding to selected microstructure images.

Cell interiors are darker matrix regions that contain other microstructural features. The underlying matrix possesses the largest amount of Co and Cr on average and the least amount of Mo and C. Cell boundaries refer to features that act as a border that encloses the underlying matrix whether in long or equiaxed grain form. The cell boundaries consist of raised features that display various carbide structures. Networked carbides are connected cell boundary regions of typically equiaxed repeating structure with singular and mixed phases containing large and small grains. These carbides possess the least amount of Cr on average but the second highest amount of C content. On the other end, thick width cell boundaries are featured prominently in long grain

structures. Consistent with prior observation, these features possess higher values of Mo with slightly lower Co and Cr. Jagged carbides have the largest amount of Mo and least amount of Co and Cr on average. These carbides exist as island-like protrusions at cell boundaries and most often occur at junctions in networked carbides and on top of long thick width cell boundaries. These island-like protrusions are Mo-rich carbides as corroborated in a follow-up study where the percentage of Mo is increased. The island-like protrusions begin to grow from their current locations within the microstructure and link together upon increasing Mo content.

Analyzing the results from the three different power levels provides insights into the microstructure and build quality. The most prominent microstructural features exist in 300W samples. The 300W 7 RPM is shown in Figure 54. Individual cells and neighboring grains appear to be packed more densely than in the other two power levels. From the micrographs, as power increases, the average cell size increases, and a larger proportion of cell interior can be observed. While all three samples show equiaxed cells, the fineness of these cells significantly reduces with the increase in power. This is consistent with the observations made by Wang et al. that the energy input of the laser beam influences cell spacing [178]. 400W samples have the largest equiaxed cells, but the shape of the cell boundary is more jagged than either of the two previous samples. This can be attributed to the cyclic reheating of the build at the highest input energy density. 350W samples show some instances of these large cells with jagged boundaries. In both power levels, the top of the sample prominently features these jagged boundary cells. Furthermore, the difference in microstructure between samples with different RPM

is evident. For 400W 7 RPM samples, the carbides structures appear to just be emerging from the underlying microstructure. These results imply that higher power levels yield larger grain growths and may have an influence on the microstructure quality.

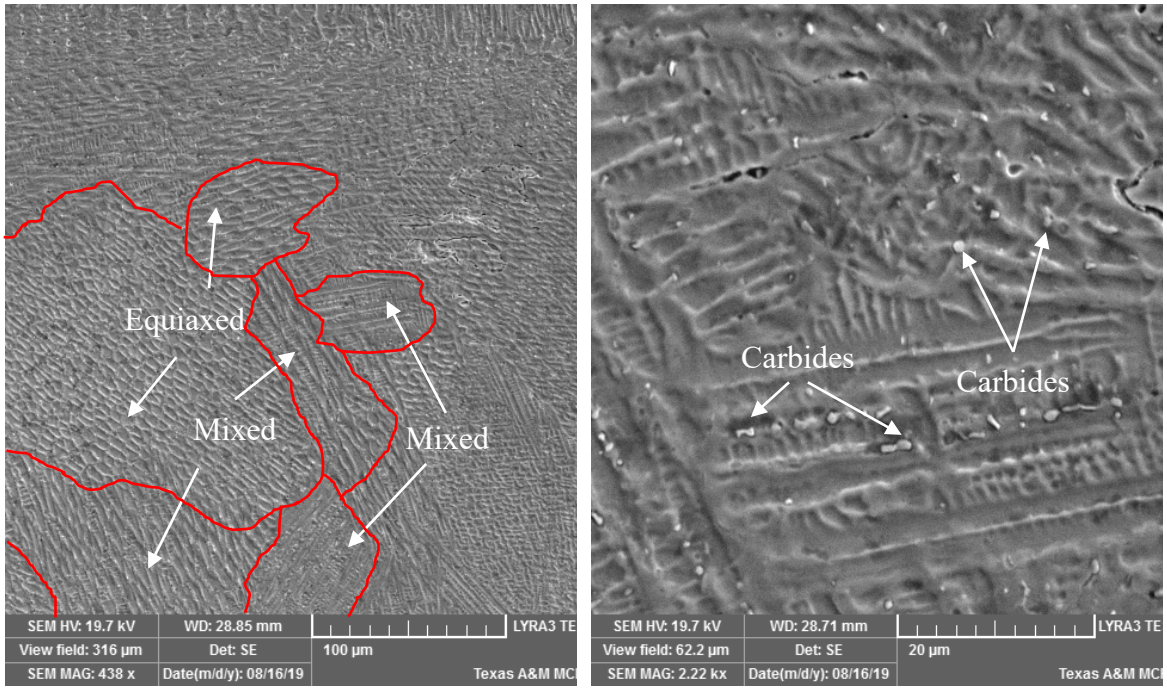

Figure 54: Microstructure of 300W 7 RPM sample at (left) 100 µm with equiaxed and mixed microstructure grains indicated with arrows and separated by red lines and (right) 20 µm with carbides indicated with arrows.

Table 7 presents the EDS measurements of the different Co-Cr-Mo microstructural features. Cell interiors are darker matrix regions that contain other microstructural features. The cell interior possesses the largest amount of Co and Cr on average and the least amount of Mo and C. Cell boundaries refer to features that act as a border that encloses the cell interior whether in long columnar or equiaxed cells. The cell boundaries consist of raised features that display various carbide structures. These

carbides possess the least amount of Cr on average but the second highest amount of C content. On the other end, thick width cell boundaries are featured prominently in the crystal structure. Consistent with prior observation, these features possess higher values of Mo with slightly lower Co and Cr. Carbides have the largest amount of Mo and C and least amount of Co and Cr on average. These carbides exist as protrusions at cell boundaries and most often occur at junctions (triple points) between equiaxed cells and on top of long thick width cell boundaries. These are Mo-rich carbides as corroborated in the follow-up study where the percentage of Mo is increased. The carbide protrusions begin to grow from their current locations within the microstructure and link together upon increasing Mo content.

Table 7: EDS Results of Co-Cr-Mo microstructural features.

Microstructure Feature	Co	Cr	Mo	C
Equiaxed Cell Interior	49.76	26.08	2.11	20.76
Equiaxed Cell Boundary	36.31	21.55	4.71	33.84
Columnar Cell Interior	49.12	25.88	2.32	21.28
Columnar Cell Boundary	37.60	21.51	3.62	35.78
Mixed Phase Cell Interior	47.62	25.17	2.56	23.24
Mixed Phase Cell Boundary	34.91	20.48	3.57	39.40

From the results, it can be inferred that Mo concentrates at cell boundaries. This is consistent with the measured smaller scale EDS spectra which show Mo patterns

tracing the cell boundaries observed in the SEM micrographs. Figure 55 presents a large-scale image of Co-Cr-Mo alongside EDS spectra for the major constituents of the microstructure. As expected, Co and Cr EDS maps show large concentrations throughout the microstructure. In the Cr EDS map, some pockets of Cr deficient zones do exist that are significant. Mo shows a similar spread of concentration across the map with pockets of Mo deficient areas that correspond with the cell interior features. The C map displays a constellation shaped concentration of carbides with smaller island-like features dotting the map. Carbide structures are most prominent in the cell boundaries specifically those that possess the lowest amounts of Co and Cr. Thick width cell boundaries that exist in the long columnar crystal structure possess a similar amount of Cr to the matrix on average. This suggests that Cr-rich features in Co-Cr-Mo tend to form at long grain cell boundaries. Equiaxed structures similarly exhibit Co and Cr accumulating at cell interiors and Mo gathering at the cell boundaries.

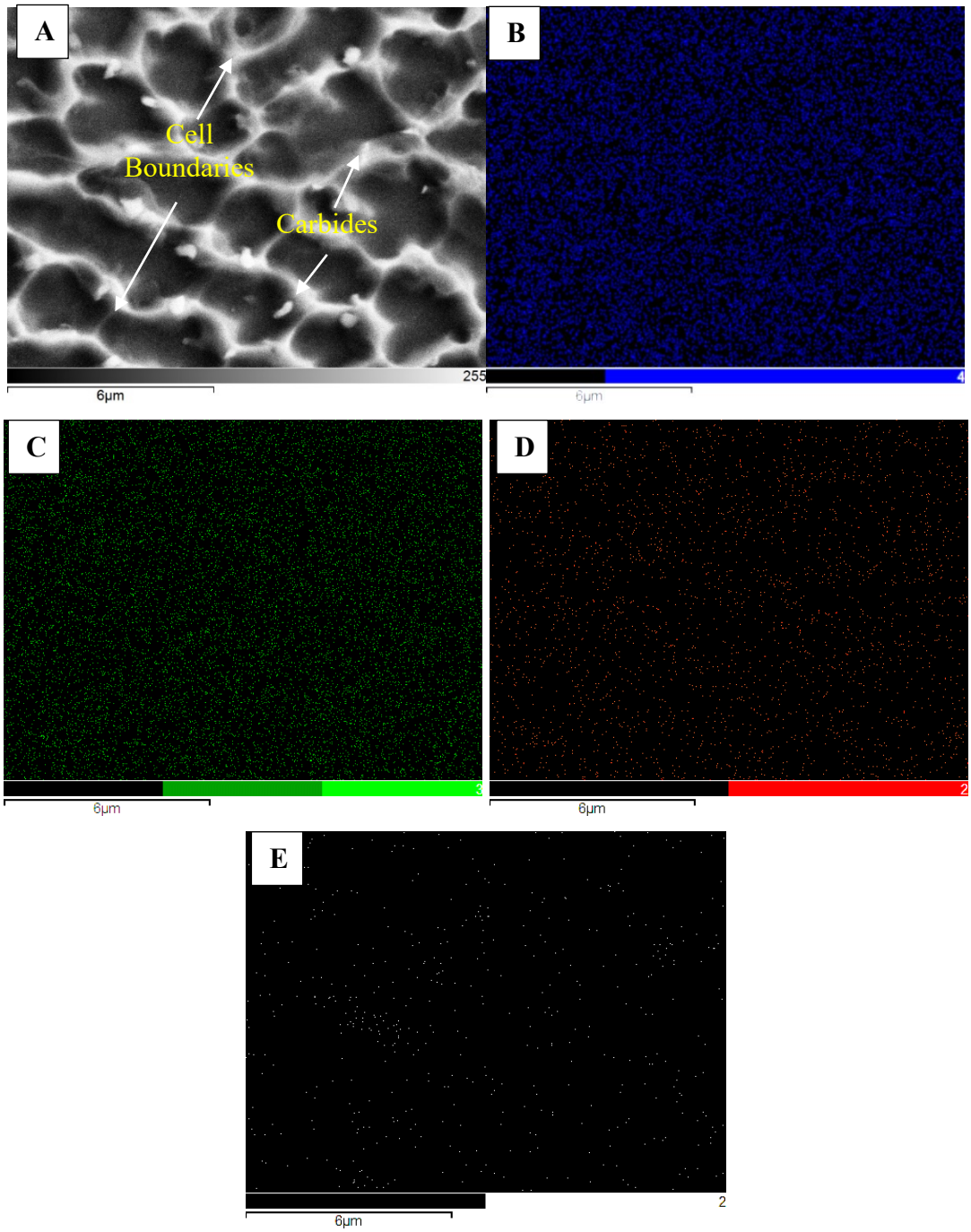

Figure 55: (A) SEM Micrograph of Co-Cr-Mo with associated EDS spectra for (B) Co, (C) Cr, (D) Mo, and (E) C.

5.2.1.1 Microstructure and Compositional Distributions of Co-Cr-ΔMo Samples

In Figure 56, SEM micrographs are presented alongside corresponding EDS analysis. Based on the progression of the samples in the micrographs, it can be shown that the addition of Mo leads to the precipitates that grow at the cell boundaries. In the +6%Mo sample, the cell interior is shown to possess the largest percentage of Co as shown in Spectrums 1 and 4 in Figure 56C. The jagged formation growing out of the grain boundary measured in Spectrum 2 contains a larger percentage of Mo and C. Based on the EDS measurement, the presence of Mo and C would infer that this formation is a carbide. The formation measured in Spectrum 3 has a lower C value but a similar amount of Mo to Spectrum 2. The C amount seems to be offset by a higher amount of Cr which indicates that both Cr and Mo are present within carbide formations.

In Figure 56E, the carbide formations begin to precipitate from the cell boundaries. Surface features become less prevalent as additional Mo levels out the difference between cell boundaries and interior. Based on comparison measurements between similar regions, the additional Mo appears to distribute between various regions such as the cell interior, cell boundaries, and carbides that form. This aligns with the previous deduction that when the Mo cannot gather at the cell boundaries any further, it begins to accumulate within the grain interior. This is indicated by the evolution of Mo content in two similar regions: Spectrum 1 of Figure 56C and Spectrum 1 of Figure 56E. The comparison of carbide formations can be seen in the evolution from Spectrum 2 of Figure 56C and Figure 56E.

As more Mo is added, these individual formations begin to connect. The trend of the microstructure losing its distinguishable features continues. The +15%Mo samples begin showing a large departure from the previous microstructural features. A flat, spanning underlying microstructure is apparent with the previously apparent features losing definition. At +18%Mo, the microstructure below the connected formations is completely flat with little resemblance to the previous iterations with lower %Mo. This coincides with a change in material properties as detailed in the mechanical testing section. The cell interior as measured in Spectrum 1 and 4 of Figure 56G show an increase in Mo content. Due to the addition of Mo content to the entire build, the presence of C per feature has decreased as expected. The cell interiors still possess the highest percentage of Co and the lowest percentages of Mo and C. Similar to Figure 56C, Figure 56E shows a feature which has a large Cr measurement further corroborating the formation of Cr and Mo based carbides.

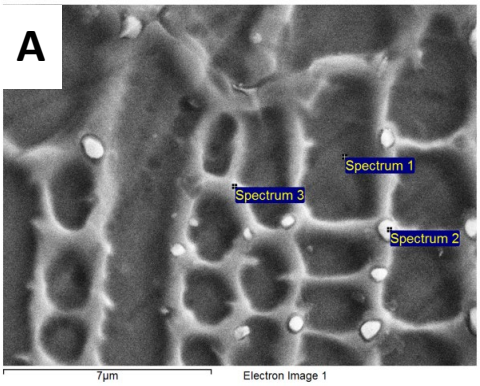

Spectrum	In stats.	C	Si	Cr	Fe	Co	Mo
Spectrum 1	Yes	17.72	0.96	26.96	0.45	52.03	1.88
Spectrum 2	Yes	20.15	1.38	27.08	0.36	47.52	3.50
Spectrum 3	Yes	19.26	0.98	15.83	0.28	27.55	2.10

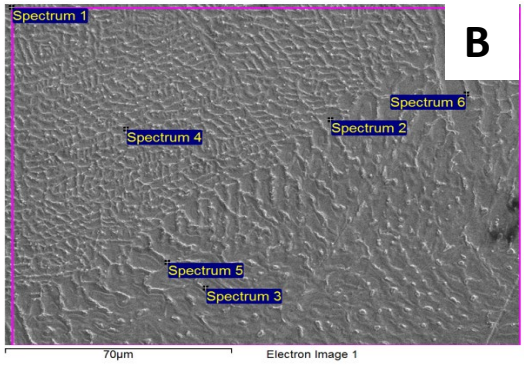

Spectrum	In stats.	C	O	Si	Cr	Co	Mo	Total
Spectrum 1	Yes	2.95		0.74	28.68	61.84	5.79	100.00
Spectrum 2	Yes	2.13		0.55	28.51	64.55	4.25	100.00
Spectrum 3	Yes	2.22		0.51	27.74	64.14	5.39	100.00
Spectrum 4	Yes	2.44		0.72	28.65	63.30	4.88	100.00
Spectrum 5	Yes	6.14	3.09	1.02	27.83	55.20	6.72	100.00
Spectrum 6	Yes	3.78		1.45	27.37	49.82	10.58	100.00

C

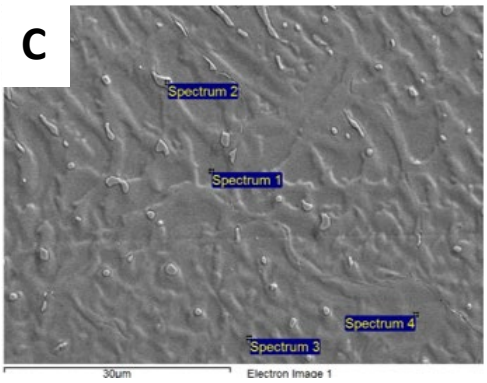

Spectrum	In stats.	C	Si	Cr	Co	Mo
Spectrum 1	Yes	4.99	0.59	26.06	64.09	4.27
Spectrum 2	Yes	14.88	0.80	26.75	45.13	12.44
Spectrum 3	Yes	9.45	0.87	31.19	45.80	12.69
Spectrum 4	Yes	7.25	0.63	26.76	60.35	5.02

D

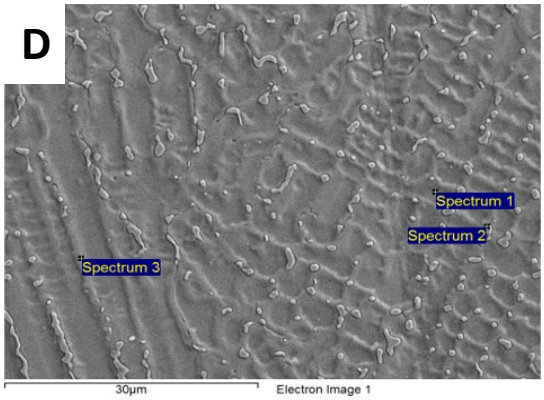

Spectrum	In stats.	C	Si	Cr	Co	Mo
Spectrum 1	Yes	4.11	0.63	26.87	63.25	5.13
Spectrum 2	Yes	3.26	1.10	31.55	48.52	15.58
Spectrum 3	Yes	2.67	0.69	28.28	62.34	6.02

E

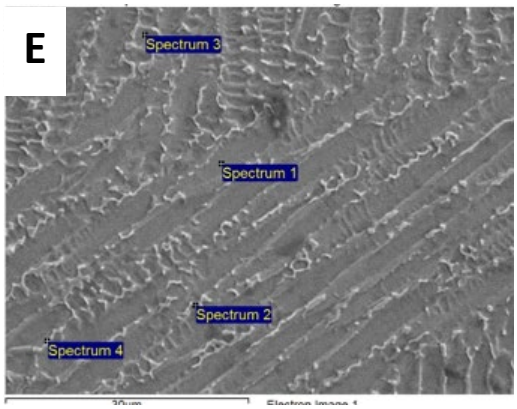

Spectrum	In stats.	C	Si	Cr	Co	Mo
Spectrum 1	Yes	3.22	0.60	25.78	64.44	5.96
Spectrum 2	Yes	5.92	0.95	27.00	49.66	16.47
Spectrum 3	Yes	5.34	0.71	24.88	61.83	7.24
Spectrum 4	Yes	5.18	0.79	25.97	59.60	8.45

F

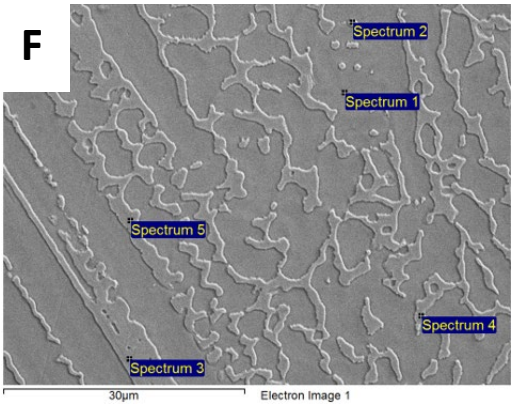

Spectrum	In stats.	C	Si	Cr	Co	Mo
Spectrum 1	Yes	2.39	0.60	25.91	62.92	8.19
Spectrum 2	Yes	3.41	1.15	27.45	47.07	20.92
Spectrum 3	Yes	2.30	1.15	27.37	49.22	19.96
Spectrum 4	Yes	2.59	0.99	27.63	48.37	20.42
Spectrum 5	Yes	2.60	0.86	28.70	48.43	19.41

G

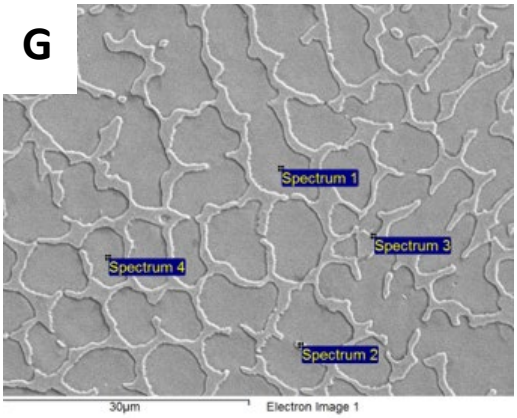

Spectrum	In stats.	C	Si	Cr	Co	Mo
Spectrum 1	Yes	2.20	0.62	26.33	63.39	7.46
Spectrum 2	Yes	2.99	0.78	30.28	47.22	18.73
Spectrum 3	Yes	3.18	1.14	27.11	50.61	17.97
Spectrum 4	Yes	2.54	0.47	26.17	63.24	7.58

H

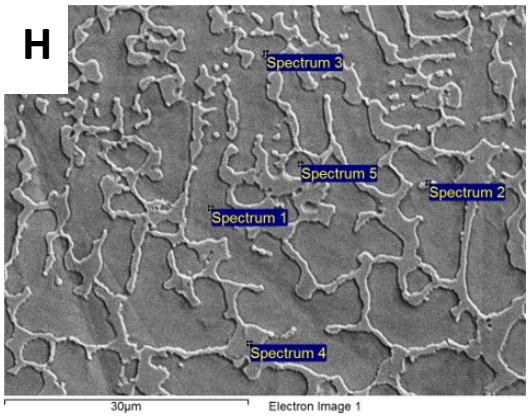

Spectrum	In stats.	C	Si	Cr	Co	Mo
Spectrum 1	Yes	3.21	0.76	25.03	62.11	8.89
Spectrum 2	Yes	3.57	0.78	28.02	49.78	17.85
Spectrum 3	Yes	3.50	0.75	27.41	50.85	17.49
Spectrum 4	Yes	2.68	0.74	27.22	49.51	19.84
Spectrum 5	Yes	2.69	0.53	25.51	61.95	9.32

I

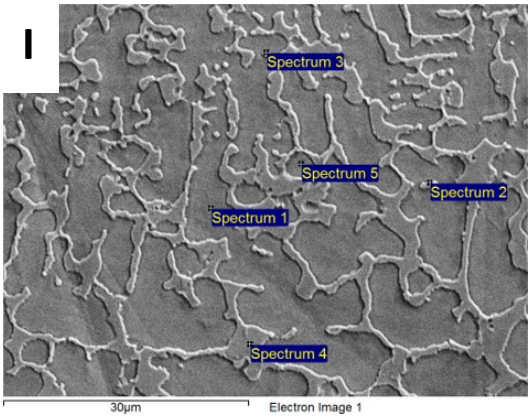

Spectrum	In stats.	C	Si	Cr	Co	Mo
Spectrum 1	Yes	3.21	0.76	25.03	62.11	8.89
Spectrum 2	Yes	3.57	0.78	28.02	49.78	17.85
Spectrum 3	Yes	3.50	0.75	27.41	50.85	17.49
Spectrum 4	Yes	2.68	0.74	27.22	49.51	19.84
Spectrum 5	Yes	2.69	0.53	25.51	61.95	9.32

J

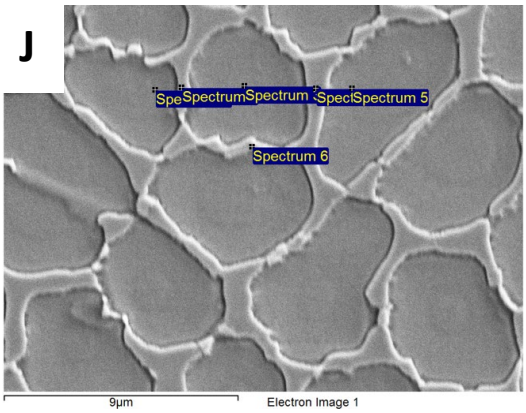

Spectrum	In stats.	C	Si	Cr	Co	Mo
Spectrum 1	Yes	2.37	0.48	25.33	63.62	8.19
Spectrum 2	Yes	2.51	0.83	29.90	47.37	19.40
Spectrum 3	Yes	2.67	0.62	25.03	63.69	7.99
Spectrum 4	Yes	2.16	0.92	27.64	49.19	20.08
Spectrum 5	Yes	2.42	0.45	27.12	61.85	8.16

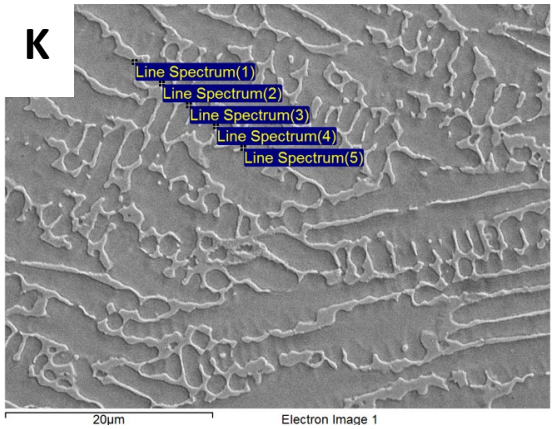

Spectrum	In stats.	C	Si	Cr	Co	Mo
Line Spectrum(1)	Yes	6.51	0.92	23.15	51.38	18.03
Line Spectrum(2)	Yes	2.47	0.71	26.60	59.56	10.66
Line Spectrum(3)	Yes	2.60	1.31	24.93	34.05	37.12
Line Spectrum(4)	Yes	7.26	0.83	25.87	48.99	17.05
Line Spectrum(5)	Yes	3.17	0.76	27.41	50.56	18.10

Figure 56: SEM micrographs and corresponding EDS analysis for PP1 samples (A) +0% Mo (B) +3% Mo (C) +6% Mo (D) +9% Mo (E) +12% Mo (F) +15% Mo (G) +18%Mo (H) +21% Mo and PP2 samples +15% Mo (I), +18% Mo (J), and +21% Mo (K).

Line scans were performed on each of the samples in the second DOE. Line scans went across boundaries of varying width to determine the concentration profile of the boundary regions. Corresponding EDS as shown in Figure 57 were generated from each of the line scans. At cell boundaries, Mo content increases while Co content decreases. Cell interiors are Co rich. Cr content remains stable in both regions. Compared to the EDS maps presented in Research Question 2, this method misses the accuracy provided by the microprobe by underestimating the change in Cr. Although small, it is difficult to measure effectively using the line EDS.

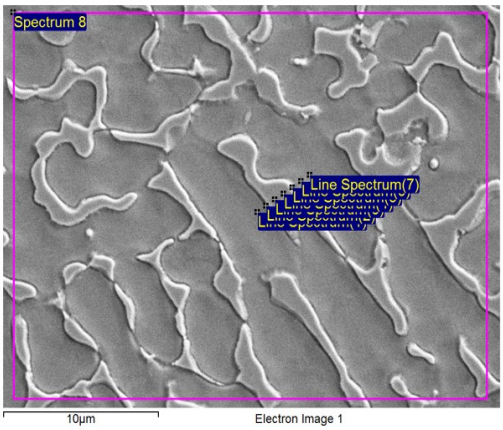

Spectrum	In stats.	C	Si	Cr	Co	Mo	Total
Line Spectrum(1)	Yes	2.42	0.63	25.93	61.09	9.93	100.00
Line Spectrum(2)	Yes		1.64	22.03	26.65	49.68	100.00
Line Spectrum(3)	Yes	2.62	0.92	27.60	49.06	19.81	100.00
Line Spectrum(4)	Yes	2.49	0.86	27.66	48.72	20.28	100.00
Line Spectrum(5)	Yes	3.50	0.63	26.19	59.62	10.06	100.00
Line Spectrum(6)	Yes	2.67	0.54	25.07	63.27	8.46	100.00
Line Spectrum(7)	Yes	2.59	0.58	24.52	63.38	8.92	100.00
Spectrum 8	Yes	3.25	0.67	25.75	58.17	12.16	100.00

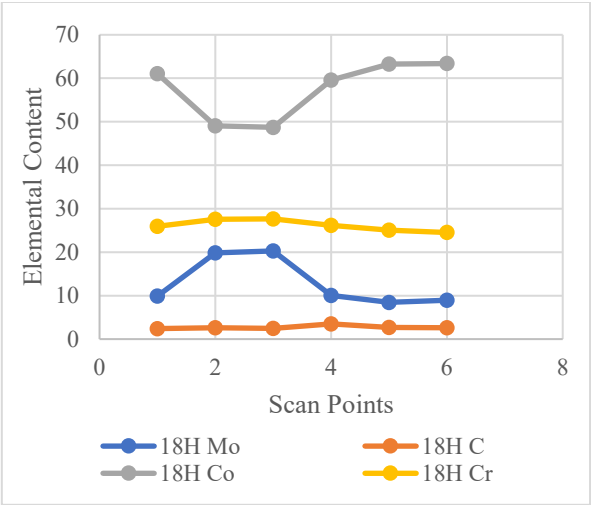

Figure 57: Line EDS depiction (left) and EDS measurement (right) of the PP2 18H sample.

Figure 58 provides the EDS measurements of microstructure features measured as a single point or area scan. The “Whole Area” measurement refers to an area EDS scan taken of the entire field of view upon the surface of the sample. “Cell Interior” refers to a composite measurement of both single point EDS and area EDS to determine the makeup of the structure below the microstructure features. “Cell Boundary” and “Cell Boundary Carbide” refer to measurements made of cell boundaries and carbides, respectively.

As expected, with the addition of Mo, it steadily increases in each measured feature/location. The Mo content in the carbides is the highest among all. When the input

%Mo was increased from +6% to +12%, the observed Mo content in the cell boundary changed from 11.53% to 18.5%. This mirrors the expected increase in Mo that should occur when adding the input %Mo to the Co-Cr-Mo used. The rate of growth in observed Mo content reduces from +15% onward. For large area measurements, higher increases in %Mo is observed (from +12% to +15% before reaching a plateau at +15%). This behavior coincides with the emergence of the carbide precipitates that grow from the cell boundaries as noted in the previous section. The matrix data corroborates this behavior as there is a large increase in observed Mo content as well. From +12% to +15%, the observed Mo content increases from 6.1% to 9.7%. After adding +15% Mo, the observed matrix Mo content slightly decreases to 8.8% at +21%. At +15%, the carbide formations begin to grow rapidly in size and link together as indicated in the +18% microstructure shown in Figure 56G. This correlates with the movement of Mo from the matrix to the cell boundaries which leads to carbide formations. The data shows that as Mo is introduced to Co-Cr-Mo, the observed Mo content continues to gather at the cell boundaries.

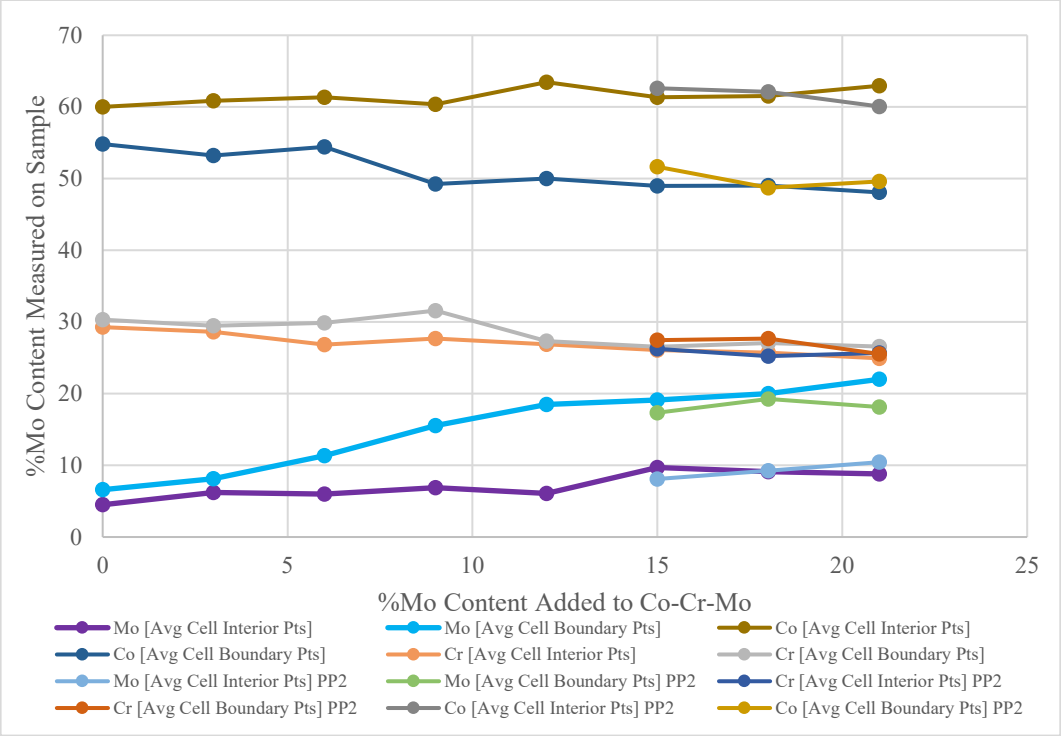

Figure 58: EDS Measurements in wt.% for various Co-Cr-ΔMo features

The %C follows a reverse pattern to %Mo as expected since no C is being introduced to the build. The whole spectrum measurements show that %C remains mostly constant throughout the addition of Mo. Each feature measured shows a decline in the amount of C, as Mo is introduced. This is expected as the introduction of Mo would increase throughout the microstructure thus reducing the amount of C at individual regions while the overall amount of C remains the same.

There is an increase of %Co in the cell interior with a significant decrease of %Co in the cell boundary at +6%Mo. The largest increase in cell interior Co content occurs at +12% and remains elevated up to +21%. The Co saturation therefore occurs in

the cell interior at +12%. The Cr content declines at +9% within cell boundaries until the curve plateaus at +12%.

5.2.2 Task 2-B: Quantify elemental distributions, phases, and microstructural features

5.2.2.1 XRD of LENS Co-Cr-Mo

XRD measurements and regions of measurement of the LENS Co-Cr-Mo are shown in Figure 59. The 350W 5 RPM sample was measured on the outside surface and the polished inside surface. This sample was chosen due to the observed consistency of mechanical properties and structural integrity. The sample was further sliced along the horizontal direction at a mid-point between the top and bottom sections to determine if different phases occur in the sample due to the temperature gradients that form during the LENS process. These measurements were compared to powder Co-Cr-Mo to determine any new phase formations. The 41.14° and 46.77° peaks correspond to the (1 0 -1 0) plane and (1 0 -1 1) plane for ε-HCP phase, respectively. The peaks at 43.9° and 50.83° come from the (111) and (200) orientations of the γ-FCC phase, respectively. XRD measurements were compared to the XRD of Co-Cr-Mo powder to determine any new phase formations.

The values recorded for the γ and ε phases are similar to those reported by Chen et al and Sahin et al. [179, 180]. For laser-deposited Co-Cr-Mo, Das et al. and Barucca et al. report similar peaks for the γ-phase (111) and (200) planes [97, 181]. All measured peaks correspond with the $M_{23}C_6$ carbide, a common formation for Co-Cr-Mo, reported by Caudillo et al. [171]. Similar results are presented by Rosenthal et al, who report the

presence of the σ phase and $M_{23}C_6$ at 44°, 47°, and 51°. Patel et al also indicate the presence of $M_{23}C_6$ in ASTM F-75 orthopedic samples. Thus, the $M_{23}C_6$ may have formed as indicated by the large peak at 43.9° and the smaller peak at 46.77° on the inner surface. The higher intensity may result from the combined presence of material phases and carbide structures. Comparing cast and LENS samples to determine the presence of carbides may prove challenging, however, LENS-based studies have been shown to form different microstructural components than traditional methods [13, 181].

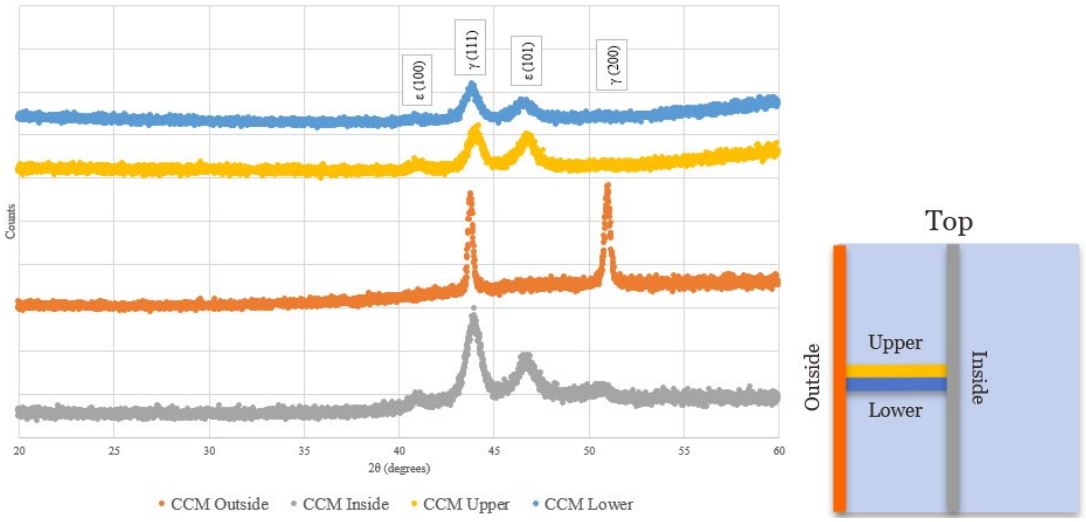

Figure 59: XRD Analysis for LENS-made Co-Cr-Mo and corresponding parts of sectioned samples analyzed.

In the second DOE shown in Figure 60, four samples were measured so that the influence of Mo content on the formation of different phases could be observed. Carbides and intermetallics are present at 44°, 47°, 51°, and 75°. In all four of the samples, γ and ε are present across over two different peaks similar to the 0% sample.

The σ phase at 42° is present of intermetallic formations ($Co_{(x)}Mo_{(y)}$). Peaks for Co_2Mo_3 and Co_3Mo occur at 46° and 47°, respectively. Co_7Mo_6 peaks occur in +12%Mo but most prominent in +18% and +21%Mo.

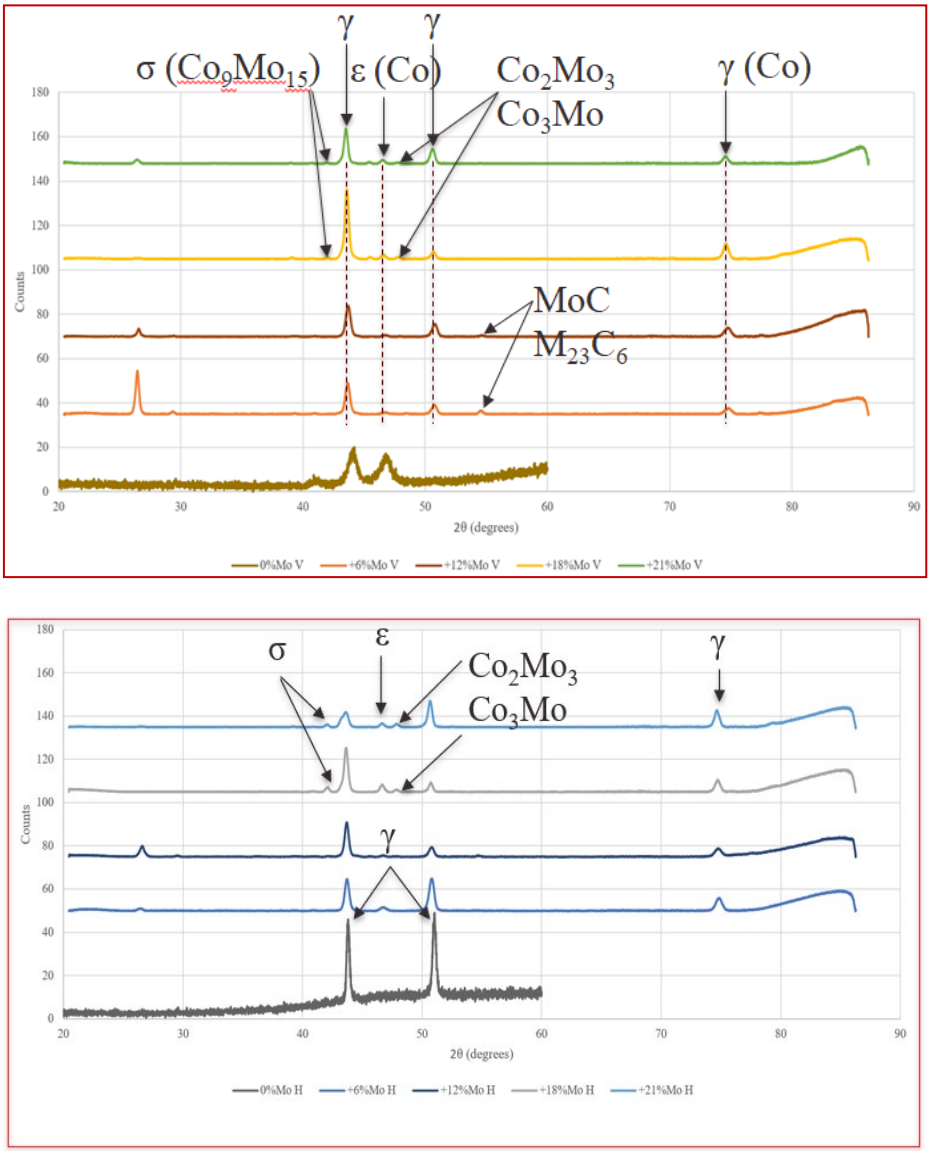

Figure 60: XRD measurements for 0%, +6%, +12%, +18%, and +21% Mo for both vertical (top) and horizontal (bottom) orientations.

5.2.2.2 Microprobe Maps of LENS Co-Cr-ΔMo

In the microprobe maps of the LENS Co-Cr-ΔMo samples, the +0%, +6%, and +18% Mo samples were all measured along the vertical direction. Darker colors and lower numbers indicate a deficiency of a particular element in the maps while brighter colors and higher numbers indicate larger composition percentages of a particular element. Figure 61, Figure 62, and Figure 63 presents the maps for the +0% Mo sample columnar, equiaxed cell, and mixed phases, respectively. In these images, bright white features occur at triple point junctions and wider cell boundaries. These regions are Mo and Cr rich. The %Mo within bright white features is similar to the expected %Mo reflected by theoretical amount of Mo. The cell interior is Co-rich similar to measurements made through EDS. The Mo gathers within large width regions. Cr and Si remain in cell boundaries with similar behavior to Mo. The mixed phase the was observed in +0% Mo has few Mo heavy regions. The observations shown in the following figures provide a side-by-side view for comparison of various elements in each of the different microstructural phase regions.

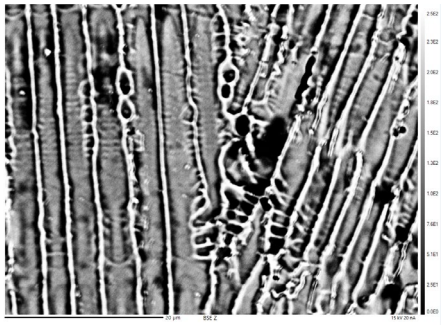

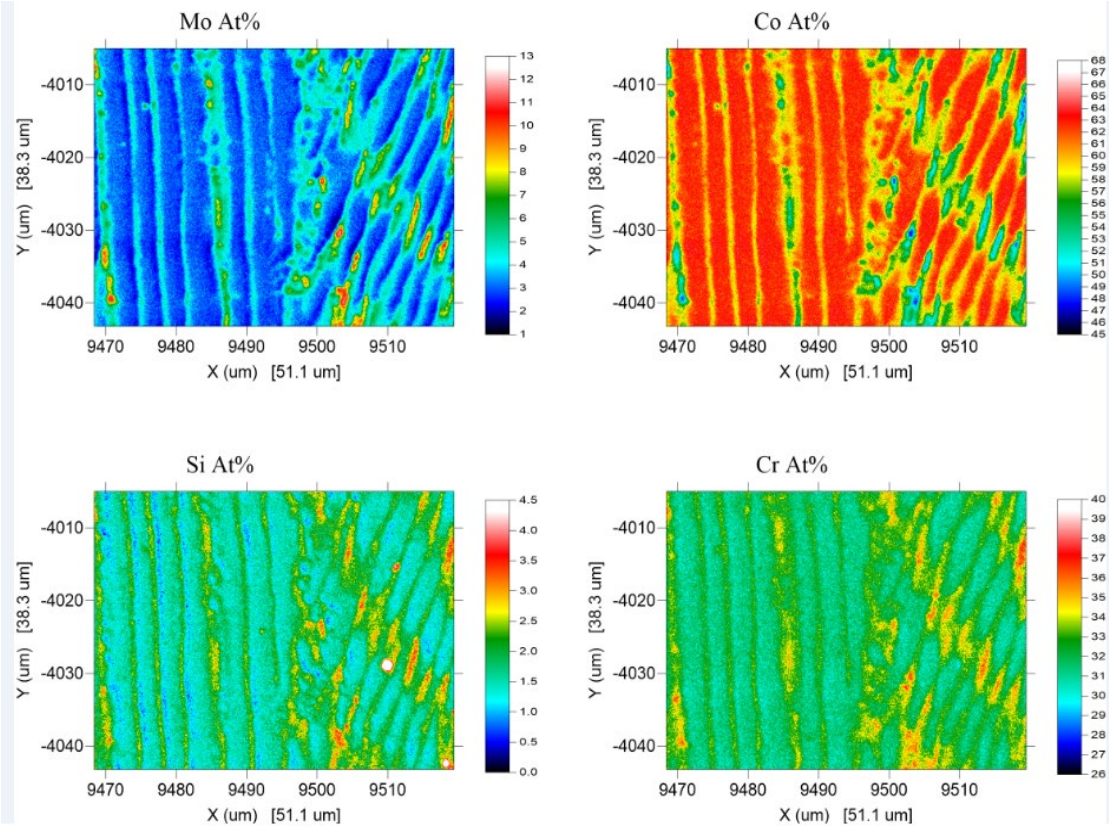

Figure 61: +0% Mo Microprobe Maps for Mo, Co, Si, and Cr in the Columnar Phase.

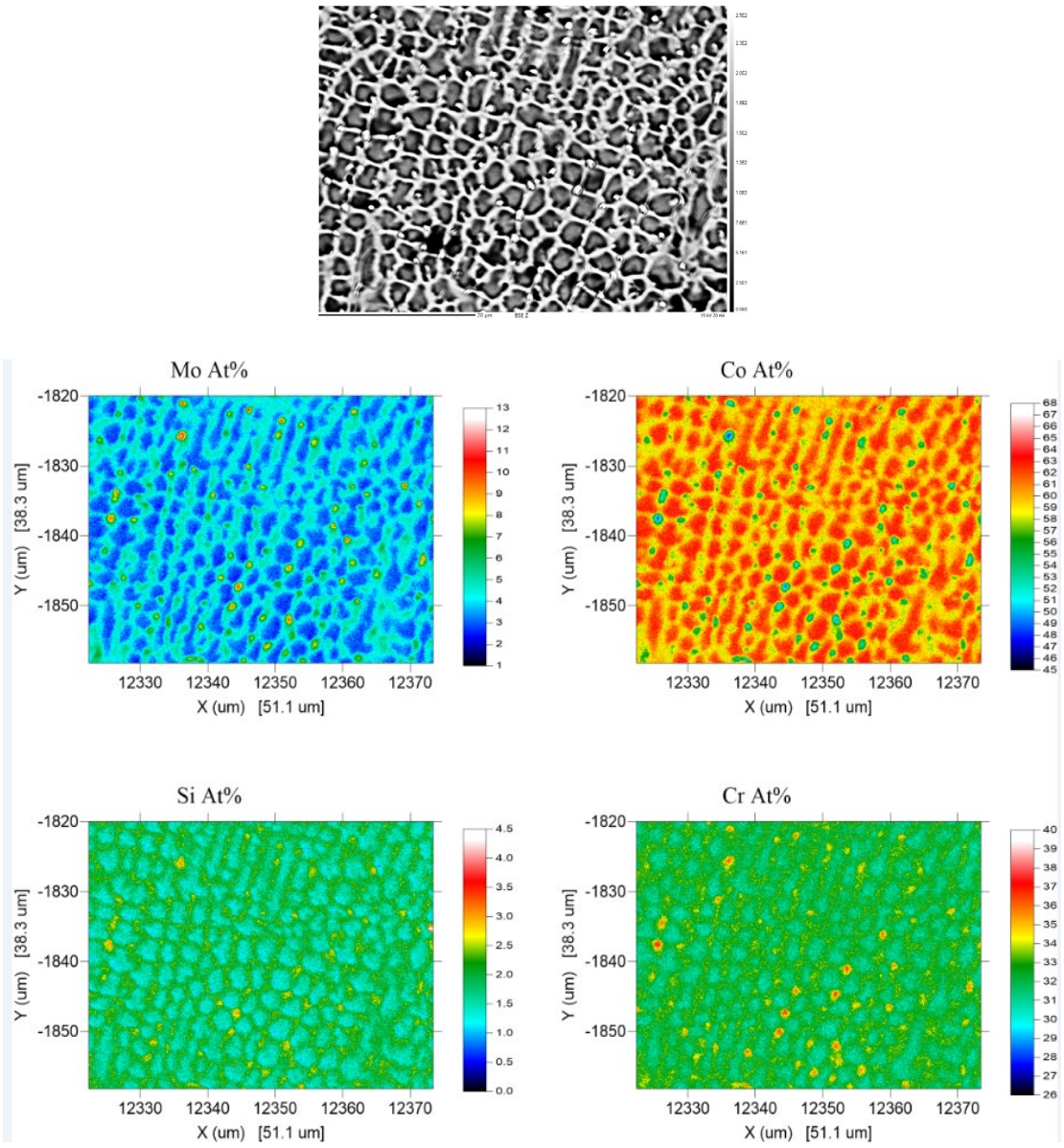

Figure 62: +0% Mo Microprobe Maps for Mo, Co, Si, and Cr in the Equiaxed Cell Phase.

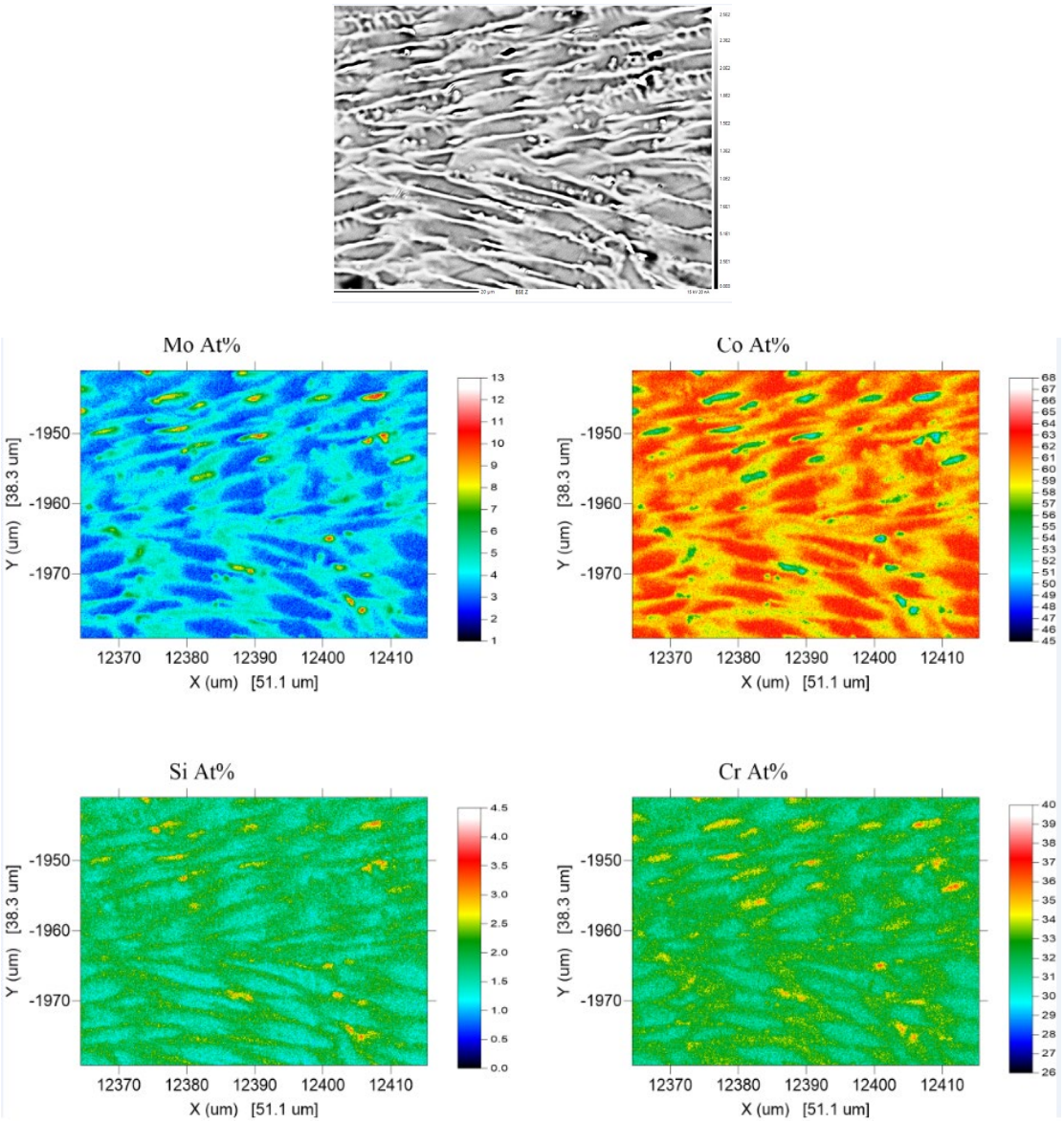

Figure 63: +0% Mo Microprobe Maps for Mo, Co, Si, and Cr in the Mixed Phase.

In the +6% Mo sample, a similar microstructure to +0% Mo is observed. Figure 64, Figure 65, and Figure 66 presents the maps of the +6% Mo sample for the columnar, equiaxed cell, and early tear drop phases, respectively. The Cr and Mo concentration shows an opposite accumulation behavior to Co. This is indicated by the elevated

topography. These maps show evidence of intercellular boundary diffusion for Mo and Cr. The dark blue Co deficient areas indicate the movement behavior of each component.

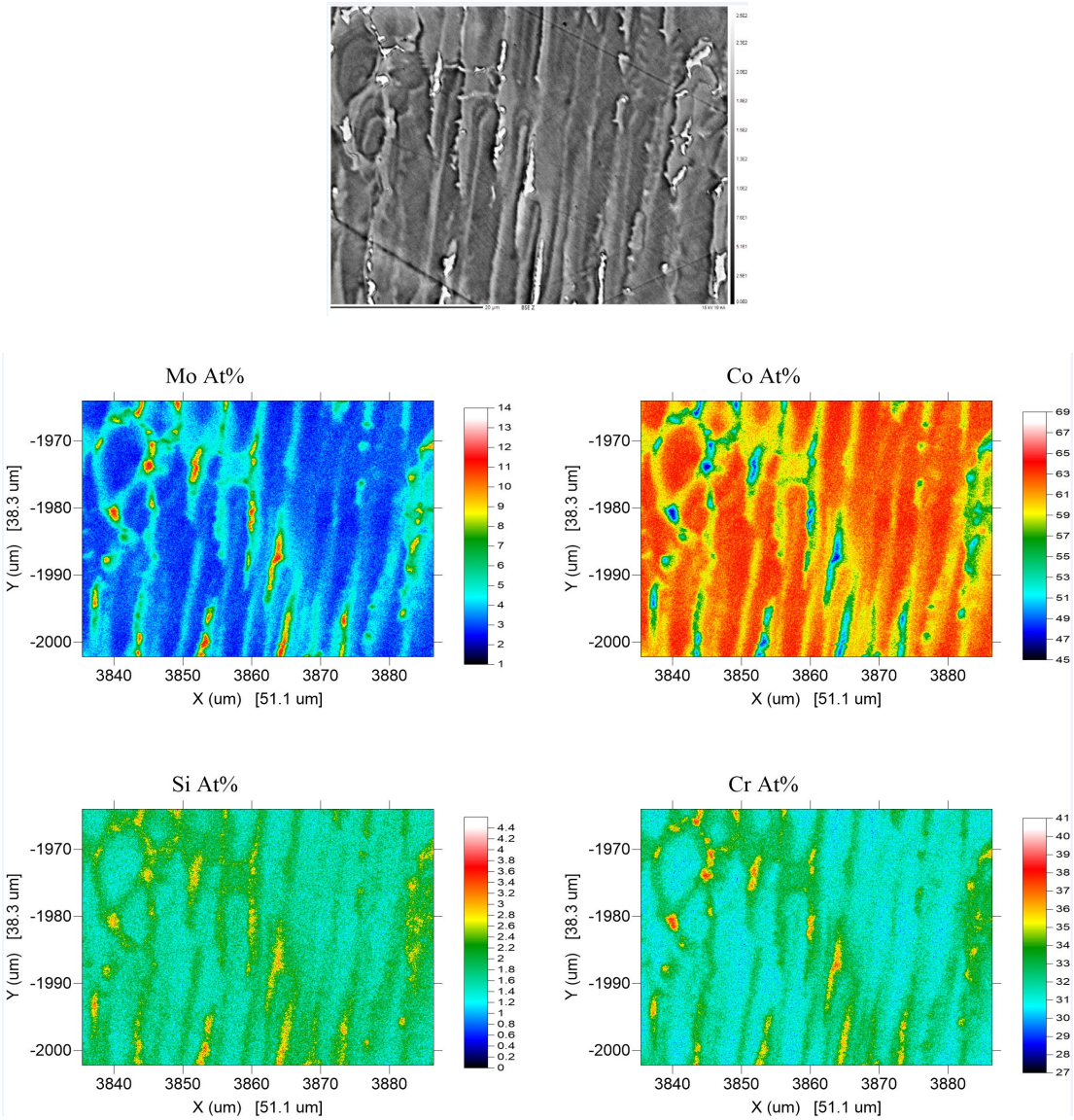

Figure 64: +6% Mo Microprobe Maps for Mo, Co, Si, and Cr in the Columnar Phase.

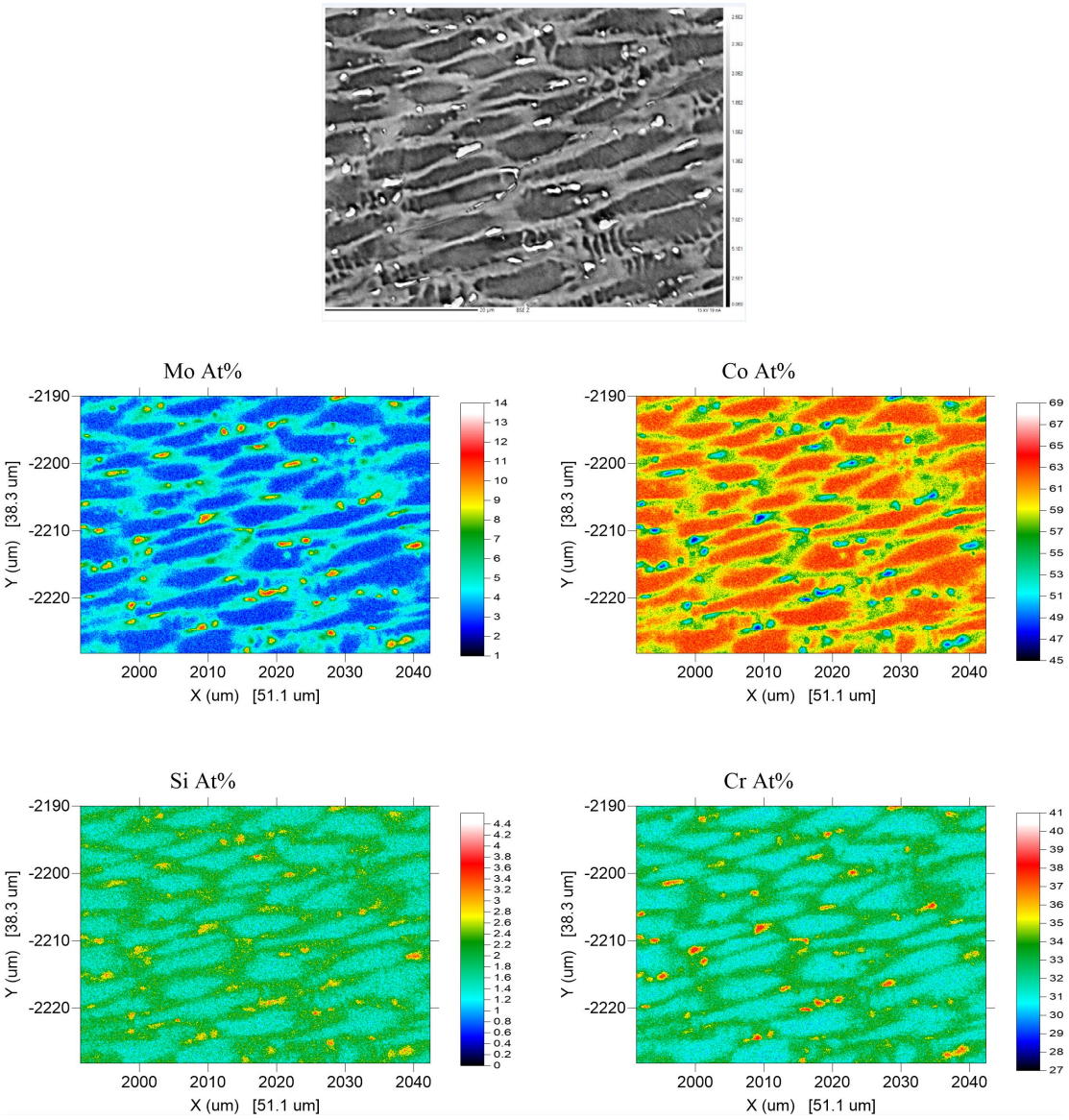

Figure 65: +6% Mo Microprobe Maps for Mo, Co, Si, and Cr in the Equiaxed Cell Phase.

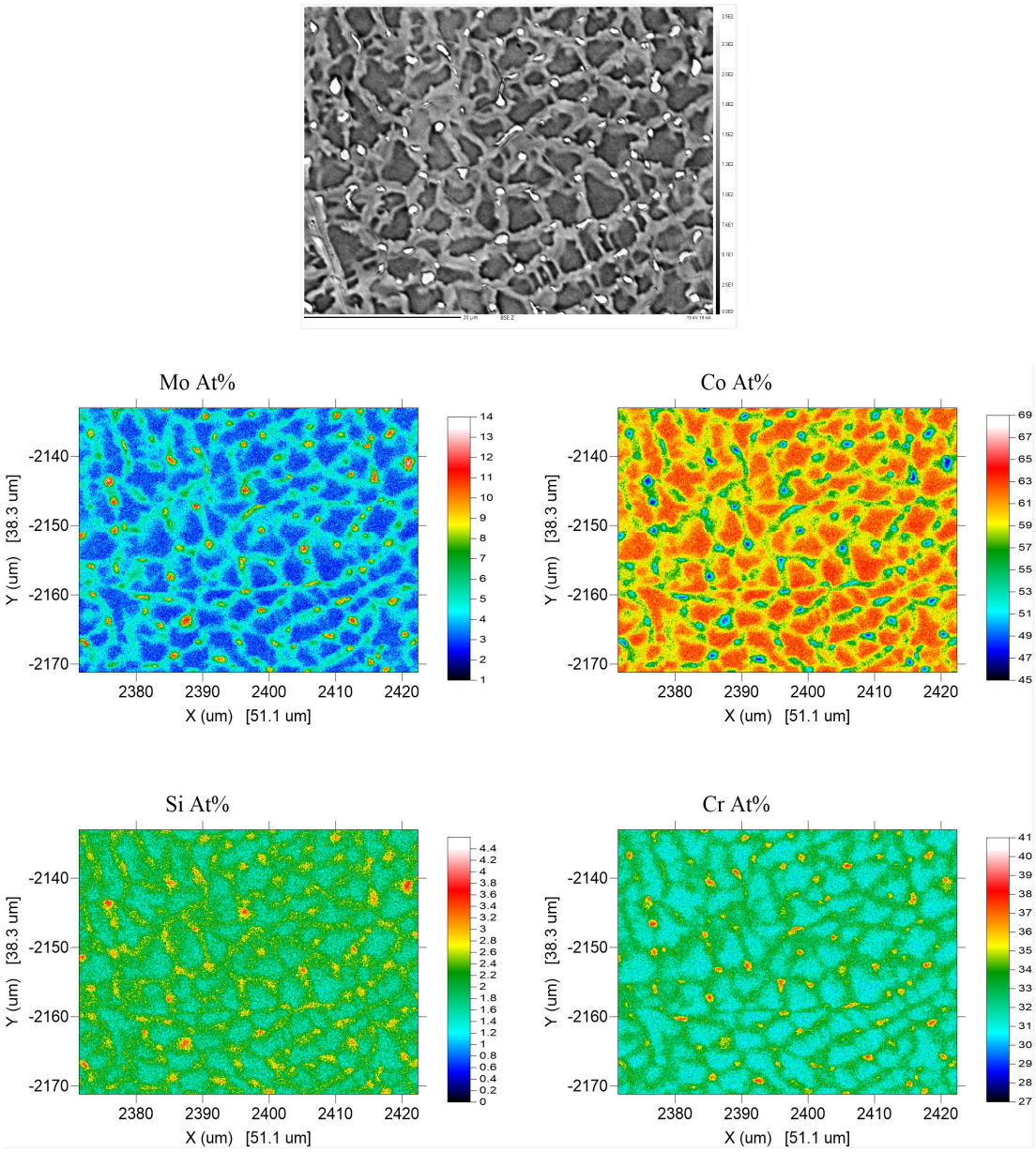

Figure 66: +6% Mo Microprobe Maps for Mo, Co, Si, and Cr in the Early Tear Drop Phase.

Figure 67, Figure 68, and Figure 69 presents the +18% microprobe maps for the columnar, equiaxed cell, and tear drop phases, respectively. In the +18%Mo measurement, the equiaxed cell phase has the lowest Cr while the columnar phase has

the highest Cr. Cr appears to gather more frequently in cell boundaries with large areas. Columnar and tear drop phases exhibit a large amount of Cr. Mo gathers heavily in interior of equiaxed and tear drop boundaries versus those of the columnar cell boundaries. Mo content shows a gradient from the linear boundary to the interior of the cell boundary.

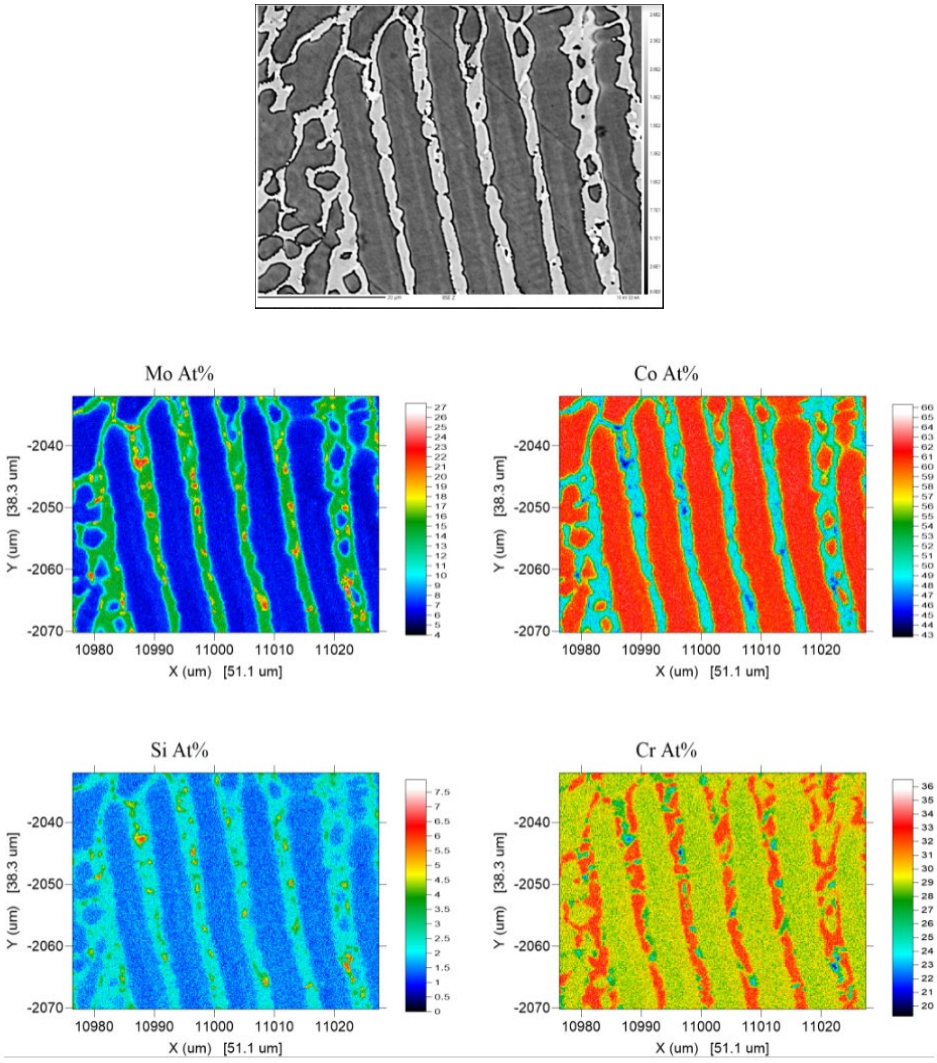

Figure 67: +18% Mo Microprobe Maps for Mo, Co, Si, and Cr in the Columnar Phase.

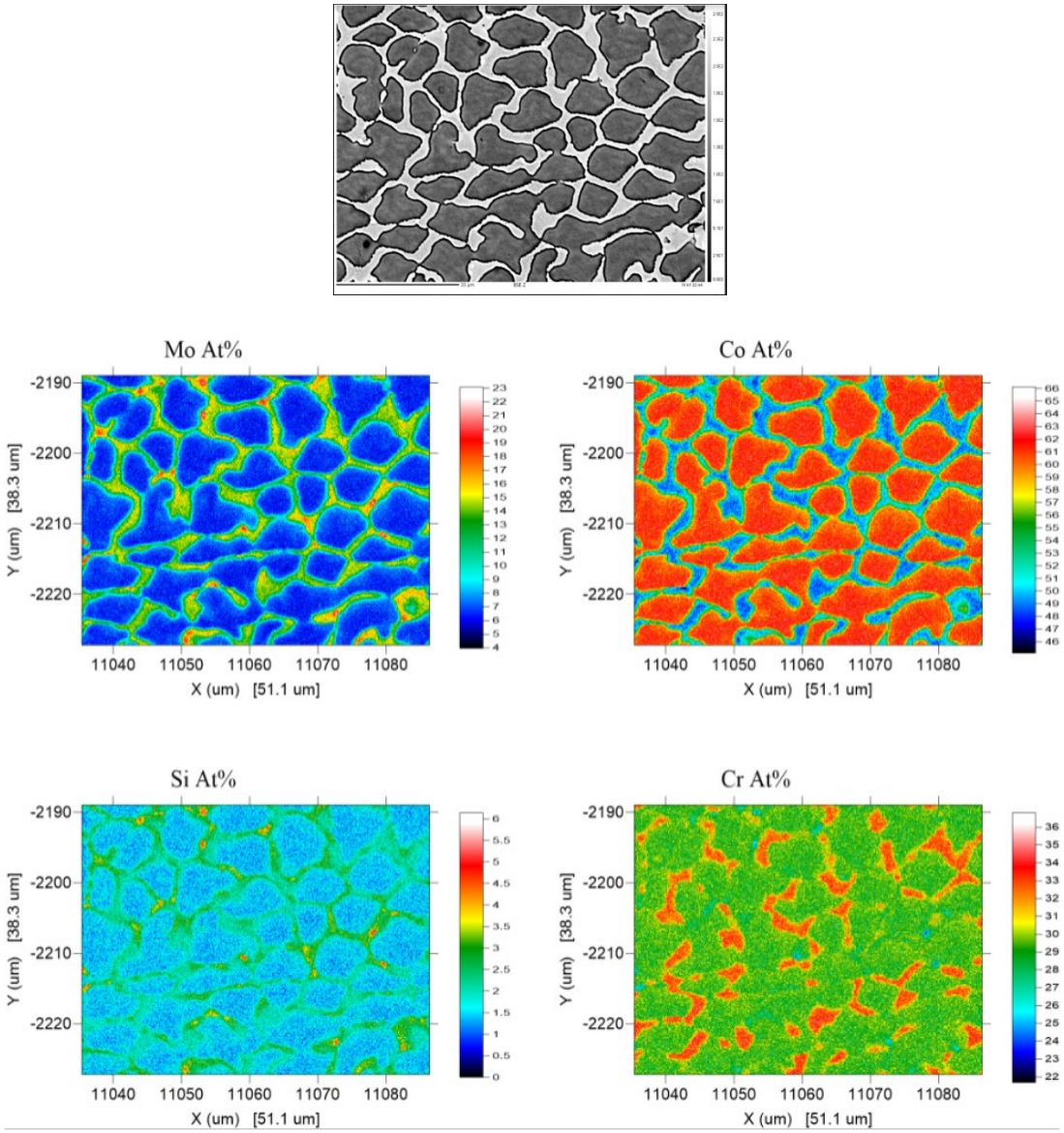

Figure 68: +18% Mo Microprobe Maps for Mo, Co, Si, and Cr in the Equiaxed Cell Phase.

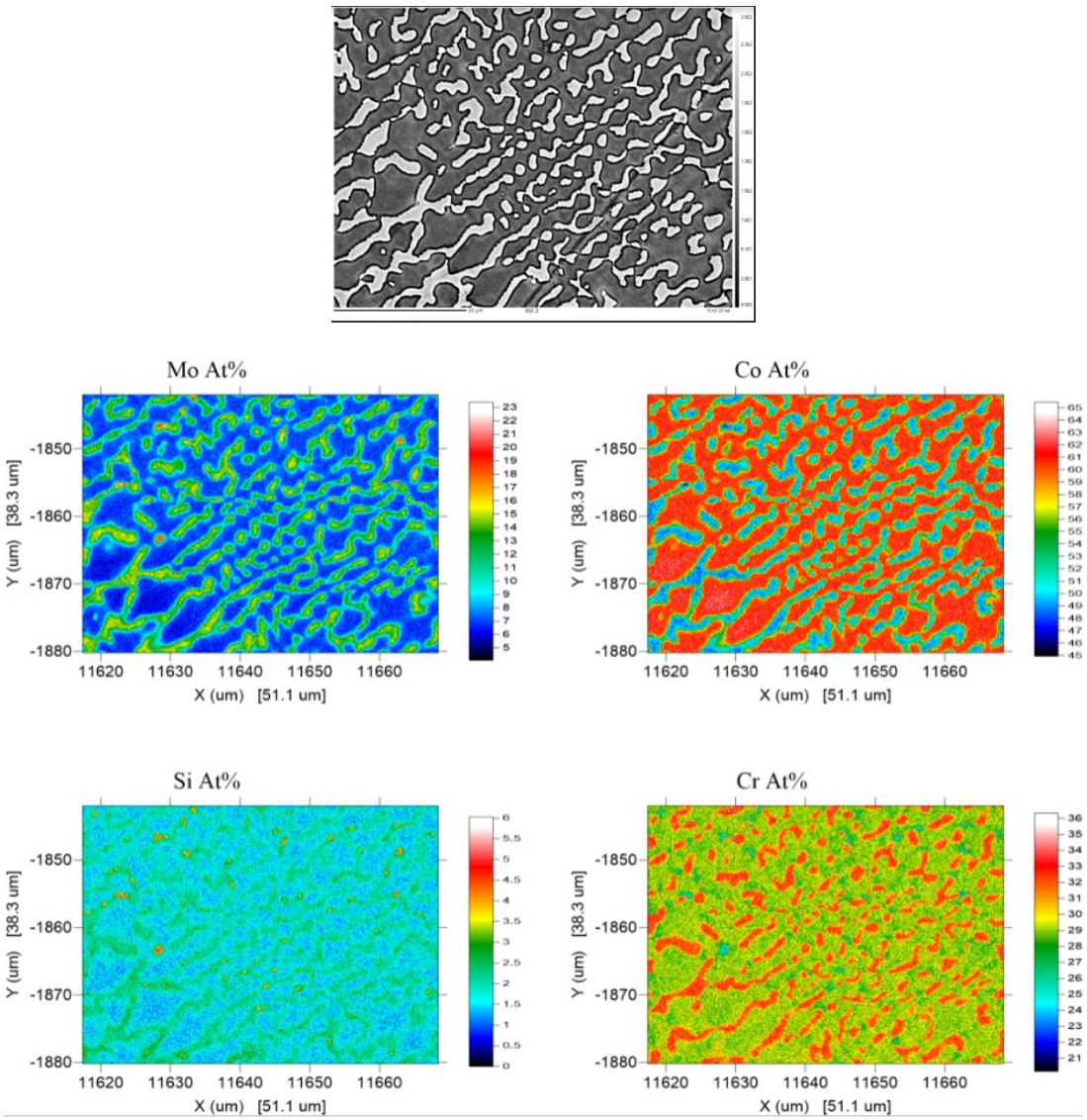

Figure 69: +18% Mo Microprobe Maps for Mo, Co, Si, and Cr in the Tear Drop Phase.

5.2.2.3 Major trends of behavior as Mo is added to Co-Cr-Mo

From the multi-level analysis of the Co-Cr-Mo microstructure as Mo is added, there are important points of behavior that occur within different ranges of additional Mo. When increasing %Mo within Co-Cr-Mo from +0% to +2%, adding Mo causes it to

act as a solid solution strengthener. The substitutional nature of Mo is showcased in Figure 70. Mo acts as a substitutional strengthener due to the comparable size of Mo particles. Mo typically takes the place of Cr in the lattice, pushing Cr out onto interdendritic regions of the microstructure.

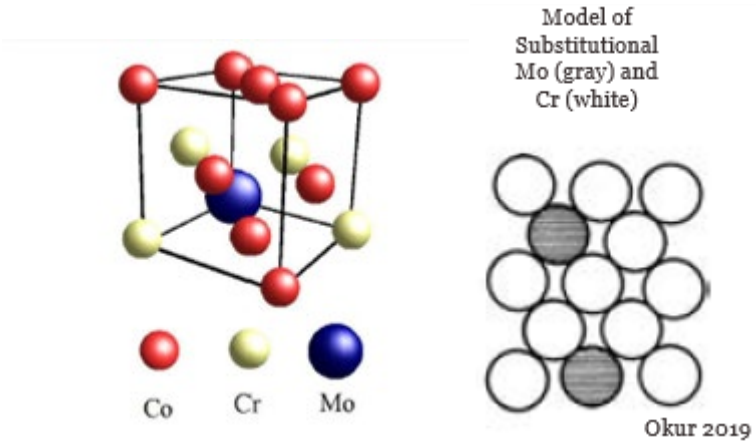

Figure 70: Schematic diagram of Mo within FCC Co-Cr-Mo (left) and model of substitutional Mo and Cr (right) [182].

From +3% to +12%, hard carbides are formed on the cell boundaries to create a carbide skeleton/network (the carbide amount wanes off at +12% as indicated in the EDS plots). Once the substitutional spots are saturated, Mo seeks out C (since the affinity to form metal carbides is generally very high). C is located mostly at the cell boundaries – hence MoC form at the cell boundaries. The Cr pushed out from the lattice, and additional %Mo form $M_{23}C_6$ ("M" => Metal [Mo or Cr]) at cell boundaries as shown in Figure 71.

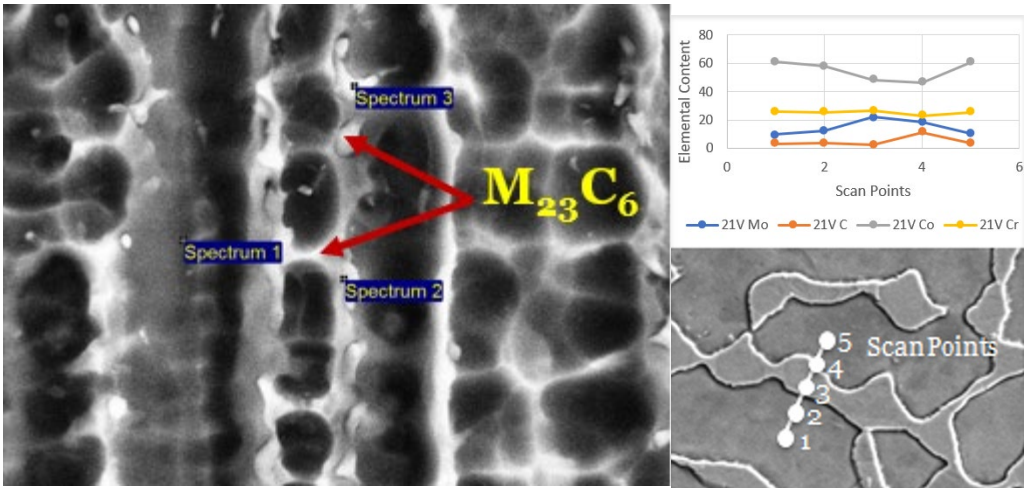

Figure 71: $M_{23}C_6$ carbide within Co-Cr-Mo (left) and EDS line scan for +21% Mo Vertical Plane

From +3% to +21%, hard intermetallic phases are formed in increasing amounts since additional %Mo cannot be accommodated as carbides or substitutional elements at cell boundaries. Hard intermetallics (Co_2Mo_3, Co_3Mo) and the σ phase grow from the cell boundaries to the interior of the cell.

5.2.3 Summary of Results and Deductions for Research Question 2

The following results were determined during the course of the work performed during Research Question 2:

- Mo and C gather at cell boundaries but not within cell interiors
    - Boundary width increases with Mo content
- Co shows opposite accumulation behavior to Mo (less on the boundaries)
- Generally, Cr is slightly higher in boundaries than in interior.
    - More Cr in teardrop and columnar interior (Microprobe maps)

- XRD results indicated the presence of two phases (γ-FCC and ε-HCP) carbides, and intermetallics
- The σ phase and intermetallics are more prominent in higher %Mo samples along with metal carbides and allotropes of Co.

From these results, various conclusions can be derived. The SEM/EDS results show that increasing %Mo into the molten pool causes a diffusion. “Triple point” junctions become a concentration point for Mo. The results indicate that the cell boundaries are enriched with Mo.

The increase of %Mo within Co-Cr-Mo provided the following insights:

- [+0% to +2%] Mo acts as a solid solution strengthener
    - Mo particle size causes the substitutional strengthening
    - Mo takes place of Cr in lattice by pushing Cr into interdendritic regions of the microstructure
- [+3% to +12%] Hard carbides form on the cell boundaries
    - Substitutional spots become saturated where Mo seeks out C
    - C is located primarily at the cell boundaries
    - Cr is pushed out and addition %Mo forms $M_{23}C_6$ (M = Mo, Cr) at cell boundaries
- [+3% to +21%] Hard intermetallic phases are formed in increasing amounts due to %Mo as carbides or substitutionals at cell boundaries
    - Hard intermetallics: Co_2Mo_3, Co_3Mo
    - Hard sigma phase intermetallics: Co_9Mo_{15}

- Intermetallic phases grow from cell boundaries to interior of cell

5.3 Effects on mechanical properties due to varying Mo content (RQ 3)

5.3.1 Task 3-A: Measure mechanical properties of bulk Co-Cr-Mo and compositional gradient samples

5.3.1.1 Microhardness Measurements

Microhardness values from literature are comparable are comparable to those Vickers hardness values reported here. A sample indentation and the indentation pattern are shown in Figure 72. Hardness values are plotted against power and RPM in Figure 73 to determine the correlation between process parameters and Vickers hardness values. 3 RPM samples have the lowest spread regardless of power (~10 HV). 5 and 7 RPM samples show much more variation (~370-410). 350W samples made at 3 RPM and 5 RPM had the least variation in values between measured regions with 5 RPM possessing a variance of ~ 5 HV. When compared to other power levels, the 400W sample values are the most consistent with the lowest spread. This could be due to consistent of melting of the powder which would mitigate some lack of fusion defects. Furthermore, the 400 W samples on average exhibit much lower hardness values than the other two power levels. The 350W 7 RPM and 300W 5 RPM samples had the largest spread from HV 370-410.

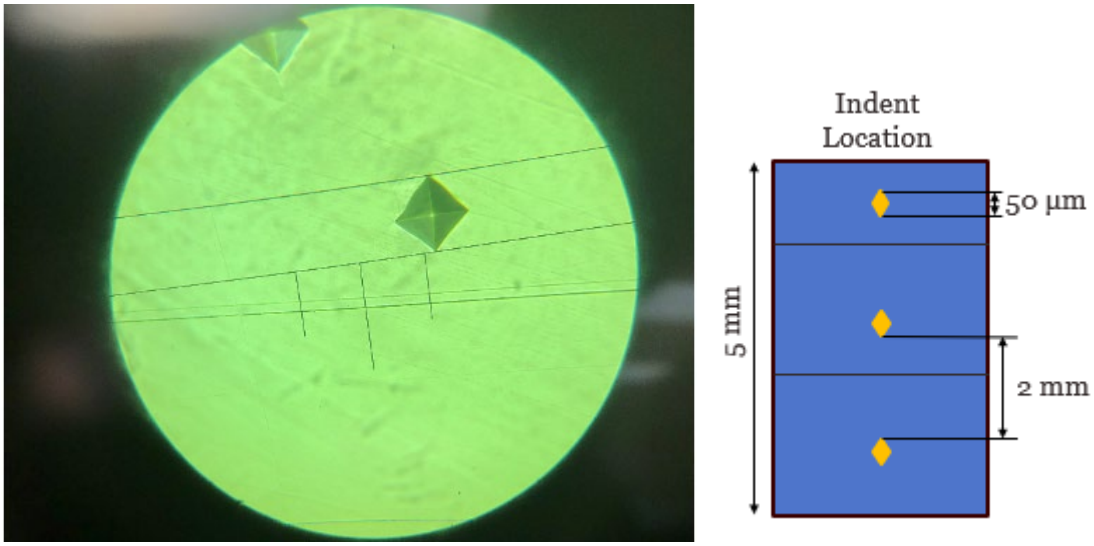

Figure 72: Vickers hardness indentation (left) and location indents on sample (right).

Hardness values from literature have shown comparable values for Vickers hardness. As-cast samples were shown to possess Vickers hardness values of 310 +/- 6 and 313 +/- 6 after Hot Isostatic Pressing and heat treatment [169]. For HV(20kg), SLM Co-Cr-Mo measured at 334 HV [183]. Zhang performed Vickers hardness testing on SLM and ASTM F75 samples and reported 387.3 and 297.5 HV, respectively. These results are similar to those reported by Stucker et al. who show that LENS Co-Cr-Mo deposits are harder than wrought for smaller depositions due to the refinement of grains and increasing number of grain boundaries [164]. The grain boundaries impede the motion of dislocations under stress thus improving hardness. Sahin performed Vickers microhardness tests with increasing load and showed similar hardness values at HV(0.5) to the results presented here [180].

The hardness values observed here are the result of the process parameters influencing the formation of the microstructure. The size of Co-Cr-Mo grains affects the recorded measurements through grain boundary strengthening and the presence of carbides. In grain boundary strengthening also known as the Hall-Petch Effect, the grain boundaries operate as points that stop the spread of dislocations [184]. The difference in lattice orientation between neighboring grains requires a higher energy to change the direction of a dislocation to move to a local grain. Dislocations create repulsive stress fields where each additional dislocation drives down the energy barrier to diffuse across the grain boundary. A pile up of dislocations causes the diffusion of dislocations leading to further plastic deformation of the material. When grain size is decreased, the dislocation pile-up decreases which raises the applied stress needed to move a dislocation across a grain boundary. The Hall-Petch equation refers to the inverse correlation between grain size and yield strength. Thus, with more grain boundaries, dislocation movement is resisted which makes the material stronger.

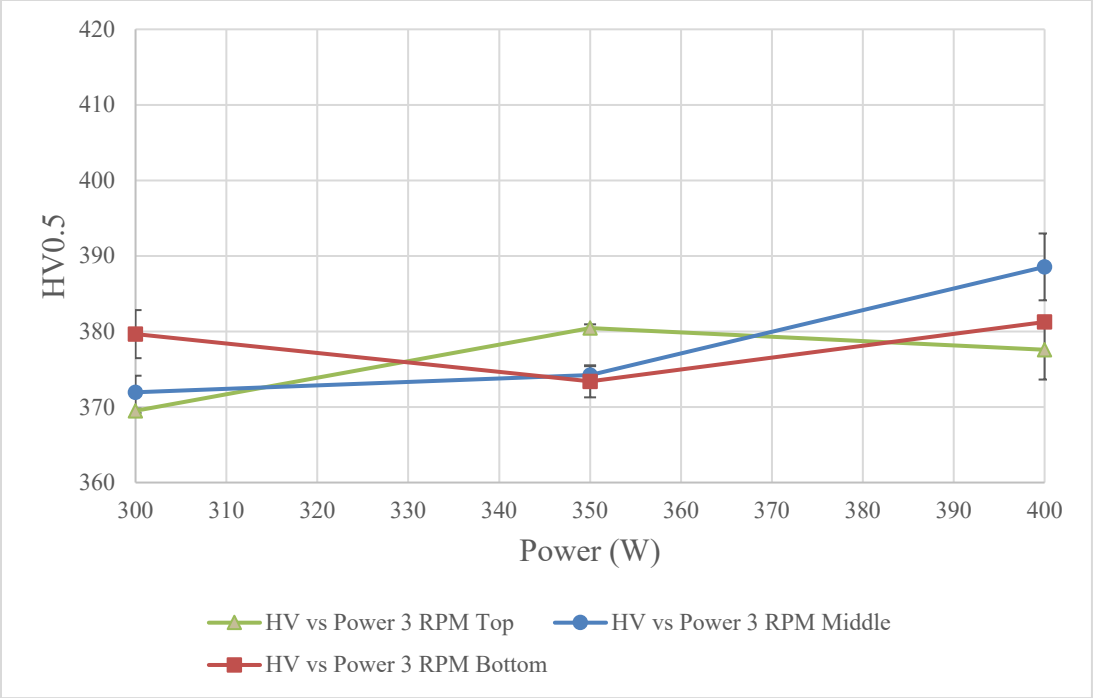
420
410
400
390
380
370
360
HV0.5
300
310
320
330
340
350
360
370
380
390
400
Power (W)
HV vs Power 3 RPM Top
HV vs Power 3 RPM Middle
HV vs Power 3 RPM Bottom

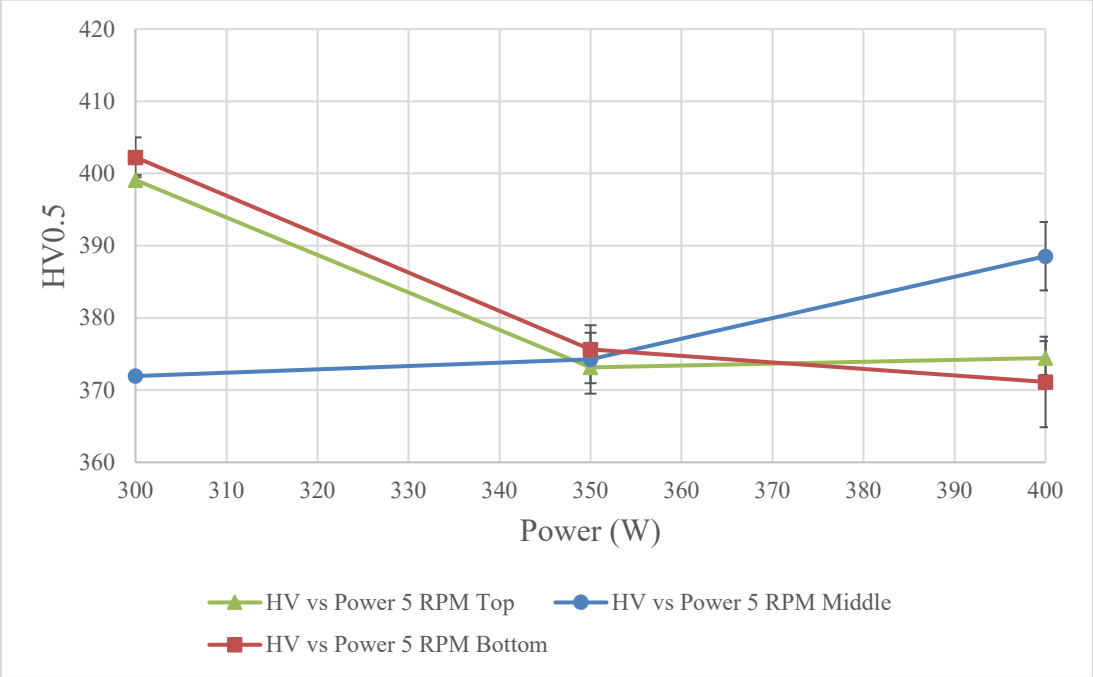
420
410
400
390
380
370
360
HV0.5
300
310
320
330
340
350
360
370
380
390
400
Power (W)
HV vs Power 5 RPM Top
HV vs Power 5 RPM Middle
HV vs Power 5 RPM Bottom

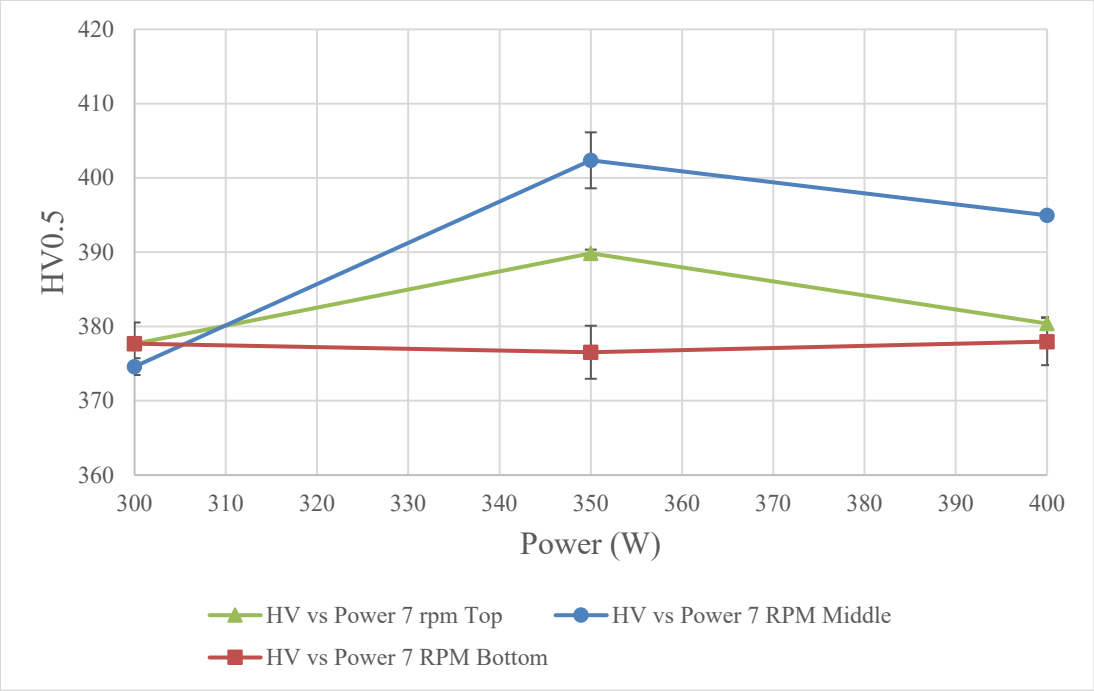

Figure 73: Vickers hardness values of Co-Cr-Mo.

Because of smaller grains, there are more grain boundaries in the microstructure. For the Co-Cr-Mo prints, carbides grow upon the cell boundaries within grains. The resolution of the indenter contributes to the observed measurements. Indents that fall primarily on small, equiaxed cells most likely produced the higher hardness values because of the Hall-Petch Effect combined with the response of the carbides.

For the second DOE, mechanical testing was performed at micro- and nano-scales to determine the material responses. Vickers microindentation measurements shown in Figure 74 indicate that the hardness of samples rises consistently as more %Mo was added. Each sample was indented three times to ensure consistency of results. The average diagonal length of each indentation is around 45.27 µm. The range of diagonal

lengths for all of the Vickers indents is 40.83-51.99 µm. While the average value of Vickers hardness for +6% to +12% Mo is similar to those readings for the original Co-Cr-Mo only study, after +12% Mo, the value for hardness increases significantly until +18% Mo. From +18% Mo, the rate of growth decreases up to +21% Mo. The max observed hardness value of 5.23 GPa occurs at +21% Mo while the min observed hardness value of 3.59 GPa occurs at +6% Mo. The average standard deviation is 0.11 across all the samples.

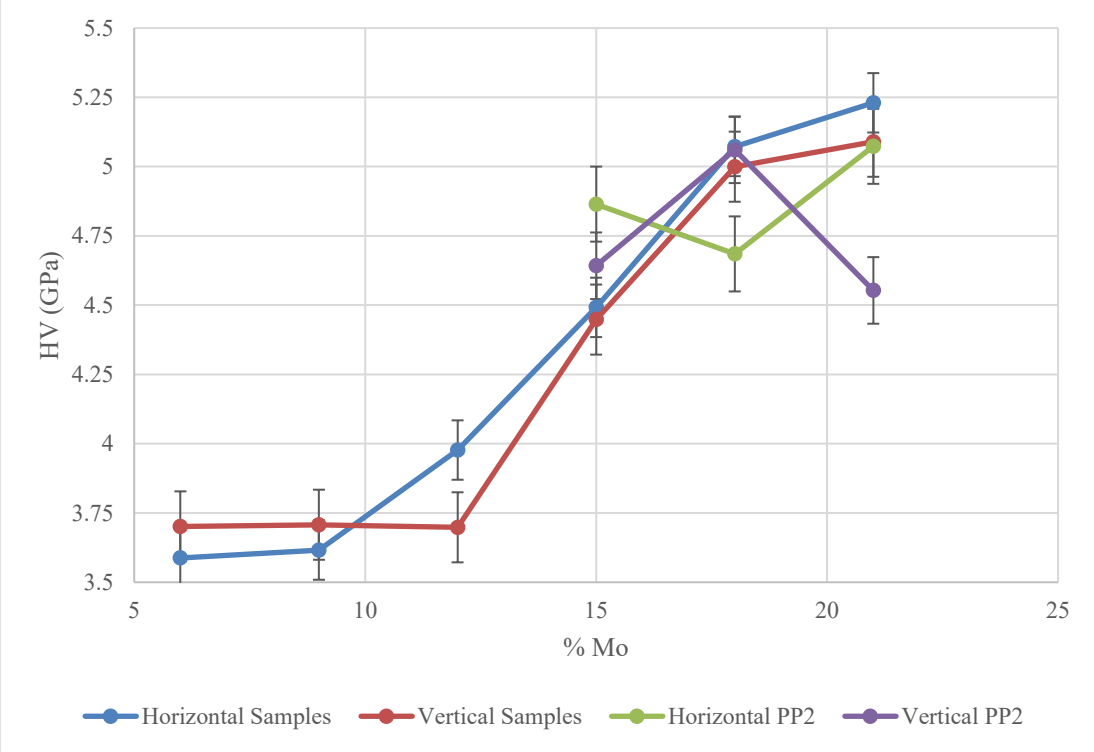

Figure 74: Vickers Hardness Measurements for Co-Cr-Mo as a function of %Mo increase.

5.3.1.2 Nano-scale Mechanical Testing

Nanoindentation and nanoscratch tests provide surface analysis of hardness and abrasion resistance of LENS Co-Cr-Mo. Nanoindentation offers a higher resolution of measurements to determine the mechanical properties of individual microstructural features within each grain. Nanoindentation data elements are shown in Figure 75. The 20 μm distance between indents is much larger than the typical dimensions of the Co-Cr-Mo cells observed in the microstructure section. This ensures that neighboring cells can be evaluated individually without fear of repeat measurements on a single cell. The outlier values are most likely due to indents on carbides protruding from the microstructure. Carbide nanohardness is shown to be much harder than the cell interior. These features are larger than the indenter diameter and could feasibly be measured individually.

Figure 76 presents the contact depth versus hardness plot of the three power levels against their respective RPM. The plot indicates a downward trend of hardness values as contact depth increases. From this data, 400W has the tightest spread of values while 350W displays the largest spread of values. Ettienne-Modeste et al report values of 8.82 +/- 0.55 GPa and elastic modulus of 214 +/- 5.31 GPa for wrought Co-Cr-Mo samples [185].

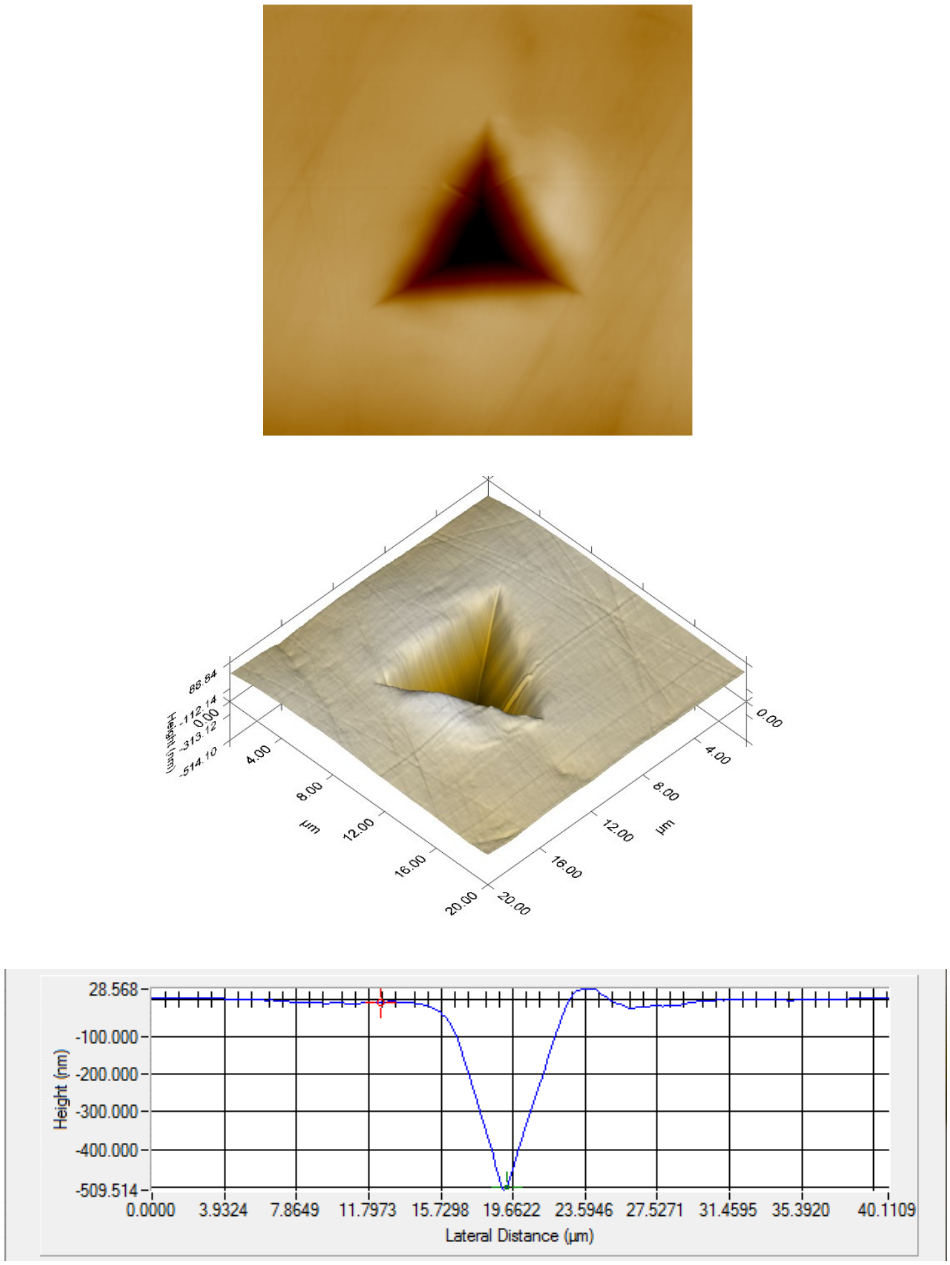

Figure 75: Nanoindentation measurements in 2D (top) and 3D (middle). Nanoindentation depth is shown (bottom).

Liao reports much higher values with a max load of 4 mN. Hardness of the matrix of cast Co-Cr-Mo was 6.4 +/- 0.3 GPa while the hard phase mixture was 15.7 +/- 0.9 GPa [118]. Indentation size effects can generate a difference between hardness

values taken at different scales specifically in the case of carbide size with respect to the indentation size. Ahmed et al. used a 50 mN load to determine the difference in hardness between the matrix phase of HIPed Co-Cr-Mo (7.9-8.8 GPa) against cast (5.9-6.9 GPa) [186]. The higher hardness of the HIPed alloy is ascribed to the high Mo content in the metal matrix.

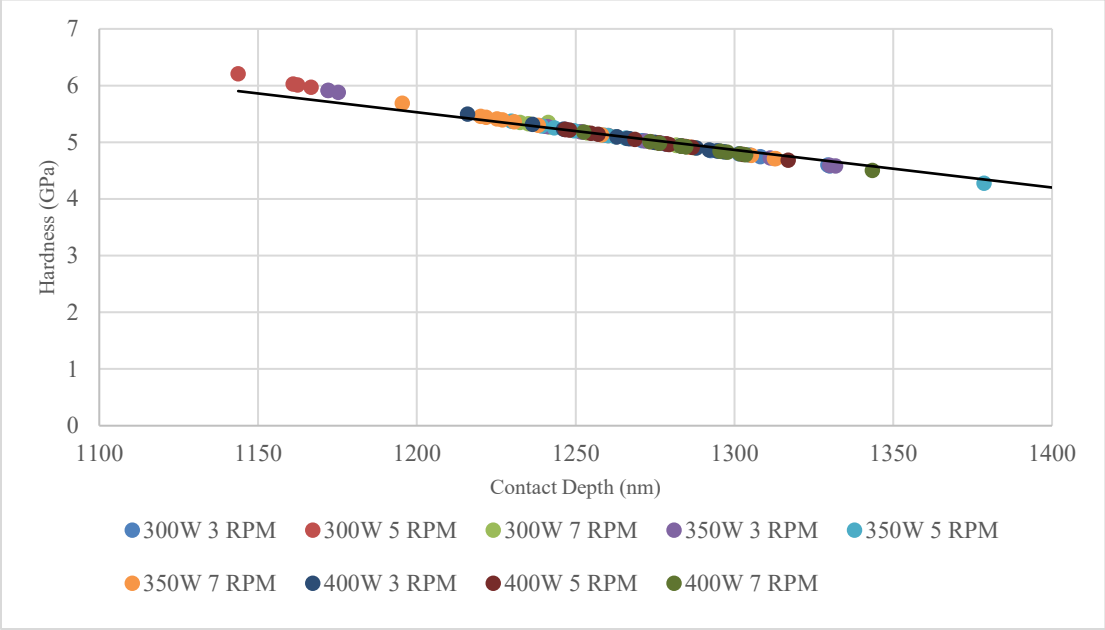

Figure 76: Contact Depth vs Hardness plots of LENS Co-Cr-Mo samples.

When measuring elastic modulus versus power, as shown in Figure 77, 400W once again has the tightest spread of values for elastic modulus. This may be due to complete melting of powder regardless of feed rate. 350W has a slightly larger range of elastic modulus values while 300W samples showed the largest variation in results. The average elastic moduli of the 350W samples are the highest. The second plot, which shows elastic modulus versus RPM, indicates that 5 RPM possesses the least variability

while 3 RPM and 7 RPM display similar but larger variability. 5 RPM further displays the highest elastic modulus value on average. Thus, the results indicate that the highest performing combination of this process parameter set would be 350W and 5 RPM as these show the most consistent hardness and elastic modulus values.

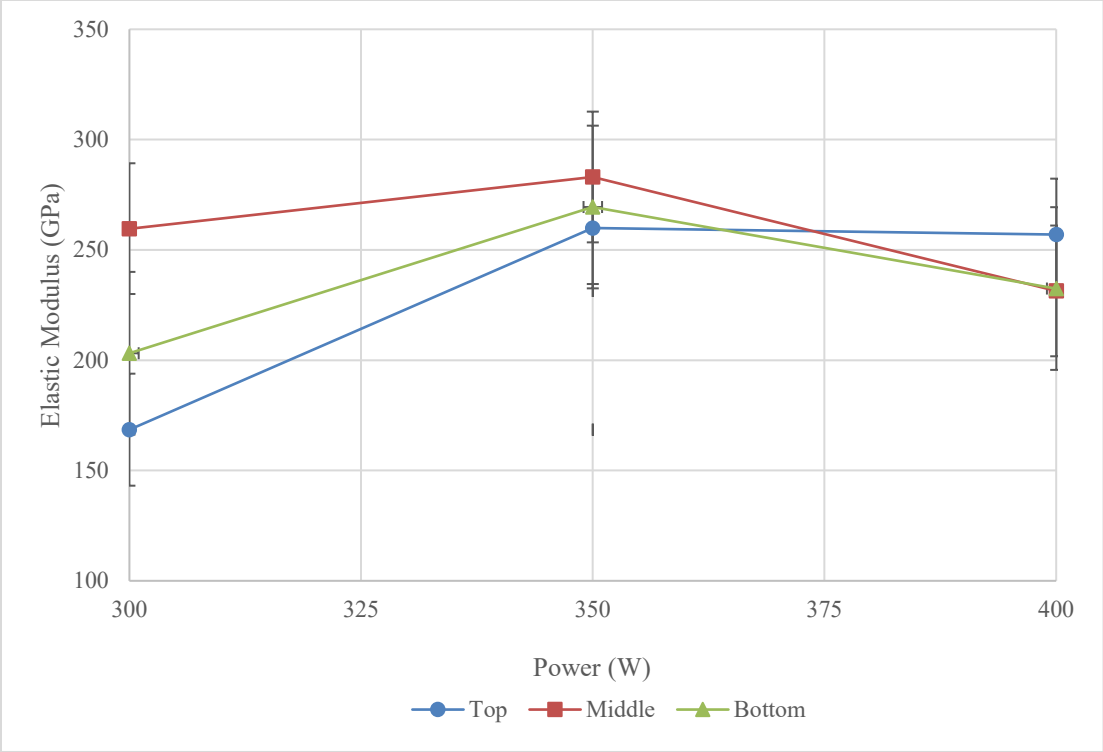

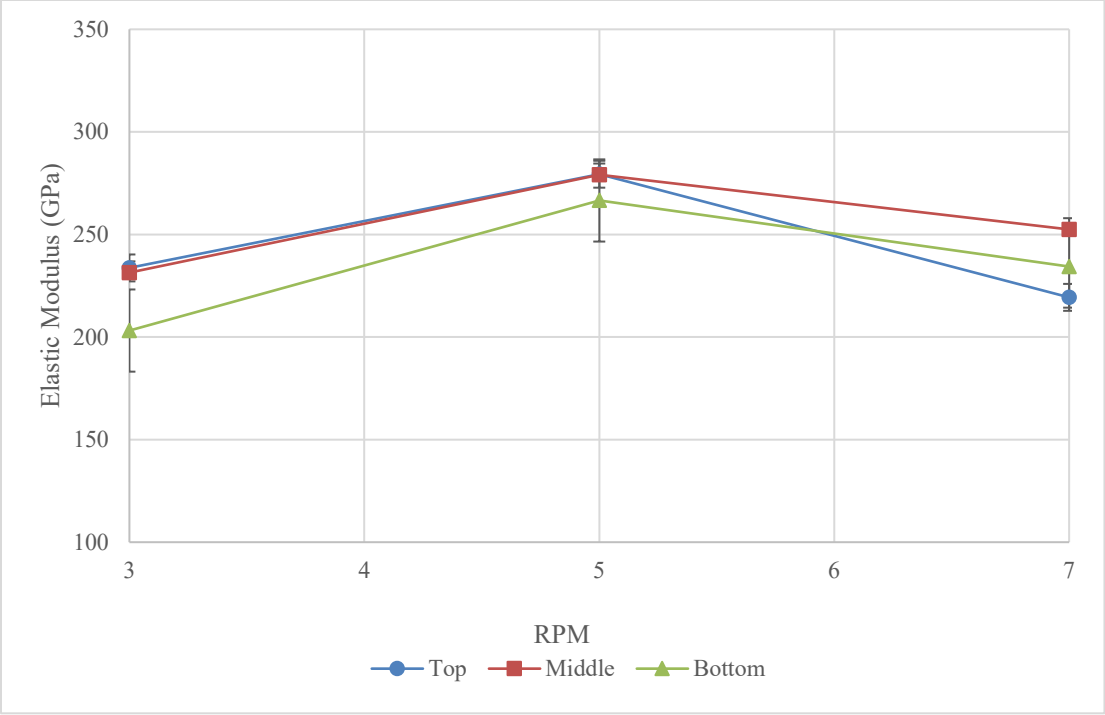

Figure 77: Elastic Modulus vs Power (top) and vs RPM (bottom) plots of LENS Co-Cr-Mo samples.

Nanoscratch tests can indicate nanoscale disparities between the material matrix and carbide formations [186]. For this work, nanoscale scratches were made along the vertical plane (relative to the print direction" in the "top" to "middle" directions, meaning that the frictional coefficient was measured across 1-layer thickness (~250 µm thick). Scratch patterns, as shown in Figure 78, were straight under the process conditions used. The 250 µm length provided enough traverse distance, so that multiple grains, cells, cell boundaries and carbides could be covered; this could be the reason for the difference in the frictional coefficient over distance. The nanoscratch results in Figure 79 show the smallest variability in 400W samples while those made at 350W show the largest disparity. 350W has the largest average friction while 400W exhibits

the smallest. At different powder feed rates, 3 RPM displays the least variability while 7 RPM displays the largest spread of values.

Figure 78: Optical image of nanoscratch on surface of Co-Cr-Mo sample.

These results likely stem from the same properties that govern the hardness response. 400W samples consistently perform lower than the other two types of samples due to the exposure to higher power reducing the structural integrity and thus lowering abrasion resistance. The only exception is the 400W 5 RPM sample which performed better than the other two 5 RPM samples. Based on the XRD results, a considerable amount of HCP (ε phase) exists in the bulk. HCP structures have one slip plane thus reducing dislocation movement and large rates of work hardening. The FCC structure exhibits more slip systems for cross slip of dislocations to occur which means a low

work hardening rate. Ahmed et al. showed that carbides in cast alloy does not show considerable wear, deformation, or fracture. This indicates that the nanoscratch response is governed by the cell interior [187]. A more homogeneous distribution of carbides offers better support to the metal matrix while experiencing abrasion.

The 3D plot in Figure 80 shows the VED space where the power and powder feed rate are measured against the microindentation hardness values. From the plot, 350W with 4-7 RPM provides optimal prints for higher microhardness. Power from 300-350W yields higher hardness values >390 HV. Powers greater than 350 yield lower hardness values, particularly those of lower RPM.

There are various methods to reduce macroscopic issues. Lower power but longer dwell time (i.e. lower scan speed) would avoid some the macro defects such as discoloration but also increase the process time. Lower powder feed rate and lower power can also improve the microhardness values as well.

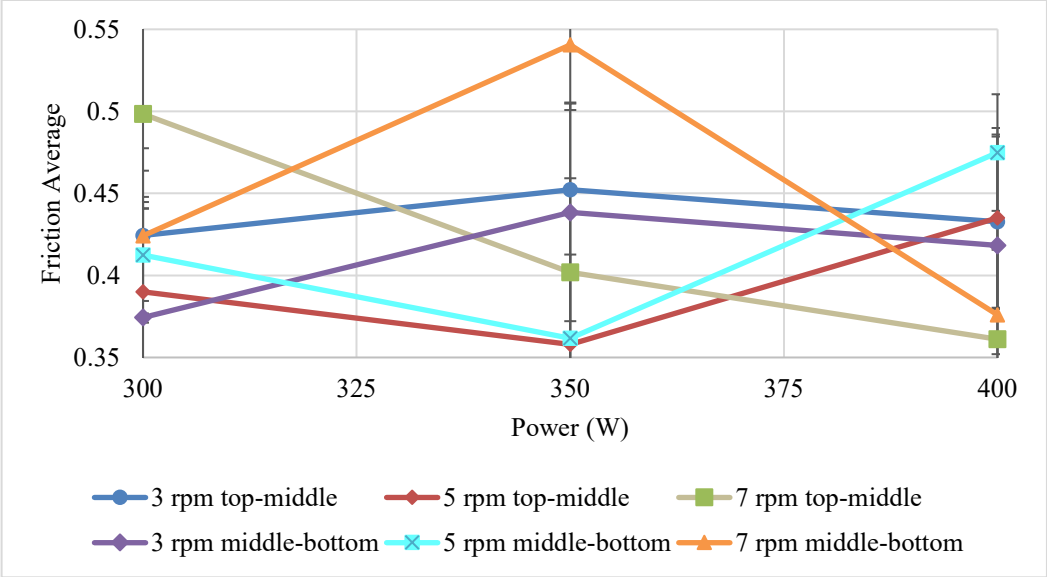

Figure 79: Friction average vs power of LENS Co-Cr-Mo.

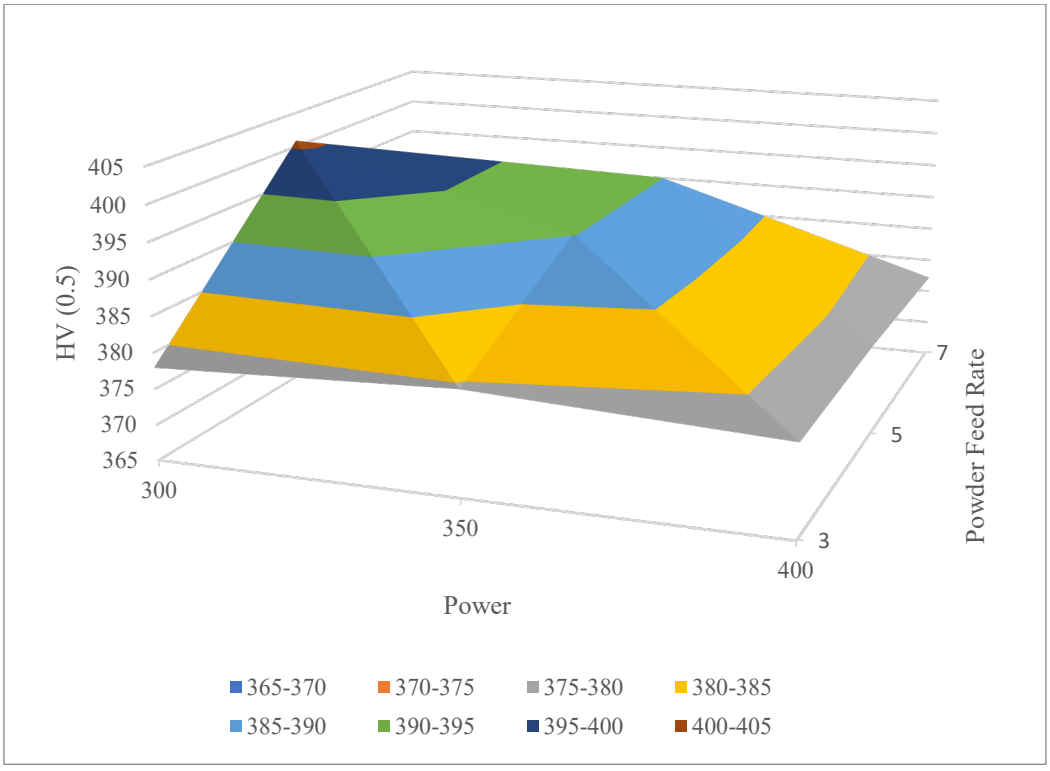

Figure 80: 3D representation of the VED design space of DOE 1.

Next, the samples were exhibited to scratch tests using a conispherical tip. Samples were scratched with 250 μN force for 250 μm. The force of scratches gradually increased with scratch length. Instead of delivering scratches to the three regions individually, the test was set up to determine differences in scratch behavior between regions. Thus, two scratches were made on each sample with each displacement being placed across the border of different regions (i.e. a scratch occurring across the top-middle boundary).

The next evolution of our study pertains to creating compositional gradients within Co-Cr-Mo. As a standalone structure built by LENS, Co-Cr-Mo possesses excellent material properties on par with traditional manufacturing methods. To understand the influence of placing additional elements into a Co-Cr-Mo structure, similar additive studies were analyzed to gather adequate strategy. Sahasrabudhe utilized LENS to compositionally grade CaP into Co-Cr-Mo for improvement in hardness and other mechanical properties [177]. With the affordances that LENS offers, an exploratory study into augmenting the alloy composition was conducted. As mentioned previously, these types of functionally graded materials have taken inspiration from biological constructs [40]. The work performed here takes similar inspiration by compositionally grading the percentage of Mo to varying degrees of thin and bulk constructs to study the final microstructure and associated material properties. As Mo possesses a higher melting temperature and laser reflectivity as a standalone element, it was conjectured that a proper ratio between the two powders mixed before printing would offer an optimal structure with the highest structural integrity.

Figure 81 presents data from testing for nanoindentation. Nanoindentation results were like those exhibited in the microindentation results. As Mo is increased, the observed hardness and elastic modulus increase. On average, these samples have much higher hardness than the previous study (with no additional Mo added). While the previous study showed an average hardness value of ~ 5.2 GPa, these samples on average yield values of ~ 7.7 GPa. For PP2, the average hardness value is much higher at ~ 8.5 GPa than the comparable samples. Samples with greater than 15% additional Mo show improved values for PP2 for hardness and elastic modulus over those of PP1. Klarstrom et al. report that alloying elements like Fe, Mn, and C increase stacking fault energy and the FCC structure. Cr, Mo, W, and Si stabilize the HCP structure and decrease stacking fault energy [188]. Low stacking fault energy obstructs cross slip movement of dislocations resulting in quick work hardening. Due to the higher energy density of PP2, more Mo was able to be melted and introduced to the melt pool. This increased the work hardening rate by allowing Mo to diffuse more easily throughout the microstructure leading to the improved hardness and stiffness response. The difference between the values of Vickers hardness and nanohardness comes from the Mo content within the metal matrix and Mo-rich carbides. The standard deviation in measurements indicate that indents were made on features with disparate hardness. The higher resolution of the nanoindenter allows measurement of individual microstructural features versus an indent the size of an entire grain (Vickers). In the Vickers measurement, the composite response of the microstructure within and the adjacent to the area of the indent contribute.

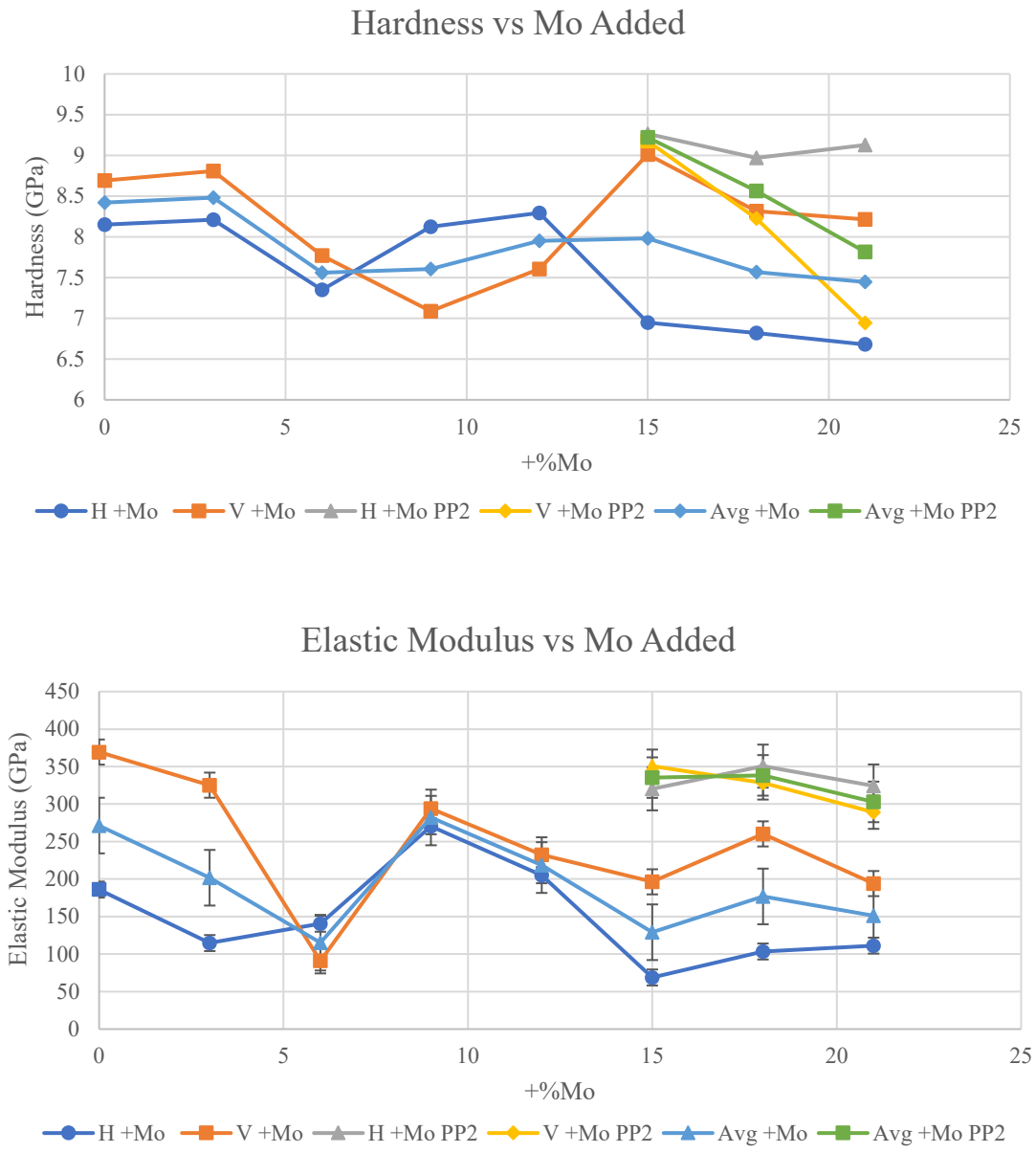

Figure 81: Nanoindentation Measurements for Co-Cr-ΔMo samples.

For the nanoscratch analysis performed on Co-Cr-ΔMo, scratches were made along both horizontal and vertical planes for both process parameter sets. Figure 82 provides a plot for the average friction measurement vs %Mo. The highest average

friction occurs at +9% Mo indicating a possible threshold where additional Mo is no longer beneficial. A drop in friction average may correlate with the development of new phases at +12%Mo. PP1 samples outperform PP2 samples other than at +21%Mo. This may be due to the higher volumetric energy density leading to better melting of powder and therefore a more stable structure.

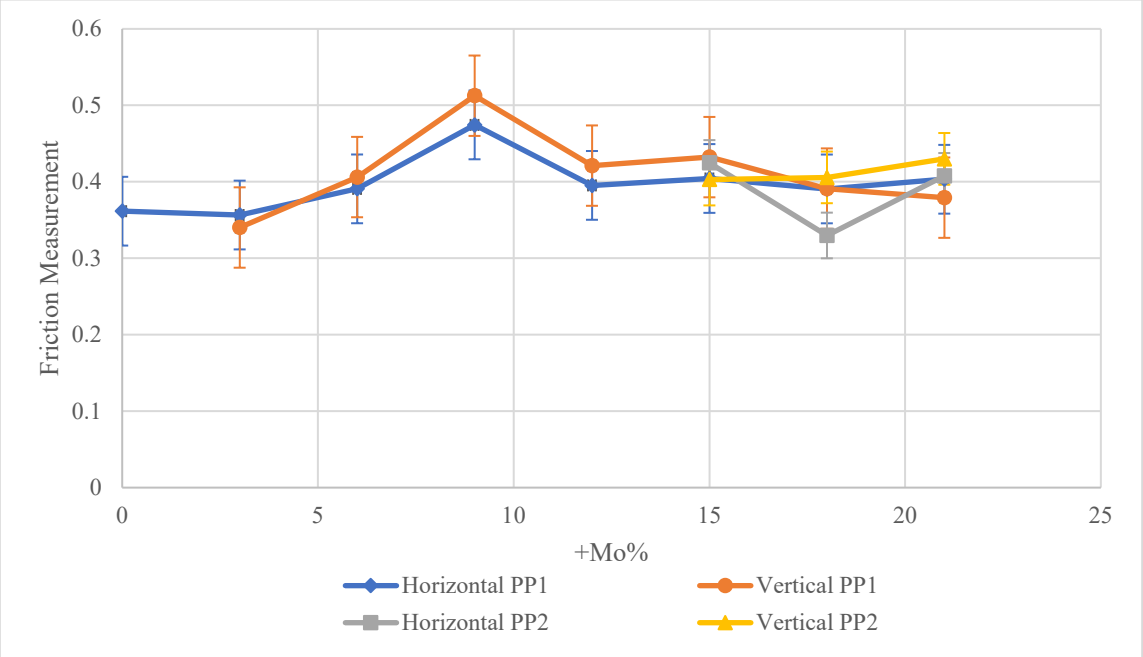

Figure 82: Friction Measurement vs +%Mo for PP1 and PP2.

5.3.2 Task 3-B: Correlate properties with composition and structural arrangement

As Mo is added to Co-Cr-Mo, an increase on hardness has been demonstrated. Similar to the last research question, there are similar ranges upon which a change in mechanical property changes is observed. From +3% to +12%, the interplay of carbides and intermetallics occurs. Though hard carbides are formed on the cell boundaries, it is

not enough to result in a substantial composite/global hardness increase. On approaching +12% Mo, carbide formation reduces, while intermetallics begin to increase. Intermetallics begin to precipitate at cell boundaries, however, the effect is substantial only up to +12% Mo.

From +12% to +18% Mo, there is an increase in intermetallic precipitates. Precipitation hardening occurs at the cell boundaries. Incoherent precipitates (those with severe misalignment with the microstructure) restrict dislocation motion. The increase in boundary widths and Mo 'hot spots' increase the volume fraction of intermetallic precipitates, thereby increasing global hardness. Co_3Mo has $L1_2$ crystals where partial screw dislocations can cross-slip, leading to Kear-Wilsdorf locks (slip inhibition increases HV). Kear-Wilsdorf locks occur when a pair of screw partial dislocations fully transfer from the (111) plane to the cross-slip plane (010). The relatively-larger Mo atoms can cause dilation resulting in stress fields that interact and mutually exert forces; each interaction acts as an energy barrier to dislocation motion.

From +18% to +21%, cell interiors show reducing %Mo and %Co suggesting drop in intermetallics there. Co-Mo saturation reduces the rate of HV increase.

5.3.2.1 The σ Phase

One significant phase formation that is accentuated as %Mo increases comes from the σ phase. The σ phase in Co-Cr-Mo made via LENS is a Co/Mo-rich intermetallic phase (Co_9Mo_{15}). This phase possesses a tetragonal structure with precipitation temperature from 600-1000 °C. Precipitates form when there is Cr content

from 25-76 wt.%. Ferrite forming elements (like Mo) promote precipitation of σ phase. At room temperature, σ phase is shown to have high hardness due to the immobility of dislocations. Hardening is shown to increase due to dispersion of σ in γ-Co.

Using the binary/ternary diagram (Figure 83 and Figure 84) in the case of this study, the first DOE shows that at +0% Mo, both γ and σ exist. Red dots and broken lines are presented to indicate the compositional trajectory of each printed sample as Mo content is increased. +0% Mo and +21% Mo are further highlighted with two other lines to demarcate the Co and Cr mass percentages. As %Mo is increased, at 1300 °C, an intermediate R phase is formed. The Co_3Mo (κ) and Co_7Mo_6 (μ) phases precipitate due to the high cooling rates associated with LENS. Co_3Mo strengthens the alloy through distortion via finely dispersed Co_3Mo particles in the slip plane. Increased precipitation of intermetallic phases (σ, κ, and μ) at the cell boundaries are a primary contributor to the significant hardness increase observed at +12% and above.

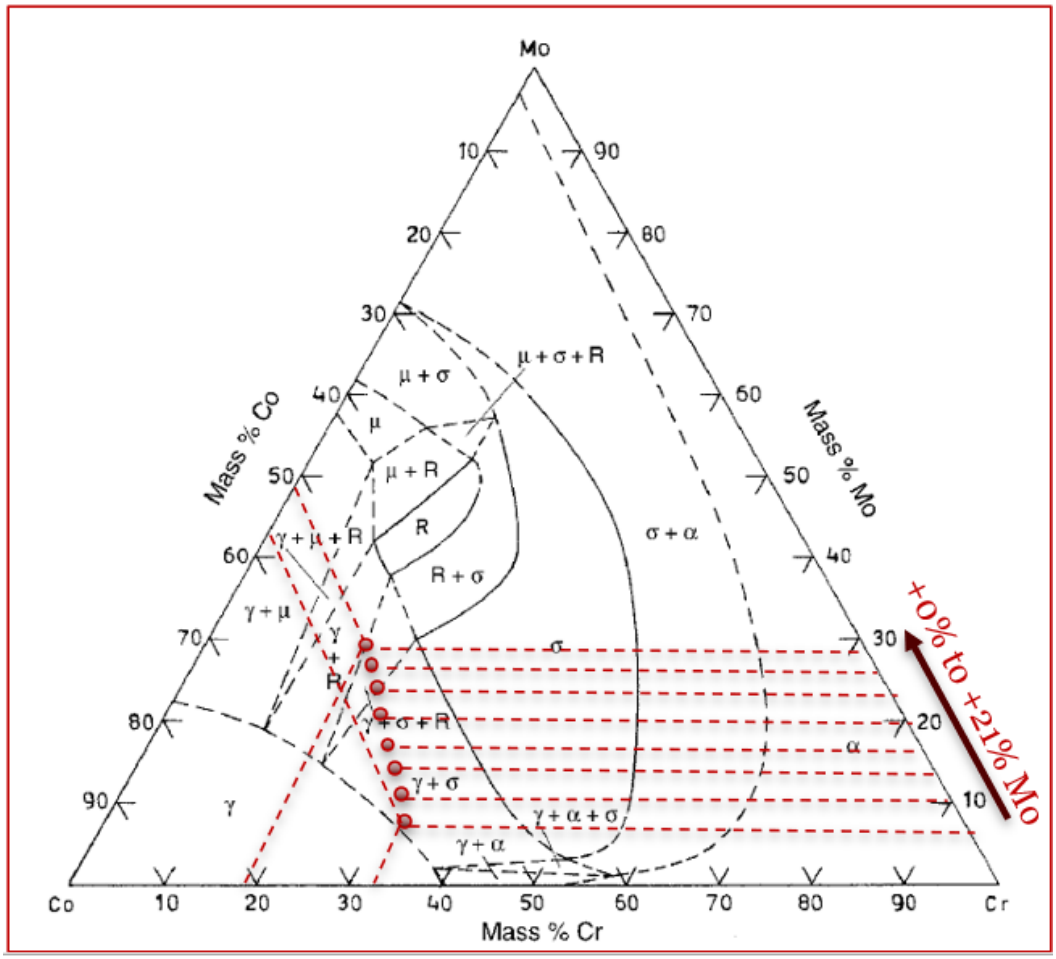

Figure 83: Ternary Phase Diagram with indicators for compositions of DOE 1 and 2 [140].

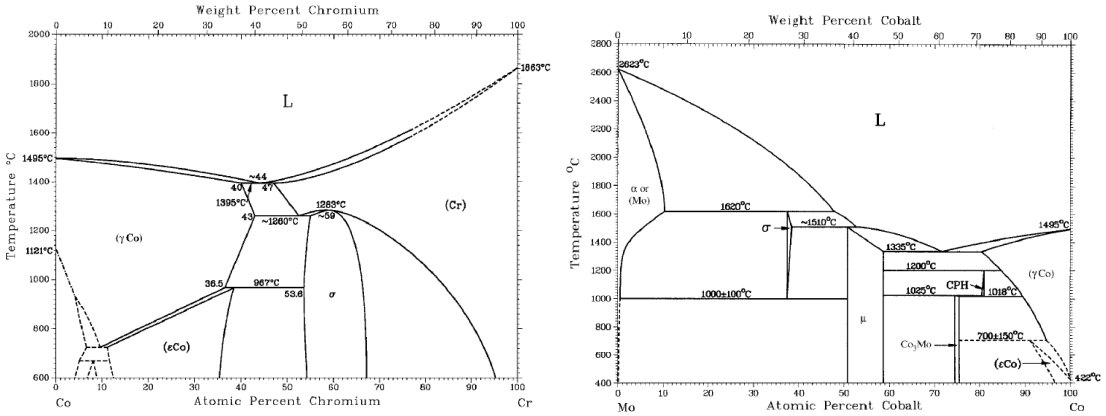

Table 1 Binary and ternary phases of the Co-Cr-Mo system and their structure data

Phase designation	Composition	Pearson's symbol	Space group	Type
α	(Cr), (Mo), (Cr,Mo)	*cI*2	$Im\bar{3}m$	W
γ	(γCo)	*cF*4	$Fm\bar{3}m$	Cu
ε	(εCo)	*hP*2	$P6_3/mmc$	Mg
σ	Cr_8Co_7 Co_9Mo_{15}	*tP*30	$P4_2/mnm$	σ(Fe,Cr)
Co_3Cr	Co_3Cr	*hP*8	$P6_3/mmc$	Ni_3Sn
Co_2Cr	Co_2Cr	…	…	…
Co_3Cr_2	Co_3Cr_2	…	…	…
π	Co_9Mo_2	*h*	…	…
κ	Co_3Mo	*hP*8	$P6_3/mcm$	Ni_3Sn
μ	Co_7Mo_6	*hR*13	$R\bar{3}m$	Fe_7W_6
R	$Co_{49}Cr_{21}Mo_{30}$	*hR*53	$R\bar{3}$	R(Co,Cr,Mo)

(a) Lattice parameters for hexagonal cell

Figure 84: Binary Phase diagrams of Co-Cr (top-left) and Co-Mo (top-right) and phases of Co-Cr-Mo system and their structure data [87].

5.3.2.2 Compositional Gradient Study

The compositional gradient samples were each indented down the vertical direction from the highest %Mo (8%) to the lowest %Mo (0%). Figure 85 presents the hardness measurements against the position of the indenter relative to the vertical position. For all three samples, the hardness values are around 5 GPa. The highest average hardness is exhibited by the C1 samples. In Figure 86, the elastic modulus

measured against position in the vertical direction is shown. In these plots, there is a large disparity between the elastic moduli of the three samples. C2 (1%/layer) exhibits the highest stiffness. This may be a product of a smaller build but could also reflect the ability of the LENS machine to deliver increasing %Mo layers. The C3 sample, built with 0.5% increases per layer, has much lower elastic modulus than the other two samples. This may indicate the resolution of the LENS machine to deliver structurally sound gradient layers.

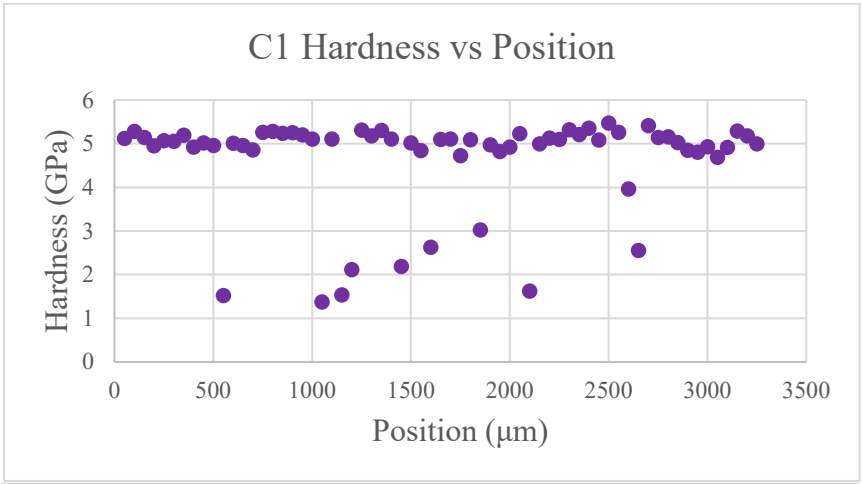

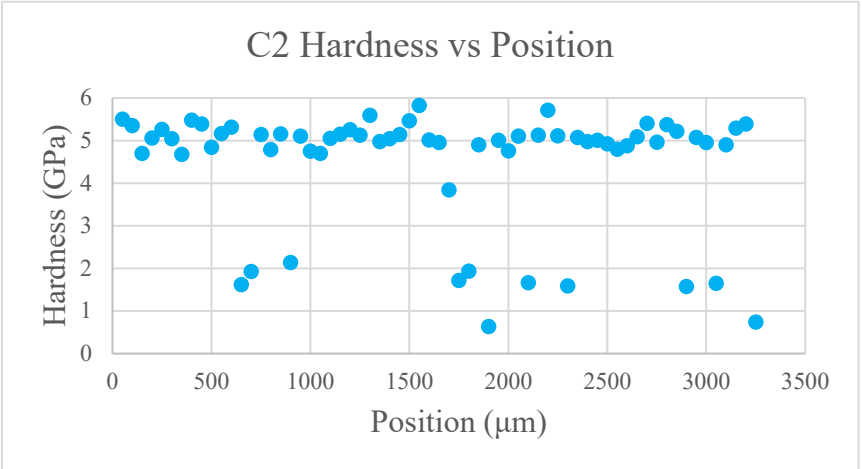

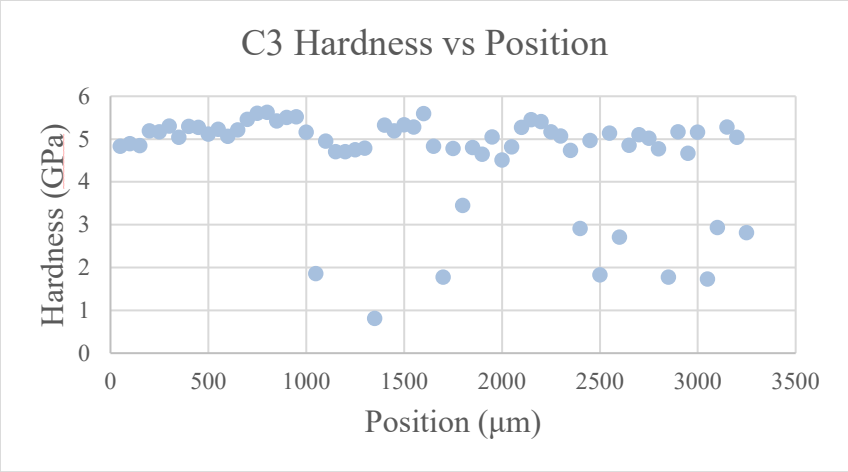

Figure 85: Hardness vs Position for all compositional gradient samples.

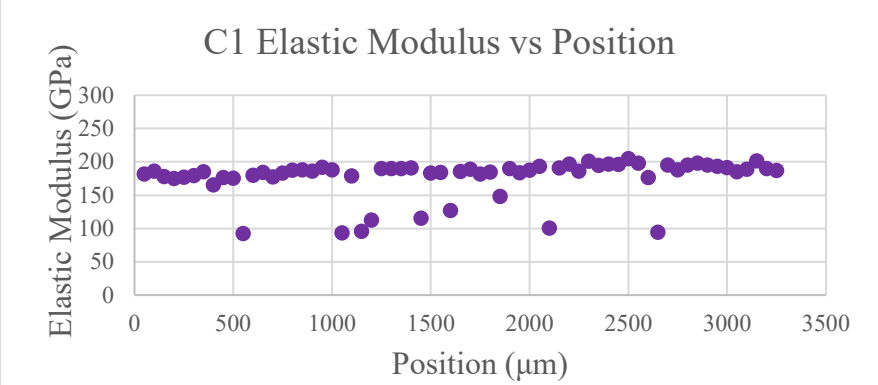

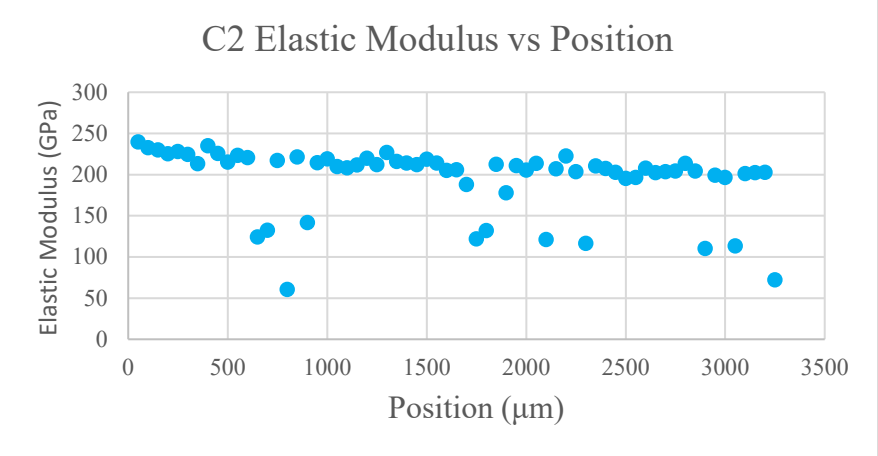

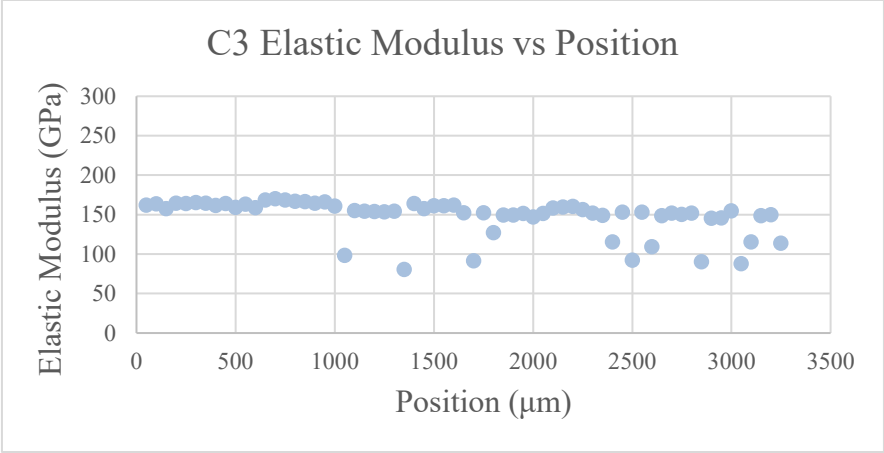

Figure 86: Elastic modulus vs position for all compositional gradient samples.

In the following compositional gradient study, the microstructure was evaluated at each different percentage of Mo. Figure 87 presents microstructures of each compositionally graded sample along with corresponding build schema. As expected, the microstructures do not deviate much apart from the aforementioned growths at triple junctions of cell boundaries.

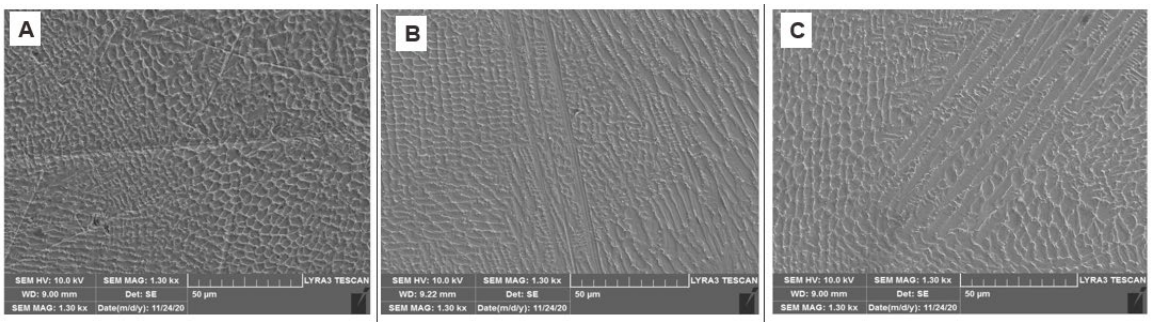

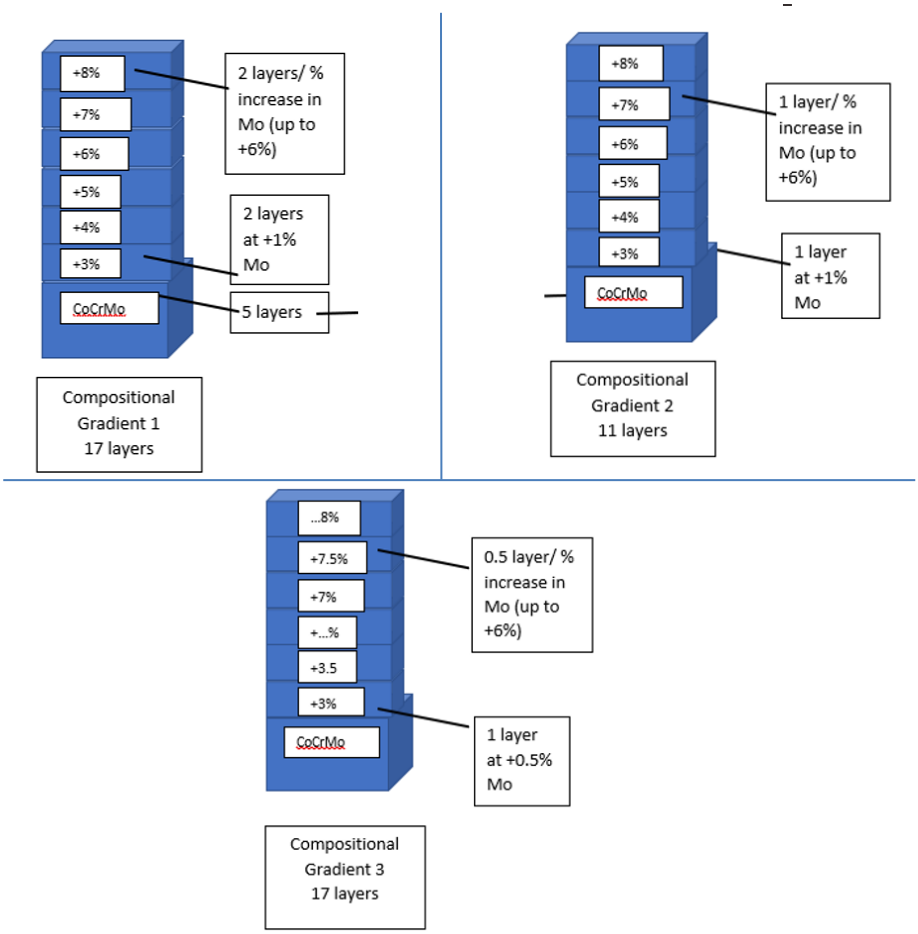

Figure 87: Microstructure of individual compositionally graded samples and corresponding build schema for CG sample 1 (top left), 2 (top right), and 3 (bottom).

Each compositional gradient sample was then studied via EDS to determine the Mo percentage against the distance. This provides a determination of the actual Mo composition against the expected amount that should have been delivered to the build. Area EDS was taken of each sample with the corresponding %Mo shown in Figure 88. It is apparent that the theoretical %Mo content does not match the values measured by EDS. As %Mo is increased, the EDS measurement trends upward as shown in the

second plot in the figure below. This may indicate that area EDS shows lower values in the matrix which is consistent with the previous measurements made.

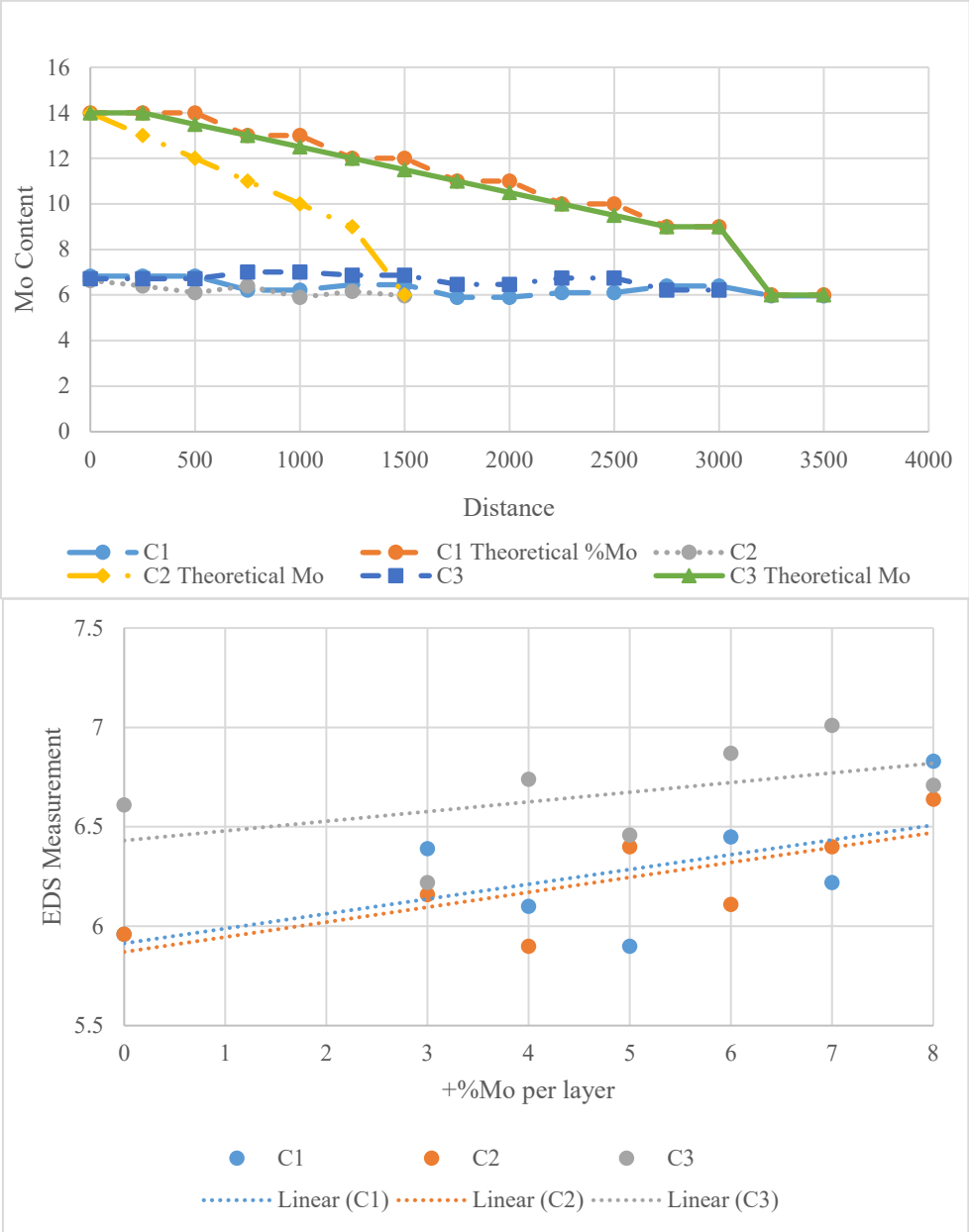

Figure 88: EDS Measurements of compositionally graded Co-Cr-Mo.

5.3.3 Summary of Results and Deductions

The following results were obtained the first two design of experiments regarding the third research question.

- 350W 5 RPM has the highest nanohardness, elastic modulus, aesthetic quality, and microstructural homogeneity.
- The 400W samples have larger cells and the lowest average hardness values.
- Elastic modulus and nanohardness of PP2 samples are higher than PP1
- There is a comparable response in microhardness for both process parameter sets
    - There is a significant increase in microhardness which correlates with change in microstructure at +12%.
- Point of inflection at +15% where Mo addition is no longer beneficial though the print is structurally sound

The following results pertain to the compositional gradient study with respect to Research Question 3:

- CG samples were built from 0%Mo, +3% to +8%Mo with increasing %Mo per 1-2 layers.
    - Samples were differentiated by layer resolution.
- Nanoindentation results:
    - Appreciable hardness differences could not be detected at the nanoscale
    - C2 has the highest stiffness
    - C3 has the lowest elastic modulus
- EDS:

    - Measured Mo content severely lags the intended Mo content
        - Similar behavior to the bulk ΔMo EDS measurements in RQ1
        - Machine is most likely not responsive enough to provide that resolution
    - A slight continuous increase in Mo composition from +3% to +8%
- XRD:
    - Indicates phases similar to previous DOEs

From these results, a variety of deductions could be made regarding the measurable mechanical properties of Co-Cr-Mo and compositionally graded variants. From these results, the following major insights can be derived:

- [+3% to +12%] Influence of carbides and intermetallics
    - Hard carbides formed on cell boundaries but not enough to result in substantial composite/global hardness increase
    - On approaching +12% Mo, carbide formation reduces, while intermetallics begin to increase
    - Intermetallics begin to precipitate at cell boundaries – effect only substantial only from +12%
- [+12% to +18%] Increase in intermetallic precipitates
    - Precipitation hardening at cell boundaries
    - Incoherent precipitates (severe misalignment with microstructure) restrict dislocation motion

    - Increase of boundary widths and Mo ‘hot pots’ increase volume fraction of intermetallic precipitates, thereby increasing global hardness
    - Co_3Mo has $L1_2$ crystals where partial screw dislocations can cross-slip, leading to Kear-Wilsdorf locks (slip inhibition increases HV)
    - The relatively-larger Mo atoms can cause dilation resulting in stress fields that interact and mutually exert forces; each interaction acts as an energy barrier to dislocation motion
- [+18% to +21%] Cell interiors show reducing %Mo and %Co suggesting a drop in intermetallics there
    - Co-Mo saturation reduces rate of HV increase
- The σ phase in Co-Cr-Mo made via LENS is a Co/Mo-rich intermetallic phase (Co_9Mo_{15})
    - Tetragonal structure with precipitation temperature from 600-1000 °C
    - Precipitates when Cr is from 25-76 wt.%
    - Ferrite forming elements (like Mo) promote precipitation of σ phase
- σ phase has high hardness due to low (room) temperature immobility of dislocations (Martins 2005, Bain & Griffiths)
    - Hardening shown to increase due to dispersion of σ in γ-Co (Hall 1999)
- Using binary/ternary diagram in our case:
    - At +0% Mo, both γ and σ exist
    - As %Mo is increased, at 1300 °C, an intermediate R phase is formed

    - The Co_3Mo (κ) and Co_7Mo_6 (μ) phases precipitate due to the high cooling rates associated with LENS
        - Co_3Mo strengthens the alloy through distortion via finely dispersed Co_3Mo particles in the slip plane
- Increased precipitation of intermetallic phases (σ, κ and μ) at the cell boundaries are a primary contributor to the significant hardness increase observed at +12% and above

CHAPTER VI

CONCLUSIONS & FUTURE WORK

In this work, the investigation of the processing-structure-property of single composition Co-Cr-Mo and Co-Cr-ΔMo and compositionally graded Co-Cr- ΔMo bulk structures made via Directed Energy Deposition DED. Samples were developed using three different design of experiments for each. Sample microstructures were analyzed via optical microscopy, scanning microscopy, EDS, XRD, and electron microprobe. Mechanical properties were determined through Vickers Hardness, nanoindentation, and nanoscratch testing.

As the adoption of LENS-based technology or similar compositional manipulation machines allow for the creation of entirely new material combinations, the progression of single element addition materials can serve to improve a variety of technologies. Specifically, the addition of Mo to Co-Cr-Mo can prove beneficial for a variety of fields. For the medical field, implant technologies can have increased corrosion prevention and tribological properties. Similarly, compositionally graded bio-coatings can be developed to increase surface hardness and wear resistance. These bio-coatings can help osteointegration, limit reaction to foreign bodies, or lower the incidence of infection. Beyond medical applications, the addition of Mo to Co-Cr-Mo can be useful towards applications that require high temperature such as for processes involving mechanical power transmission or oil and petrochemical processes. As this technology is further developed, the viability of changing a single element can become a solution for various engineering problems.

The purpose of this study is to generate a greater understanding of the LENS process for compositionally-graded metallic alloys, specifically Co-Cr-Mo, in terms of its process-structure-property framework.

6.1 Original contributions

The original contributions from this work are:

1. A set of DED process parameter recipes was developed to successfully create Co-Cr-Mo structures that have varying constituent compositions. This has profound implications on the future development of metal alloys specifically for improvements in mechanical and chemical properties.
    a. As Mo% changes, the 350W 5 RPM sample yielded best combination of build height, hardness, and discoloration. This acted as the baseline set of successful parameters for power and powder feed rate with acceptable quality. By creating a set of bounds, a manufacturer could develop a methodology similar to this study to create gradients with targeted material properties.
    b. Higher power leads to slightly larger cell sizes. This discovery indicates the large influence that power has upon the manufacturing quality. Particularly, the effect of power on the microstructure leads to a shift in mechanical properties. In a manufacturing context, the strategic use of different power levels can therefore further cultivate targeted material properties.

c. Samples created using LENS are comparable those made by wrought or cast samples in microhardness and microstructure. This result opens the possibility to use of LENS manufacturing in applications where an increase in hardness is desirable without the manufacturing restrictions imposed by traditional methods like casting. Further, the use of AM technologies reduces the amount of waste which present positive considerations for “green”, environmentally conscious enterprises.

2. There are a number of microstructural implications and trends with increasing %Mo.

   a. Increasing %Mo leads to Mo concentration hot spots such as the triple point junctions. By understanding the concentration behavior of Mo, the manufacturing via LENS can be a more predictable process in terms of microstructure and therefore mechanical properties. Mo hotspots are leading regions of development for carbides and intermetallics.

   b. The addition of Mo causes cell boundaries to become thicker. This behavior may further influence the resulting mechanical property measurements (i.e. nanohardness).

   c. Addition of Mo leads to formation of carbides and intermetallics. These microstructural features have been reported as hardness increasers in various pieces of literature. Understanding the

development behavior of both can further improve the manufacturing process. In many cases, the brittle nature of intermetallics can make them undesirable as a phase formation. Thus, knowing the formation behavior and the concentration band upon which they are likely to form can lead to more informed manufacturing decisions in the future.

3. Mechanical property and performance as a function of %Mo is an important development of this study. The influence of increasing %Mo in the context of compositional gradients can provide a greater understanding of the compositional band that proves useful depending on the application.
    a. There was a significant increase in microhardness at +12% Mo due to microstructure change. This was seen in the change of the underlying matrix where a distinct flat plane appeared to replace the former multifaceted structure.
    b. There exists a point of inflection in nanohardness at +15% Mo where Mo addition is not beneficial. This manifests as a significant drop in nanohardness from +15% to +21% Mo for both process parameter sets (PP1 and PP2).
    c. For compositional gradient samples, there were differences in the elastic modulus based on the layer resolution.
        i. While the hardness of each of the graded samples was generally the same, the elastic modulus of C2 (+1%Mo/layer)

was almost 100 GPa higher than C3 (+0.5%/layer). This was attributed to the layer deposition-%Mo step size build strategy utilized in the study.

ii. In particular, C2 has the highest elastic modulus while C3 has the lowest

REFERENCES

[1] C. Weber, V. Peña, M. Micali, E. Yglesias, S. Rood, J.A. Scott, B. Lal, The role of the national science foundation in the origin and evolution of additive manufacturing in the United States, Science & Technology Policy Institute 1 (2013).

[2] S.M. Thompson, L. Bian, N. Shamsaei, A. Yadollahi, An overview of Direct Laser Deposition for additive manufacturing; Part I: Transport phenomena, modeling and diagnostics, *Additive Manufacturing* 8 (2015) 36-62.

[3] A. Sola, D. Bellucci, V. Cannillo, Functionally graded materials for orthopedic applications - an update on design and manufacturing, *Biotechnol Adv* 34(5) (2016) 504-531.

[4] W.Q. Toh, X. Tan, A. Bhowmik, E. Liu, S.B. Tor, Tribochemical Characterization and Tribocorrosive Behavior of CoCrMo Alloys: A Review, Materials (Basel) 11(1) (2017).

[5] Y. Liao, E. Hoffman, M. Wimmer, A. Fischer, J. Jacobs, L. Marks, CoCrMo metal-on-metal hip replacements, Phys Chem Chem Phys 15(3) (2013) 746-56.

[6] W.C. Rodrigues, L.R. Broilo, L. Schaeffer, G. Knörnschild, F.R.M. Espinoza, Powder metallurgical processing of Co–28%Cr–6%Mo for dental implants: Physical, mechanical and electrochemical properties, Powder Technology 206(3) (2011) 233-238.

[7] Y.S. Hedberg, B. Qian, Z. Shen, S. Virtanen, I.O. Wallinder, In vitro biocompatibility of CoCrMo dental alloys fabricated by selective laser melting, Dent Mater 30(5) (2014) 525-34.

[8] D. Jevremovic, T. Puskar, B. Kosec, Đ. Vukelic, I. Budak, S. Aleksandrovic, D. Egbeer, R. Williams, The analysis of the mechanical properties of F75 Co-Cr alloy for use in selective laser melting (SLM) manufacturing of removable partial dentures (RPD), Metalurgija-Zagreb 51(2) (2012) 171.

[9] A. Takaichi, Suyalatu, T. Nakamoto, N. Joko, N. Nomura, Y. Tsutsumi, S. Migita, H. Doi, S. Kurosu, A. Chiba, N. Wakabayashi, Y. Igarashi, T. Hanawa, Microstructures and mechanical properties of Co-29Cr-6Mo alloy fabricated by selective laser melting process for dental applications, J Mech Behav Biomed Mater 21 (2013) 67-76.

[10] O.M. Pearson, D.E. Lieberman, The aging of Wolff's “law”: ontogeny and responses to mechanical loading in cortical bone, American journal of physical anthropology 125(S39) (2004) 63-99.

[11] S. Yager, J. Ma, H. Ozcan, H.I. Kilinc, A.H. Elwany, I. Karaman, Mechanical properties and microstructure of removable partial denture clasps manufactured using selective laser melting, Additive Manufacturing 8 (2015) 117-123.

[12] C. Song, Y. Yang, Y. Wang, D. Wang, J. Yu, Research on rapid manufacturing of CoCrMo alloy femoral component based on selective laser melting, *The International Journal of Advanced Manufacturing Technology* 75(1-4) (2014) 445-453.

[13] B. Vamsi Krishna, W. Xue, S. Bose, A. Bandyopadhyay, Functionally graded Co-Cr-Mo coating on Ti-6Al-4V alloy structures, *Acta Biomater* 4(3) (2008) 697-706.

[14] F.A. España, V.K. Balla, S. Bose, A. Bandyopadhyay, Design and fabrication of CoCrMo alloy based novel structures for load bearing implants using laser engineered net shaping, *Materials Science and Engineering: C* 30(1) (2010) 50-57.

[15] J.M. Wilson, N. Jones, L. Jin, Y.C. Shin, Laser deposited coatings of Co-Cr-Mo onto Ti-6Al-4V and SS316L substrates for biomedical applications, J Biomed Mater Res B Appl Biomater 101(7) (2013) 1124-32.

[16] A. Kratky, Production of hard metal alloys, Patent# US 2076952 (1937).

[17] I. Harter, Method of forming structures wholly of fusion deposited weld metal, Patent# US 2299747A Google Scholar (1942).

[18] H.N. Farmer Jr, Process of rebuilding steel structures, Google Patents, 1970.

[19] A. Ujiie, Method of constructing substantially circular cross-section vessel by welding, Google Patents, 1972.

[20] H.T. Brandi, H. Luckow, Method of making large structural one-piece parts of metal, particularly one-piece shafts, Google Patents, 1976.

[21] R.J.U.P. Housholder, 247,508, Molding process, (1981).

[22] C.O. Brown, E.M. Breinan, B.H. Kear, Method for fabricating articles by sequential layer deposition, Google Patents, 1982.

[23] G.K. Lewis, R. Nemec, J. Milewski, D.J. Thoma, D. Cremers, M. Barbe, Directed light fabrication, Presented at the Applications of Lasers and Electro-Optics, Orlando, FL, 17-20 Oct. 1994, 1994.

[24] F.P. Jeantette, D.M. Keicher, J.A. Romero, L.P. Schanwald, Method and system for producing complex-shape objects, Google Patents, 2000.

[25] N. Shamsaei, A. Yadollahi, L. Bian, S.M. Thompson, An overview of Direct Laser Deposition for additive manufacturing; Part II: Mechanical behavior, process parameter optimization and control, *Additive Manufacturing* 8 (2015) 12-35.

[26] W. Hofmeister, M. Wert, J. Smugeresky, J.A. Philliber, M. Griffith, M.J.J. Ensz, Investigating solidification with the laser-engineered net shaping (LENSTM) process, 51(7) (1999) 1-6.

[27] M. Grujicic, G. Cao, R.J.A.S.S. Figliola, Computer simulations of the evolution of solidification microstructure in the LENS™ rapid fabrication process, 183(1-2) (2001) 43-57.

[28] Z. Lu, D. Li, B. Lu, A. Zhang, G. Zhu, G.J.O. Pi, L.i. Engineering, The prediction of the building precision in the Laser Engineered Net Shaping process using advanced networks, 48(5) (2010) 519-525.

[29] T. Hua, C. Jing, L. Xin, Z. Fengying, H.J.J.o.M.P.T. Weidong, Research on molten pool temperature in the process of laser rapid forming, 198(1-3) (2008) 454-462.

[30] T.A. Davis, The effect of process parameters on laser-deposited TI-6A1-4V, (2004).

[31] D. Srivastava, I. Chang, M.J.I. Loretto, The effect of process parameters and heat treatment on the microstructure of direct laser fabricated TiAl alloy samples, 9(12) (2001) 1003-1013.

[32] M. Griffith, M. Schlienger, L. Harwell, M. Oliver, M. Baldwin, M. Ensz, M. Essien, J. Brooks, C. Robino, e.J.J.M. Smugeresky, design, Understanding thermal behavior in the LENS process, 20(2-3) (1999) 107-113.

[33] D.M. Keicher, W.D.J.M.P.R. Miller, LENSTM moves beyond RP to direct fabrication, 12(53) (1998) 26-28.

[34] M.L. Griffith, W.H. Hofmeister, G.A. Knorovsky, D.O. MacCallum, M.E. Schlienger, J.E. Smugeresky, Direct laser additive fabrication system with image feedback control, Google Patents, 2002.

[35] M. Griffith, D. Keicher, C. Atwood, J. Romero, J. Smugeresky, L. Harwell, D. Greene, Free form fabrication of metallic components using laser engineered net shaping (LENS), *Solid Freeform Fabrication Proceedings*, Proc. 1996 Solid Freeform Fabrication Symposium, Austin, 1996, pp. 125-131.

[36] S.N. Laboratories, Laser Engineered Net Shaping, (2007).

[37] A. Pinkerton, W. Wang, L. Li, Component repair using laser direct metal deposition, *Proceedings of the Institution of Mechanical Engineers, Part B: Journal of Engineering Manufacture* 222(7) (2008) 827-836.

[38] P. Korinko, T. Adams, S. Malene, D. Gill, J. Smugeresky, Laser Engineered Net Shaping® for Repair and Hydrogen Compatibility, *Welding Journal* 90(9) (2011).

[39] R.P.M.N.R. Wald, Laser Engineered Net Shaping Advances Additive Manufacturing and Repair, Welding Journal (2007).

[40] R.M. Mahamood, E.T. Akinlabi, Functionally graded materials, Springer2017.

[41] A. Mortensen, S.J.I.M.R. Suresh, Functionally graded metals and metal-ceramic composites: Part 1 Processing, 40(6) (1995) 239-265.

[42] J.J. Sobczak, L. Drenchev, Metallic Functionally Graded Materials: A Specific Class of Advanced Composites, *Journal of Materials Science & Technology* 29(4) (2013) 297-316.

[43] B. Onuike, B. Heer, A. Bandyopadhyay, Additive manufacturing of Inconel 718—Copper alloy bimetallic structure using laser engineered net shaping (LENS™), *Additive Manufacturing* 21 (2018) 133-140.

[44] A.E.S. Giannakopoulos, S; Finot, M; Olsson, M., Elastoplastic analysis of thermal cycling: layered materials with compositional gradients, Acta Metallic Materials 43(4) (5 August 1994) 1335-1354.

[45] B. Kieback, A. Neubrand, H.J.M.S. Riedel, E. A, Processing techniques for functionally graded materials, 362(1-2) (2003) 81-106.

[46] R. Zybala, K.T. Wojciechowski, Anisotropy analysis of thermoelectric properties of Bi2Te2. 9Se0. 1 prepared by SPS method, AIP Conference Proceedings, AIP, 2012, pp. 393-396.

[47] T.H. Niino, M. and Watanabe, R, 1987.

[48] M. Yamanouchi, M. Koizumi, T. Hirai, I. Shiota, FGM-90, Proceedings of the First International Symposium on Functionally Gradient Materilas, FGM Forum, Tokyo, Japan, 1990.

[49] S. Suresh, A. Mortenson, H.J.M.B. Mcmanus, MIT-ONR Workshop Covers Functionally Graded Structural Materials, 20(1) (1995) 54-55.

[50] M. Chmielewski, K. Pietrzak, Metal-ceramic functionally graded materials – manufacturing, characterization, application, Bulletin of the Polish Academy of Sciences Technical Sciences 64(1) (2016) 151-160.

[51] O.L. Harrysson, O. Cansizoglu, D.J. Marcellin-Little, D.R. Cormier, H.A.J.M.S. West II, E. C, Direct metal fabrication of titanium implants with tailored materials and mechanical properties using electron beam melting technology, 28(3) (2008) 366-373.

[52] A. Gebhardt, Understanding additive manufacturing: rapid prototyping-rapid tooling-rapid manufacturing, Carl Hanser Verlag GmbH Co KG2012.

[53] J. Dávila, M. Freitas, P. Inforçatti Neto, Z. Silveira, J. Silva, M.J.J.o.A.P.S. d’ Ávila, Fabrication of PCL/β‐TCP scaffolds by 3D mini‐screw extrusion printing, 133(15) (2016).

[54] S. Suresh, A. Mortensen, Fundamentals of functionally graded materials, The Institut of Materials1998.

[55] S. Suresh, M. Olsson, A. Giannakopoulos, N. Padture, J.J.A.M. Jitcharoen, Engineering the resistance to sliding-contact damage through controlled gradients in elastic properties at contact surfaces, 47(14) (1999) 3915-3926.

[56] B.E. Carroll, R.A. Otis, J.P. Borgonia, J.-o. Suh, R.P. Dillon, A.A. Shapiro, D.C. Hofmann, Z.-K. Liu, A.M. Beese, Functionally graded material of 304L stainless steel and inconel 625 fabricated by directed energy deposition: Characterization and thermodynamic modeling, Acta Materialia 108 (2016) 46-54.

[57] R. Messler, Principles of welding: processes, physics, chemistry, and metallurgy, 3 (1999) 60-66.

[58] Z. Sun, R.J.J.o.M.P.T. Karppi, The application of electron beam welding for the joining of dissimilar metals: an overview, 59(3) (1996) 257-267.

[59] S. Kou, Welding metallurgy, (2003) 431-446.

[60] A. Valarezo, G. Bolelli, W.B. Choi, S. Sampath, V. Cannillo, L. Lusvarghi, R. Rosa, Damage tolerant functionally graded WC–Co/Stainless Steel HVOF coatings, Surface and Coatings Technology 205(7) (2010) 2197-2208.

[61] W.Y. Lee, D.P. Stinton, C.C. Berndt, F. Erdogan, Y.D. Lee, Z.J.J.o.t.A.C.S. Mutasim, Concept of functionally graded materials for advanced thermal barrier coating applications, 79(12) (1996) 3003-3012.

[62] A.M. Limarga, S. Widjaja, T.H.J.S. Yip, C. Technology, Mechanical properties and oxidation resistance of plasma-sprayed multilayered Al2O3/ZrO2 thermal barrier coatings, 197(1) (2005) 93-102.

[63] K. Khor, Y.J.T.S.F. Gu, Thermal properties of plasma-sprayed functionally graded thermal barrier coatings, 372(1-2) (2000) 104-113.

[64] L.B. Drenchev, J.J. Sobczak, Gasars: A Specific Class of Porous Materials, ITS, 2009.

[65] C. Chu, C. Chung, Y. Pu, P.J.S.m. Lin, Graded surface structure in chemically polished NiTi shape memory alloy after NaOH treatment, 52(11) (2005) 1117-1121.

[66] T. Hu, L. Chen, S. Wu, C. Chu, L. Wang, K. Yeung, P.K.J.S.M. Chu, Graded phase structure in the surface layer of NiTi alloy processed by surface severe plastic deformation, 64(11) (2011) 1011-1014.

[67] H. Sato, T. Murase, T. Fujii, S. Onaka, Y. Watanabe, M.J.A.M. Kato, Formation of a wear-induced layer with nanocrystalline structure in Al–Al3Ti functionally graded material, 56(17) (2008) 4549-4558.

[68] F. Wang, J. Mei, X.J.A.S.S. Wu, Microstructure study of direct laser fabricated Ti alloys using powder and wire, 253(3) (2006) 1424-1430.

[69] J.J.F.S.W. Schneider, A.I. Processing, Temperature distribution and resulting metal flow, (2007) 37-49.

[70] D.C. Hofmann, J. Kolodziejska, S. Roberts, R. Otis, R.P. Dillon, J.-O. Suh, Z.-K. Liu, J.-P.J.J.o.M.R. Borgonia, Compositionally graded metals: A new frontier of additive manufacturing, 29(17) (2014) 1899-1910.

[71] D.C. Hofmann, K.S.J.M.S. Vecchio, E. A, Submerged friction stir processing (SFSP): An improved method for creating ultra-fine-grained bulk materials, 402(1-2) (2005) 234-241.

[72] M. Sam, N. Radhika, Effect of Heat Treatment on Mechanical and Tribological Properties of Centrifugally Cast Functionally Graded Cu/Al2O3 Composite, Journal of Tribology 140(2) (2017).

[73] S. Ferreira, L. Rocha, E. Ariza, P. Sequeira, Y. Watanabe, J.J.C.S. Fernandes, Corrosion behaviour of Al/Al3Ti and Al/Al3Zr functionally graded materials produced by centrifugal solid-particle method: Influence of the intermetallics volume fraction, 53(6) (2011) 2058-2065.

[74] M. Barmouz, P. Asadi, M.B. Givi, M.J.M.S. Taherishargh, E. A, Investigation of mechanical properties of Cu/SiC composite fabricated by FSP: Effect of SiC particles' size and volume fraction, 528(3) (2011) 1740-1749.

[75] P. Sequeira, Y. Watanabe, L. Rocha, Particle distribution and orientation in Al-Al3Zr and Al-Al3Ti FGMs produced by the centrifugal method, Materials Science Forum, Trans Tech Publ, 2005, pp. 609-614.

[76] K. Kinoshita, H. Sato, Y. Watanabe, Development of compositional gradient simulation for centrifugal slurry-pouring methods, Materials Science Forum, Trans Tech Publ, 2010, pp. 455-460.

[77] Y.J.J.J.S.P.P.M. Watanabe, Fabrication of functionally graded materials by centrifugal slurry-pouring method and centrifugal mixed-powder method, 57 (2010) 321-326.

[78] M. Jayachandran, H. Tsukamoto, H. Sato, Y. Watanabe, Formation Behavior of Continuous Graded Composition in Ti-ZrO2Functionally Graded Materials Fabricated by Mixed-Powder Pouring Method, Journal of Nanomaterials 2013 (2013) 1-8.

[79] S. Tammas-Williams, I. Todd, Design for additive manufacturing with site-specific properties in metals and alloys, *Scripta Materialia* 135 (2017) 105-110.

[80] S. Sampath, H. Herman, N. Shimoda, T.J.M.b. Saito, Thermal spray processing of FGMs, 20(1) (1995) 27-31.

[81] S. Suresh, A. Giannakopoulos, J.J.A.M. Alcala, Spherical indentation of compositionally graded materials: theory and experiments, 45(4) (1997) 1307-1321.

[82] R.M. Mahamood, E.T. Akinlabi, Laser metal deposition of functionally graded Ti6Al4V/TiC, Materials & Design 84 (2015) 402-410.

[83] Y. Zhang, A. Bandyopadhyay, Direct fabrication of compositionally graded Ti-Al 2 O 3 multi-material structures using Laser Engineered Net Shaping, *Additive Manufacturing* 21 (2018) 104-111.

[84] A. Reichardt, R.P. Dillon, J.P. Borgonia, A.A. Shapiro, B.W. McEnerney, T. Momose, P. Hosemann, Development and characterization of Ti-6Al-4V to 304L stainless steel gradient components fabricated with laser deposition additive manufacturing, Materials & Design 104 (2016) 404-413.

[85] F.-J. Kahlen, A.J.J.o.m.s. Kar, engineering, Tensile strengths for laser-fabricated parts and similarity parameters for rapid manufacturing, 123(1) (2001) 38-44.

[86] L. Peng, Y. Taiping, L. Sheng, L. Dongsheng, H. Qianwu, X. Weihao, Z. Xiaoyan, Direct laser fabrication of nickel alloy samples, *International Journal of Machine Tools and Manufacture* 45(11) (2005) 1288-1294.

[87] J.R. Davis, ASM Specialty Handbook: Nickel, Cobalt, & Their Alloys, *ASM International* 2000 (2000) 344-406.

[88] L. Costa, R. Vilar, T. Reti, A. Deus, Rapid tooling by laser powder deposition: Process simulation using finite element analysis, *Acta Materialia* 53(14) (2005) 3987-3999.

[89] V. Manvatkar, A. Gokhale, G.J. Reddy, A. Venkataramana, A. De, Estimation of melt pool dimensions, thermal cycle, and hardness distribution in the laser-engineered net shaping process of austenitic stainless steel, *Metallurgical and materials transactions A* 42(13) (2011) 4080-4087.

[90] J. Xiong, Z. Guo, M. Yang, B.J.I.J.o.R.M. Shen, H. Materials, Preparation of ultra-fine TiC0. 7N0. 3-based cermet, 26(3) (2008) 212-219.

[91] G. Dinda, A. Dasgupta, J.J.M.S. Mazumder, E. A, Laser aided direct metal deposition of Inconel 625 superalloy: Microstructural evolution and thermal stability, 509(1-2) (2009) 98-104.

[92] M. Mori, K. Yamanaka, S. Sato, S. Tsubaki, K. Satoh, M. Kumagai, M. Imafuku, T. Shobu, A. Chiba, Strengthening of biomedical Ni-free Co-Cr-Mo alloy by multipass "low-strain-per-pass" thermomechanical processing, Acta Biomater 28 (2015) 215-224.

[93] D. Matlock, D. Olson, Novel concepts in weld metal science: Role of gradients and composite structure, Colorado School of Mines, Golden, CO (United States). Center for Welding and …, 1991.

[94] J.F. Blowey, C.M.J.E.J.o.A.M. Elliott, The Cahn–Hilliard gradient theory for phase separation with non-smooth free energy Part I: Mathematical analysis, 2(3) (1991) 233-280.

[95] V.K. Balla, P.P. Bandyopadhyay, S. Bose, A. Bandyopadhyay, Compositionally graded yttria-stabilized zirconia coating on stainless steel using laser engineered net shaping (LENS™), Scripta Materialia 57(9) (2007) 861-864.

[96] U. Savitha, G. Jagan Reddy, A. Venkataramana, A. Sambasiva Rao, A.A. Gokhale, M. Sundararaman, Chemical analysis, structure and mechanical properties of discrete and compositionally graded SS316–IN625 dual materials, Materials Science and Engineering: A 647 (2015) 344-352.

[97] M. Das, V.K. Balla, T.S.S. Kumar, I. Manna, Fabrication of Biomedical Implants using Laser Engineered Net Shaping (LENS™), Transactions of the Indian Ceramic Society 72(3) (2013) 169-174.

[98] B. Bax, R. Rajput, R. Kellet, M. Reisacher, Systematic evaluation of process parameter maps for laser cladding and directed energy deposition, *Additive Manufacturing* 21 (2018) 487-494.

[99] H. Kim, W. Cong, H.C. Zhang, Z. Liu, Laser Engineered Net Shaping of Nickel-Based Superalloy Inconel 718 Powders onto AISI 4140 Alloy Steel Substrates: Interface Bond and Fracture Failure Mechanism, *Materials (Basel)* 10(4) (2017).

[100] W. Liu, J.J.S.M. DuPont, Fabrication of functionally graded TiC/Ti composites by laser engineered net shaping, 48(9) (2003) 1337-1342.

[101] G.D.J.Y. Ram, Y.; Stucker, B.E. , Deposition of Ti/TiC Composite Coatings on Implant Structures using Laser Engineered Net Shaping, *Solid Free Form* (2007).

[102] J.R. Brevick, Energy-Saving Melting and Revert Reduction Technology (E-SMARRT): Use of Laser Engineered Net Shaping for Rapid Manufacturing of Dies with Protective Coatings and Improved Thermal Management, Technical Report (2014).

[103] C.H. Zhang, H. Zhang, C.L. Wu, S. Zhang, Z.L. Sun, S.Y. Dong, Multi-layer functional graded stainless steel fabricated by laser melting deposition, Vacuum 141 (2017) 181-187.

[104] H.W. Yingbin Hua, Fuda Ninga, Weilong Conga, Yuzhou Lib, COMPRESSIVE PROPERTY COMPARISONS BETWEEN LASER ENGINEERED NET SHAPING OF IN SITU TIBW-TMCS AND CP-TI MATERIALS, Solid Free Form (2016).

[105] K.I. Schwendner, R. Banerjee, P.C. Collins, C.A. Brice, H.L.J.S.M. Fraser, Direct laser deposition of alloys from elemental powder blends, 45(10) (2001) 1123-1129.

[106] Y. Zhai, H. Galarraga, D.A. Lados, Microstructure, static properties, and fatigue crack growth mechanisms in Ti-6Al-4V fabricated by additive manufacturing: LENS and EBM, *Engineering Failure Analysis* 69 (2016) 3-14.

[107] H. Attar, S. Ehtemam-Haghighi, D. Kent, X. Wu, M.S. Dargusch, Comparative study of commercially pure titanium produced by laser engineered net shaping, selective laser melting and casting processes, *Materials Science and Engineering: A* 705 (2017) 385-393.

[108] G.A.K. E. Amsterdam, High Cycle Fatigue of Laser Beam Deposited Ti 6Al 4V and Inconel 718, ICAF (Bridging the Gap between Theory and Operational Practice) (2009) 1261–1274.

[109] Y. Zhai, D.A. Lados, E.J. Brown, G.N. Vigilante, Fatigue crack growth behavior and microstructural mechanisms in Ti-6Al-4V manufactured by laser engineered net shaping, International Journal of Fatigue 93 (2016) 51-63.

[110] T. Devine, J. Wulff, Cast vs. wrought cobalt‐chromium surgical implant alloys, Journal of biomedical materials research 9(2) (1975) 151-167.

[111] T. Kilner, R. Pilliar, G. Weatherly, C. Allibert, Phase identification and incipient melting in a cast Co‐Cr surgical implant alloy, Journal of biomedical materials research 16(1) (1982) 63-79.

[112] Y.S. Al Jabbari, Physico-mechanical properties and prosthodontic applications of Co-Cr dental alloys: a review of the literature, J Adv Prosthodont 6(2) (2014) 138-45.

[113] I. Radu, D.Y. Li, R. Llewellyn, Tribological behavior of Stellite 21 modified with yttrium, Wear 257(11) (2004) 1154-1166.

[114] A. Mani, R. Salinas, H.F. Lopez, Deformation induced FCC to HCP transformation in a Co–27Cr–5Mo–0.05C alloy, Materials Science and Engineering: A 528(7-8) (2011) 3037-3043.

[115] I. Peter, M. Rosso, S. Lombardo, Sequential Casting of Functionally Graded Material, Key Engineering Materials 750 (2017) 153-158.

[116] K. Yamanaka, M. Mori, A. Chiba, Developing high strength and ductility in biomedical Co-Cr cast alloys by simultaneous doping with nitrogen and carbon, Acta Biomater 31 (2016) 435-447.

[117] E. Bettini, T. Eriksson, M. Boström, C. Leygraf, J. Pan, Influence of metal carbides on dissolution behavior of biomedical CoCrMo alloy: SEM, TEM and AFM studies, Electrochimica Acta 56(25) (2011) 9413-9419.

[118] Y. Liao, R. Pourzal, P. Stemmer, M.A. Wimmer, J.J. Jacobs, A. Fischer, L.D. Marks, New insights into hard phases of CoCrMo metal-on-metal hip replacements, J Mech Behav Biomed Mater 12 (2012) 39-49.

[119] J.-C.D. Shin, Jung-Man ; Yoon, Jin-Kook ; Lee, Dok-Yol ; Kim, Jae-Soo, Effect of molybdenum on the microstructure and wear resistance of cobalt-base Stellite hardfacing alloys, Surface and Coatings Technology 166 (2003) 117-126.

[120] K. Asgar, F.A.J.J.o.d.r. Peyton, Effect of microstructure on the physical properties of cobalt-base alloys, 40(1) (1961) 63-72.

[121] A. Chiba, K. Kumagai, N. Nomura, S. Miyakawa, Pin-on-disk wear behavior in a like-on-like configuration in a biological environment of high carbon cast and low carbon forged Co–29Cr–6Mo alloys, Acta Materialia 55(4) (2007) 1309-1318.

[122] H. Koseki, M. Tomita, A. Yonekura, T. Higuchi, S. Sunagawa, K. Baba, M. Osaki, Effect of carbon ion implantation on the tribology of metal-on-metal bearings for artificial joints, Int J Nanomedicine 12 (2017) 4111-4116.

[123] J.H. Dumbleton, M.T. Manley, Metal-on-metal total hip replacement: what does the literature say?, The Journal of arthroplasty 20(2) (2005) 174-188.

[124] D. Langton, S. Jameson, T. Joyce, N. Hallab, S. Natu, A. Nargol, Early failure of metal-on-metal bearings in hip resurfacing and large-diameter total hip replacement: a consequence of excess wear, The Journal of bone and joint surgery. British volume 92(1) (2010) 38-46.

[125] H. Koseki, H. Shindo, I. Furuichi, K. Baba, Carbon‐ion implantation improves the tribological properties of Co□ Cr□ Mo alloy against ultra‐high molecular weight polyethylene, Surface and Interface Analysis: An International Journal devoted to the development and application of techniques for the analysis of surfaces, interfaces and thin films 40(9) (2008) 1278-1283.

[126] J. Fisher, X. Hu, T. Stewart, S. Williams, J. Tipper, E. Ingham, M. Stone, C. Davies, P. Hatto, J. Bolton, Wear of surface engineered metal-on-metal hip prostheses, Journal of Materials Science: Materials in Medicine 15(3) (2004) 225-235.

[127] T. Matković, P. Matković, J. Malina, Effects of Ni and Mo on the microstructure and some other properties of Co–Cr dental alloys, Journal of Alloys and Compounds 366(1-2) (2004) 293-297.

[128] N. Yang, J. Yee, B. Zheng, K. Gaiser, T. Reynolds, L. Clemon, W.Y. Lu, J.M. Schoenung, E.J. Lavernia, Process-Structure-Property Relationships for 316L Stainless Steel Fabricated by Additive Manufacturing and Its Implication for Component Engineering, *Journal of Thermal Spray Technology* 26(4) (2016) 610-626.

[129] K. Sonofuchi, Y. Hagiwara, Y. Koizumi, A. Chiba, M. Kawano, M. Nakayama, K. Ogasawara, Y. Yabe, E. Itoi, Quantitative in vivo biocompatibility of new ultralow-nickel cobalt-chromium-molybdenum alloys, J Orthop Res 34(9) (2016) 1505-13.

[130] A. Handbook, Alloy Phase Diagrams, vol. 3, ASM International, Materials Park, OH 285 (1992).

[131] K. Yamanaka, M. Mori, A. Chiba, Nanoarchitectured Co–Cr–Mo orthopedic implant alloys: nitrogen-enhanced nanostructural evolution and its effect on phase stability, Acta biomaterialia 9(4) (2013) 6259-6267.

[132] K. Yamanaka, M. Mori, A. Chiba, Effects of nitrogen addition on microstructure and mechanical behavior of biomedical Co-Cr-Mo alloys, J Mech Behav Biomed Mater 29 (2014) 417-26.

[133] K. Yoda, Suyalatu, A. Takaichi, N. Nomura, Y. Tsutsumi, H. Doi, S. Kurosu, A. Chiba, Y. Igarashi, T. Hanawa, Effects of chromium and nitrogen content on the microstructures and mechanical properties of as-cast Co-Cr-Mo alloys for dental applications, Acta Biomater 8(7) (2012) 2856-62.

[134] S.-H. Lee, N. Nomura, A. Chiba, Significant improvement in mechanical properties of biomedical Co-Cr-Mo alloys with combination of N addition and Cr-enrichment, Materials transactions (2008) 0801150296-0801150296.

[135] M. Podrez-Radziszewska, Characteristic of intermetallic phases in cast dental CoCrMo alloy, Archives of Foundry Engineering 10(3/2010) (2010).

[136] P. Vizureanu, M.G. Minciună, D.C. Achiţei, A.V. Sandu, K. Hussin, Mechanical Behaviour of CoCrMo Alloy with Si Content, Applied Mechanics and Materials 754-755 (2015) 1017-1022.

[137] M.G. Minciună, Vizureanu Petrica, Geanta Victoras, Voiculescu Ionelia, Sandu Andrei Victor, Architei Dragos Christian, Vitalariu Anca Mihaela, Effect of Si on the Microstructure and Mechanical Properties of Biomedical CoCrMo Alloy, Rev. Chim. 66(6) (2015).

[138] A. Aherwar, A.K. Singh, A. Patnaik, Current and future biocompatibility aspects of biomaterials for hip prosthesis, AIMS Bioengineering 3(1) (2015) 23-43.

[139] I. Radu, D.Y. Li, The wear performance of yttrium-modified Stellite 712 at elevated temperatures, Tribology International 40(2) (2007) 254-265.

[140] K.P. Gupta, The Co-Cr-Mo (Cobalt-Chromium-Molybdenum) System, Journal of Phase Equilibria & Diffusion 26(1) (2005) 87-92.

[141] R. Liu, M.X. Yao, P.C. Patnaik, X. Wu, Effects of heat treatment on mechanical and tribological properties of cobalt-base tribaloy alloys, Journal of materials engineering and performance 14(5) (2005) 634-640.

[142] S. Rideout, W. Manly, E. Kamen, B. Lement, P.A. Beck, Intermediate phases in ternary alloy systems of transition elements, JOM 3(10) (1951) 872-876.

[143] J. Darby, P. Beck, Intermediate Phases in the Cr-Mo-Co System at 1300 C, JOM 7(6) (1955) 765-766.

[144] J. Marciniak, M. Kaczmarek, A. Ziębowicz, Biomaterials in stomatology, Editorial Office of Silesian University of Technology, Gliwice (2008).

[145] A. Marti, Cobalt-base alloys used in bone surgery, Injury 31 (2000) D18-D21.

[146] S. Mineta, S. Namba, T. Yoneda, K. Ueda, T. Narushima, Carbide Formation and Dissolution in Biomedical Co-Cr-Mo Alloys with Different Carbon Contents during Solution Treatment, Metallurgical and Materials Transactions A 41(8) (2010) 2129-2138.

[147] K. Yamanaka, M. Mori, A. Chiba, Effects of carbon concentration on microstructure and mechanical properties of as-cast nickel-free Co–28Cr–9W-based dental alloys, Materials Science and Engineering: C 40 (2014) 127-134.

[148] K. Yamanaka, M. Mori, A. Chiba, Effects of Carbon Addition on Mechanical Properties and Microstructures of Ni-Free Co–Cr–W-Based Dental Alloys, Interface Oral Health Science 2014, Springer, Tokyo2015, pp. 225-236.

[149] S. Kurosu, N. Nomura, A. Chiba, Microstructure and mechanical properties of Co-29Cr-6Mo alloy aged at 1023 K, Materials transactions 48(6) (2007) 1517-1522.

[150] M. Mori, K. Yamanaka, A. Chiba, Phase decomposition in biomedical Co–29Cr–6Mo–0.2 N alloy during isothermal heat treatment at 1073 K, Journal of Alloys and Compounds 590 (2014) 411-416.

[151] A. Karaali, K. Mirouh, S. Hamamda, P. Guiraldenq, Microstructural study of tungsten influence on Co–Cr alloys, Materials Science and Engineering: A 390(1-2) (2005) 255-259.

[152] W. Xu, R. Liu, P. Patnaik, M. Yao, X. Wu, Mechanical and tribological properties of newly developed Tribaloy alloys, Materials Science and Engineering: A 452 (2007) 427-436.

[153] H.A. Zaman, S. Sharif, D.-W. Kim, M.H. Idris, M.A. Suhaimi, Z. Tumurkhuyag, Machinability of Cobalt-based and Cobalt Chromium Molybdenum Alloys - A Review, Procedia Manufacturing 11 (2017) 563-570.

[154] H. Lopez, A. Saldivar-Garcia, Martensitic transformation in a cast Co-Cr-Mo-C alloy, Metallurgical and Materials Transactions A 39(1) (2008) 8-18.

[155] A. Clemow, B. Daniell, Solution treatment behavior of Co‐Cr‐Mo alloy, Journal of Biomedical Materials Research 13(2) (1979) 265-279.

[156] B. Senior, A critical review of precipitation behaviour in 1Cr Mo V rotor steels, Materials Science and Engineering: A 103(2) (1988) 263-271.

[157] K. Kuo, C. Jia, Crystallography of M23C6 and M6C precipitated in a low alloy steel, Acta Metallurgica 33(6) (1985) 991-996.

[158] S.-H. Lee, E. Takahashi, N. Nomura, A. Chiba, Effect of carbon addition on microstructure and mechanical properties of a wrought Co–Cr–Mo implant alloy, Materials transactions 47(2) (2006) 287-290.

[159] C. Montero‐Ocampo, A. Salinas Rodriguez, Effect of carbon content on the resistance to localized corrosion of as‐cast cobalt‐based alloys in an aqueous chloride solution, Journal of biomedical materials research 29(4) (1995) 441-453.

[160] J.B. Wu, B. McKee, I. Purvis, Cobalt-based industrial cutting tool inserts and alloys therefor, Google Patents, 2004.

[161] C.V. Vidal, A.I. Muñoz, Effect of thermal treatment and applied potential on the electrochemical behaviour of CoCrMo biomedical alloy, Electrochimica Acta 54(6) (2009) 1798-1809.

[162] C. Song, H. Park, H. Seong, H. Lopez, Development of athermal and isothermalε-martensite in atomized Co-Cr-Mo-C implant alloy powders, Metallurgical and Materials Transactions A 37(11) (2006) 3197-3204.

[163] C. Song, H. Park, H. Seong, H. Lopez, Development of athermal ε-martensite in atomized Co–Cr–Mo–C implant alloy powders, Acta Biomaterialia 2(6) (2006) 685-691.

[164] B.E. Stucker, Esplin, C, Justin, D, An investigation of LENS-Deposited Medical-Grade CoCrMo Alloys, (2004).

[165] D. Faidel, D. Jonas, G. Natour, W. Behr, Investigation of the selective laser melting process with molybdenum powder, Additive Manufacturing 8 (2015) 88-94.

[166] G.D. Janaki Ram, C.K. Esplin, B.E. Stucker, Microstructure and wear properties of LENS deposited medical grade CoCrMo, J Mater Sci Mater Med 19(5) (2008) 2105-11.

[167] K.M. Mantrala, M. Das, V.K. Balla, C.S. Rao, V.K. Rao, Laser-deposited CoCrMo alloy: Microstructure, wear, and electrochemical properties, Journal of Materials Research 29(17) (2014) 2021-2027.

[168] A. Bandyopadhyay, Varmi Krishna Balla, Mangal Roy, and Susmita Bose, Laser Surface Modification of Metallic Biomaterials, Surface Engineering (2011).

[169] J. Cawley, J. Metcalf, A.H. Jones, T. Band, D. Skupien, A tribological study of cobalt chromium molybdenum alloys used in metal-on-metal resurfacing hip arthroplasty, Wear 255(7-12) (2003) 999-1006.

[170] R. Taylor, R. Waterhouse, The metallography of a cobalt-based implant alloy after solution treatment and ageing, Journal of materials science 21(6) (1986) 1990-1996.

[171] M. Caudillo, M. Herrera–Trejo, M. Castro, E. Ramirez, C. Gonzalez, J. Juarez, On carbide dissolution in an as‐cast ASTM F‐75 alloy, Journal of Biomedical Materials Research: An Official Journal of The Society for Biomaterials, The Japanese Society for Biomaterials, and The Australian Society for Biomaterials and the Korean Society for Biomaterials 59(2) (2002) 378-385.

[172] I. Hutchings, ‘Tribology: friction and wear of engineering materials'; 1992, London, Edward Arnold.

[173] M. Wimmer, J. Loos, R. Nassutt, M. Heitkemper, A. Fischer, The acting wear mechanisms on metal-on-metal hip joint bearings: in vitro results, Wear 250(1-12) (2001) 129-139.

[174] G.D. Janaki Ram, Stucker, B. E. , A Feasibility Study of LENS Deposition of CoCrMo Coating on a Titanium Substrate, *Journal of Manufacturing Science and Engineering* 130 (2007).

[175] K. Monroy, J. Delgado, J. Ciurana, Study of the Pore Formation on CoCrMo Alloys by Selective Laser Melting Manufacturing Process, Procedia Engineering 63 (2013) 361-369.

[176] Z.W. Chen, K. Darvish, T. Pasang, Effects of Laser Power on Track Profile and Structure Formation during Selective Laser Melting of CoCrMo Alloy, Materials Science Forum 879 (2016) 330-334.

[177] H. Sahasrabudhe, S. Bose, A. Bandyopadhyay, Laser processed calcium phosphate reinforced CoCrMo for load-bearing applications: Processing and wear induced damage evaluation, Acta Biomater 66 (2018) 118-128.

[178] D. Wang, C. Song, Y. Yang, Y. Bai, Investigation of crystal growth mechanism during selective laser melting and mechanical property characterization of 316L stainless steel parts, Materials & Design 100 (2016) 291-299.

[179] Y. Chen, Y. Li, S. Kurosu, K. Yamanaka, N. Tang, Y. Koizumi, A. Chiba, Effects of sigma phase and carbide on the wear behavior of CoCrMo alloys in Hanks' solution, Wear 310(1-2) (2014) 51-62.

[180] O. Sahin, A.R. Tuncdemir, x1d6a, za, H.A. Cetinkara, H.S. Guder, E. Sahin, Production and Mechanical Behaviour of Biomedical CoCrMo Alloy, Chinese Physics Letters 28(12) (2011).

[181] G. Barucca, E. Santecchia, G. Majni, E. Girardin, E. Bassoli, L. Denti, A. Gatto, L. Iuliano, T. Moskalewicz, P. Mengucci, Structural characterization of biomedical Co-Cr-Mo components produced by direct metal laser sintering, Mater Sci Eng C Mater Biol Appl 48 (2015) 263-9.

[182] C.P. Emerson, The Microstructure and the Electrochemical Behavior of Cobalt Chromium Molybdenum Alloys from Retrieved Hip Implants, FIU Digital Commons (Thesis) (2015).

[183] M. Mergulhão, Investigation of mechanical, microstructural and thermal behavior of CoCrMo alloy manufactured by selective laser melting and casting techniques, Anais do IX Congresso Brasileiro de Engenharia de Fabricação, 2017.

[184] W.D. Callister Jr, D.G. Rethwisch, Fundamentals of materials science and engineering: an integrated approach, John Wiley & Sons2012.

[185] G.A. Ettienne-Modeste, L.D.T. Topoleski, Nanomechanical and Wear Behavior of Microtextured Carbide-Coated CoCrMo Alloy Surfaces, Journal of Tribology 135(4) (2013).

[186] R. Ahmed, H.L. de Villiers Lovelock, N.H. Faisal, S. Davies, Structure–property relationships in a CoCrMo alloy at micro and nano-scales, Tribology International 80 (2014) 98-114.

[187] R. Ahmed, A. Ashraf, M. Elameen, N.H. Faisal, A.M. El-Sherik, Y.O. Elakwah, M.F.A. Goosen, Single asperity nanoscratch behaviour of HIPed and cast Stellite 6 alloys, Wear 312(1-2) (2014) 70-82.

[188] D. Klarstrom, J. Wu, Metallography and microstructures of cobalt and cobalt alloys, Materials Park, OH: ASM International, 2004. (2004) 762-774.

[189] P. Collins, R. Banerjee, S. Banerjee, H. Fraser, Laser deposition of compositionally graded titanium–vanadium and titanium–molybdenum alloys, Materials Science and Engineering: A 352(1-2) (2003) 118-128.

[190] A. Ambroziak, Friction welding of molybdenum to molybdenum and to other metals, International Journal of Refractory Metals and Hard Materials 29(4) (2011) 462-469.

[191] D. Wang, C. Yu, J. Ma, W. Liu, Z. Shen, Densification and crack suppression in selective laser melting of pure molybdenum, Materials & Design 129 (2017) 44-52.

[192] P.-k. Bai, W.-f. Wang, Selective laser sintering mechanism of polymer-coated molybdenum powder, Transactions of Nonferrous Metals Society of China 17(3) (2007) 543-547.

APPENDIX A

MECHANICAL PROPERTIES OF CO-CR-MO VS TI-6AL-4V

Table 8: Mechanical Properties of the Ti-6Al-4V and Co-28Cr-6Mo alloys [153]

Mechanical Properties	Ti-6Al-4V	Co-28Cr-6Mo
Young Modulus (GPa)	110-119	235-247
Tensile Strength (MPa)	862-1200	1290-1420
Yield Strength (elastic limit) [MPa]	786-910	760-839
Elongation [%]	10-14	25-29
Hardness [HV]	337-357	363-402

APPENDIX B

LENS CALIBRATION CURVES

For the Co-Cr-Mo prints, powder flow samples were collected from the nozzle head at different RPMs (from 2-6 with a step size of 0.5) with a constant carry gas flow rate to determine a "calibration curve" of mass flow in the system for the specific powder, in a specific hopper, in a specific position. The following was assumed regarding the prints made in this work: the volumetric flow curves are inherent attributes of the machine and mass flow of a system could be predicted by finding the slope of the appropriate volumetric flow cluster, translating it to mass flow through density, and basing mass flow calculations off the resulting curves.

B.1 Mass Flow in the LENS System

After calculating the appropriate parameters, the necessary mass flows are translated into RPMs for the appropriate hopper through the mass calibration curve (previously found from the volumetric flow curves). The RPM values are programmed into the machine, the LENS process begins, then the printing continues until completion or stop via an operator for machine/personnel safety reasons. Mass flow changes are controlled via the appropriate RPM for the hopper containing the use material.

B.2 Calculation of Used Processing Parameters

From the first design of experiments (DOE 1) that successfully printed Stellite, power, base speed, and carry gas flow rate were already known. The steps to determine

mass flow (and thus RPM) for each composition are through the following procedure with calculated values found in Table 9.

The higher average densities of Co-Cr-Mo and pure Mo meant that the larger hoppers should be used for this experiment to make sure enough powder could be stored at one time to complete the experiment in one go. Using this, the slope and intercept of the volumetric flow calibration curve was calculated with the linear regression tool Igor Pro. Slopes for both of the powders were then determine with no apparent difference between the two (values were the same to the 5^{th} decimal place). Both curves demonstrated almost the same slopes but with varying intercepts. The lighter material intercepted at 0.001 while heavier intercepted at a 0.024. Thus to be conservative, the intercept of 0.024 was used for this print.

Since Mo is 25% more dense than Co-Cr-Mo, it was used to run calculations for RPMS from 0.5-10 to determine the most reasonable values of mass flow for the varying compositions. From the range of RPMs, the volumetric flow was first calculated using the volumetric slope, volumetric intercept, and value of RPM (equation of line: $y = a + bx$), where y is the volume of powder for a given RPM, a is the intercept of linear regression, and b is the slope of the linear regression, and x is the respective RPM. For the mass of a given RPM through the density of the material. The process was then repeated for each value in the RPM range. The mass flow slope and intercept were calculated by translating the respective volumetric flow value from the materials' respective densities. This process built the needed information to translate the additional amount of Mo for a specific composition into RPMs.

Table 9: Calibration Curves for Mo and Co-Cr-Mo.

RPM	Volume Flow	Mass Flow	Slope (Vol)	Intercept (vol)
0.5	0.077965	0.8014802	0.10718	0.024375
1	0.131555	1.3523854		
2	0.238735	2.4541958	Slope (mass)	Intercept (Mass)
3	0.345915	3.5560062	1.1018104	0.250575
4	0.453095	4.6578166		
5	0.560275	5.759627		Mo Density
6	0.667455	6.8614374		10.28
7	0.774635	7.9632478		
8	0.881815	9.0650582		
9	0.988995	10.1668686		
10	1.096175	11.268679		
RPM	Volume Flow	Mass Flow	Slope (Vol)	Intercept (vol)
0.5	0.077965	0.654906	0.10718	0.024375
1	0.131555	1.105062		
2	0.238735	2.005374	Slope (mass)	Intercept (Mass)
3	0.345915	2.905686	0.900312	0.20475
4	0.453095	3.805998		
5	0.560275	4.70631		Co-Mo Density
6	0.667455	5.606622		8.4
7	0.774635	6.506934		
8	0.881815	7.407246		
9	0.988995	8.307558		
10	1.096175	9.20787		

Calculating potential mass flow rates for a specific composition, all possible RPMs for Co-Cr-Mo were considered, and respective additional amount of Mo (based on additional wt.% of Mo) was determined. In Figure 89, the RPM for Co-Cr-Mo is

given in the bold outlined box; the desired additional weight percent of Mo in the next column; followed by the mass flow needed to meet the desired criteria in the next column (determined by taking the mass flow for the respective RPM of Co-Cr-Mo and multiplying by the desired extra weight percentage). Finally, the necessary RPM is determined by solving the reverse linear regression equation ($x = \frac{y-a}{b}$), through the mass slope and intercept for Mo. Knowing the target composition is achieved through blending (in the melt poo/laser pool) of two separate and distinct powders, consideration to select process parameters to ensure enough of each powder to achieve the desired composition. From this, the proceeding classification criteria was used:

- RPM < 0: Unusable – cannot achieve composition (impossible marked as red)
- 0 < RPM < 0.1: Pick if no other valid option (large concern that device may not function properly at RPMs of < 0.1, providing stable mass flow: marked as yellow)
- RPM > 0.1: Preferred, use as first selection (confidence was held for stable mass flow at RPMs greater than 0.1: marked as green)

This classification provided final decisions for RPMs to achieve desired compositions where balancing the minimization of powder for Co-Cr-Mo was the major determination and achieving the largest possible mass flow rate of Mo for the accurate composition.

The Co-Cr-Mo powder flow was minimized since the original powder was packed in air and humidity levels were unknown. Thus the powder needed to be dried at 100 °C for a minimum of 12 hours in an arid, inert gas chamber to ensure proper flow of the powder within the LENS system. This batch process required a large lead time along

with an unknown amount of powder to complete the builds, a reserved approach was used to make sure enough powder could be used to complete the experiment in one attempt. This approach required a balance with the need to flow enough Mo to ensure homogeneous and accurate composition through the print.

	Additional Mo Wt%	Mo Mass Needed	Mo RPM
Stellite RPM = 9	6.00%	0.49845348	0.224974
	9.00%	0.74768022	0.451171
	12.00%	0.99690696	0.677369
	15.00%	1.2461337	0.903566
	18.00%	1.49536044	1.129764
	21.00%	1.74458718	1.355961

	Additional Mo Wt%	Mo Mass Needed	Mo RPM
Stellite RPM = 6	6.00%	0.33639732	0.077892
	9.00%	0.50459598	0.230549
	12.00%	0.67279464	0.383205
	15.00%	0.8409933	0.535862
	18.00%	1.00919196	0.688519
	21.00%	1.17739062	0.841175

	Additional Mo Wt%	Mo Mass Needed	Mo RPM
Stellite RPM = 8	6.00%	0.44443476	0.175947
	9.00%	0.66665214	0.37763
	12.00%	0.88886952	0.579314
	15.00%	1.1110869	0.780998
	18.00%	1.33330428	0.982682
	21.00%	1.55552166	1.184366

	Additional Mo Wt%	Mo Mass Needed	Mo RPM
Stellite RPM = 5	6.00%	0.2823786	0.028865
	9.00%	0.4235679	0.157008
	12.00%	0.5647572	0.285151
	15.00%	0.7059465	0.413294
	18.00%	0.8471358	0.541437
	21.00%	0.9883251	0.66958

	Additional Mo Wt%	Mo Mass Needed	Mo RPM
Stellite RPM = 7	6.00%	0.39041604	0.126919
	9.00%	0.58562406	0.30409
	12.00%	0.78083208	0.48126
	15.00%	0.9760401	0.65843
	18.00%	1.17124812	0.8356
	21.00%	1.36645614	1.012771

	Additional Mo Wt%	Mo Mass Needed	Mo RPM
Stellite RPM = 4	6.00%	0.22835988	-0.02016
	9.00%	0.34253982	0.083467
	12.00%	0.45671976	0.187096
	15.00%	0.5708997	0.290726
	18.00%	0.68507964	0.394355
	21.00%	0.79925958	0.497985

Figure 89: Mo RPM values measured against Co-Cr-Mo RPM values.

APPENDIX C

LENS MANUFACTURE OF PURE MO

C.1 Introduction

The objective of this work is to build and measure the validity of building a LENS made pure Mo build with process parameters estimated from a previous standard used in a study for Co-Cr-Mo ASTM F-75. This procedure was performed to measure the resulting structural integrity of LENS made Mo. The study was performed to determine porosity and feasibility of Mo builds. For this study, small scale Mo cylinders were made with same dimensions of 5 mm diameter and 5 mm height. Individual layers were deposited via LENS to reach the desired build height. Through this procedure, the solid Mo structures were not able to produce large HV values as compared to Co-Cr-Mo. These results show that despite Mo's large melting point, it can still be feasibly printed into a solid structure.

Mo is also a widely used refractory metal that can be used to produce Mo parts as well [189]. Due to the favorable energy state of metals in the period table group VI, like Mo, have high melting points. Mo specifically has a melting point of 2620 °C [190]. Mo particularly is an important refractory metal even though 6% of its total production is processed into structural applications. Mo has good physical-thermal properties such as high relative strength in high temperatures, low thermal expansion coefficient, and high conductivity in thermal and electrical fields. For joining Mo, vacuum soldering and electron beam welding has been described by various sources as being effective. Friction welding has also been reported as an alternative to these techniques.

Faidel et al. investigated Mo powder for development using SLM technology due to the ability of Mo to endure high temperatures [165]. In this case, process parameters such as laser power, laser velocity, and powder layer thickness were analyzed to create high density of the parts. In high temperature applications, Mo is suitable to be added but cracks can occur when welding occurs. In the resulting study, Faidel used spherical atomized Mo powder with 99.95% purity with 10-45 μm powder size. This work showed that Mo powder can yield stable parts, but porosity is high. If the overlap parameter of the laser is too small, the metal particles did not fully fuse together. The part stability reduced, and the number and size of defects increases. Higher density of the part can be achieved by increasing the laser power or lowering the layer thickness. Wang et al. later created a dense, crack free pure Mo via SLM [191]. In work pertaining to compositional gradients, Collins et al. compositionally graded binary Ti-V and Ti-Mo alloys have been deposited using LENS [192].

In this study, LENS prints of pure Mo was attempted. No previous studies have reported successful builds of pure Mo. Similar methods have been utilized in SLM with a large amount of porosity, but this undertaking is to observe the ability to build the structure and observe the efficacy of the method and structural integrity. Since LENS allows for the fabrication of complex parts, for a hard to machine metal, the understanding of LENS provides manufacturers an opportunity to make previously unattainable material structures for applications heretofore impossible.

C.2 Materials and Methods

For this study, the process parameters were changed based on the previous study on Co-Cr-Mo. Since Co-Cr-Mo has a lower melting point, it was pragmatic to increase the laser power in order to completely melt the powder and make a layered structure. 350W was the optimum power choices from the previous experiment with Co-Cr-Mo only and thus utilizing that power, we wanted to observe its efficacy in depositing. 400W was kept from the previous experiment as the higher melting point would favor a higher power utilizing than for Co-Cr-Mo. 450W was the highest bound that was outside the bounds of the original designs of experiments. For powder feed rate, 5 RPM was kept consistent throughout the builds as this feed rate had produced the most consistent builds in our previous work.

To study the samples, the inner microstructure and defects were etched by electro-polishing using NaOH solution as the electrolyte at voltage of 10V. Micrographs were obtained using scanning electron microscopy via the Tescan Lyra SEM. Samples then underwent Vickers hardness testing on both horizontal and vertical planes. 3 indents were made adequately far apart in order for proper readings to be obtained and consistency in measurements. Nanoindentation patterns were made in a 2x3 array on each orientation (horizontal, vertical) with 50 μm apart to ensure that indents feel within different grains.

C.3 Results

C.3.1 Analysis of outside surface

Macroscopic analysis of the outside surface was performed first. Samples appear to have a basketweave structure where layers fold into each other. Samples were not built to the intended height of 8 mm. Samples appear to have had difficulty building due to large cooling rates associated with DED along with the introduction of the Mo powder which possesses a high melting point. Samples appeared with a jagged edge around the circumference of the top layer. Samples are gray from the bottom to the top layer with a copper color top layer.

SEM of the outside surface (Figure 90) showed a similar threaded type of structure. Samples show waviness in the layers which contribute to the basketweave type structure. Ridges appear in a periodic structure while valleys are shown as the second half. Basketweaves are shown as structures that fold into each other with repeating patterns. There is a small amount of unmelted powder on the outer surface other than the top layer. The top layer shows a large portion of unmelted powder. Some cracks are shown on the outside surface as well. There appear to be some regions where melting did not occur completely that show a large amount of unmelted powder and recesses that show lack of cohesion.

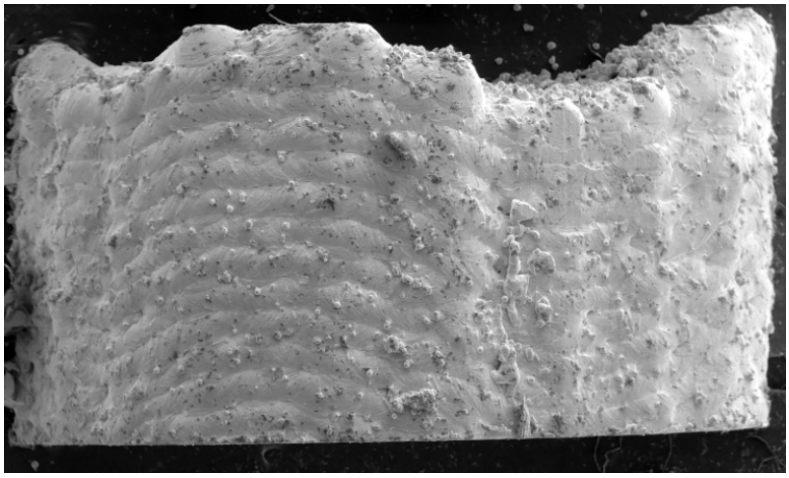

Figure 90: SEM image of outside surface of LENS pure Mo sample.

C.3.2 Microindentation

Microindents were made on the surface of each of the horizontal and vertical surfaces. The average indent size was 75 μm x 75 μm. According to the data shown in Figure 91, 350W samples performed the best in the Vickers Hardness, this is due to a phenomenon that was observed in our Co-Cr-Mo experiments. Higher powers cause deeper melt pools that reduce the efficacy of the structure. These Mo builds already appear to have a large amount of porosity according to experiments done by Faidel et al. The steady decrease in hardness values indicates a similar trend for both horizontal and vertical planes

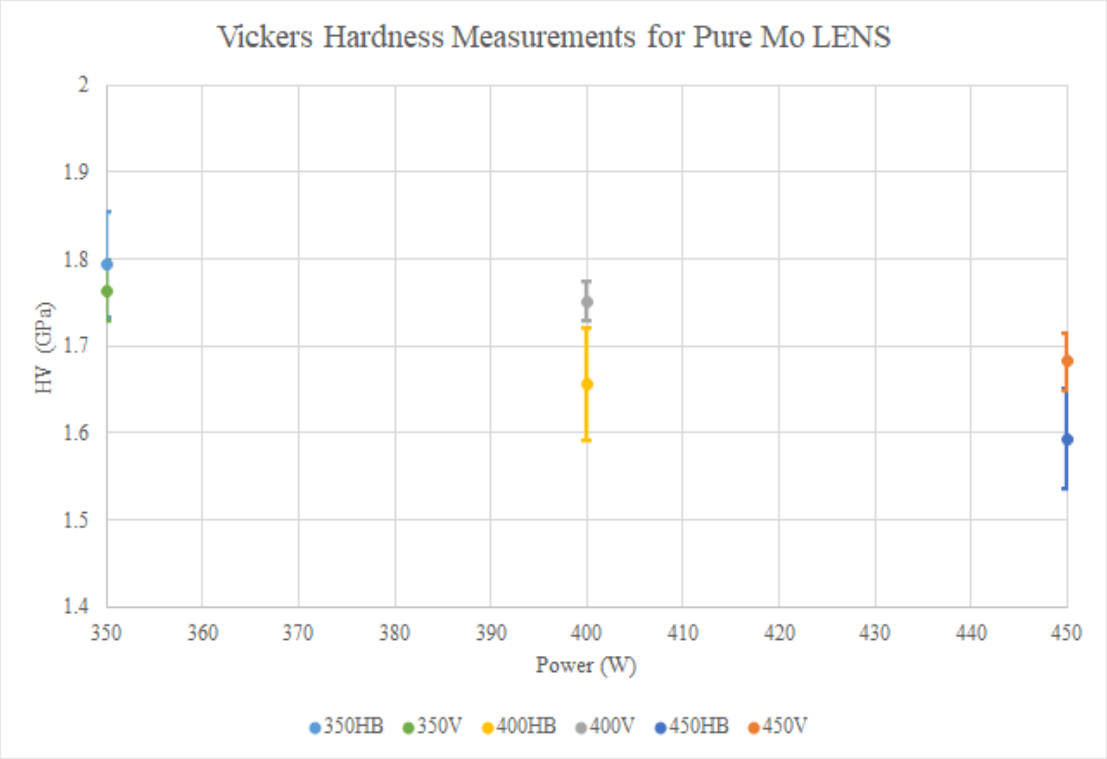

Figure 91: Vickers Hardness measurements for LENS Pure Mo.

C.3.3 Nanoindentation

In nanoindentation measurements shown in Figure 92, there appears to be larger values for the vertical plane. Across the board, the values for the horizontal plane are much smaller but also do not deviate very much. Reduced modulus appears to grow larger from 350 to 400 indicating that the process parameters are more optimized for Mo with 400W although the hardness value is the lowest. This may be due to the lack of fusion of powder as there appears to be a good deal of unmelted powder as shown in the SEM outside surface pictures above. Secondly, 450W prints were getting too hot during

the build process which may have caused the highest hardness values but also contribute the lack of structural integrity. The reduced modulus is lowest at 450W.

Figure 92: LENS Pure Mo Hardness Measurements

C.3.4 Nanoscratch

Nanoscratch test results (Figure 93) show that horizontal scratches decline as the power is increased, this may be due to the higher power reducing surface structural integrity. Vertical scratch mechanical behavior appears to follow an opposite trajectory similar to nanohardness.

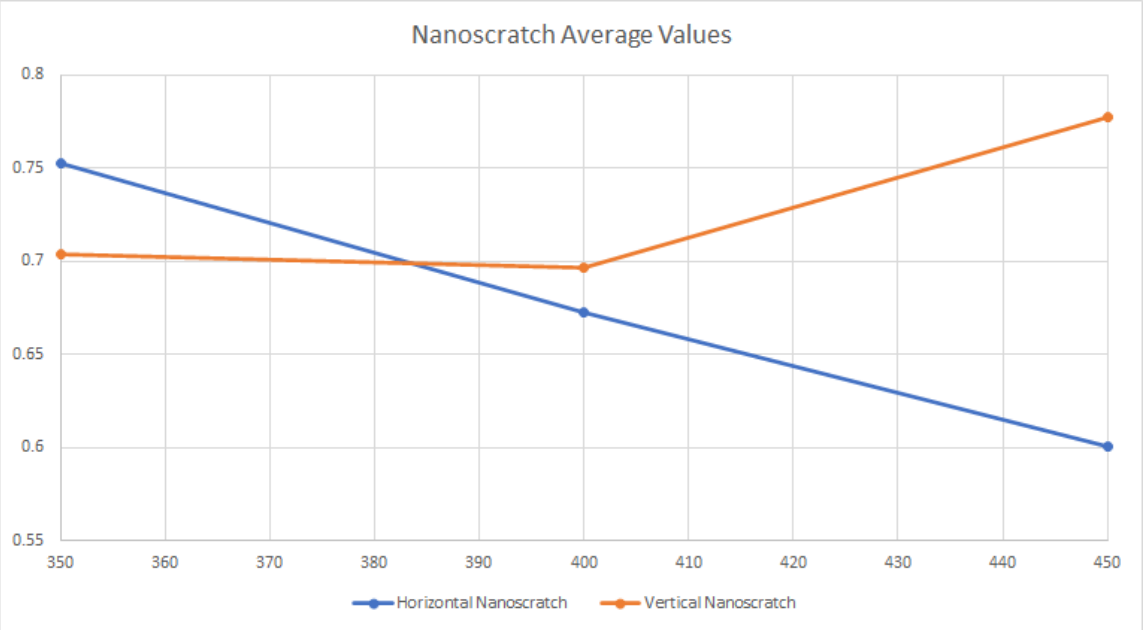

Figure 93: Nanoscratch Average Values for LENS Pure Mo.